PB2003-100181

# MONITORING OF LONG-TERM CREEP AND TEMPERATURE BEHAVIOR OF THE JAMESTOWN-VERRAZZANO BRIDGE

FHWA-RIDOT-RTD-02-1
JUNE 2002

George Tsiatas
Everett E. McEwen
Hong Chen

University of Rhode Island

Sponsored By Rhode Island Department of Transportation

Rhode Island
Department of Transportation

RESEARCH AND
TECHNOLOGY
DEVELOPMENT

**Technical Report Documentation Page**

| 1. Report No. | 2. Government Accession No. | 3. Recipient's Catalog No. |
|---|---|---|
| FHWA-RI-RTD-02-1 | | |

| 4. Title and Subtitle | 5. Report Date |
|---|---|
| Monitoring of Long Term Creep and Temperature Behavior of the Jamestown-Verrazzano Bridge | June 2002 |
| | 6. Performing Organization Code |

| 7. Author(s) | 8. Performing Organization Report No. |
|---|---|
| George Tsiatas, Everett E. McEwen, and Hong Chen | URI-CVE-ST02-1 |

| 9. Performing Organization Name and Address | 10. Work Unit No. (TRAIS) |
|---|---|
| Civil Engineering Department<br>University of Rhode Island<br>Kingston, RI 02881 | 11. Contract or Grant No.<br>SPR-2 (25) 2221 |

| 12. Sponsoring Agency Name and Address | 13. Type of Report and Period Covered |
|---|---|
| Rhode Island Department of Transportation<br>Two Capitol Hill<br>Providence, RI | Final Report |
| | 14. Sponsoring Agency Code |

15. Supplementary Notes

16. Abstract

The Jamestown-Verrazzano bridge is a double-cell segmental concrete bridge that was constructed in Rhode Island in the early 90's to replace the aging old Jamestown bridge. In order to verify design procedures and expand the knowledge of the time varying effects on segmental bridges, a monitoring program was undertaken. Two sections of the bridge were instrumented with thermocouples and Carlson strain meters. An Automated Data Acquisition System (ADAS) was also installed for continuous and remote monitoring of the temperature and strain sensors. This report provides the data collected during a one year period, from September 1997 to September 1998.

Seasonal as well as characteristic daily temperature variations are studied. A probability density function modeling the distribution of the extreme temperature differentials is developed. Temperature distributions in the superstructure are nonlinear. Maximum positive and negative gradients are developed. A good agreement is obtained with gradients provided in recent AASHTO design guidelines. Temperature gradients result in $50\times10^{-6}$in/in strains.

Concrete creep and shrinkage strains obtained from experimental test data are compared to standard prediction methods established by ACI and two European specifications, namely the Improved CEB-FIP MC 78 specification and the CEB-FIP 90 code.

| 17. Key Word | 18. Distribution Statement |
|---|---|
| Segmental Bridges<br>Monitoring<br>Creep<br>Temperature Effects | No Restrictions |

| 19. Security Classif. (of this report) | 20. Security Classif. (of this page) | 21. No. of Pages | 22. Price |
|---|---|---|---|
| Unclassified | Unclassified | 193 | |

## Disclaimer

This report was sponsored by the Rhode Island Department of Transportation. The contents of the report reflect the views of the authors who are responsible for the facts and accuracy of the data presented herein. The contents do not necessarily reflect the official views or policies of the Rhode Island Department of Transportation or the US Department of Transportation's Federal Highway Administration. This report does not constitute a standard, specification, or regulation.

TABLE OF CONTENTS

## LIST OF TABLES

## LIST OF FIGURES

# EXECUTIVE SUMMARY

The Jamestown-Verrazzano bridge is a double-cell segmental concrete bridge that was constructed in Rhode Island in the early 90's to replace the aging old Jamestown bridge. The approach spans were constructed using the span-by-span lift method whereas the cast-in-place cantilever technique was used in the middle portion. Segmental concrete bridges represent a relatively new type of construction in the United States. One of the design problems of such bridges is the time dependency of various properties including creep and shrinkage effects. In addition, thermal effects can be important design factor due to the large superstructure mass.

In order to verify design procedures and expand the knowledge of the time varying effects on segmental bridges, a monitoring program was undertaken. Two sections of the bridge were instrumented with thermocouples and Carlson strain meters. The monitoring was manual at first but an Automated Data Acquisition System (ADAS) was installed in the Fall of 1997. This allowed for continuous and remote monitoring of the temperature and strain sensors. This report provides the data collected during a one year period, from September 1997 to September 1998.

Seasonal as well as characteristic daily temperature variations are studied. A probability density function modeling the distribution of the extreme temperature differentials is developed. This can be used for predictions of the occurrence of various temperature differentials. It is found that the average temperature differential between the top and bottom slab is about 6 °F, but temperature differentials reached 35 °F well above the 10 °F used during the original design of the bridge. A small temperature difference between the north and south side of the bridge is also observed (less than 3 °F).

Temperature distributions in the superstructure are nonlinear. Maximum positive and negative gradients are developed. A good agreement is obtained with gradients provided in recent AASHTO design guidelines. Temperature gradients result in $50\times10^{-6}$in/in strains. Positive temperature gradients invoke compressive thermal stresses and negative temperature gradients induce tensile thermal forces in the bottom of the bridge.

Concrete creep and shrinkage strains obtained from experimental test data are compared to standard prediction methods established by ACI and two European specifications, namely the Improved CEB-FIP MC 78 specification and the CEB-FIP 90 code.

The measured shrinkage strains agree well with the ACI 209 predictions. The two European model codes predict shrinkage strains that are close to each other but lower than the measured and the ACI results. The opposite is true for the case of the creep strains where ACI 209 results are lower than the measured creep whereas the CEB 90 and CEB 78 results are comparable to the measurements. However, the total strains, i.e. both shrinkage and creep strains considered togather are comparable for all cases. These results are in line with other studies.

# 1. BRIDGE DESCRIPTION AND INSTRUMENTATION

## 1.1 Bridge Description

The Jamestown-Verrazzano Bridge, Fig. 1.1, is located over the Narragansett Bay between North Kingstown and Jamestown, to the south of Providence, Rhode Island. The total length of the bridge is 7,350 ft with a main span navigational clearance of 600 ft in horizontal and 135 ft in vertical direction. The roadway width of the bridge is 74 ft and supports two lanes of traffic in each direction. The bridge is made up of 52 spans, 29 of which comprise the approach spans and the remaining 23 are the main structure. Eleven spans of the main structure form the west approach, nine spans form the east approach and the remaining three comprise the main span section. It is the main span section which is the focus of the present study.

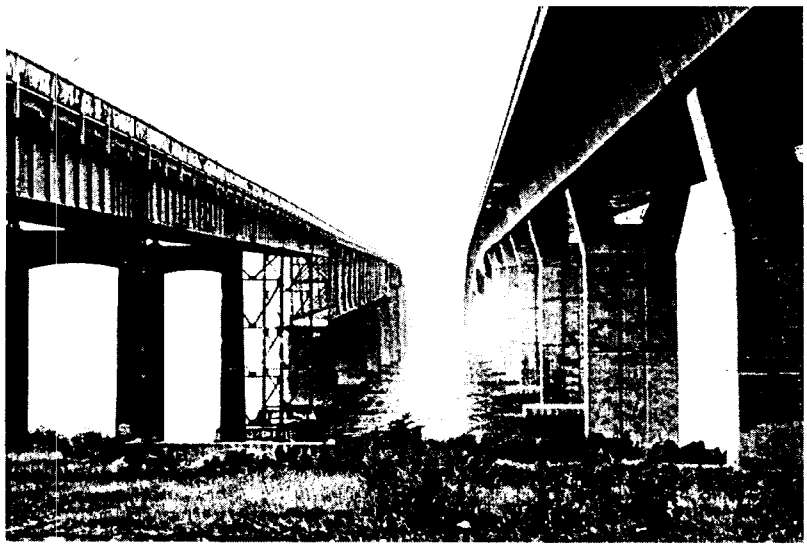

Fig. 1.1 The Jamestown-Verrazzano Bridge Looking West.
The Old Jamestown Bridge is also Shown on the Left

The main bridge structure consists of three spans made from a double-cell, post tensioned concrete box girder built by the balanced cantilever, cast-in-place, box girder technique. The center span is 674 ft long and the two side spans are 359 ft long each. The depth of the box girder changes from 10 ft at the main span closure to 30 ft 10 in at the pier supports.

### 1.2 Field Instrumentation

In 1992, during the Jamestown-Verrazzano bridge construction, strain gages and thermocouples were installed at selected locations in the main span of the bridge as an Experimental Features Project by Construction Technology Laboratories, Inc. (CTL) and RIDOT. The locations were selected during a joint meeting between CTL, RIDOT, and Dr. E. McEwen of the University of Rhode Island (URI) during a May 6, 1992 meeting in Saunderstown, RI. During that meeting two bridge cross-sections were selected for instrumentation: a) the main span closure segment to measure longitudinal strain and temperature gradients, and b) the segment adjacent to pier 14 to measure longitudinal strains (P14MS1), Fig. 1.2.

In order to measure concrete strains, a total of 19 Carlson strain meters Type A-10 with 4-wire conductor cable were installed. Eight of the meters were installed in the main span closure segment and the remaining eleven were installed in segment P14MS1. Out of the eight strain meters in the main span closure segment, four were embedded in the concrete by placement in the formwork prior to concrete casting but the remaining four were retrofitted and placed after concrete setting in order to establish some correlation between the embedded and the retrofitted ones. Fig. 1.3 shows the exact locations of the embedded and retrofitted strain meters in the main span closure segment. The eleven Carlson strain meters that were placed in

segment P14MS1 were all retrofitted since the installation occurred after the concrete had been placed and cured. Fig. 1.4 shows the exact locations of the gages in P14MS1. Figures 1.5 and 1.6 show a typical embedded strain gage and a typical retrofitted strain gage respectively.

Temperature measurements were made with Type T thermocouples and the Carlson strain meters which can also provide temperatures. Thermocouples were located only at the main span closure segment at four locations; two in the top slab and two in the bottom slab of the double box-girder, Fig. 1.7. A sensor located under the main span closure section provides outside bottom temperature readings. The temperatures provided by the Carlson strain meters are used primarily for strain correction calculations.

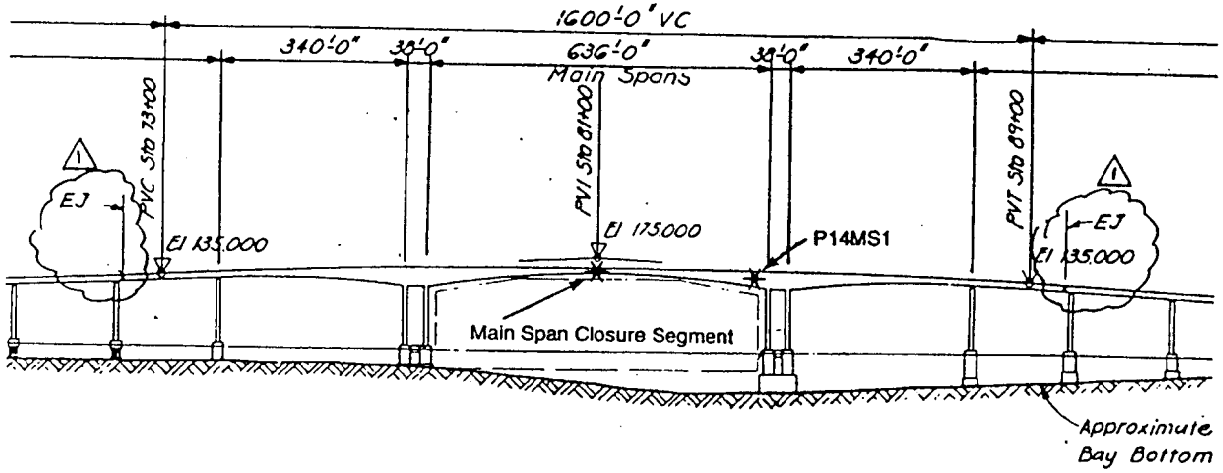


Fig. 1.2 Main Span Section Showing Locations of Two Instrumented Segments

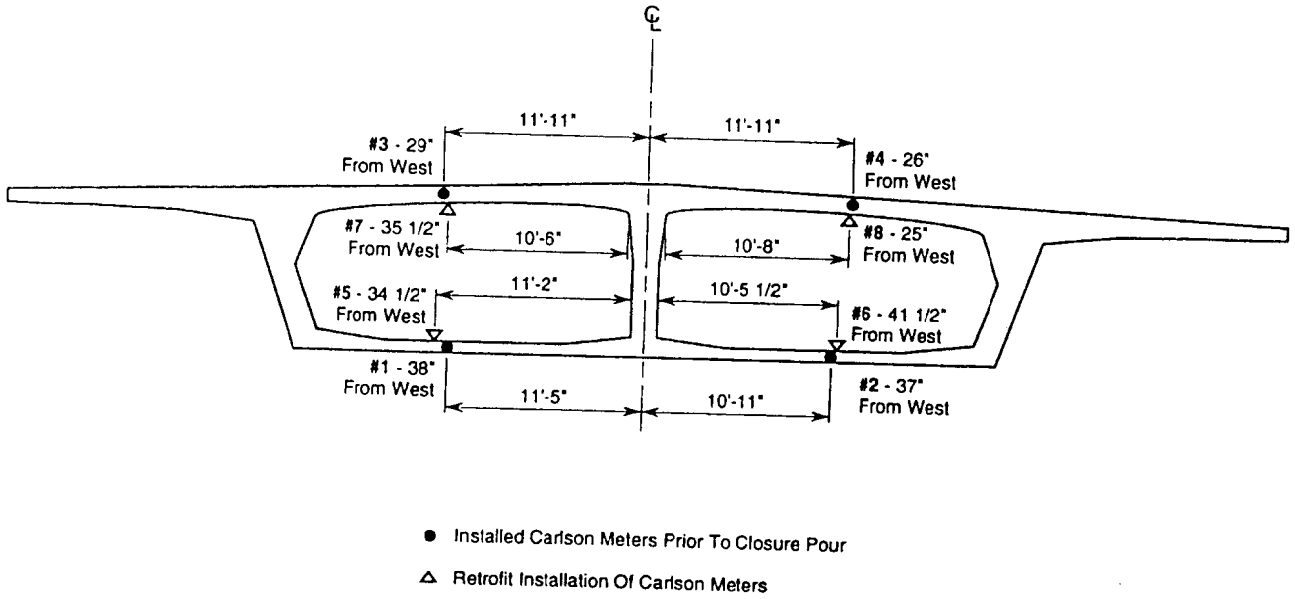


Fig. 1.3 Locations of Carlson Strain Meters (Looking West) at Main Span Closure Segment

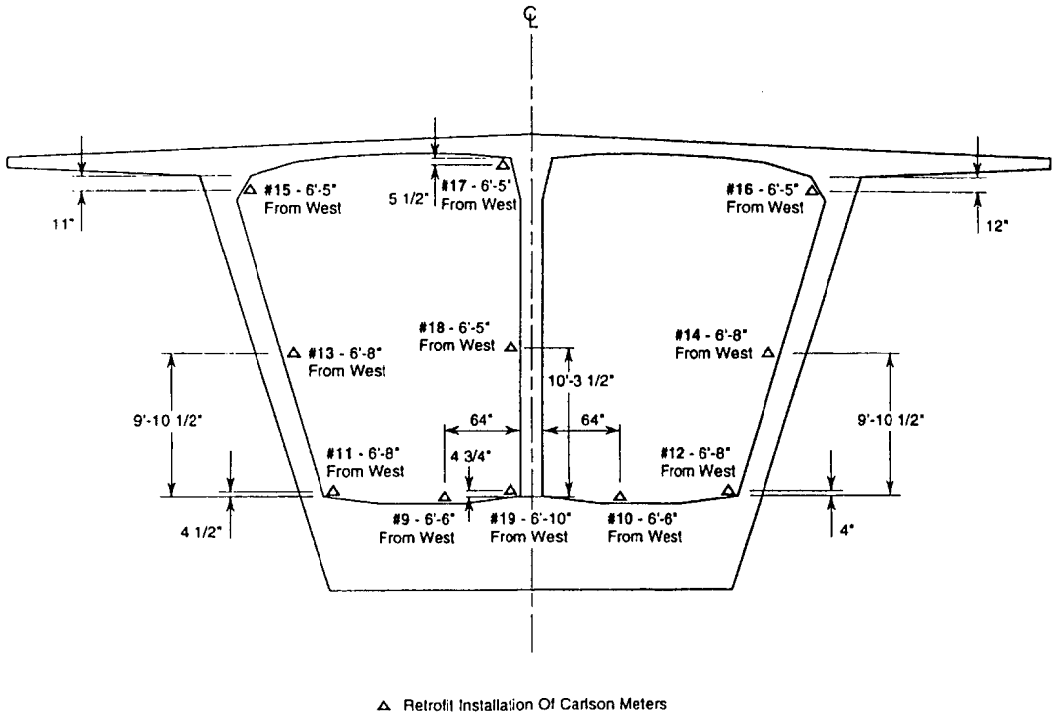


Fig. 1.4 Locations of Carlson Strain Meters (Looking West) at Segment P14MS1

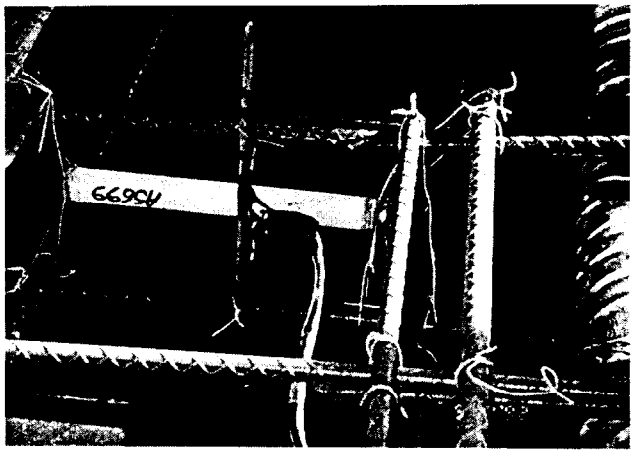


Fig. 1.5 Embedded Carlson Strain Meter (A5699)

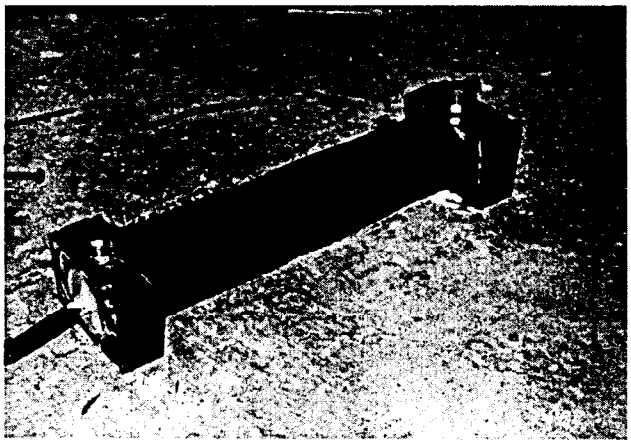

Fig. 1.6 Retrofitted Carlson Strain Meter

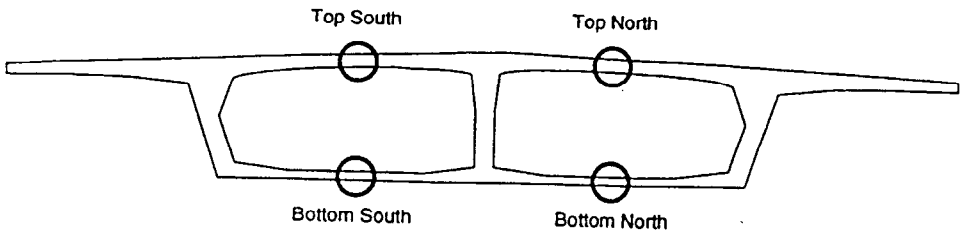


Temperature Gradient Measurement Locations
(Approximate center of each box girder centerline)

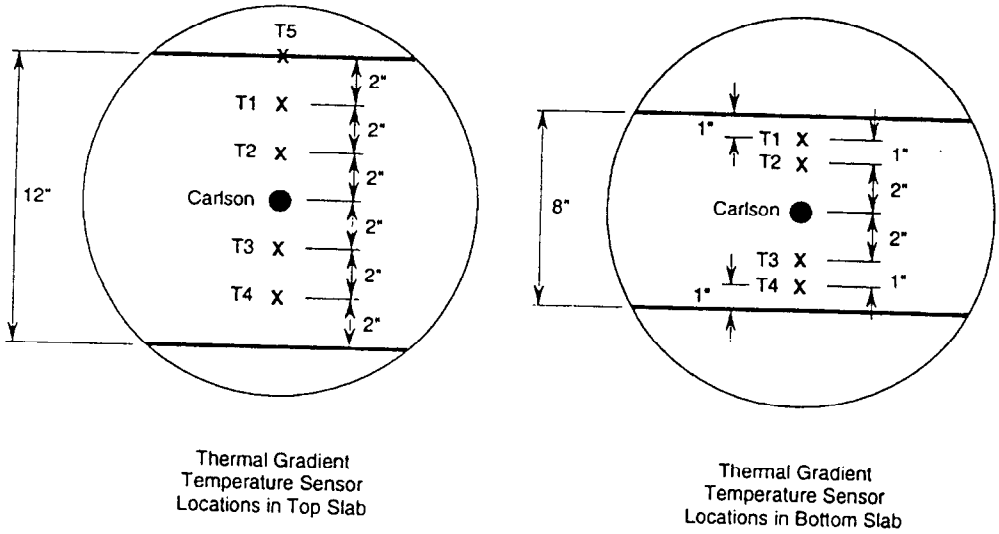


Thermal Gradient
Temperature Sensor
Locations in Top Slab

Thermal Gradient
Temperature Sensor
Locations in Bottom Slab

Fig. 1.7 Location of Temperature Measurements in Main Span Closure Segment

## 1.3 Manual Measurements

Initial manual readings were taken during and after the construction of the bridge by CTL and RIDOT. These are documented in a 1994 Report by Weinmann and Russell titled "*Instrumentation of the Jamestown-Verrazzano Bridge at Jamestown, Rhode Island.*" Most of these readings were taken in 1992 soon after the completion of the mid-span segment closure. Nine readings are listed in 1993 and one in 1994. It is noted that the T5 thermocouple located in the top slab of the north girder stopped functioning on July 9, 1992. One additional reading was taken by RIDOT in July, 1996.

On January 1st, 1997 the current project was initiated with main objective to study long term creep and temperature effects on the main span of the Jamestown-Verrazzano bridge. In order to facilitate the research project, it was decided to install an Automatic Data Acquisition System (ADAS). The first task of the URI team was to continue manual readings until the time that the ADAS system was installed and operable. The purpose of this task was to ensure that the sensors were operating without any problem before the ADAS system could be installed.

There were four such readings made by URI, specifically on February 6, May 16, July 11 and August 27, 1997. During these times a team of URI and RIDOT personnel entered the bridge at the Jamestown shore, walked through the box girder and took measurements at the two locations, Fig. 1.8. All data were reduced using the procedures and formulae provided by CTL. These interim measurement readings are included in "*Interim Report, Task 1*" by Tsiatas, G. and Chen, H., October 1997 and are not repeated here. In summary, the plots of the strain and temperature data appeared to be in line with previous readings in CTL report. It was therefore assumed that the sensors were functioning properly.

## 1.4 Automatic Data Acquisition System, ADAS.

In the week of September 15, 1997, CTL installed the ADAS inside the Jamestown-Verrazano bridge. This allowed for automated acquisition of the data via modem. The ADAS station is located in the main span closure segment and consists of a Data-Logger and three Multiplexers, Figs. 1.9 and 1.10. Multiplexer1 connects the eight Carlson strain meters in the main span closure segment. Multiplexer2 registers the eleven Carlson strain meters in segment P14MS1 and Multiplexer3 connects the nine thermocouples in the main span closure segment.

Instructions for the operation of the Data-logger system, including remote access and control, are included in a Report by CTL, (Weinmann, et al. 1997). CTL also provided a procedure to import the data into Excel for further analysis. It is noted that thermocouple readings are directly in °F. Carlson strain meter readings need to be reduced using the equations and methods of Appendix A to obtain engineering quantities.

A computer station with a modem was set up in the Structural Engineering Laboratory at URI in order to facilitate the continuous monitoring of the bridge, Fig. 1.11. The station became operable on September 19, 1997. For the purposes of this project, the bridge was continuously monitored for a year with readings taken at least every 2-hours with most readings taken at every hour, some readings at 30-minute intervals and some of the readings at 15-minute intervals. These readings are presented and analyzed in Chapter 2 of this report.

Fig. 1.8 URI Students Take Measurements Inside Jamestown Bridge

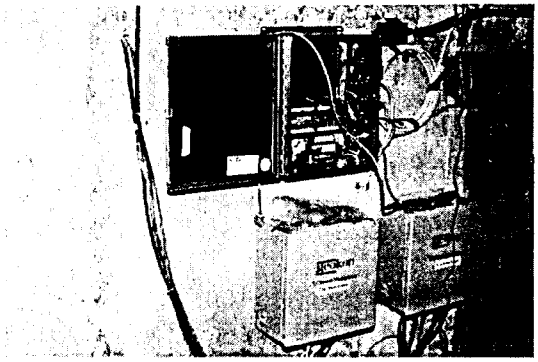

Fig. 1.9 ADAS System

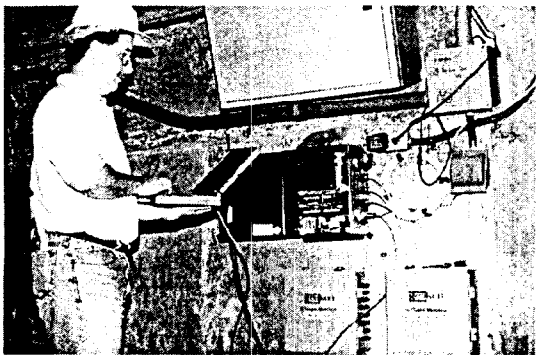

Fig. 1.10 J. Bak from RIDOT checks System

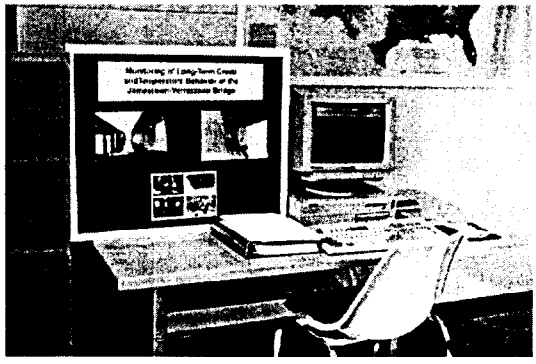

Fig. 1.11 Computer and Modem Setup at URI

# 2. DATA MEASUREMENT AND PROCESSING

## 2.1 Introduction

Data were collected with ADAS from September 21, 1997 to September 23, 1998. Most readings were taken at 2-hour or 1-hour intervals to capture seasonal variations. On selected periods, readings were taken every 30-minute or 15-minute intervals to obtain accurate daily characteristics. The raw data downloaded from ADAS were processed using the CTL templates to obtain useful engineering parameters. In the case of the Carlson meters the data had to be further reduced using the procedure outlined by CTL (Weinmann, 1994) in order to obtain the temperatures and strains.

The following data are presented and analyzed in the present chapter:

- Seasonal concrete temperatures at main span closure (section 2.2)
- Daily concrete temperatures at main span closure (section 2.3)
- Seasonal temperatures from Carlson Strain Meters (section 2.4)
- Seasonal strain measurements (section 2.5)
- Daily strain measurements (section 2.6)

Finally, section 2.7 presents a comparison of temperatures between the north and south girders. All results appear reasonable and follow intuitive patterns.

## 2.2 Seasonal Concrete Temperature Measurements

The seasonal temperature variations in the top and bottom slabs of the main span closure segment are shown in Figures 2.1 through 2.8. By analyzing the entire data set, it was determined that peak temperature variations occur around 2:00 p.m. whereas the bridge is at the most stable

temperature condition at 6:00 a.m. Figs. 2.1, 2.2, 2.3, and 2.4 show the temperatures for both the north and south sides of the bridge at main span closure segment as measured at 6:00 a.m. Figs. 2.5, 2.6, 2.7, and 2.8 present the same quantities but for 2:00 p.m. The figures include temperature readings from the thermocouples as well as the embedded Carlson meters at the respective locations. It should be noted that thermocouple T5 at the top north slab is not functioning and the corresponding temperatures are not available.

The following comments can be made by inspecting Figs. 2.1 to 2.8:

i) A clear seasonal variation is obvious with temperatures dropping during the winter months and rising again in early spring. There is a very good agreement between the temperatures in September 1997 and the temperatures in September 1998. It should be noted that this was an unusually mild winter and no single digit temperatures were observed in the bridge.

ii) At 2:00 pm the concrete temperature variation within the bridge is the highest and at 6:00 am it is the smallest. The variation is much bigger in the top slab whereas it is smaller in the bottom slab. Solar exposure of the top of the bridge appears to be the main factor contributing to larger temperature variations within the top slab. The temperature variation in the bottom slab at 6:00 am is very small.

iii) The temperatures measured with the Carlson meters show some small difference from the temperatures obtained using the thermocouples. It should be noted that the thermocouples are in direct contact with the concrete whereas the Carlson meters measure the temperature of a strain meter which is enclosed and is not in a direct contact with the surrounding concrete. Typically the Carlson meters lag behind the thermocouples getting warmer or cooler at a slightly slower rate.

iv) The temperature variation is not linear within the slab. For example the temperature

difference between T1 and T2 is much bigger than the difference between T3 and T4.

v) The readings at T5 are typically larger than any other reading at 2:00 pm and smaller at 6:00 am. That clearly demonstrates that the top of the bridge is typically warmer during the day but cooler during the night.

vi) The lowest temperatures occurred on top of the bridge (thermocouple T5) during a winter morning. At that instant, the bottom of the bridge was warmer than the top and the maximum negative thermal gradient took place. Maximum positive temperature gradients usually occur in the summer months but due to the unusual weather of this year some of the peak temperatures and the corresponding maximum positive gradients happened late spring.

## 2.3 Daily Concrete Temperature Readings

In order to study the daily concrete temperature variations, it was desirable to concentrate on time periods with large temperature fluctuations. To this effect, Fig. 2.9 shows the outside bottom temperature variations at 6:00 am and 2:00 pm for the whole year under study. Fig. 2.10 is developed by looking at the temperature differences between 6:00 am and 2:00 pm. A positive value indicates that the temperature increased, whereas a negative value signifies that during that particular day the temperature dropped from the early morning to the afternoon. With the help of Figs. 2.9 and 2.10 seven 48-hour time periods were selected to evaluate daily concrete temperature variations. Four time periods correspond to maximum temperatures and three time periods correspond to minimum temperatures. Table 2.1 lists the exact time intervals of the seven periods.

| | Fall | Winter | Spring | Summer |
|---|---|---|---|---|
| Max Temperature | Sept. 21-23, 1997 | January 13-15, 1998 | May 21-23, 1998 | Sept. 5-7, 1998 |
| Min Temperature | | January 25-27, 1998 | April 27-29, 1998 | July 21-23, 1998 |

Table 2.1 Selected Critical Dates for Analysis of Daily Temperature Changes

Figures 2.11 through 2.38 present the temperature variations in the top and bottom slabs for both north and south girders at the main span closure segment. All 48 hour segments start from 12 noon and end at 12 noon 48 hours later. The following observations can be made by inspecting Figs. 2.11 to 2.38:

i) Temperature variations are large in the top slab but they are much smaller in the bottom slab. In fact, within the bottom slab the temperature varies only by a few degrees whereas in the top slab the variation can get closer to 26 °F. Solar exposure of the top of the bridge appears to be the main factor contributing to larger temperature variations within the top slab.

ii) Larger temperature variations are indicated in the early fall and late spring seasons. This is consistent with other studies who have found biggest temperature variations during the fall and spring seasons.

iii) The nonlinear variation of the temperature within the thickness of the slab is evident. For example the temperature change between thermocouples T1 and T2 is much larger than the temperature difference between T3 and T4.

iv) The temperature obtained from the Carlson strain meters is not consistent with the

thermocouples. The difference is usually small.

v) 6:00 AM and 2:00 PM are the approximate times when the top slab temperature becomes the smallest and largest respectively. This is also indicated in other studies (Shiu, et al. 1991).

vi) It appears that at 8:00 AM and 8:00 PM the temperature variation within the slab is very small since these are the approximate times that the plots of the top and bottom thermocouples within a slab switch sides. One would expect that at these times concrete strains due to temperature gradients would be minimum.

### 2.4 Seasonal Temperatures from Retrofitted Carlson Strain Meters

Fifteen retrofitted Carlson strain meters were installed in the bridge, four at the main span closure segment and eleven at the pier P14MS1 section. Figs. 2.39, 2.40, and 2.41 show the Carlson temperatures at pier 14MS1 from 9/19/97 to 9/23/98 at 2:00 pm. Fig. 2.42 presents the temperatures from the retrofitted Carlson meters at the main span closure segment. The following comments can be made from these figures:

i) All temperature data follow the expected seasonal pattern, i.e. drop during the winter, rise in early spring, and peak in the summer.

ii) These are temperatures from the retrofitted strain meters. The readings are basically the temperatures in the cell of the box girder section. In the case of the pier, the cell is very deep, since the box girder at that location has a depth of about 30 ft. In the case of the main span closure section the cell is smaller since the box girder at that location has a depth of about 10 ft. The variation of the data at any given day is very small for the case of the main span closure segment as can be seen from Fig. 2.42. The variation is somewhat larger,

although still small for the case of the pier, Figs. 2.39, 2.40, and 2.41.

iii) At the pier support there is a 3 °F to 7 °F temperature difference between the north and south cell. The temperature difference between the two cells is smaller at the main span closure segment, of the order of 1 °F to 2 °F. The cell of the south side has consistently higher temperature than the corresponding north cell. This difference is due to different solar exposure due to the orientation of the bridge.

## 2.5 Seasonal strain measurements

The raw data from the Carlson strain meters were processed into strains using the formula in Appendix A. Measured concrete strains represent concrete movements recorded between the date of the measurement and the zero readings taken when the gages were installed. Figs. 2.43, 2.44, 2.45, 2.46, and 2.47 present the one-year strains at 2:00 p.m. and Figs. 2.48, 2.49, 2.50, 2.51, and 2.52 show the year around seasonal strains at 6:00 a.m. Positive values indicate compressive strains whereas negative values indicate tensile strains. The gages measure long term concrete strains. Since most of the creep and shrinkage have already taken place, the variations of the strain between 6:00 a.m. and 2:00 p.m. are mostly due to the temperature changes. Strain readings in this study have been adjusted to a reference temperature of 73 °F.

Most of the strain measurements can be explained by solar radiation. The following observations can be made:

i) The strain variations at 2:00 pm are bigger than the variations at 6:00 am.

ii) Seasonal variations in the main span closure section are bigger during the spring.

iii) Strains at retrofitted meters show a small but gradual increase during the winter period.

iv) At the main span closure segment the strains from the embedded meters at the north side are

larger than the ones in the south side. This is consistent with the manual readings since the beginning of the monitoring. The difference between north and south sides is much smaller in the case of the retrofitted meters.

v) At the main span closure segment there is a large difference between the data from the embedded and the retrofitted meters. The values of the retrofitted meters are much smaller. This, again, is consistent with the manual readings.

vi) The strains from the retrofitted meters at the pier need to be further examined because they do not always follow a specific pattern. For example in certain cases the values from one meter are much different from the rest with no clear pattern. The validity of the retrofitted meters still needs to be determined. It is possible that in the case of some meters the anchoring to the concrete slab does not transmit all concrete deformations to the meter.

The measured strain depends on many factors such as concrete shrinkage and creep, seasonal and daily temperature effects, and added dead load among others. It is noted that the embedded strain gages started registering strain when the main span closure took place. Retrofitted gages were installed later, after the concrete had already hardened. Table 2.2 compares the strains recorded one year after the main span closure with strains recorded about six years after the main span closure. The table shows that for the embedded gages strains increased somewhat. However, no clear pattern is observed for the case of the retrofitted gages.

| Gage No | 1:45 pm on 6/11/93 | 2:00 pm on 9/22/98, |
|---|---|---|
| 1 | 642 | 742 |
| 2 | 798 | 907 |
| 3 | 356 | 538 |
| 4 | 526 | 725 |
| 5 | 159 | 83 |
| 6 | 112 | 124 |
| 7 | 40 | -5 |
| 8 | -47 | -29.6 |
| 9 | 64 | -25 |
| 10 | - | -24.5 |
| 11 | 58 | -13.5 |
| 12 | -37 | 243 |
| 13 | 28 | -70 |
| 14 | -128 | -56 |
| 15 | 23 | -19 |
| 16 | 101 | 12.6 |
| 17 | -31 | -117 |
| 18 | 132 | 23 |
| 19 | 62 | 19 |

Table 2.2 One Year and Six Year Concrete Strains ($10^{-6}$)

## 2.6 Daily Concrete Strain Monitoring

Figures 2.53 through 2.87 present the daily variations of the strain data for seven sets of 48 hour periods. These are the same time periods as the ones used to show the daily variation of the thermocouples. The following comments can be made based on these figures:

i) At an enlarged scale the data from the embedded strain meters show a small daily variation. Note that the peaks relate to a certain degree with the temperature peaks determined by thermocouple T3 which is close to the Carlson meter. This peak is later in the day than the temperature peak of the thermocouple T5 located at the top of the slab. Thermocouple T5 usually peaks about 2:00 PM, whereas thermocouple T3 peaks around 6:00 PM.

ii) Comparisons of the strains in the top and bottom slabs indicate that there is a distinct time lag in the fluctuation of strains between the top and bottom slabs. It is between 8 to 12 hours in the middle of the main span section and 2 to 8 hours in the pier section. In addition, the magnitude of strain fluctuation is bigger in the top slab than the bottom slab especially in the pier section. This may be caused by the temperature effects since the temperatures also show bigger variations in the top slab than the bottom slab. An additional study of strain-temperature variations is included in the next chapter.

iii) The irregularities of the retrofitted Carlson meters appear also in the daily strain variations. The applicability of these sensors needs to be further studied.

## 2.7 North-South Temperature Differences

In order to evaluate the effect of bridge orientation on temperatures registered, the temperature differences between the north and south side of the bridge are plotted in Figs. 2.88 through 2.94 for the seven 48-hour time intervals indicated in Table 2.1. The numbers shown in the

graphs represent south side temperatures minus north side temperatures at the same level of the thermocouples. The following observations can be made:

i) Temperature differences are small, typically less than 3 °F.

ii) Maximum temperature differences occurred in April and May. The absolute maximum difference during the monitoring period took place at noon on May 21, 1998. At that moment the north girder was 3.8 °F warmer than the south girder at the bottom slab.

iii) There is a seasonal dependence of the temperature differences.

iv) The north-south temperature differences of the top and bottom slabs usually have opposite signs.

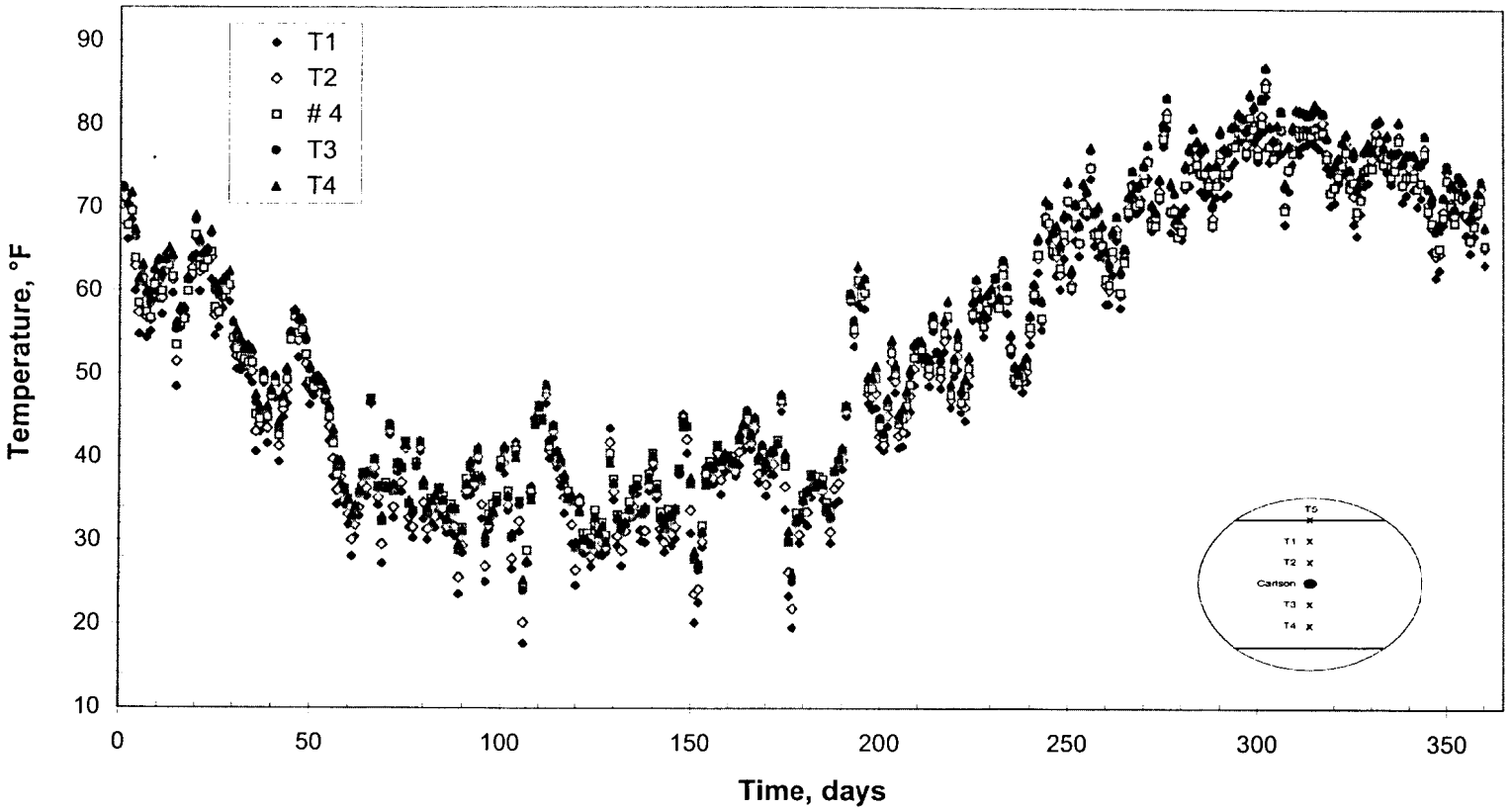


Figure 2.1 Concrete Temperatures in Top of the North Slab of Main Span Closure Segment at 6:00 a.m. from 9/19/97 to 9/23/98

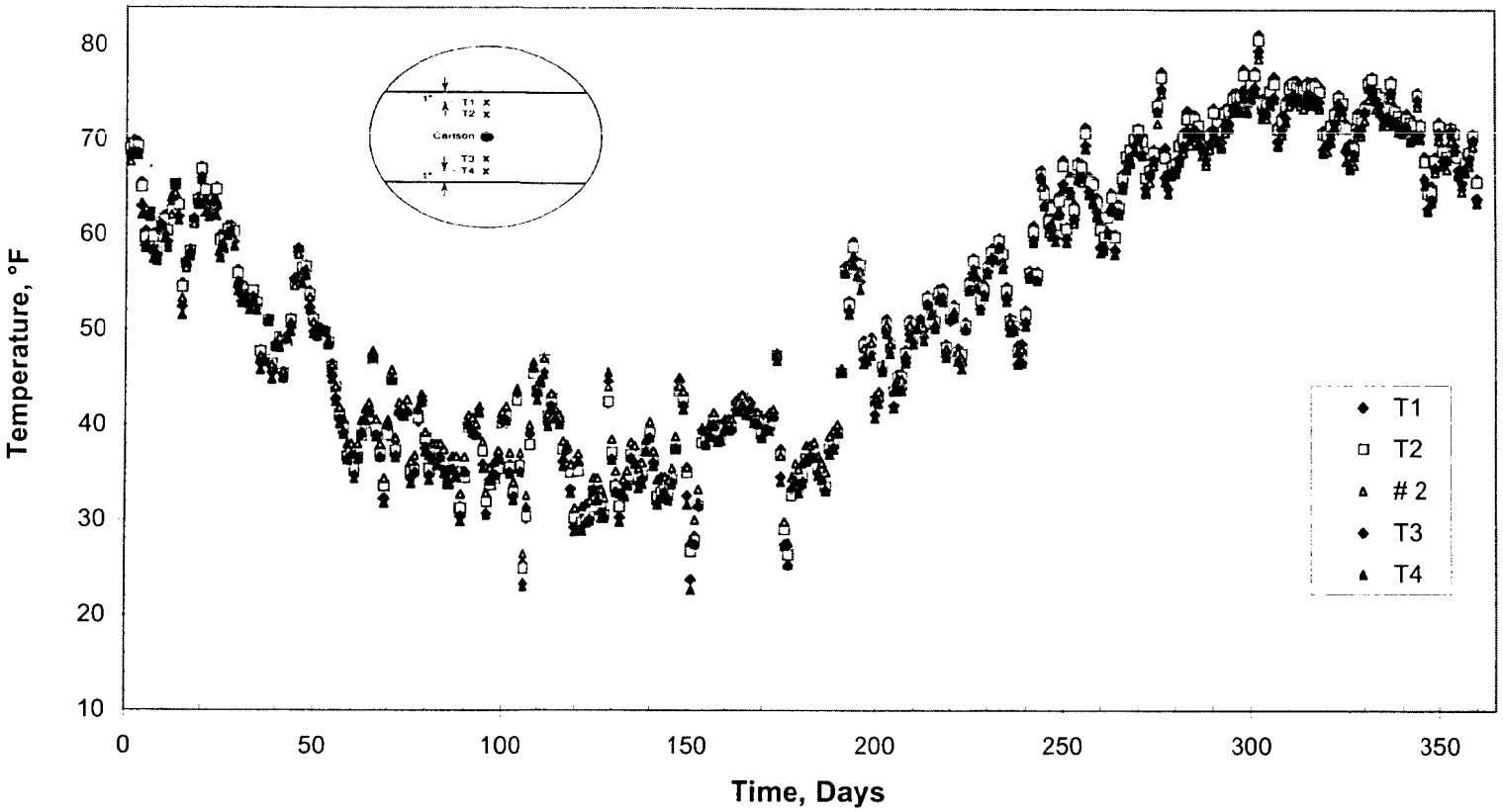


Figure 2.2 Concrete Temperatures in Bottom of the North Slab of Main Span Closure Segment at 6:00 a.m. from 9/19/97 to 9/23/98

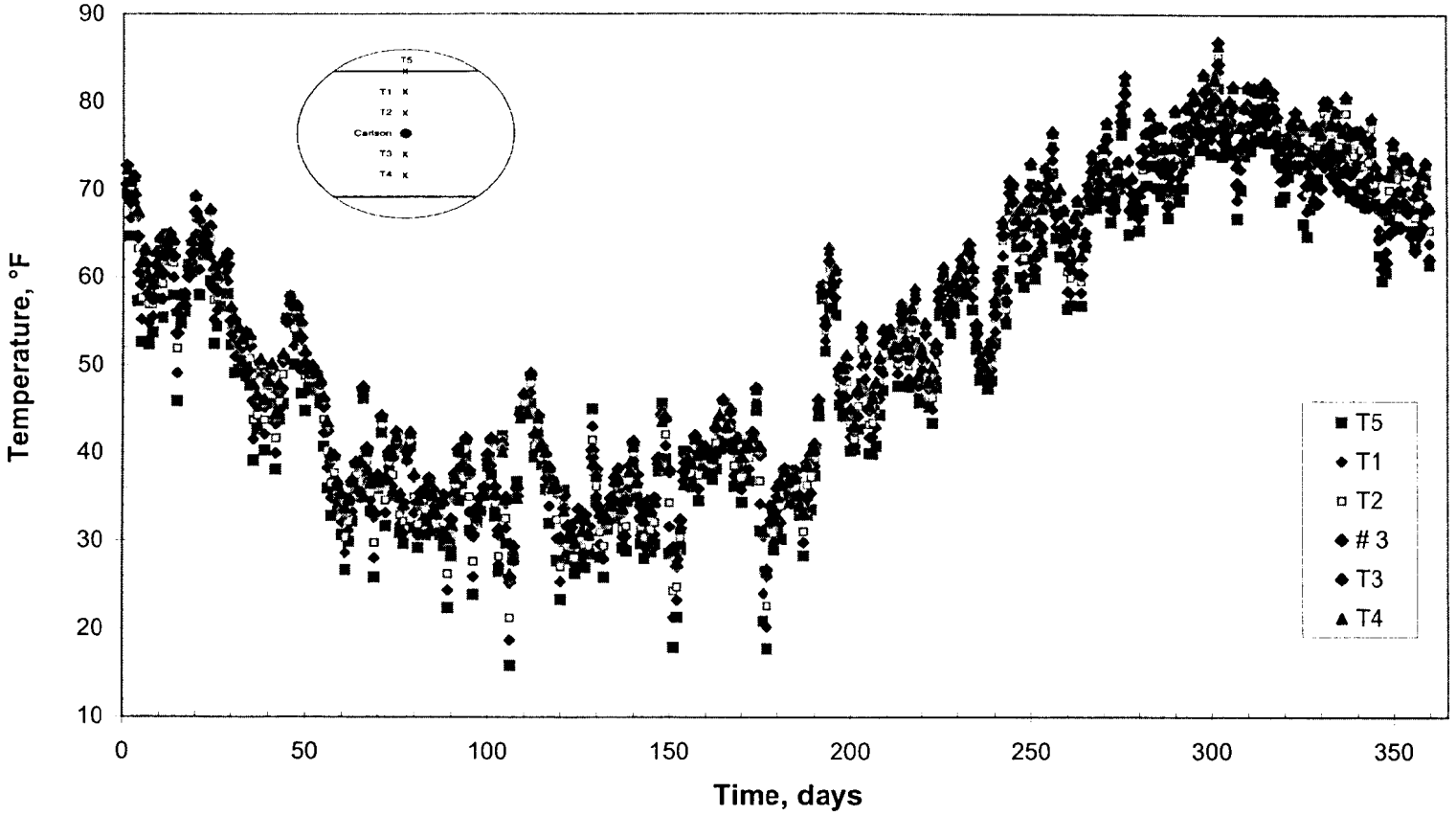


Figure 2.3 Concrete Temperatures in Top of the South Slab of Main Span Closure Segment at 6:00 a.m. from 9/19/97 to 9/23/98

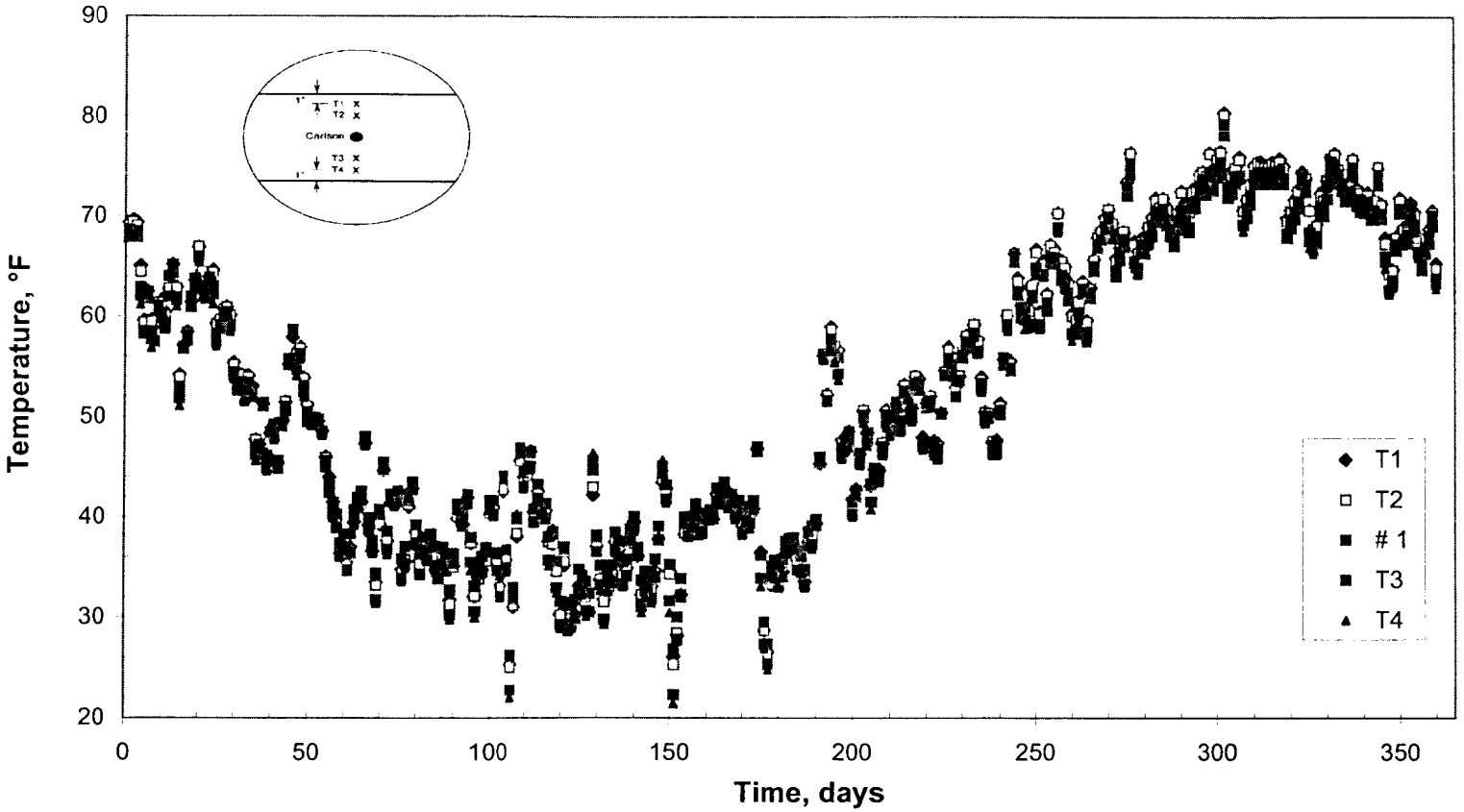


Figure 2.4 Concrete Temperatures in Bottom of the South Slab of Main Span Closure Segment at 6:00 a.m. from 9/19/97 to 9/23/98

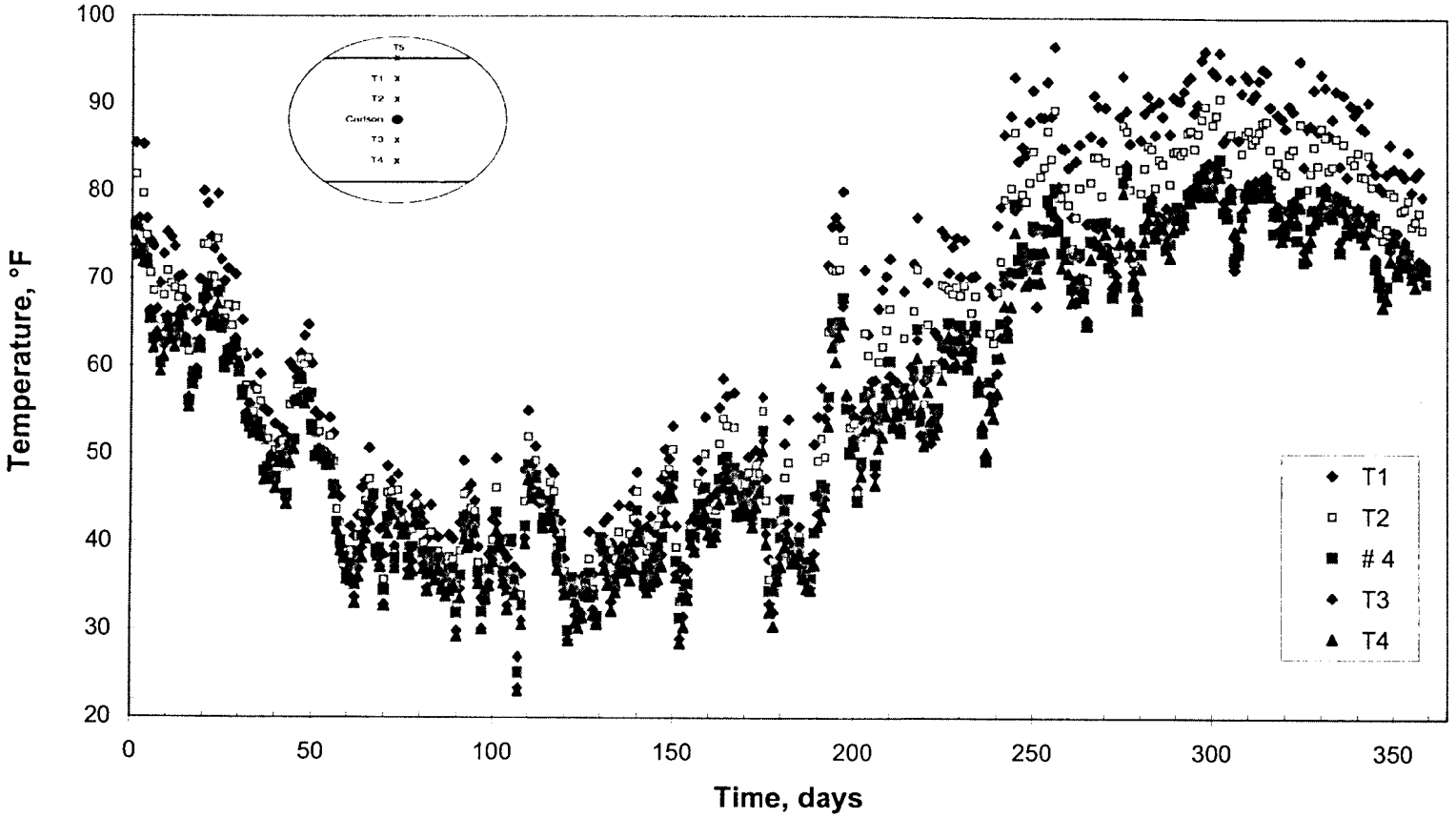


Figure 2.5 Concrete Temperatures in Top of the North Slab of Main Span Closure Segment at 2:00 p.m. from 9/19/97 to 9/22/98

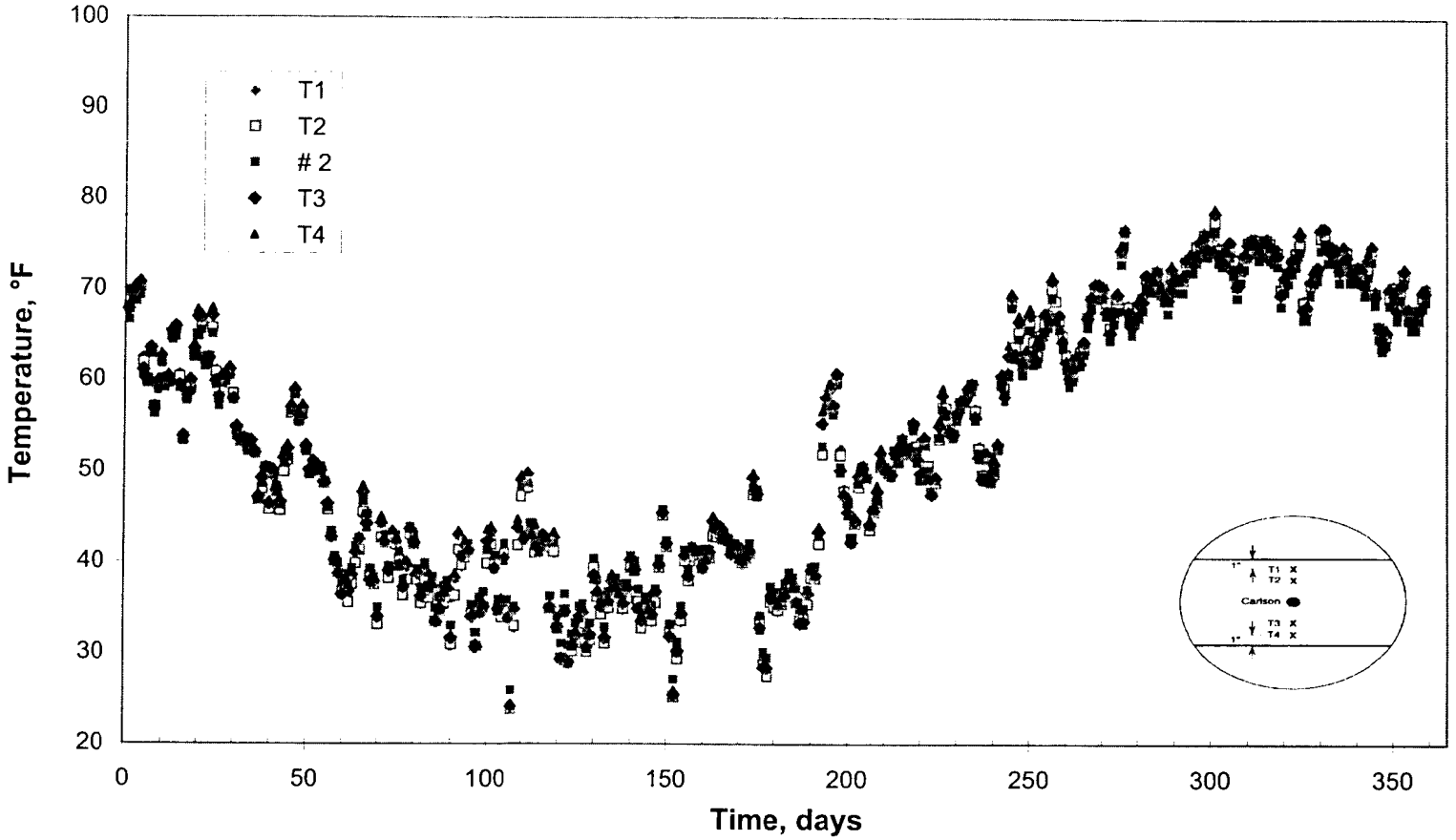


Figure 2.6 Concrete Temperatures in Bottom of the North Slab of Main Span Closure Segment at 2:00 p.m. from 9/19/97 to 9/22/98

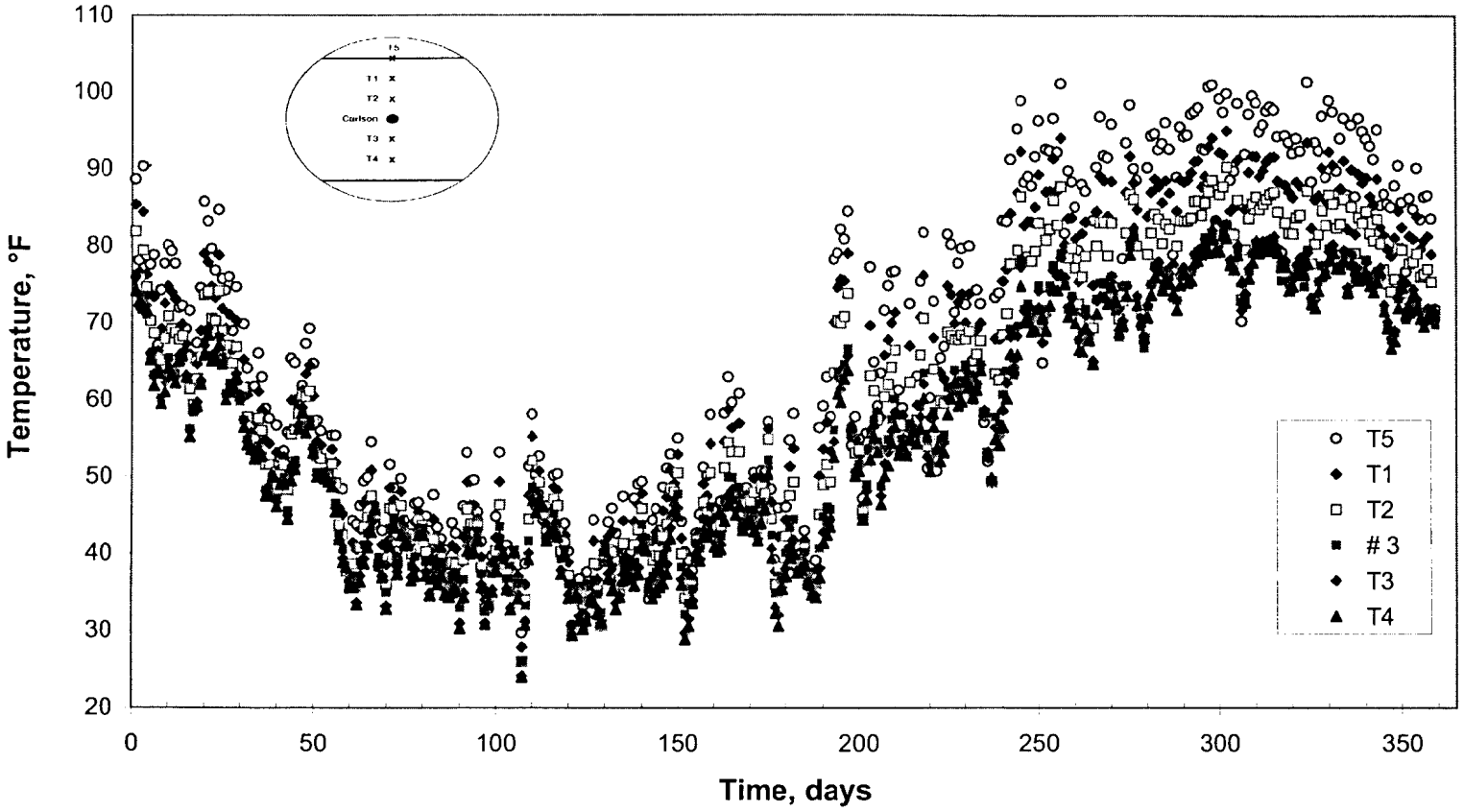


Figure 2.7 Concrete Temperatures in Top of the South Slab of Main Span Closure Segment at 2:00 p.m. from 9/19/97 to 9/22/98

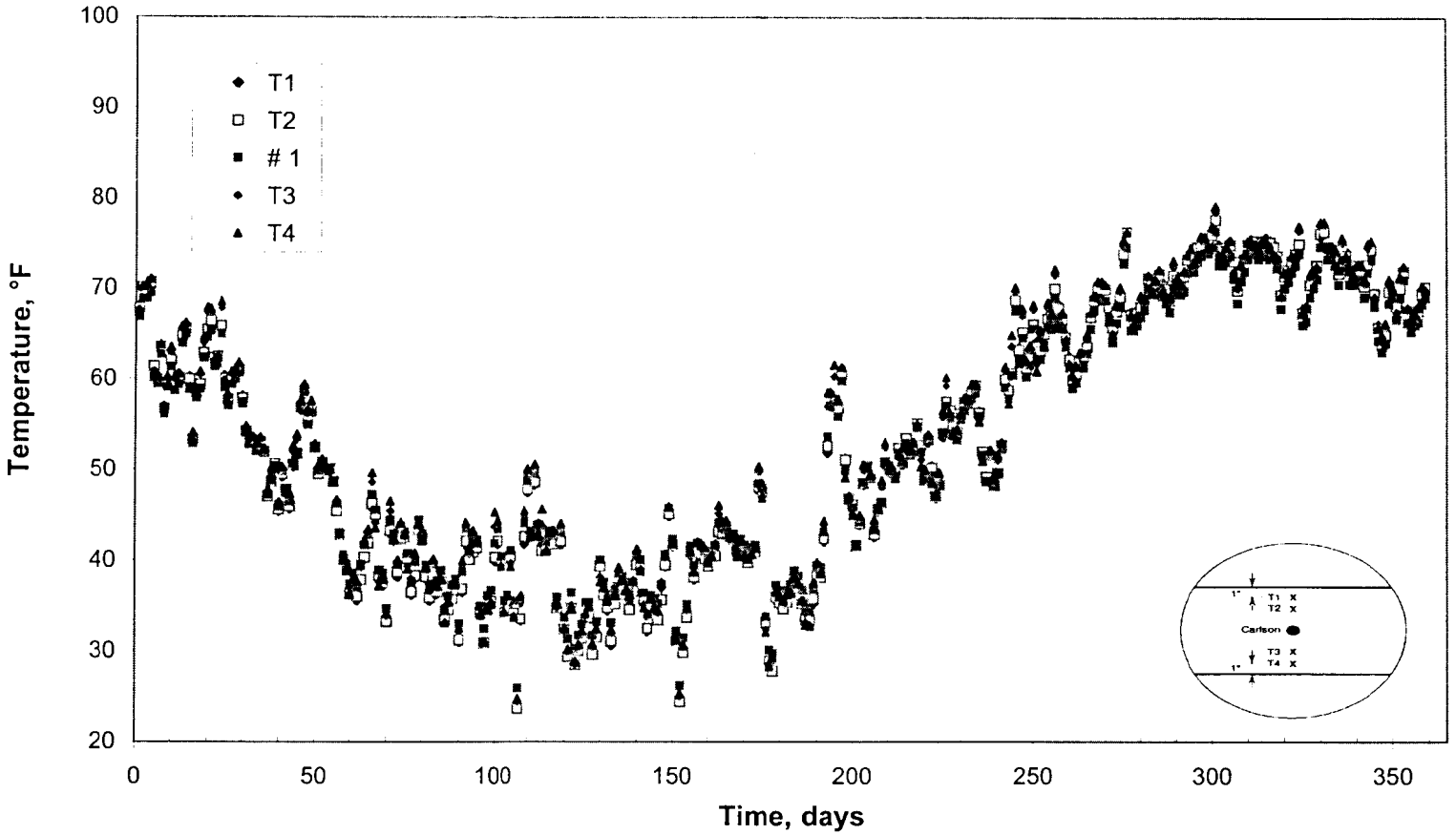


Figure 2.8 Concrete Temperatures in Bottom of the South Slab of Main Span Closure Segment at 2:00 p.m. from 9/19/97 to 9/22/98

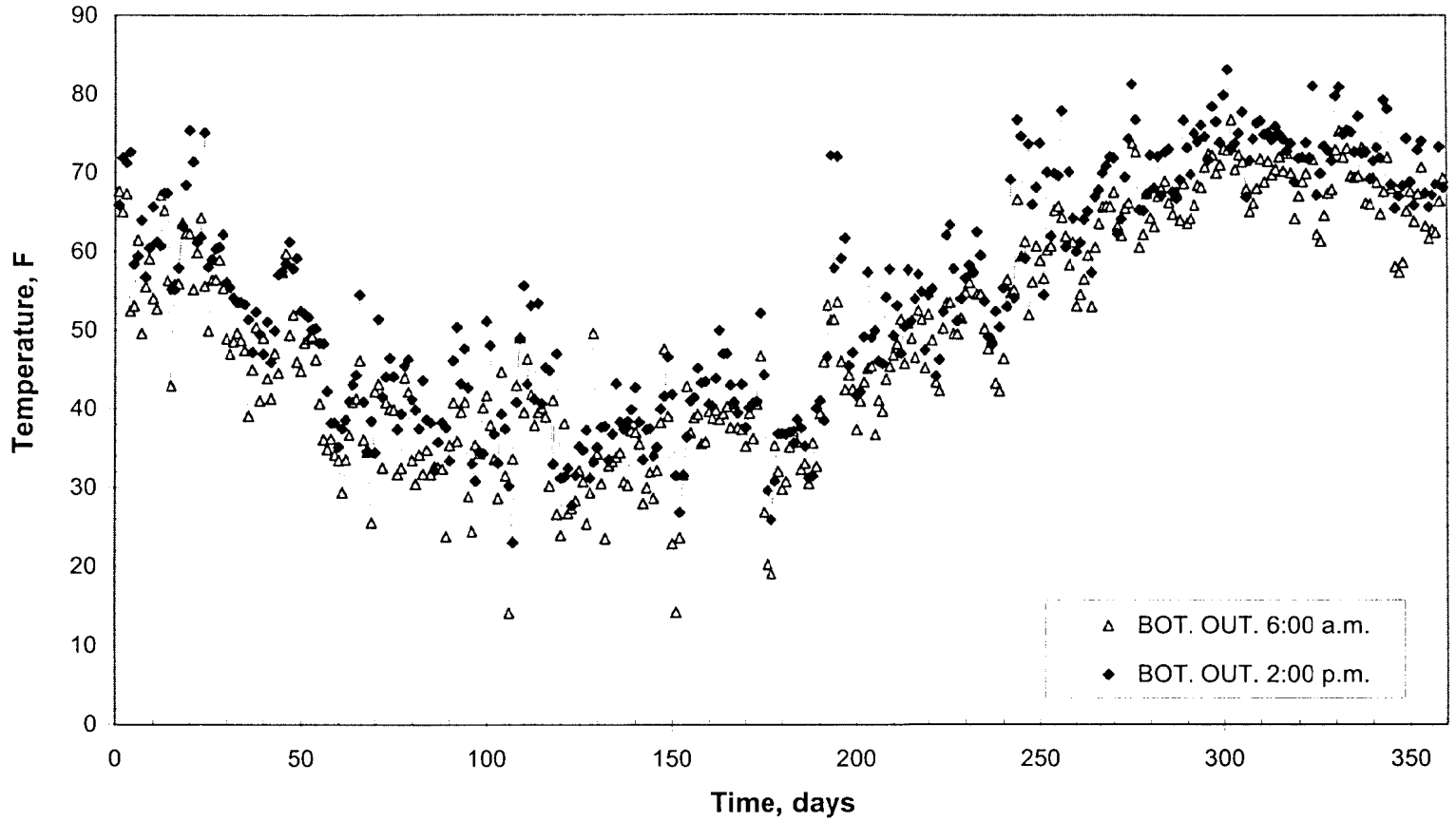


Figure 2.9 Outside Temperatures at Bottom of the Slab of Main Span Closure Segment at 6:00 a.m. and 2:00 p.m. from 9/19/97 to 9/23/98

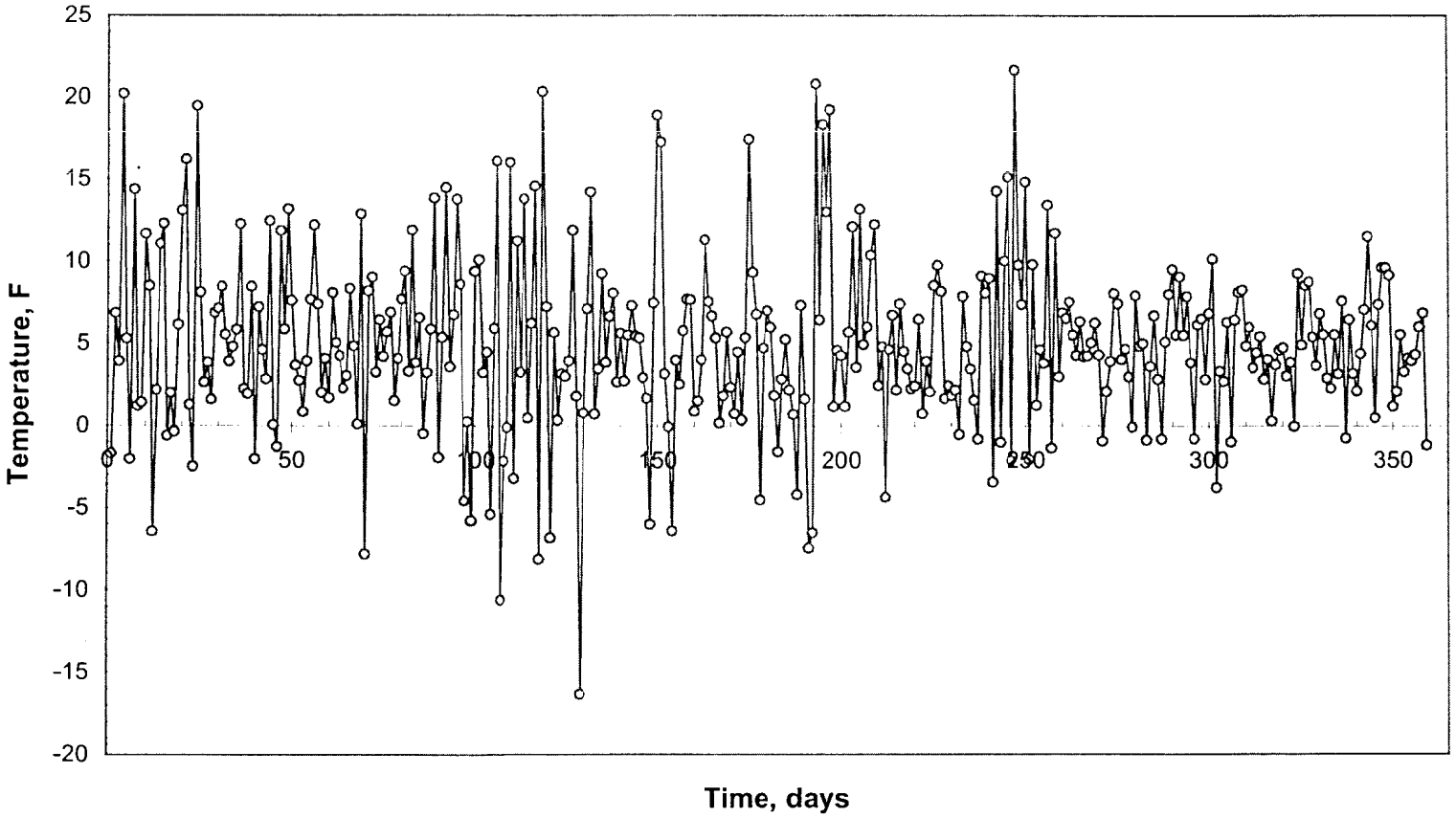


Figure 2.10 Outside Temperature Change between 6:00 am and 2:00 p.m.
9/19/97 to 9/23/98

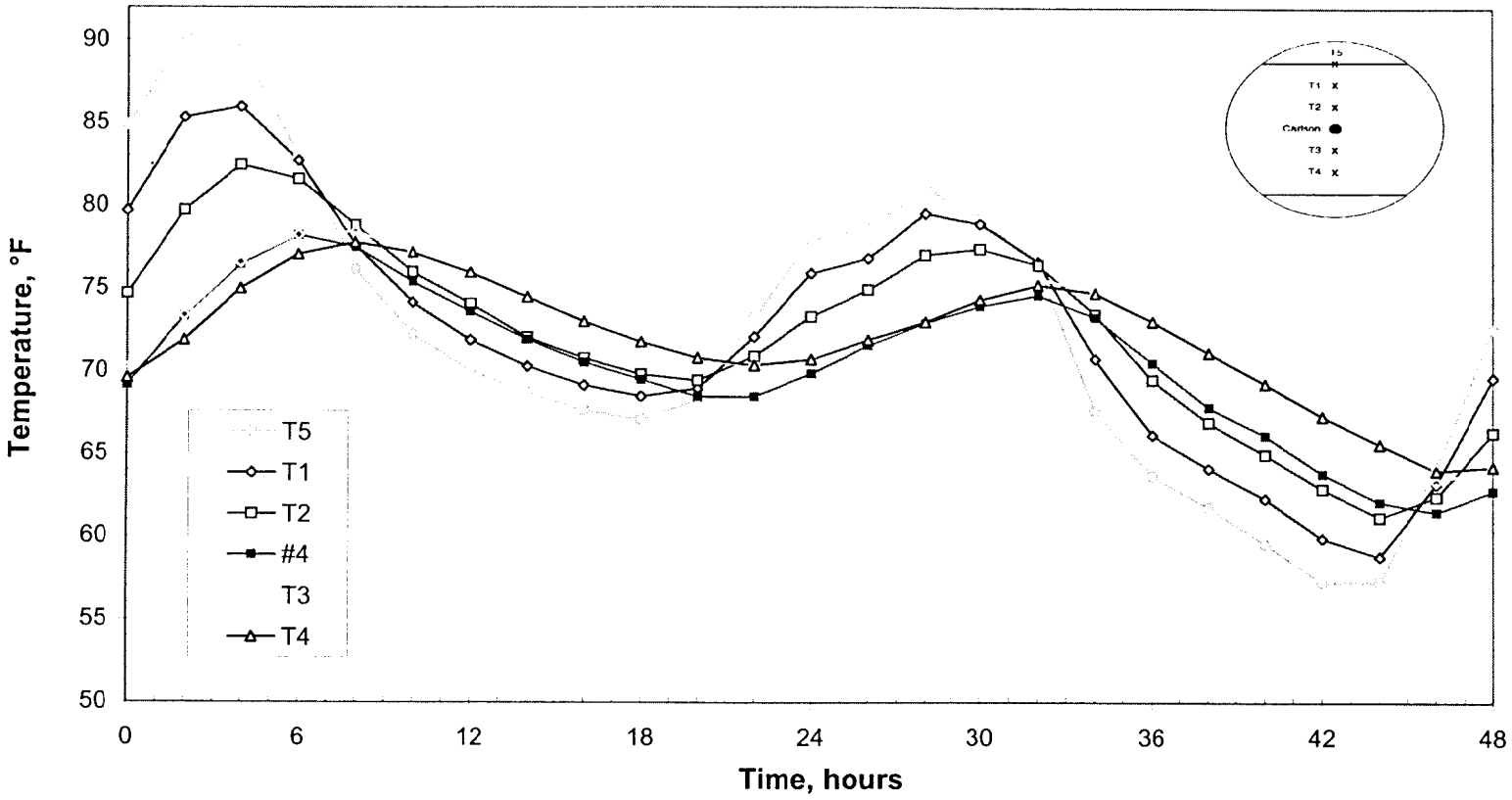


Figure 2.11 Concrete Temperatures in Top of the North Slab of Main Span Closure Segment, 9/21/97, 12:00 p.m. to 9/23/97, 12:00 p.m.

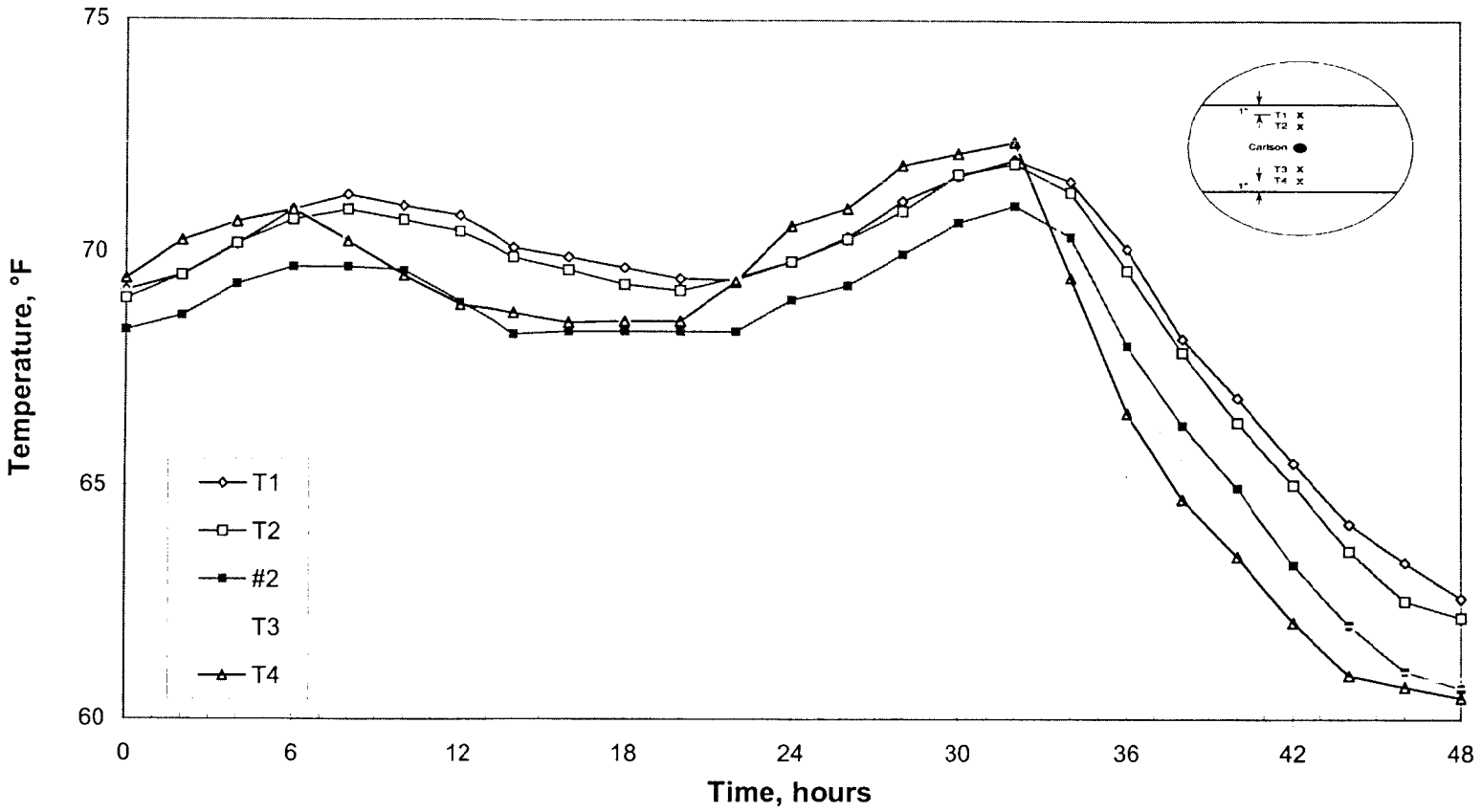


Figure 2.12 Concrete Temperatures in Bottom of the North Slab of Main Span Closure Segment, 9/21/97, 12:00 p.m. to 9/23/97, 12:00 p.m.

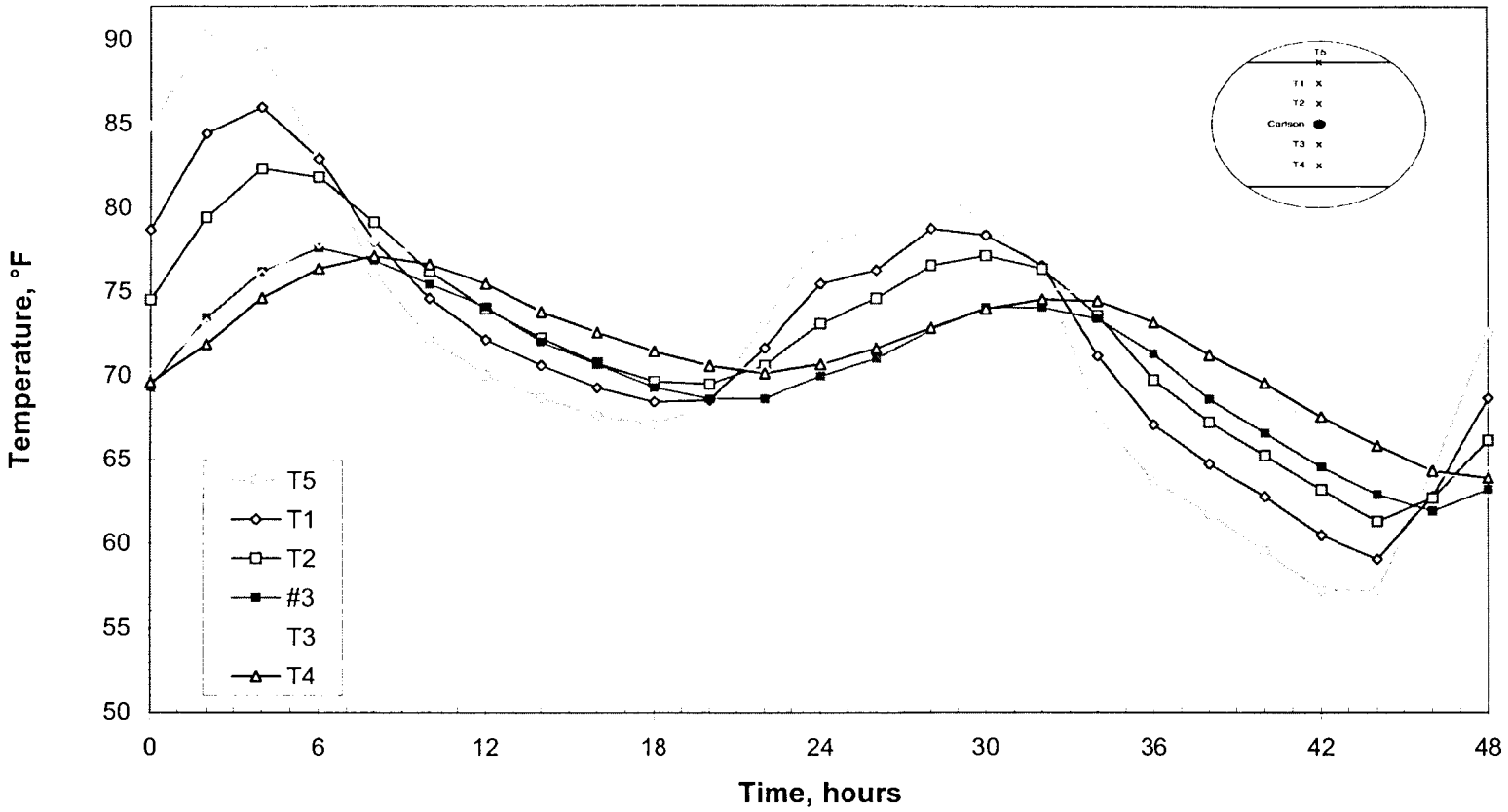


Figure 2.13 Concrete Temperatures in Top of the South Slab of Main Span Closure Segment, 9/21/97, 12:00 p.m. to 9/23/97, 12:00 p.m.

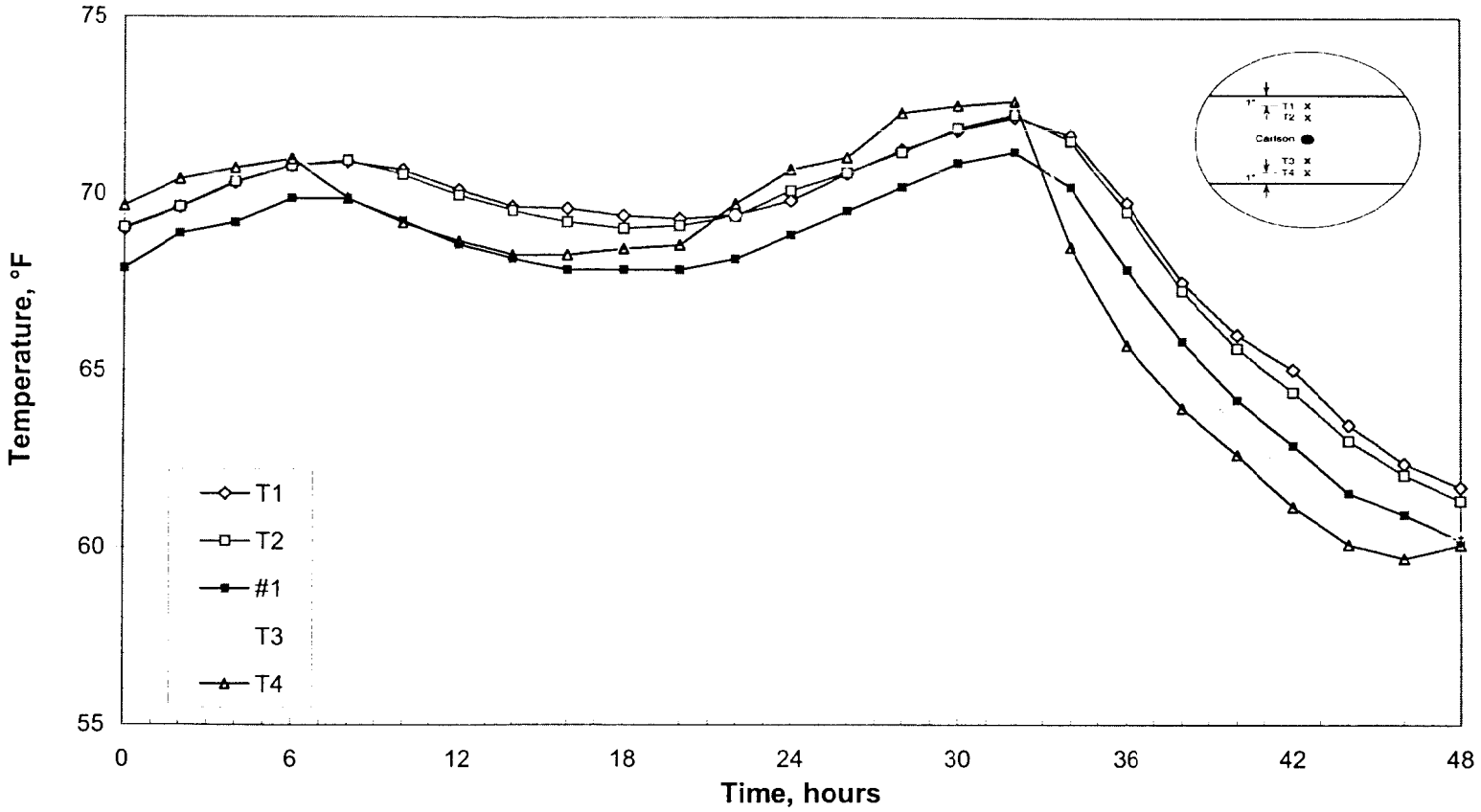


Figure 2.14 Concrete Temperatures in Bottom of the South Slab of Main Span Closure Segment, 9/21/97, 12:00 p.m. to 9/23/97, 12:00 p.m.

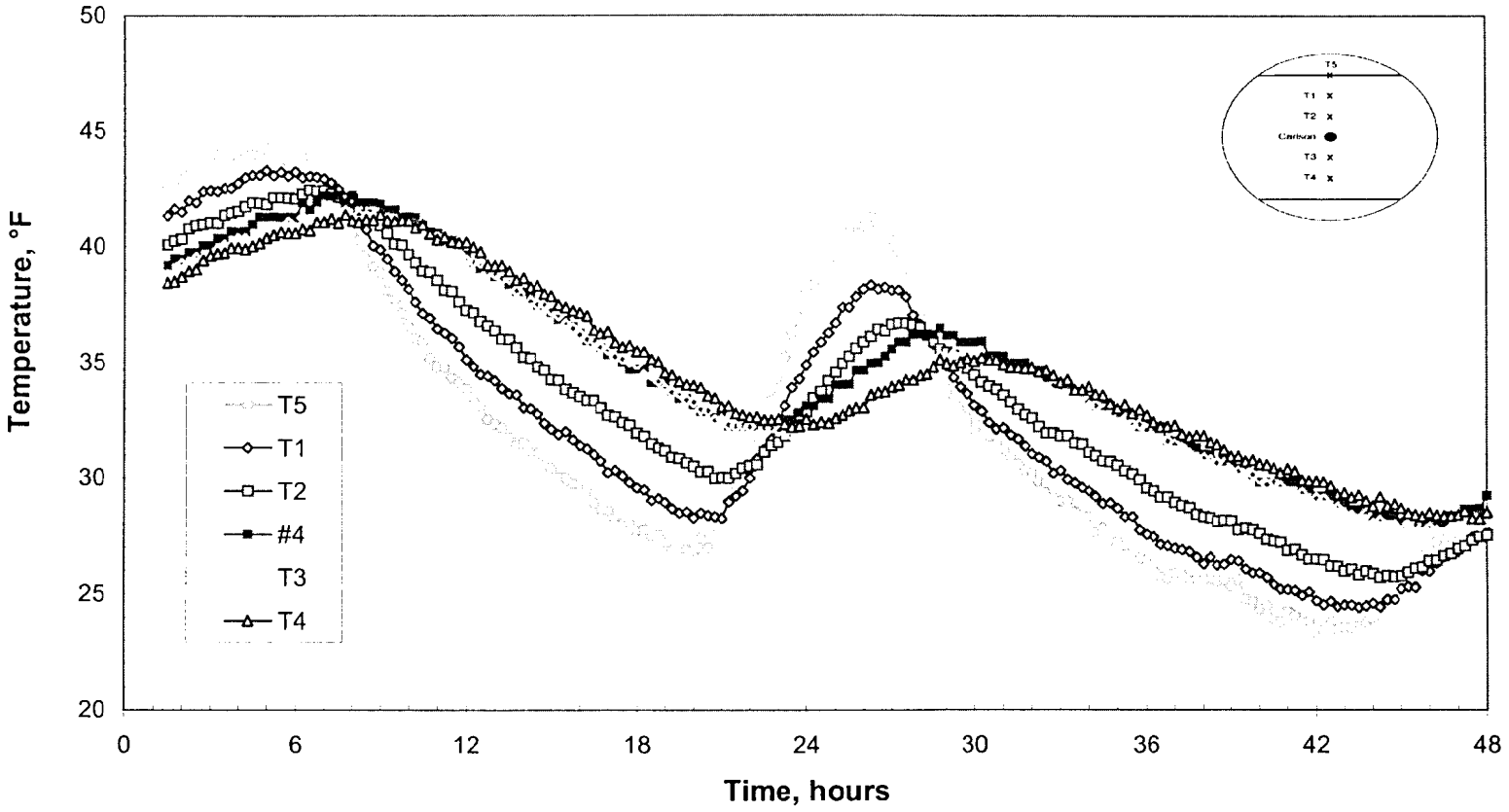


Figure 2.15 Concrete Temperatures in Top of the North Slab of Main Span Closure Segment, 1/13/98, 12:00 p.m. to 1/15/98, 12:00 p.m.

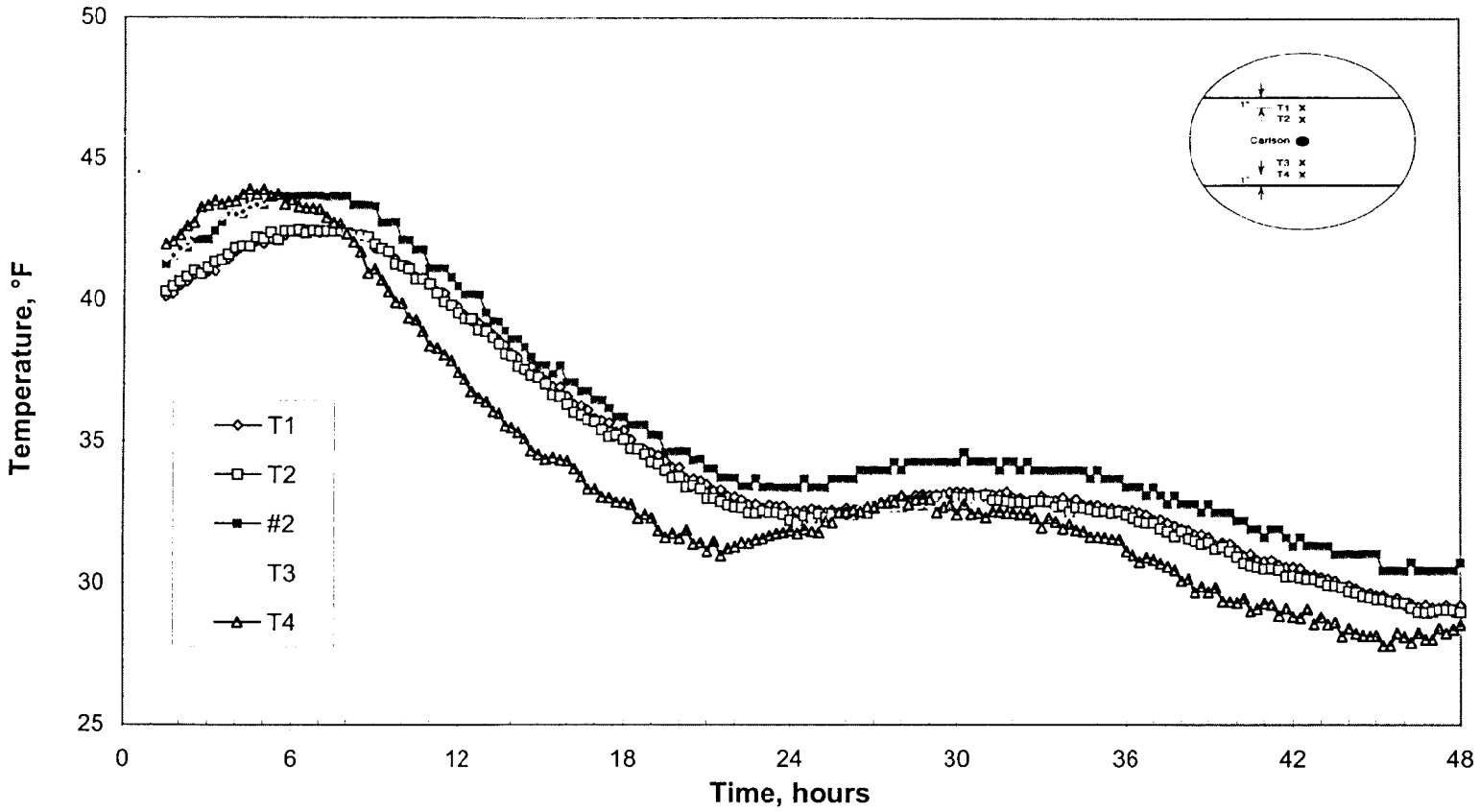


Figure 2.16 Concrete Temperatures in Bottom of the North Slab of Main Span Closure Segment, 1/13/98, 12:00 p.m. to 1/15/98, 12:00 p.m.

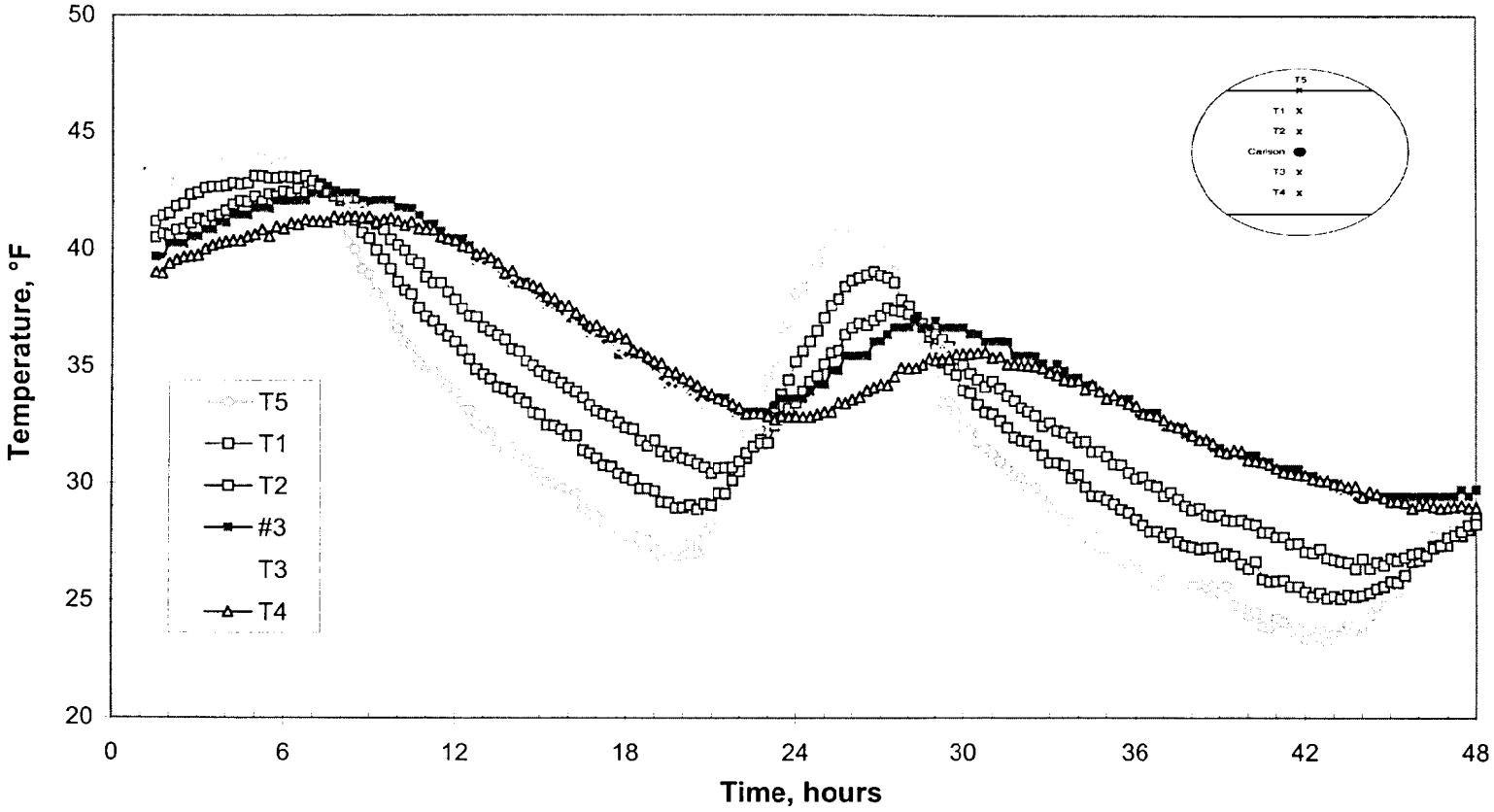


Figure 2.17 Concrete Temperatures in Top of the South Slab of Main Span Closure Segment, 1/13/98, 12:00 p.m. to 1/15/98, 12:00 p.m.

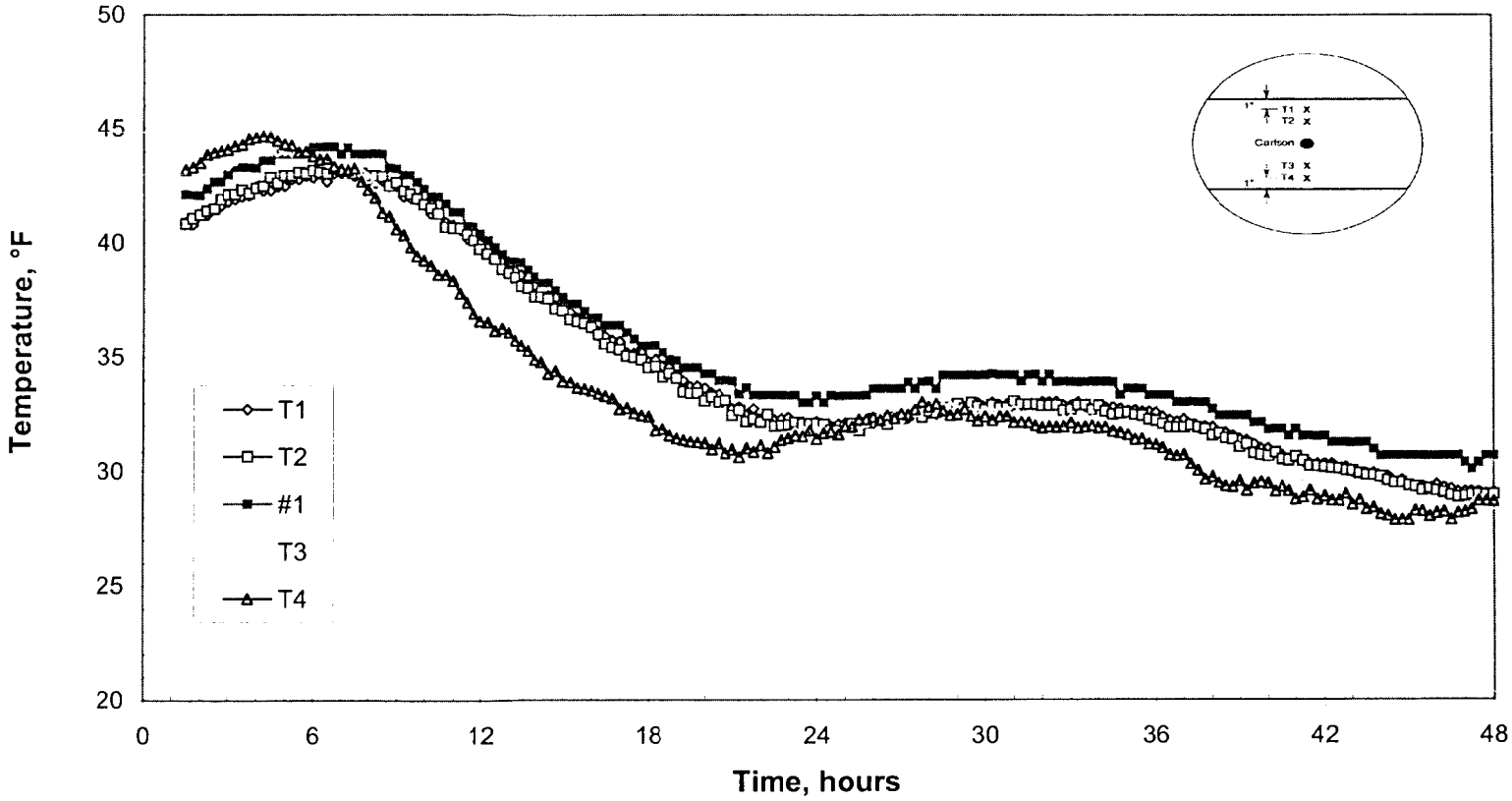


Figure 2.18 Concrete Temperatures in Bottom of the South Slab of Main Span Closure Segment, 1/13/98, 12:00 p.m. to 1/15/98, 12:00 p.m.

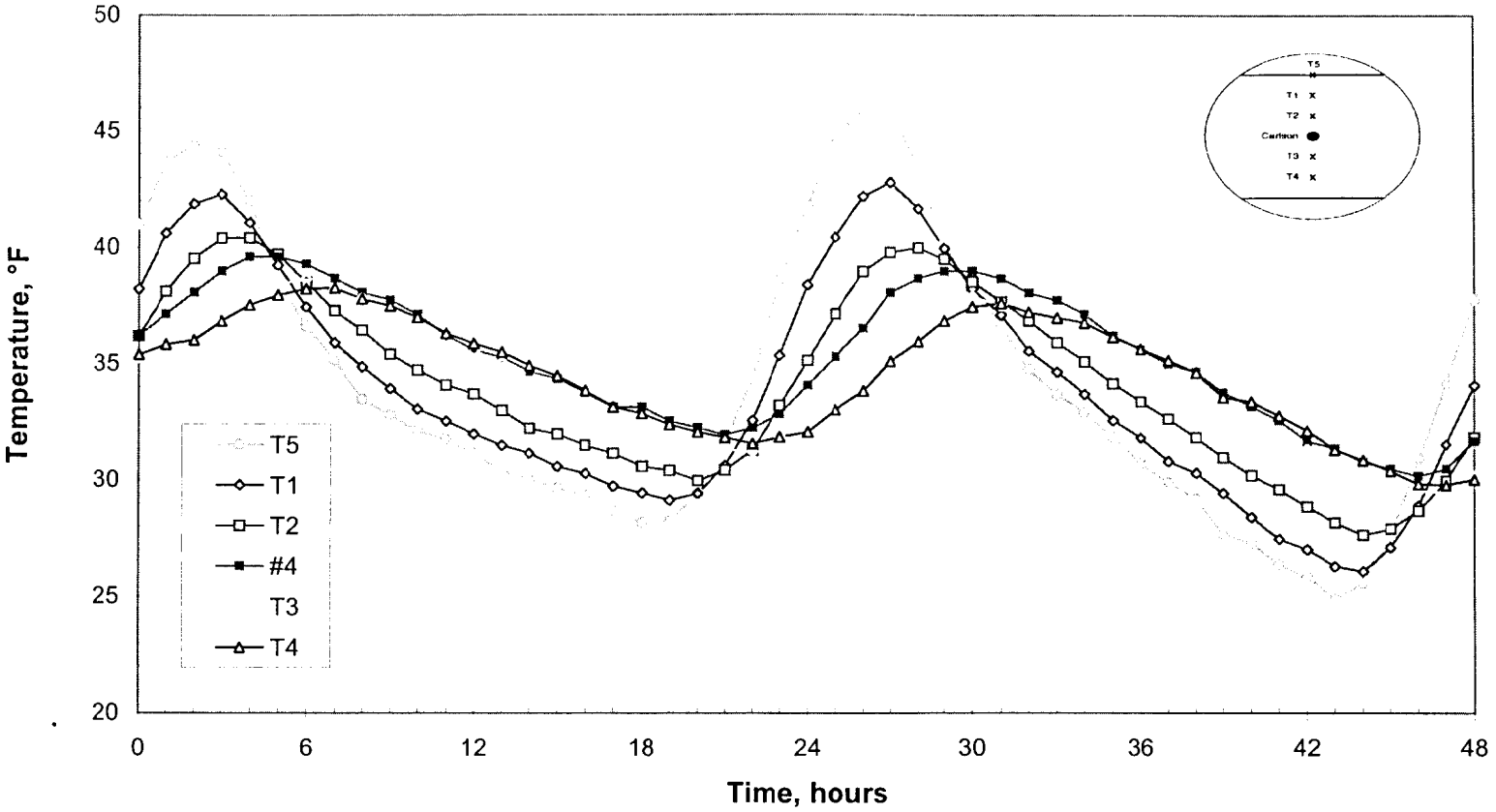


Figure 2.19 Concrete Temperatures in Top of the North Slab of Main Span Closure Segment, 1/25/98, 12:00 p.m. to 1/27/98, 12:00 p.m.

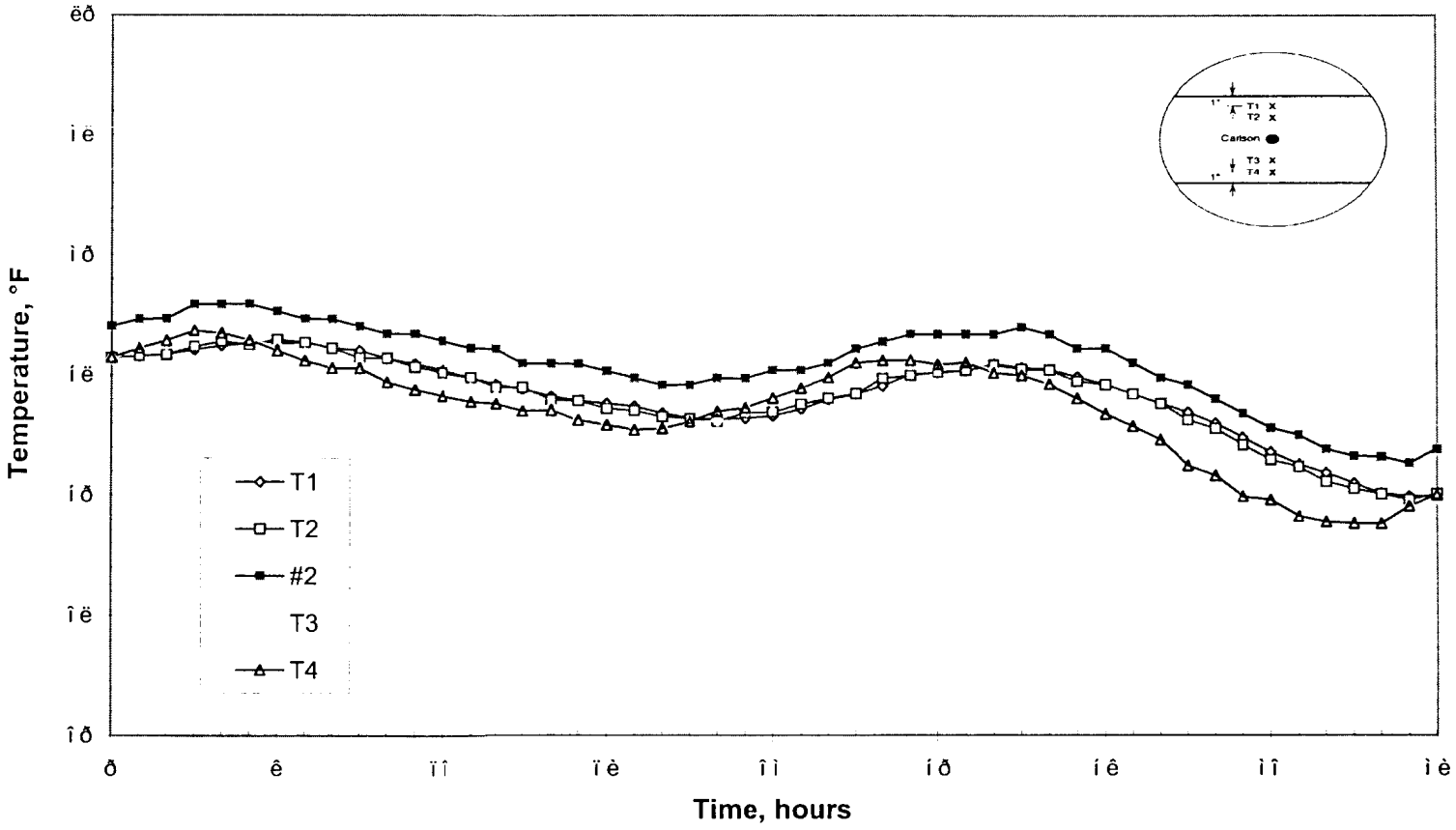


Figure 2.20 Concrete Temperatures in Bottom of the North Slab of Main Span Segment, 1/25/98, 12:00 p.m. to 1/27/98, 12:00 p.m.

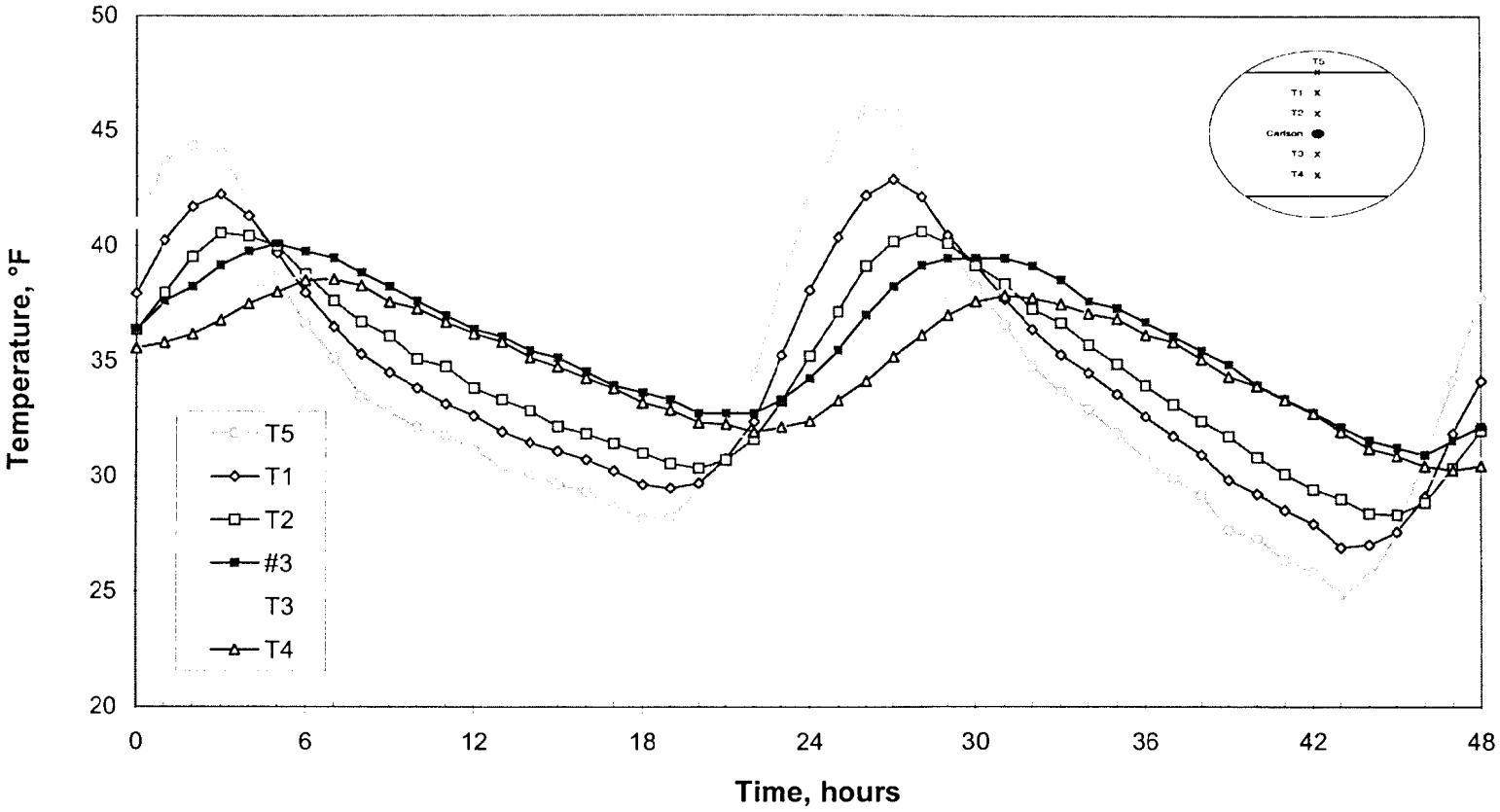


Figure 2.21 Concrete Temperatures in Top of the South Slab of Main Span Closure Segment, 1/25/98, 12:00 p.m. to 1/27/98, 12:00 p.m.

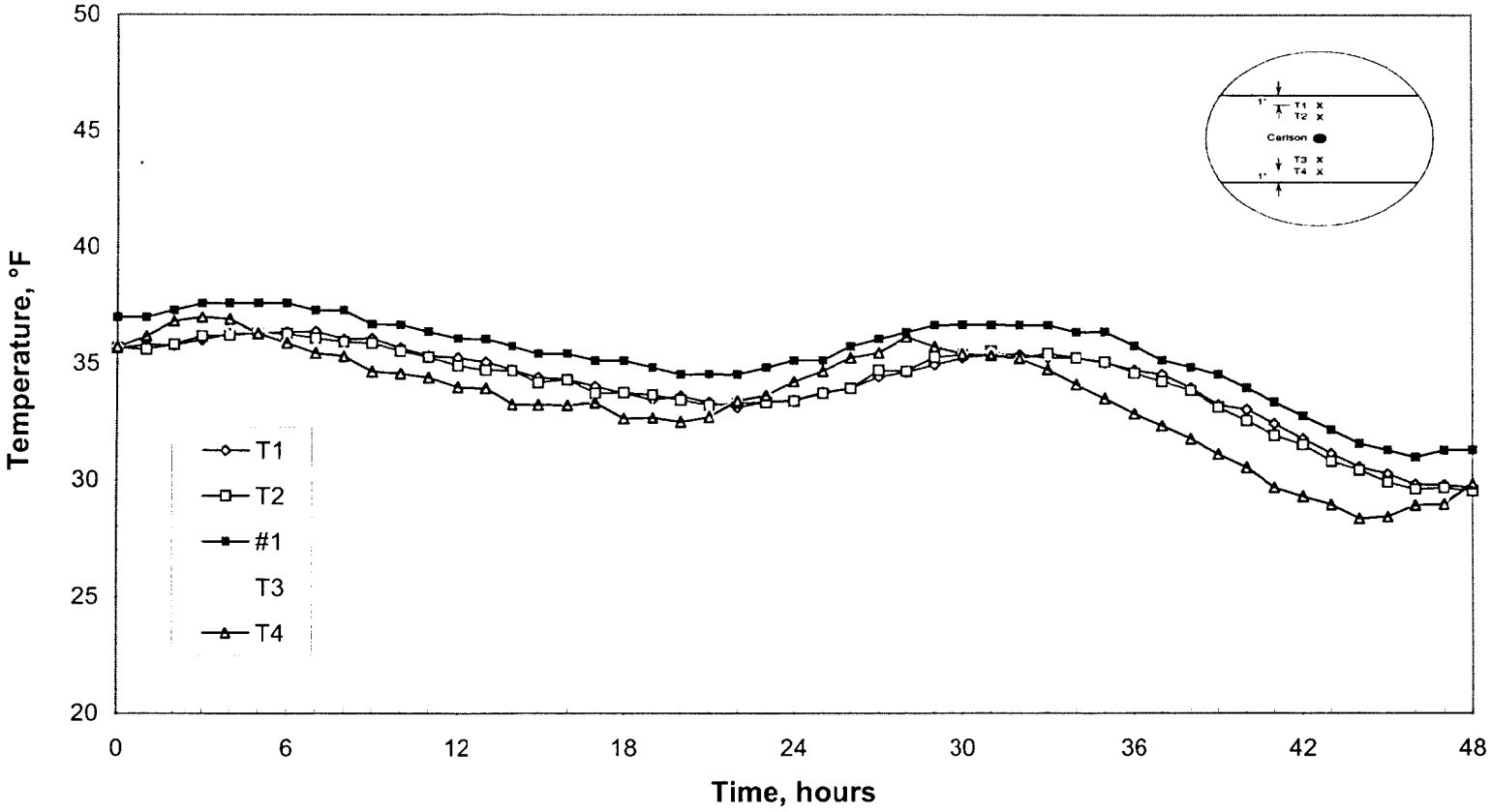


Figure 2.22 Concrete Temperatures in Bottom of the South Slab of Main Span Closure Segment, 1/25/98, 12:00 p.m. to 1/27/98, 12:00 p.m.

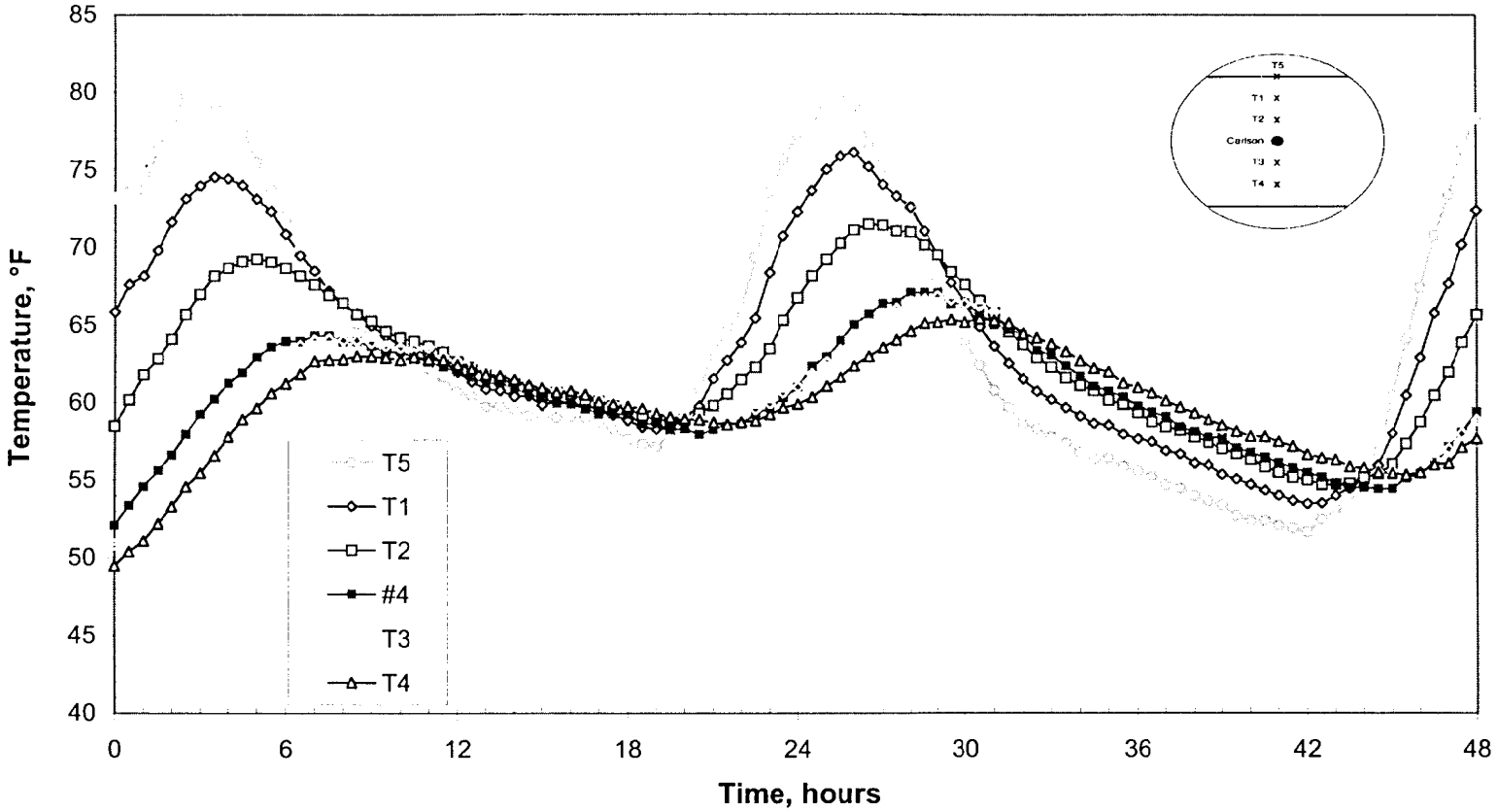


Figure 2.23 Concrete Temperatures in Top of the North Slab of Main Span Closure Segment, 4/27/98, 12:00 p.m. to 4/29/98, 12:00 p.m.

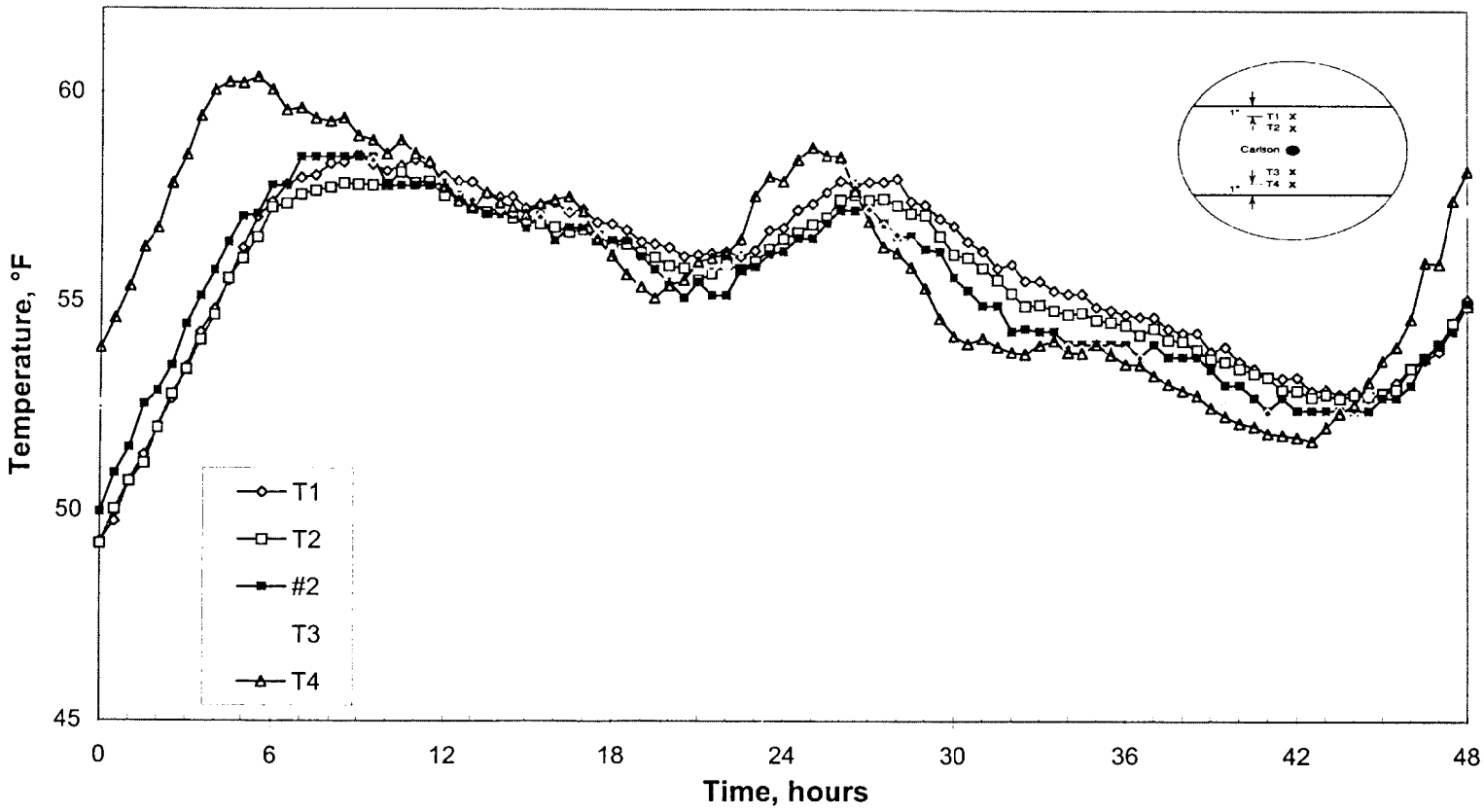


Figure 2.24 Concrete Temperatures in Bottom of the North Slab of Main Span Closure Segment, 4/27/98, 12:00 p.m. to 4/29/98, 12:00 p.m.

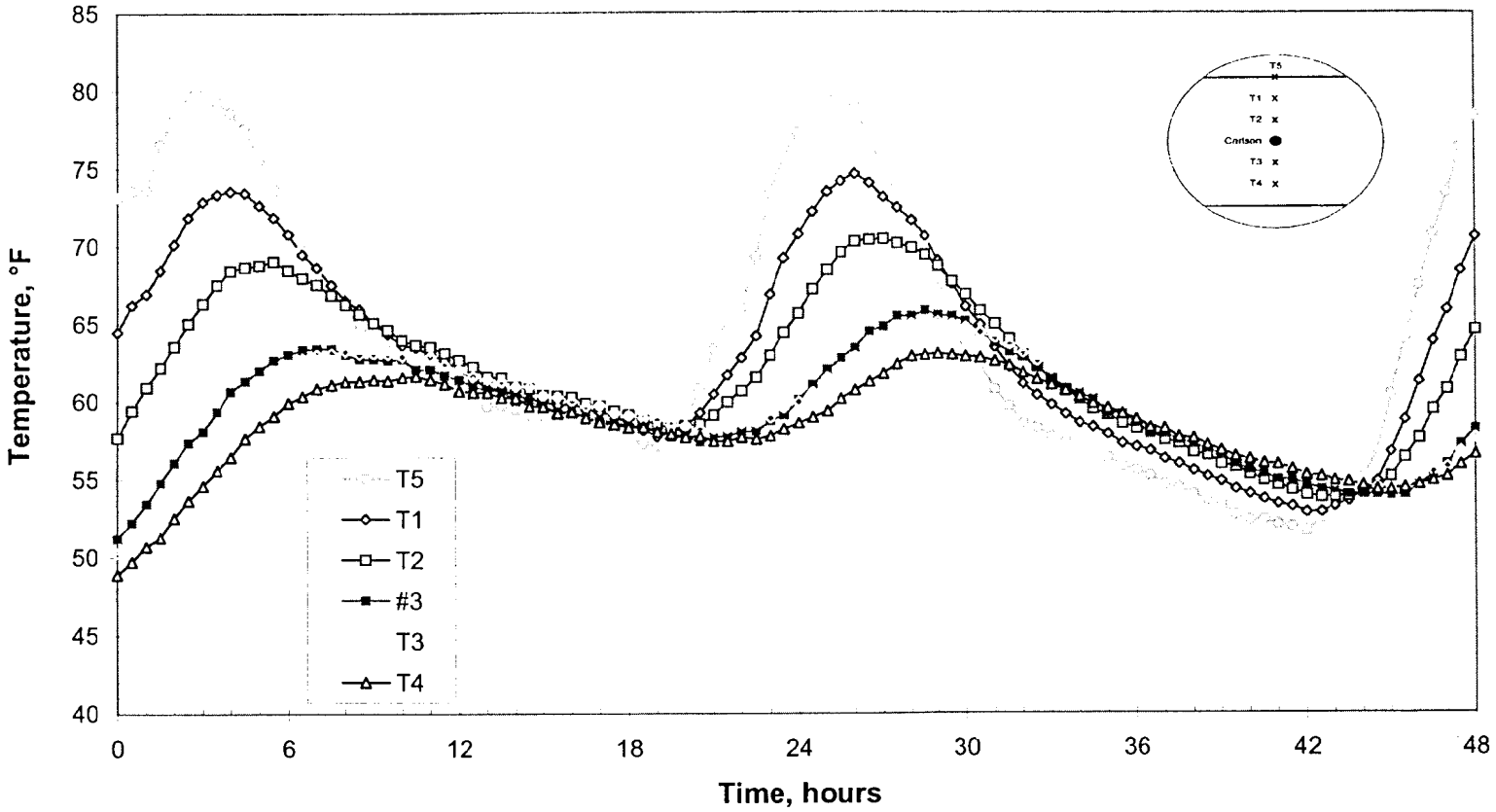


Figure 2.25 Concrete Temperatures in Top of the South Slab of Main Span Closure Segment, 4/27/98, 12:00 p.m. to 4/29/98, 12:00 p.m.

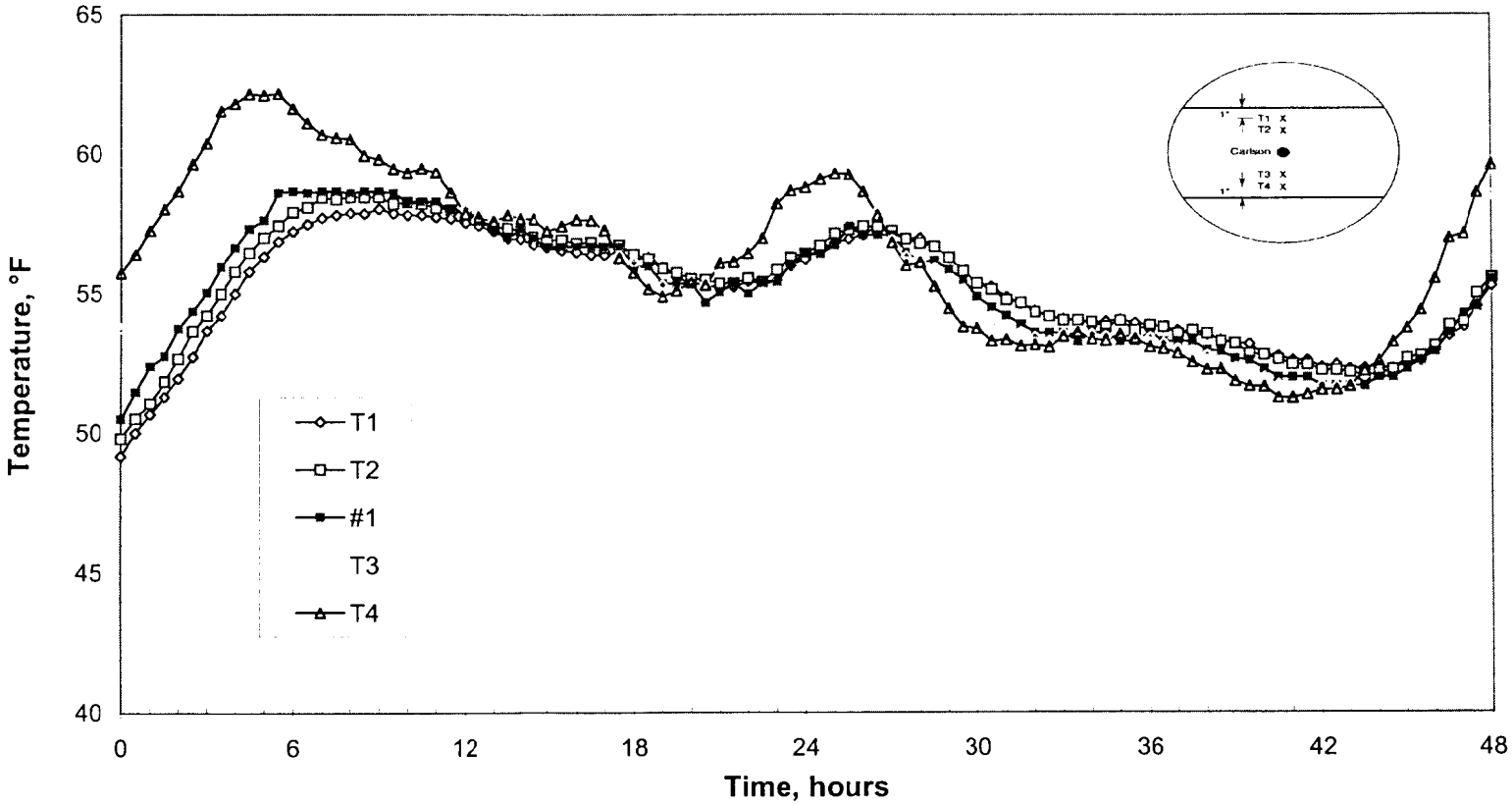


Figure 2.26 Concrete Temperatures in Bottom of the South Slab of Main Span Closure Segment, 4/27/98, 12:00 p.m. to 4/29/98, 12:00 p.m.

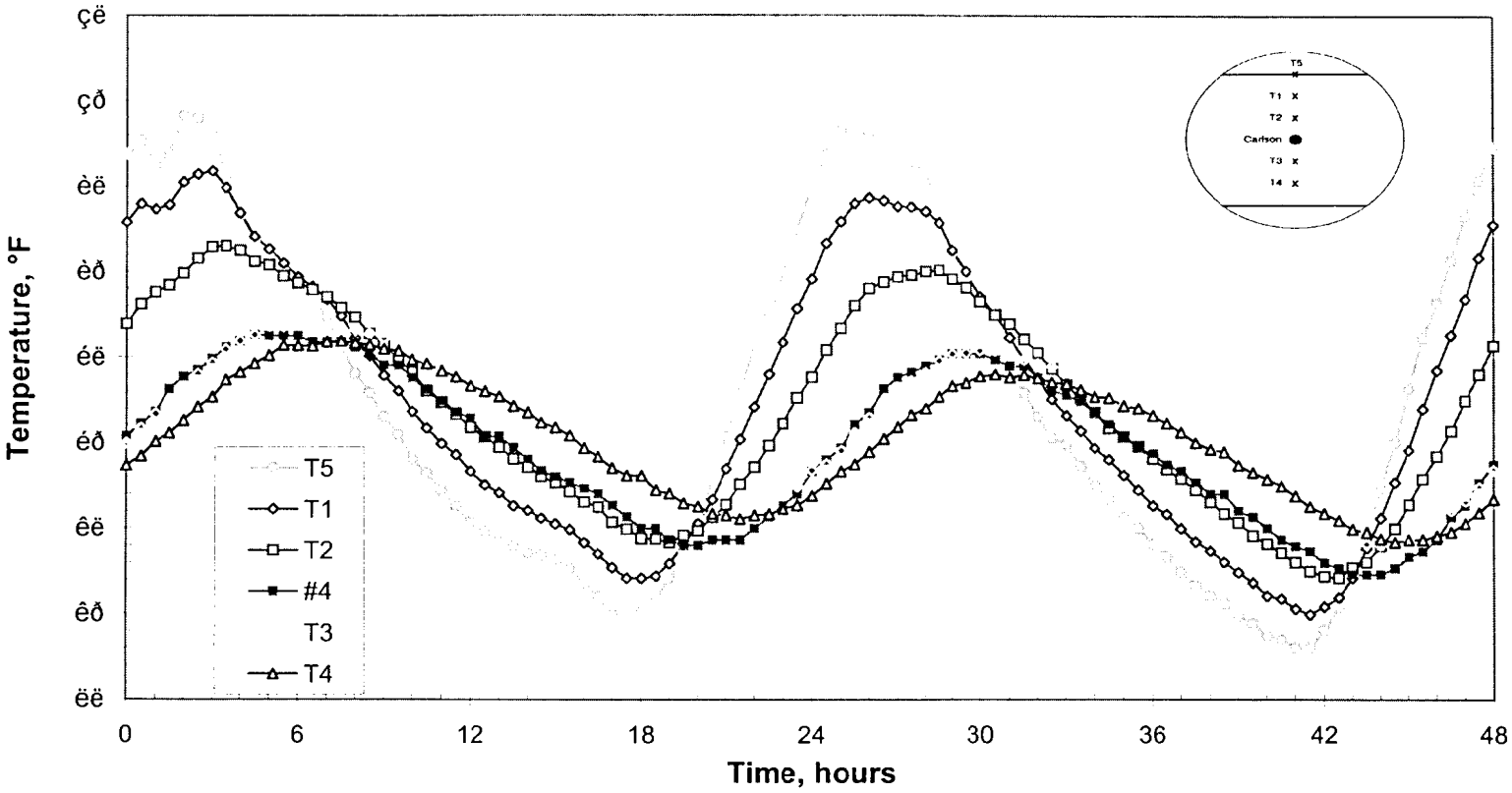


Figure 2.27 Concrete Temperatures in Top of the North Slab of Main Span Closure Segment, 5/21/98, 12:00 p.m. to 5/23/98, 12:00 p.m.

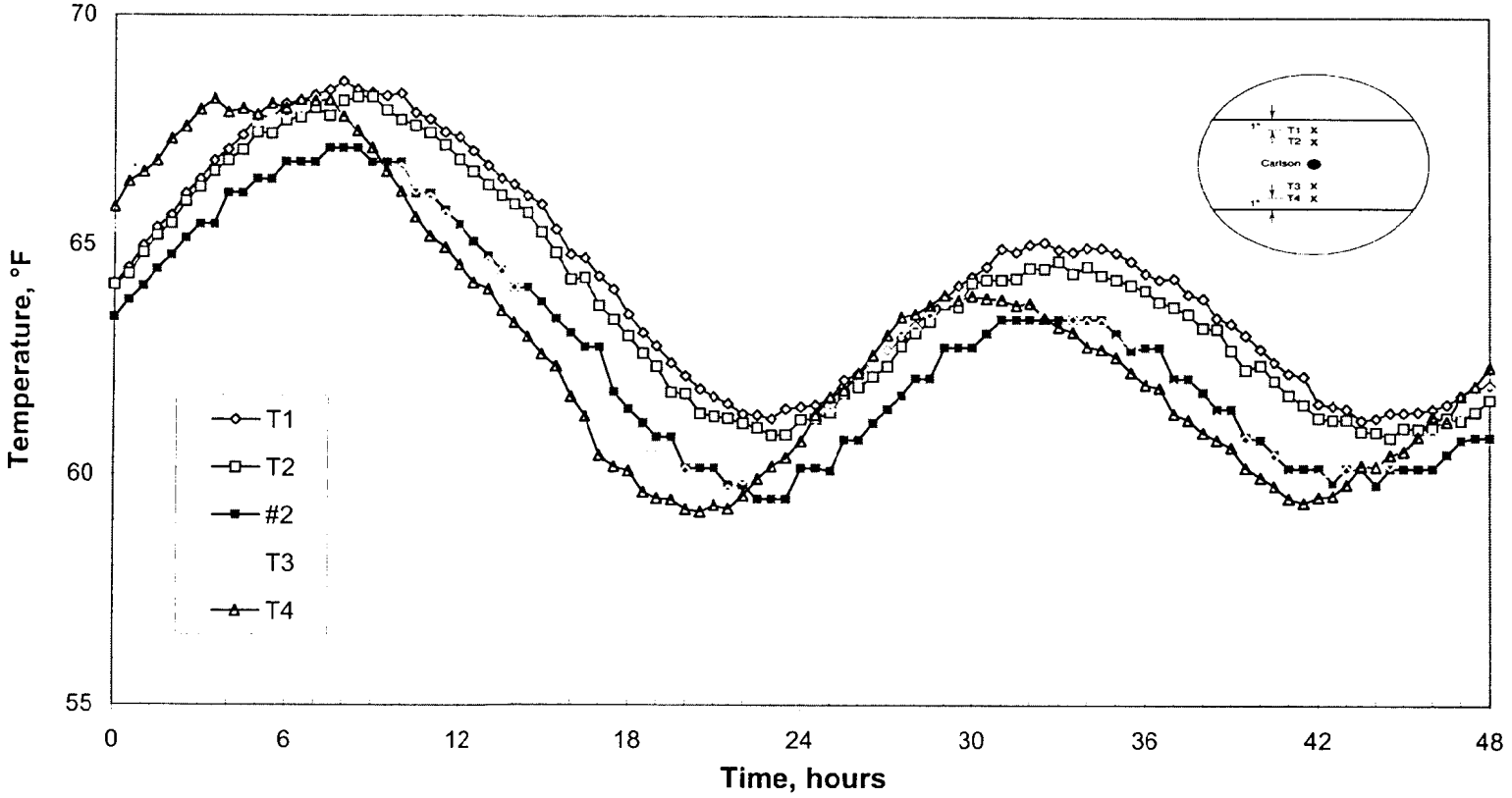


Figure 2.28 Concrete Temperatures in Bottom of the North Slab of Main Span Closure Segment, 5/21/98, 12:00 p.m. to 5/23/98, 12:00 p.m.

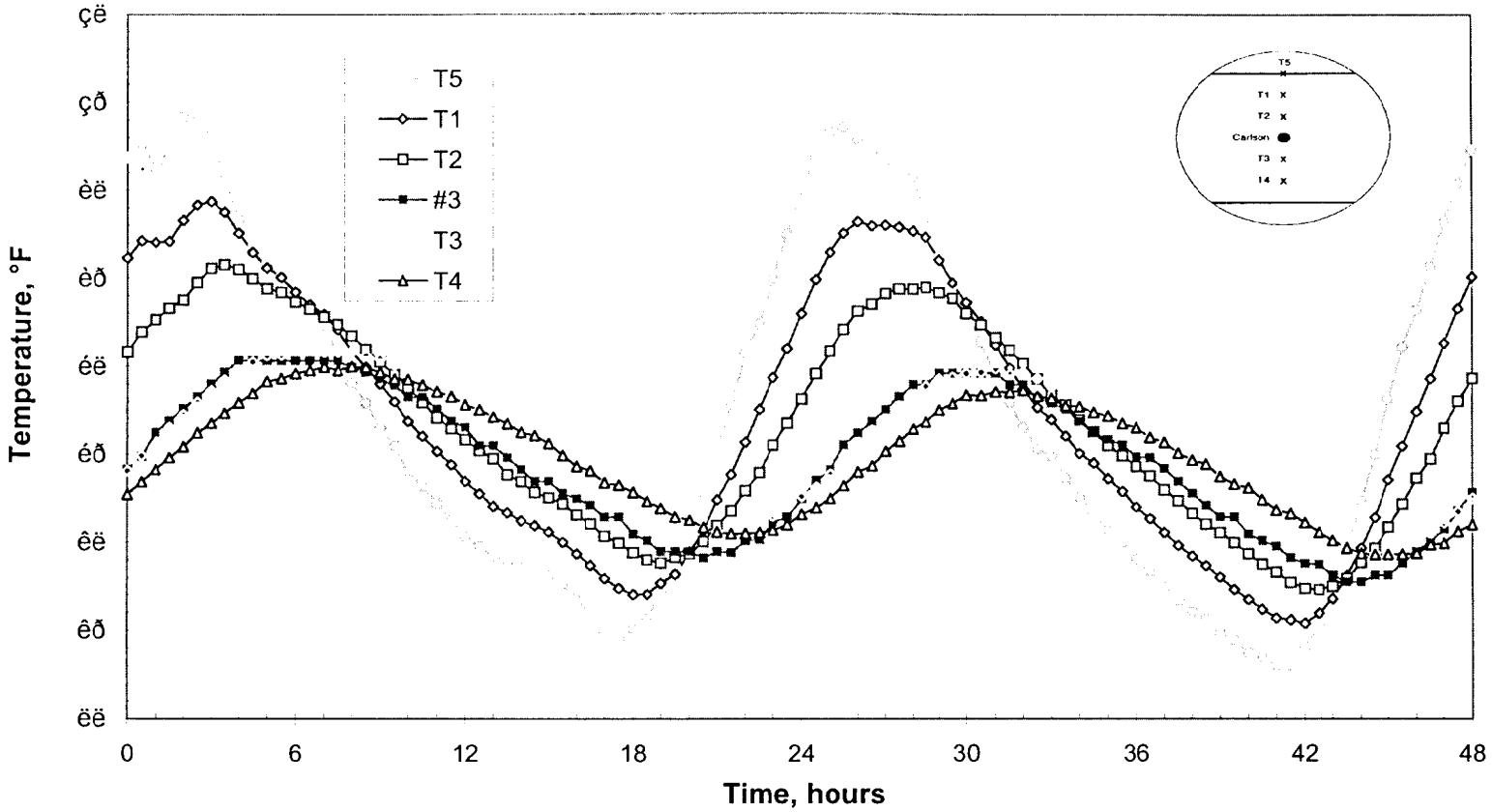


Figure 2.29 Concrete Temperatures in Top of the South Slab of Main Span Closure Segment, 5/21/98, 12:00 p.m. to 5/23/98, 12:00 p.m.

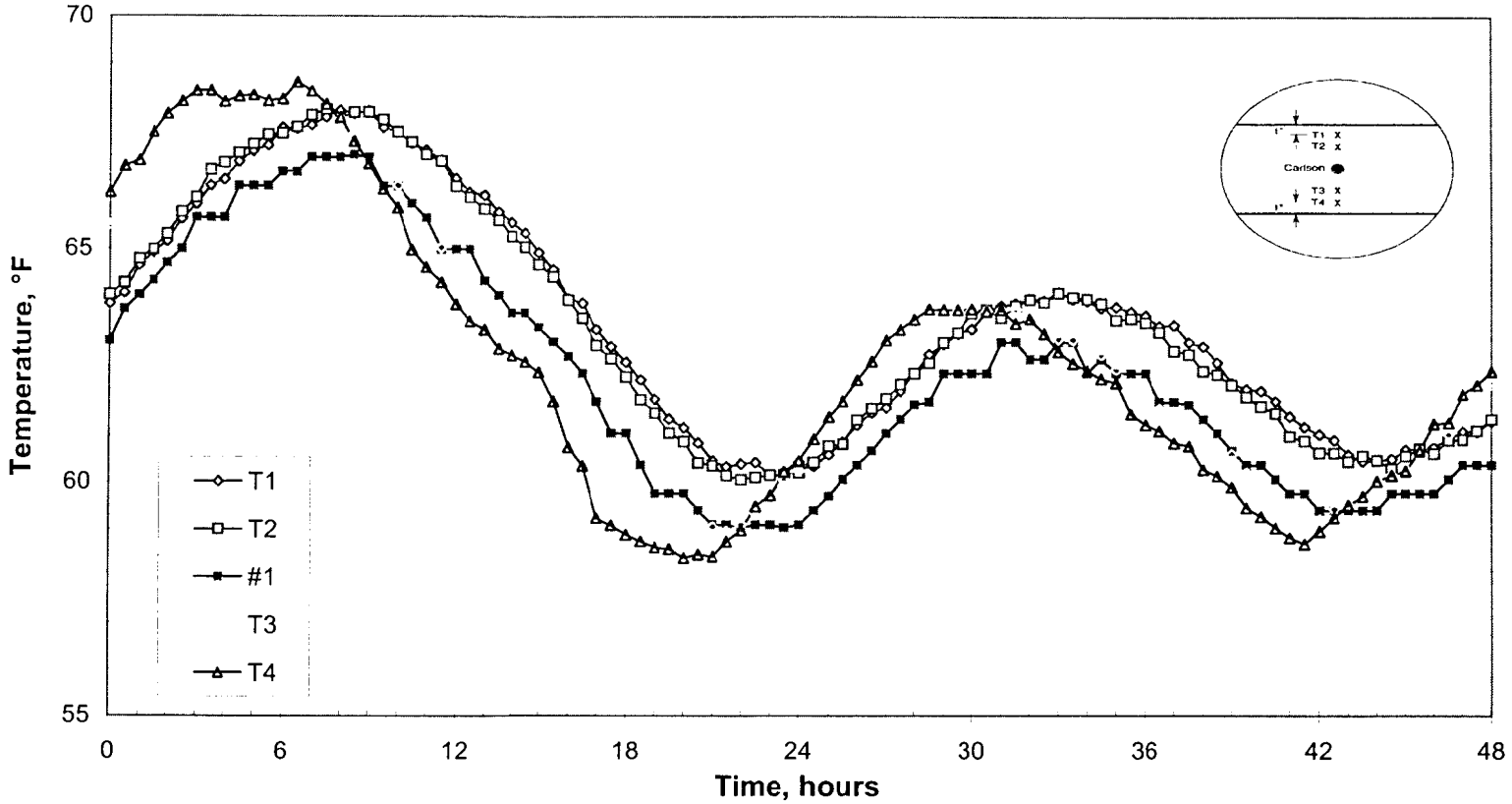


Figure 2.30 Concrete Temperatures in Bottom of the South Slab of Main Span Closure Segment, 5/21/98, 12:00 p.m. to 5/23/98, 12:00 p.m.

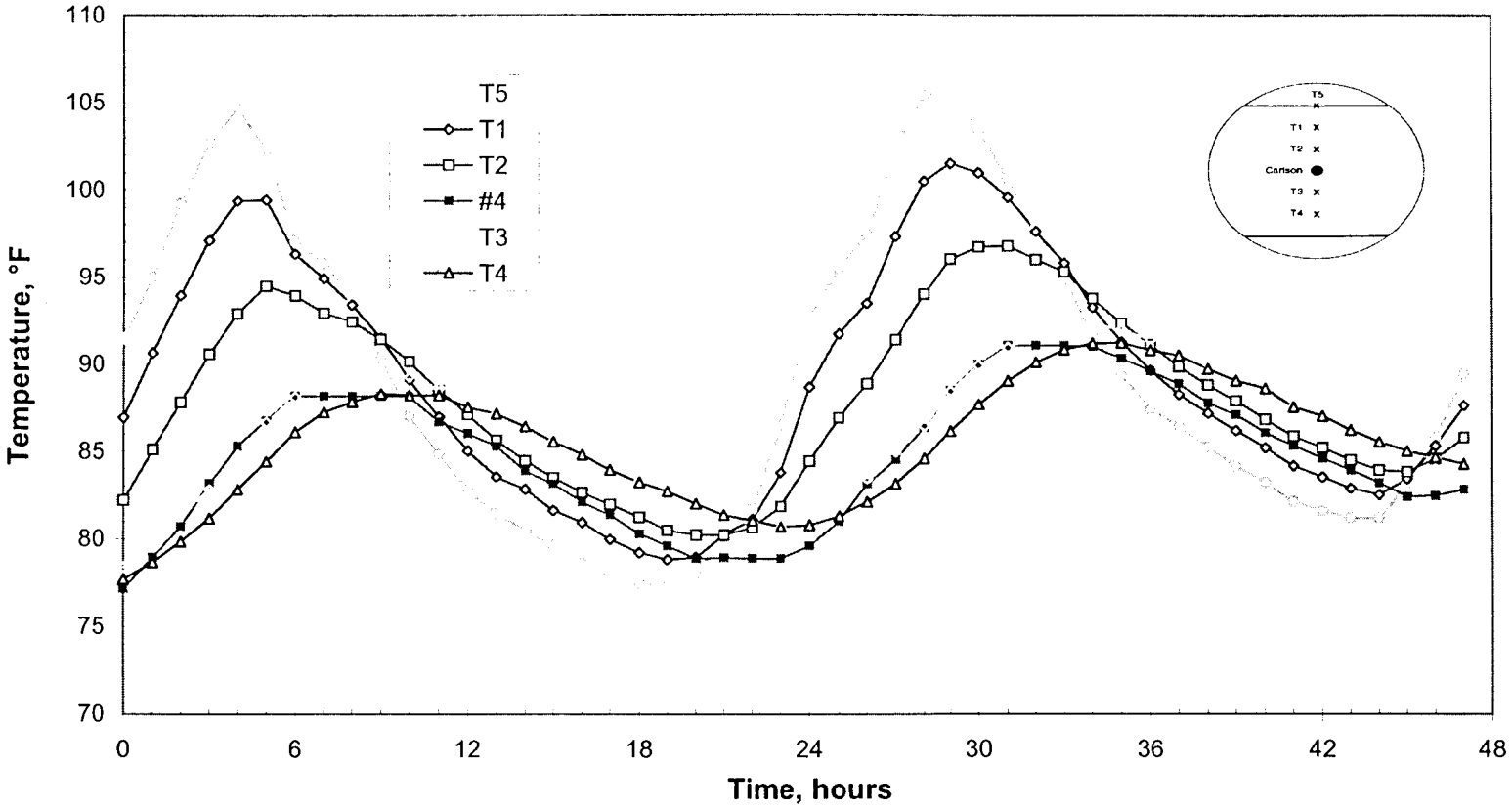


Figure 2.31 Concrete Temperatures in Top of the North Slab of Main Span Closure Segment, 7/21/98, 12:00 p.m. to 7/23/98, 11:00 a.m.

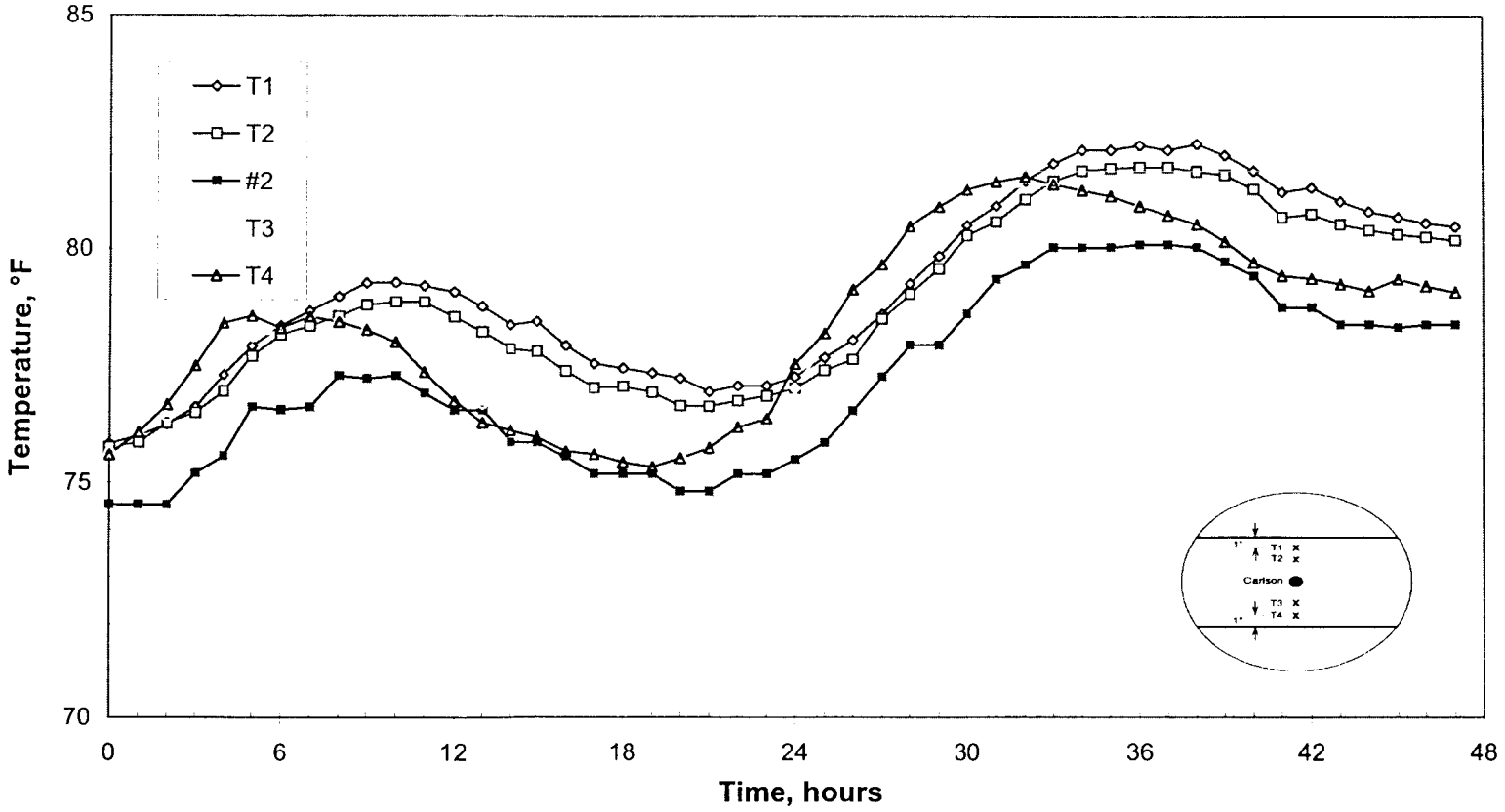


Figure 2.32 Concrete Temperatures in Bottom of the North Slab of Main Span Closure Segment, 7/21/98, 12:00 p.m. to 7/23/98, 11:00 a.m.

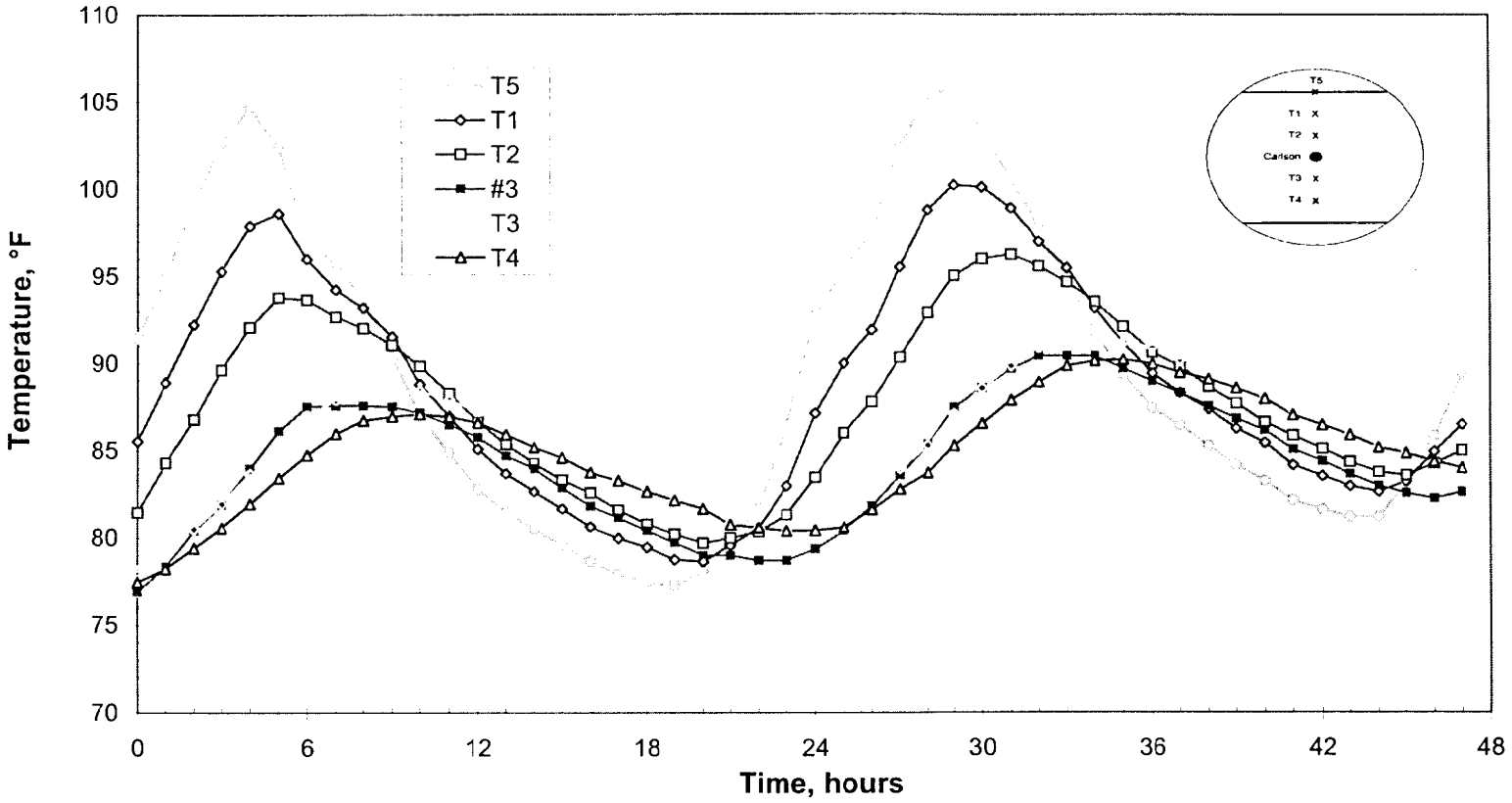


Figure 2.33 Concrete Temperatures in Top of the South Slab of Main Span Closure Segment, 7/21/98, 12:00 p.m. to 7/23/98, 11:00 a.m.

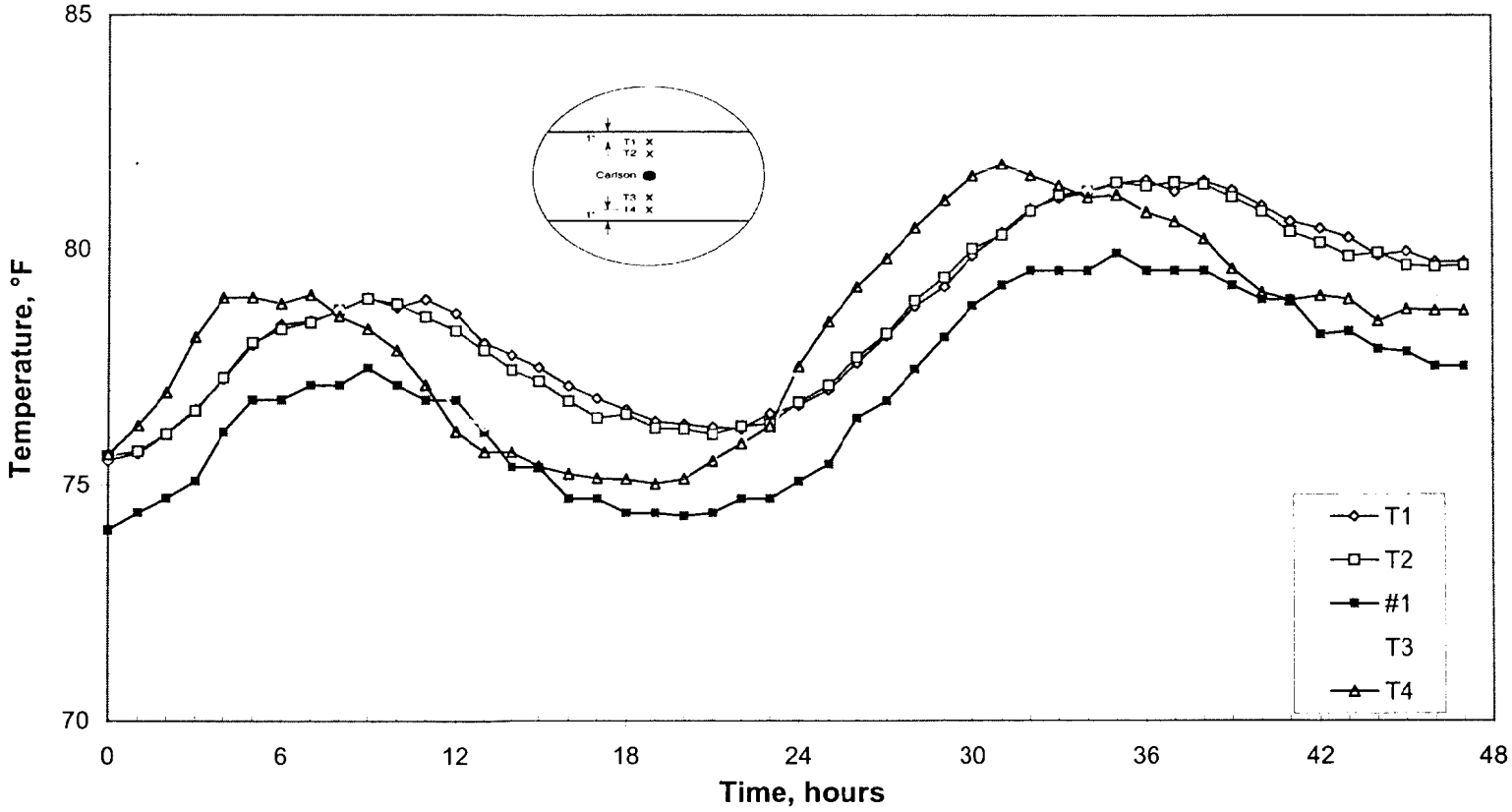


Figure 2.34 Concrete Temperatures in Bottom of the South Slab of Main Span Closure Segment, 7/21/98, 12:00 p.m. to 7/23/98, 11:00 a.m.

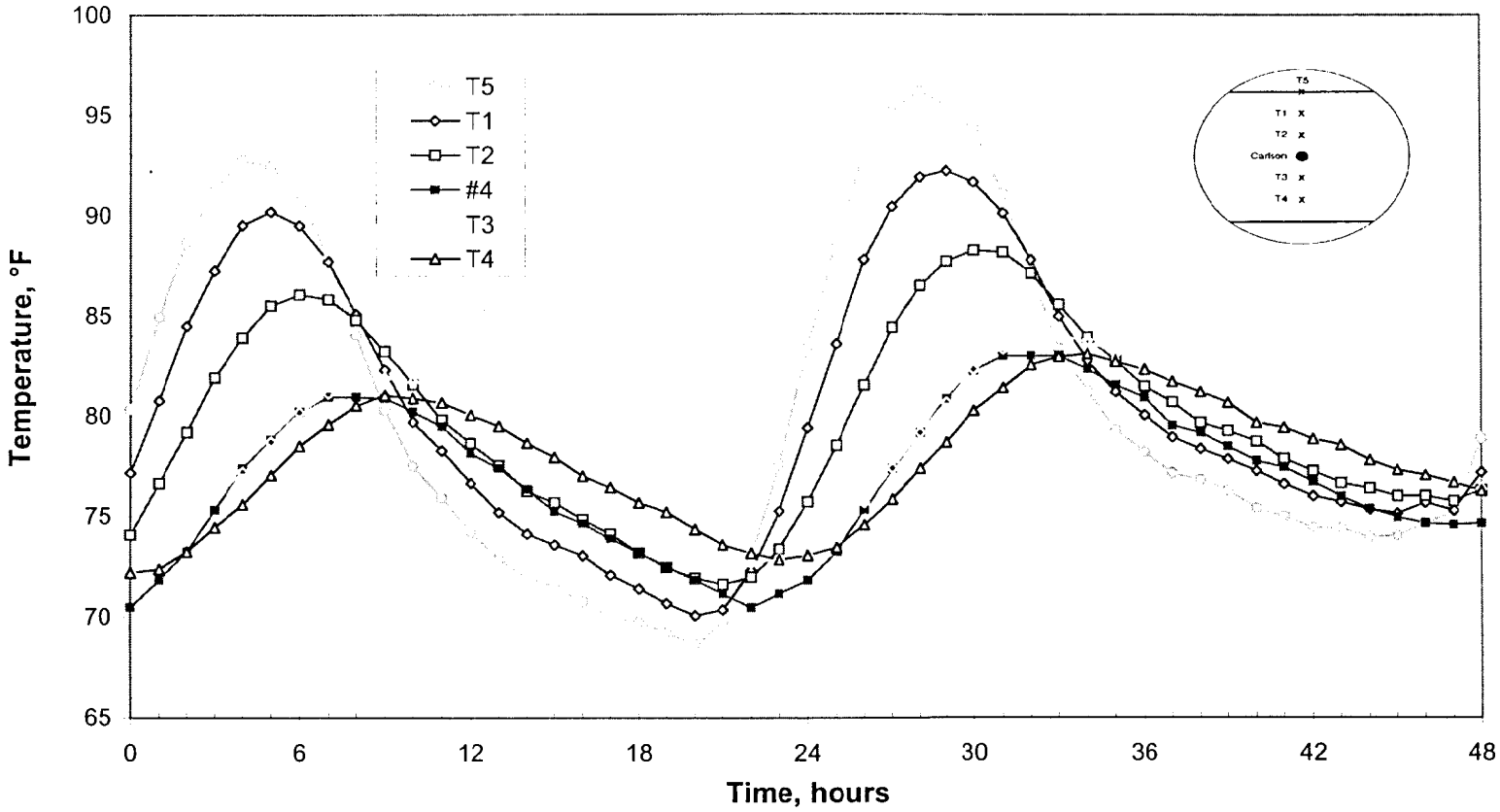


Figure 2.35 Concrete Temperatures in Top of the North Slab of Main Span Closure Segment, 9/5/98, 12:00 p.m. to 9/7/98, 12:00 p.m.

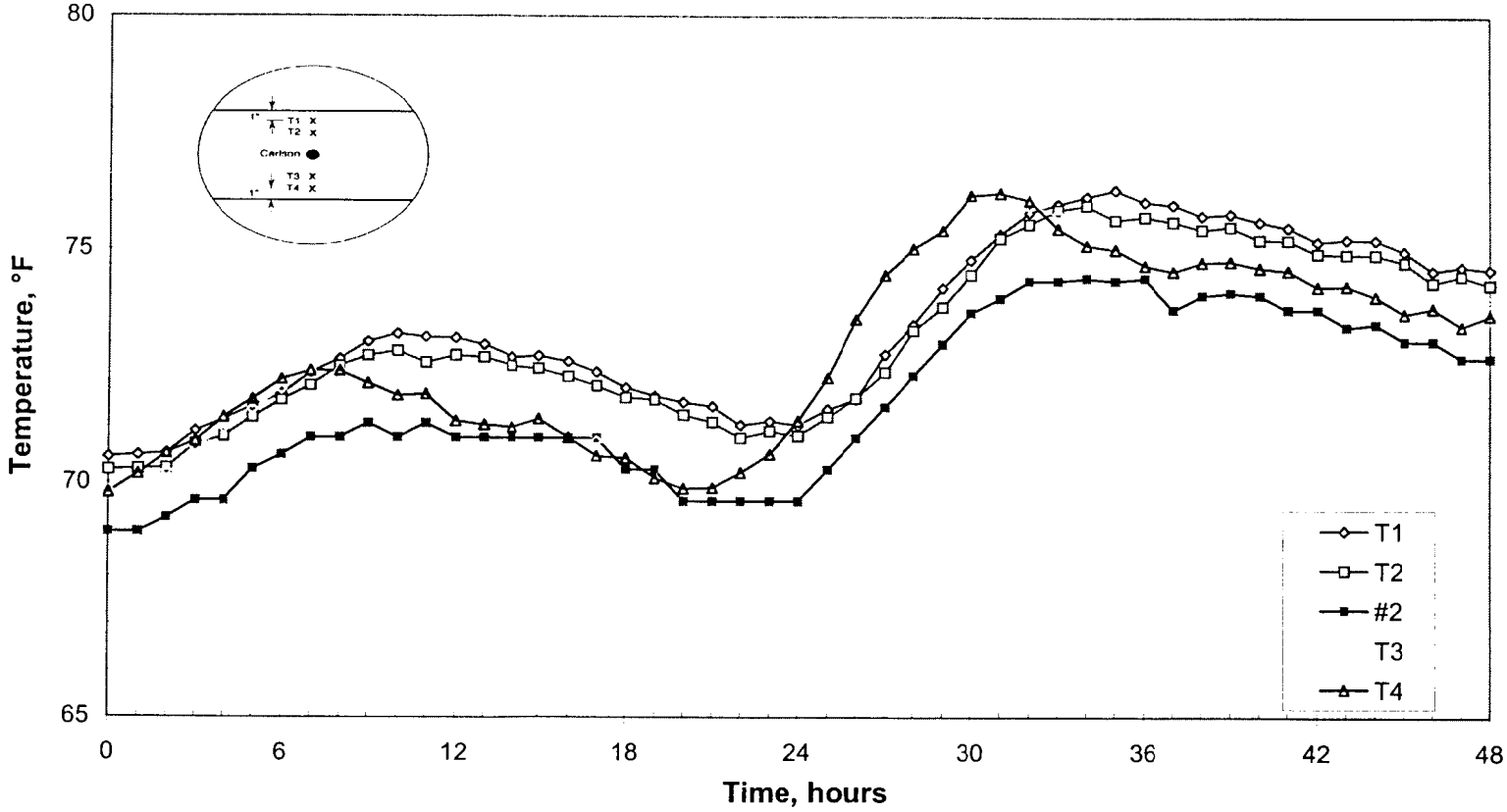


Figure 2.36 Concrete Temperatures in Bottom of the North Slab of Main Span Closure Segment, 9/5/98, 12:00 p.m. to 9/7/98, 12:00 p.m.

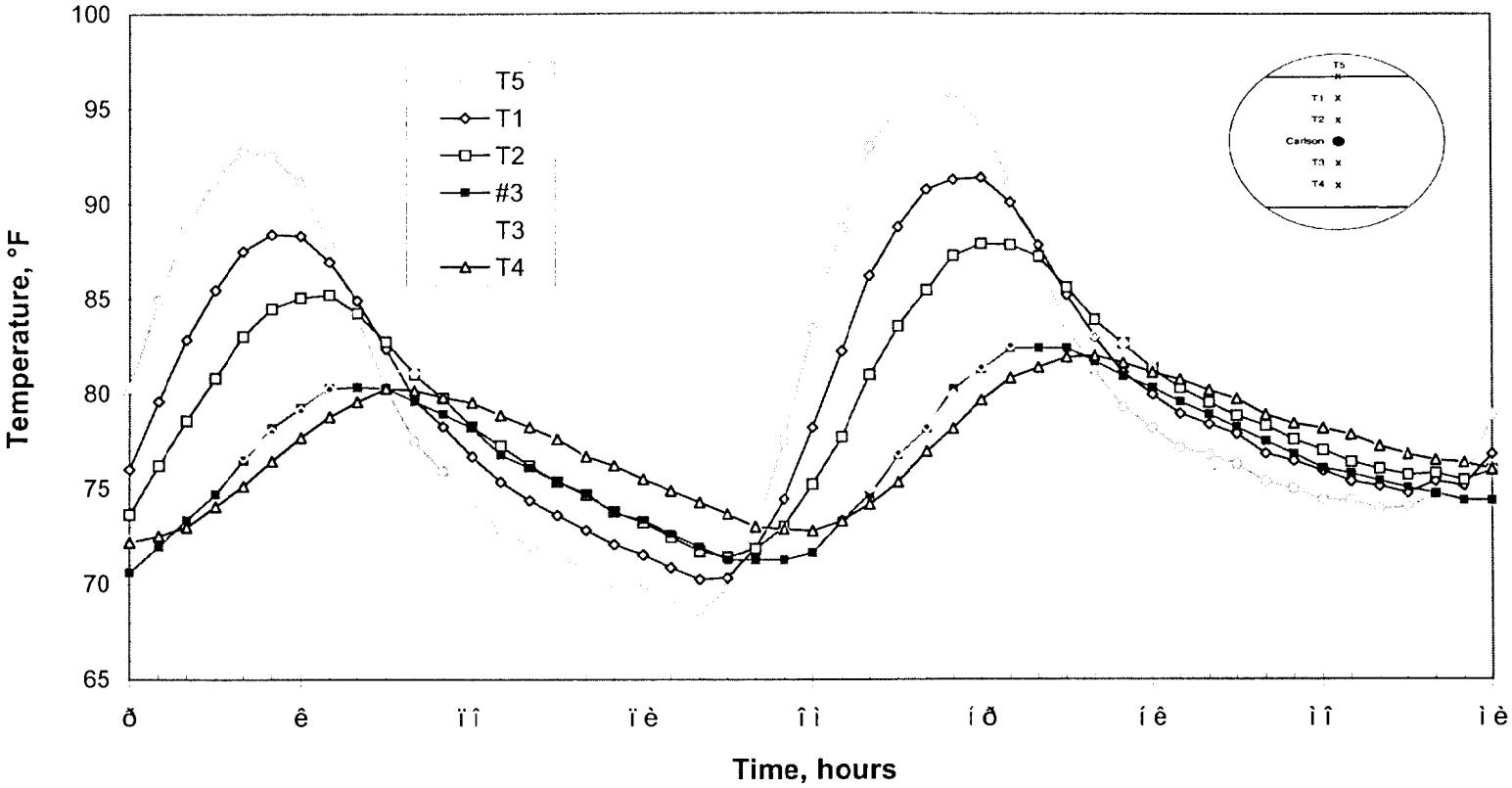


Figure 2.37 Concrete Temperatures in Top of the South Slab of Main Span Closure Segment, 9/5/98, 12:00 p.m. to 9/7/98, 12:00 p.m.

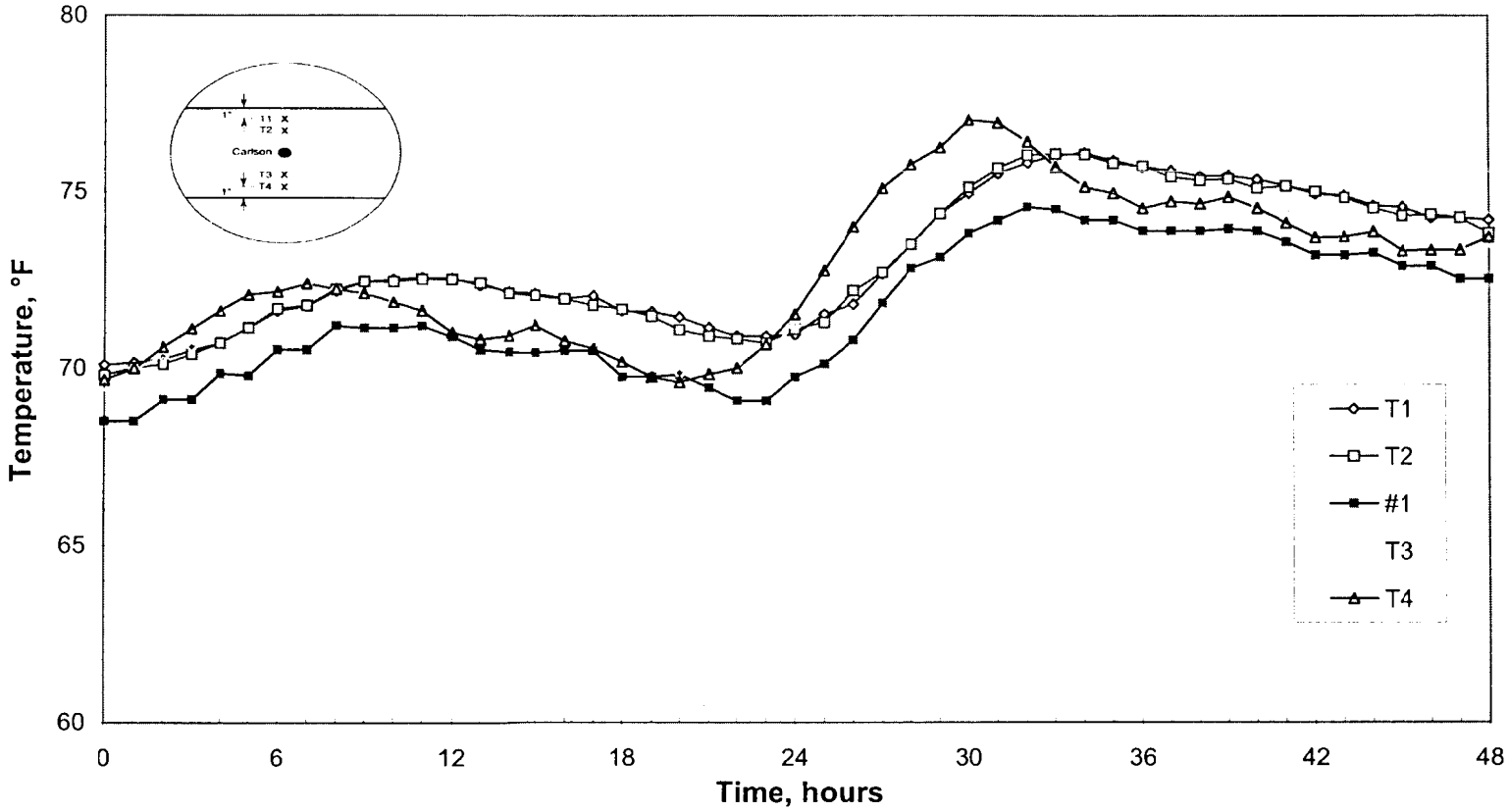


Figure 2.38 Concrete Temperatures in Bottom of the South Slab of Main Span Closure Segment, 9/5/98, 12:00 p.m. to 9/7/98, 12:00 p.m.

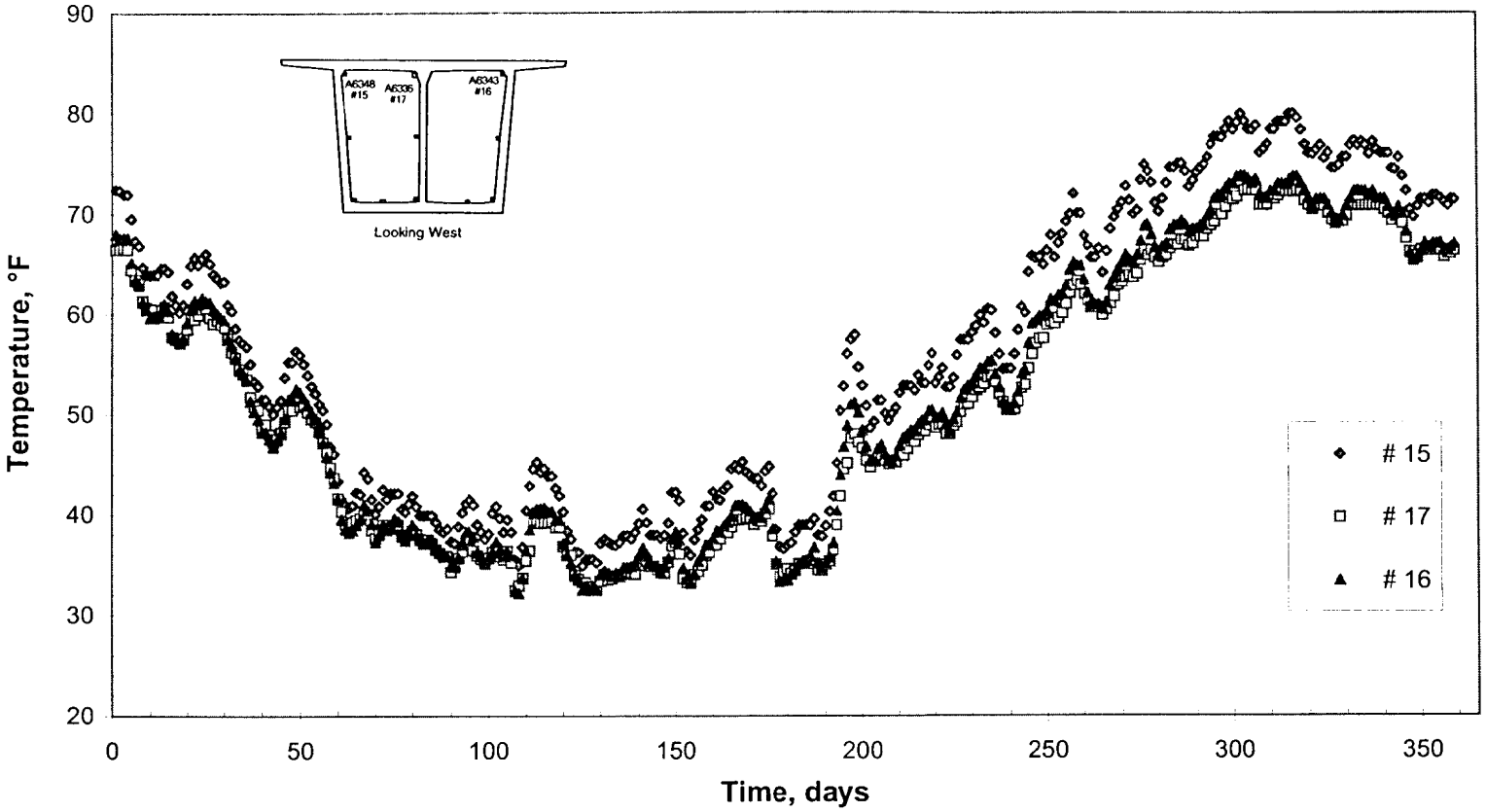


Figure 2.39 Concrete Temperatures from Carlson Strain Meters at P14MS1, from 9/19/97 to 9/23/98, 2:00 p.m.

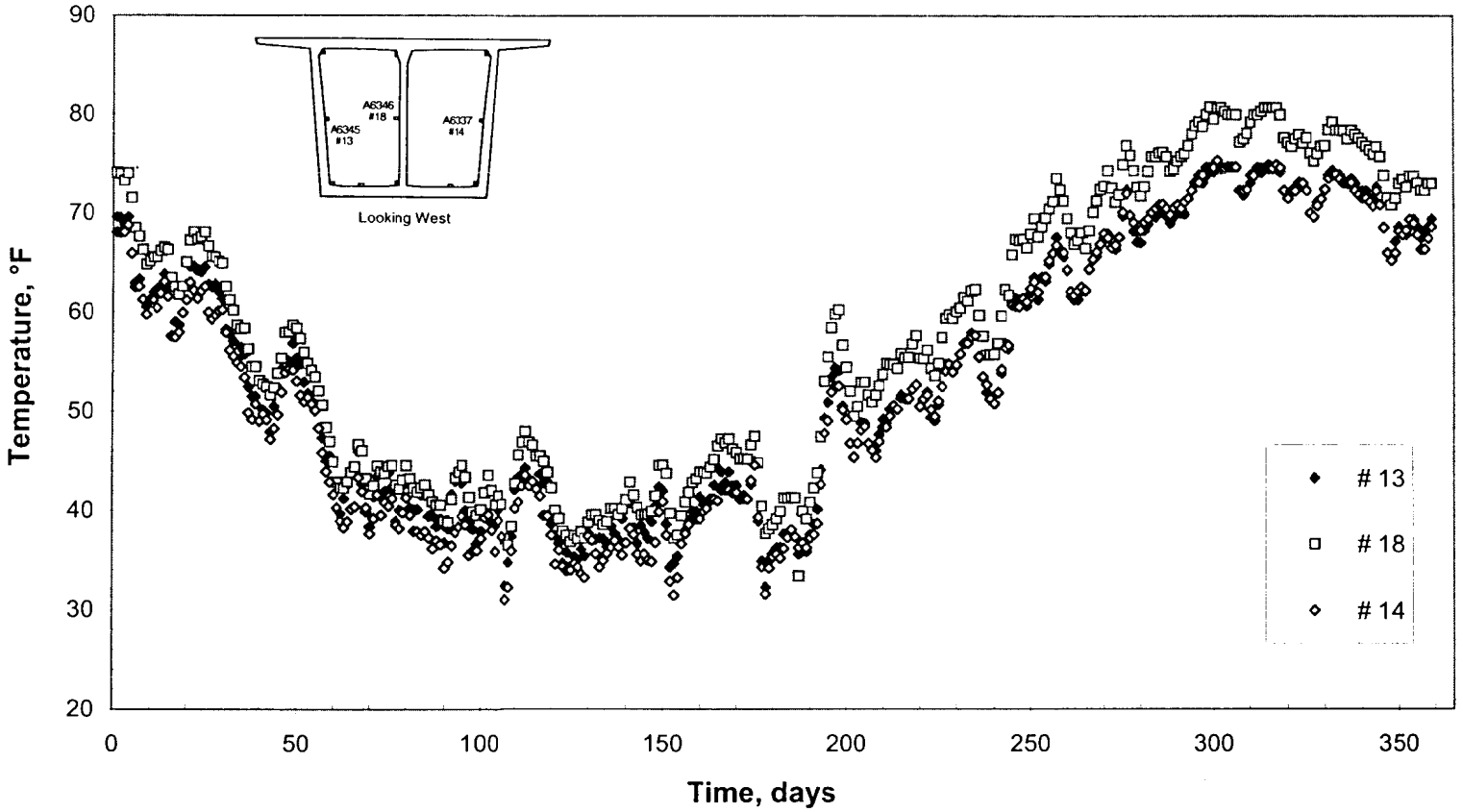


Figure 2.40 Concrete Temperatures from Carlson Strain Meters at P14MS1, from 9/19/97 to 9/23/98, 2:00 p.m.

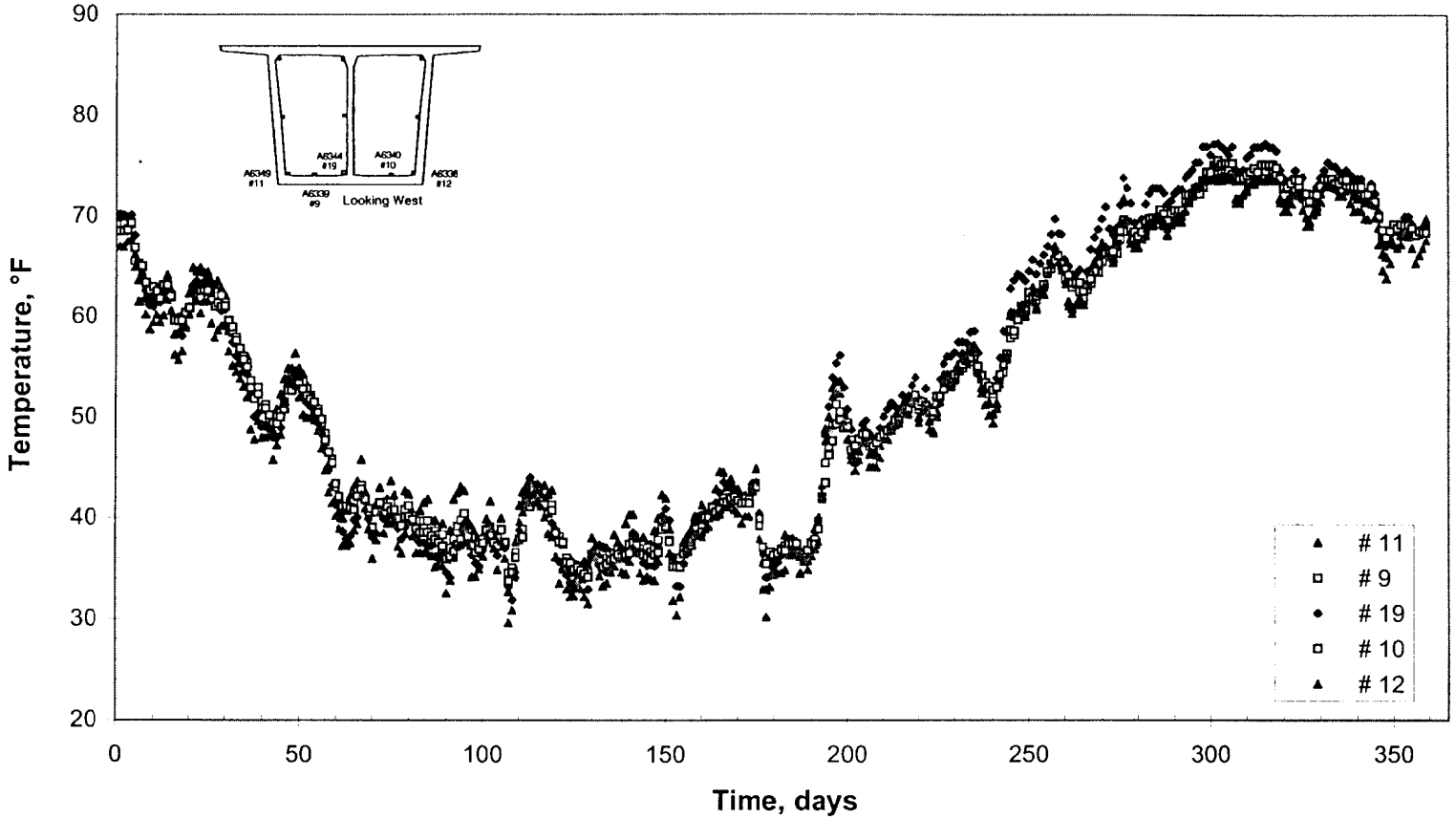


Figure 2.41 Concrete Temperatures form Carlson Strain Meters at P14MS1, from 9/19/97 to 9/23/98, 2:00 p.m.

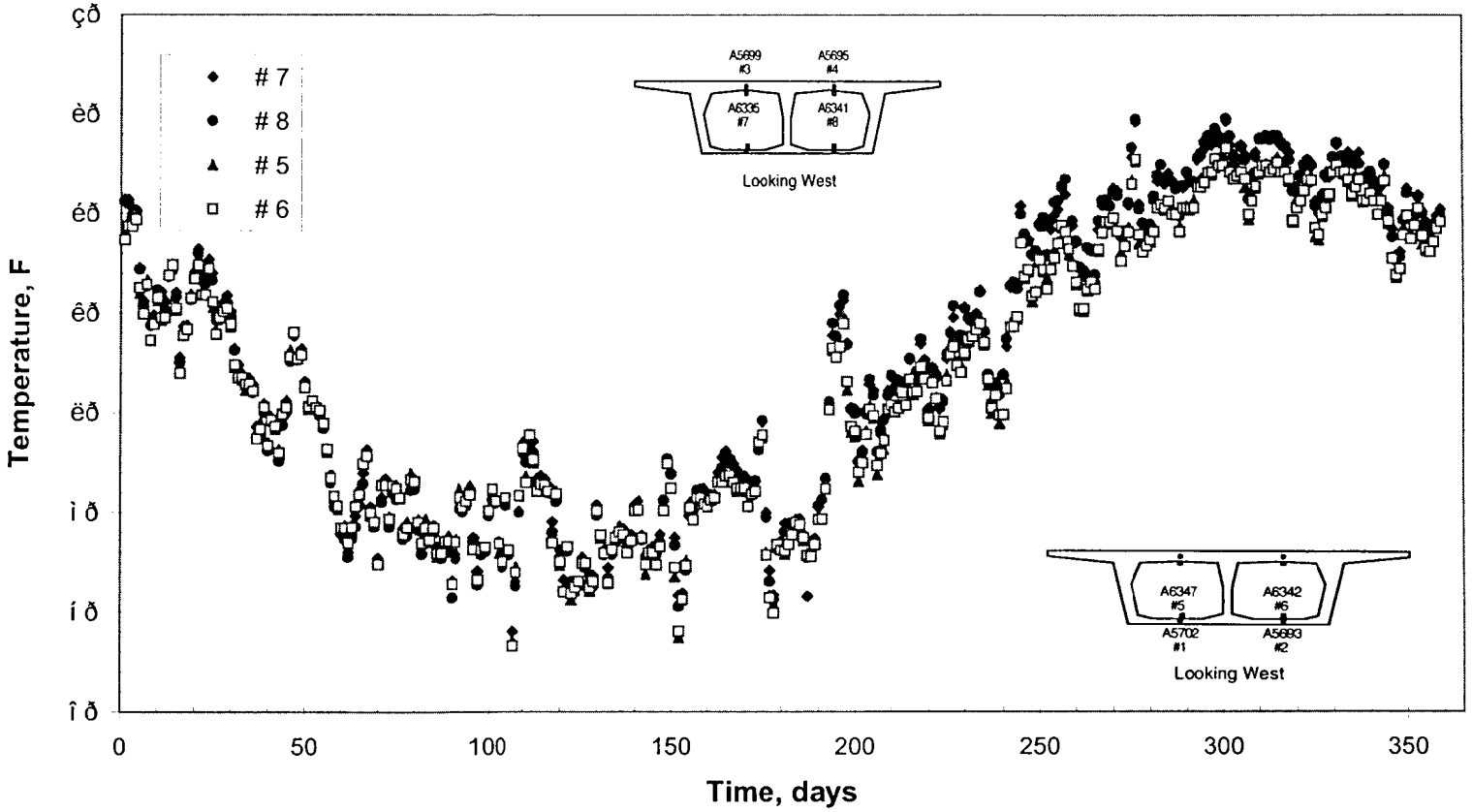


Figure 2.42 Concrete Temperatures from Carlson Strain Meters at Main Span Closure Segment from 9/19/97 to 9/23/98, 2:00 p.m.

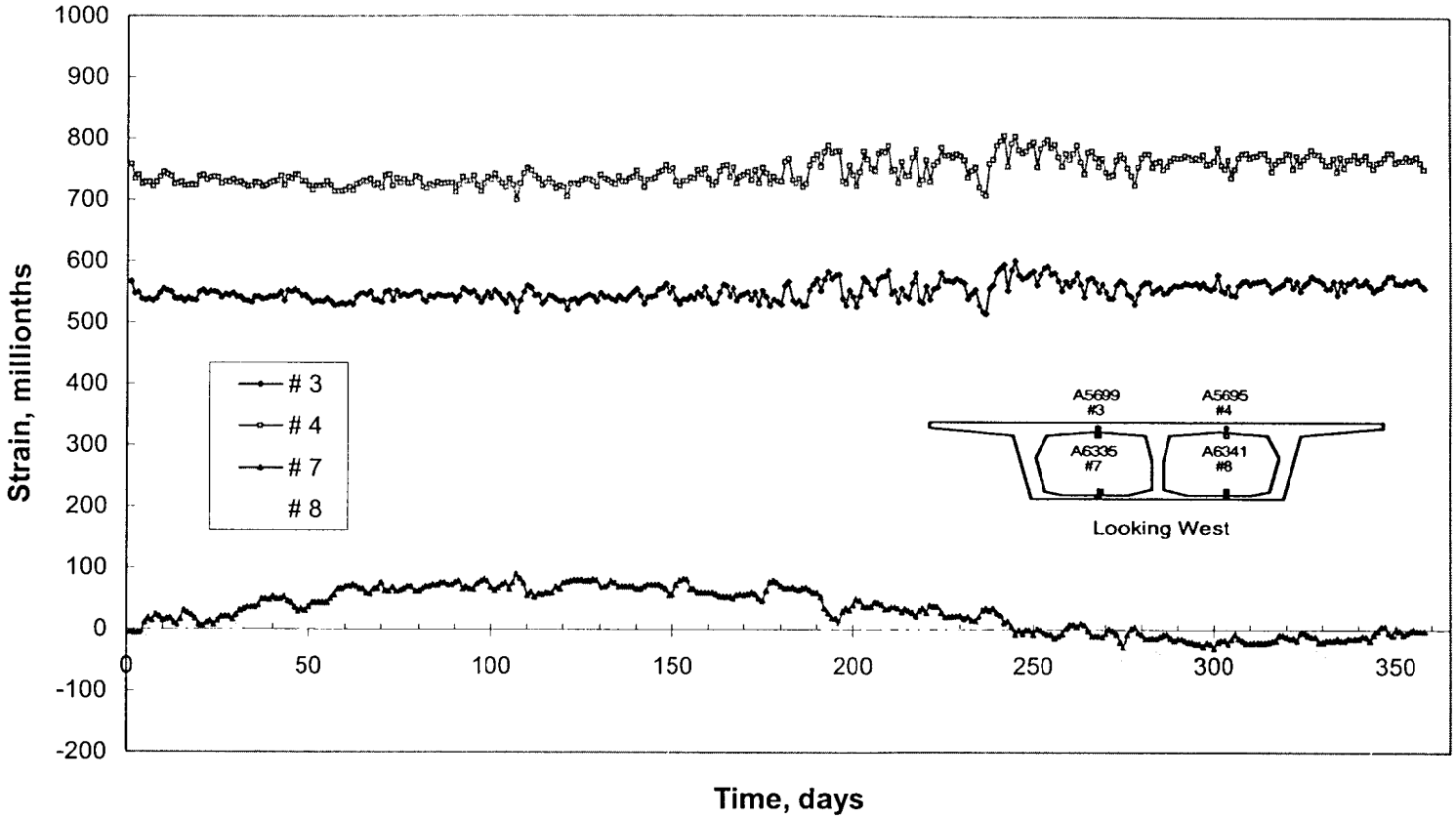


Figure 2.43 Concrete Compressive Strain in the Top Slab of the Main Span Closure Segment at 2:00 p.m. from 9/19/97 to 9/22/98

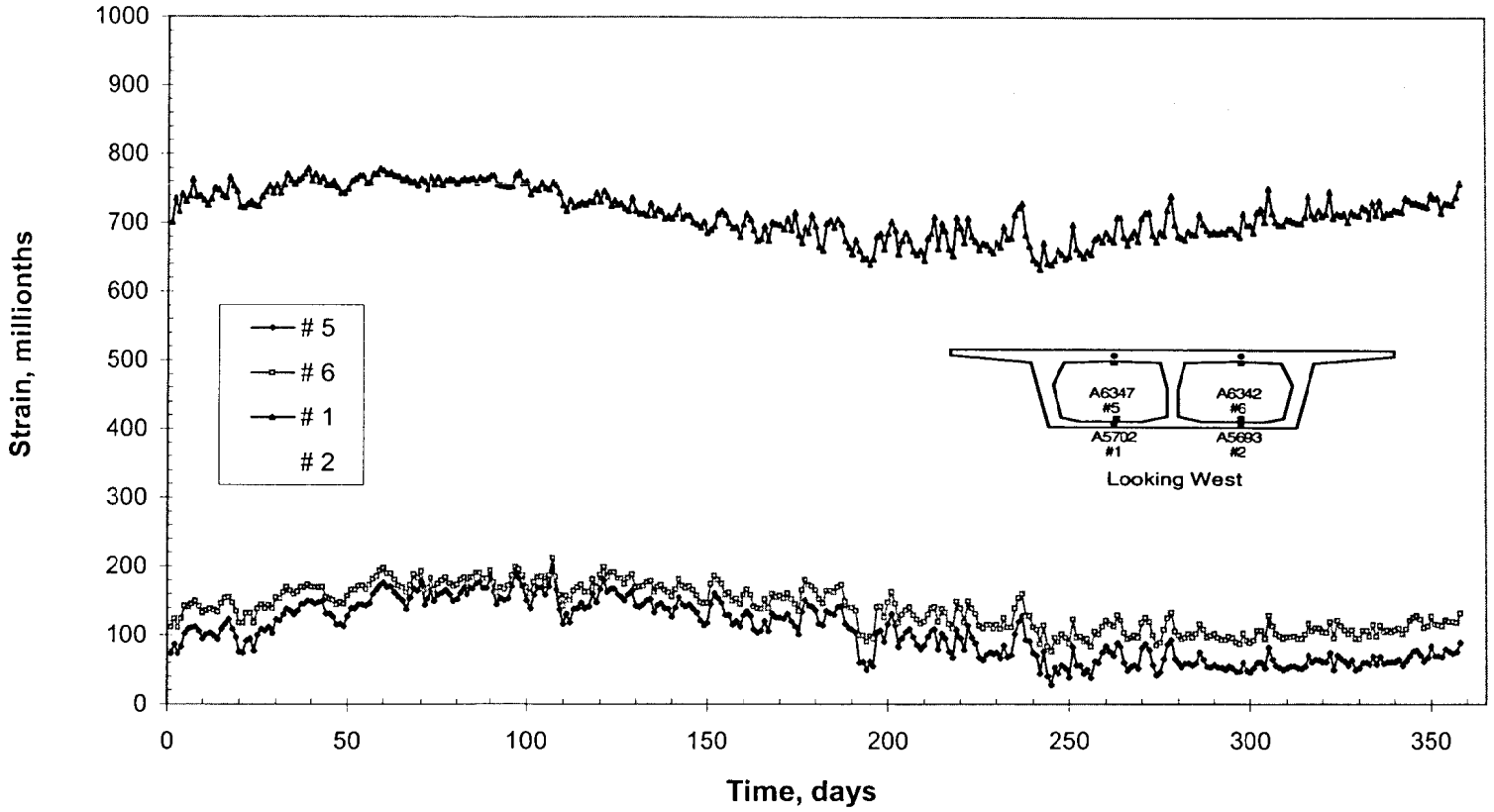


Figure 2.44 Concrete Compressive Strain in the Bottom Slab of the Main Span Closure Segment at 2:00 p.m. from 9/19/97 to 9/22/98

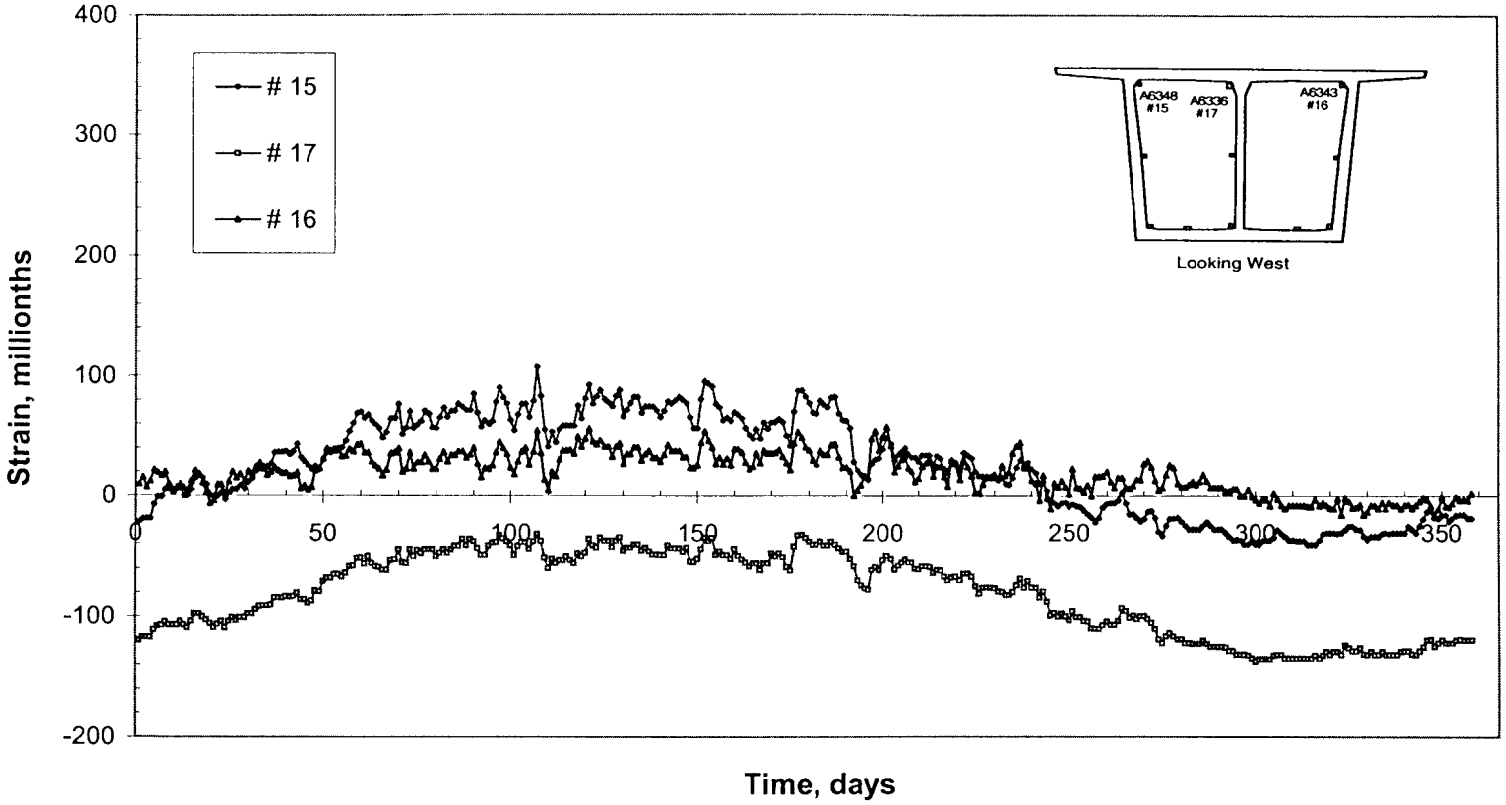


Figure 2.45 Concrete Compressive Strain in the Top Horizontal Section of Segment P14MS1 at 2:00 p.m. from 9/19/97 to 9/22/98

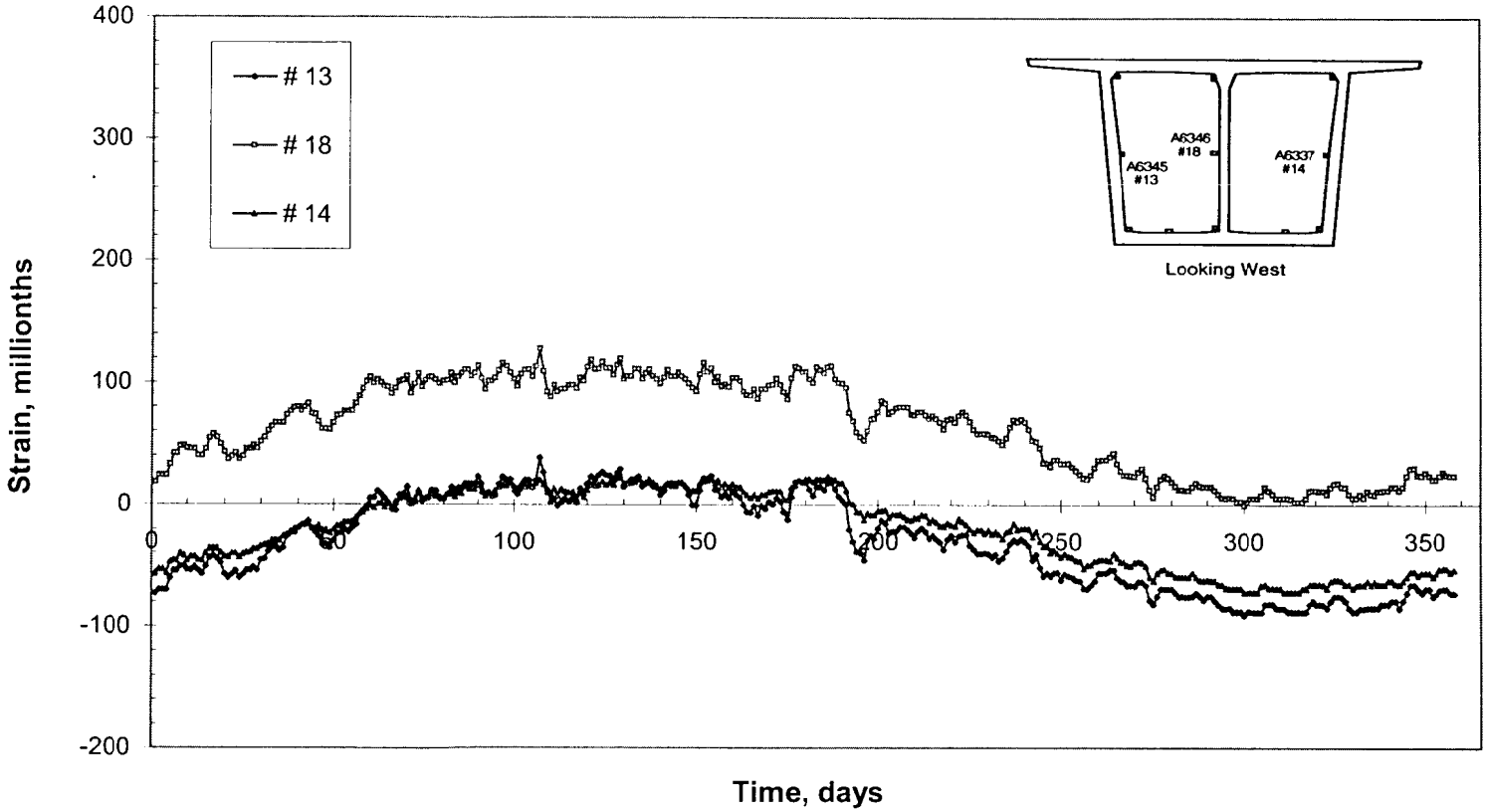


Figure 2.46 Concrete Compressive Strain in the Center Horizontal Section of Segment P14MS1 at 2:00 p.m. from 9/19/97 to 9/22/98

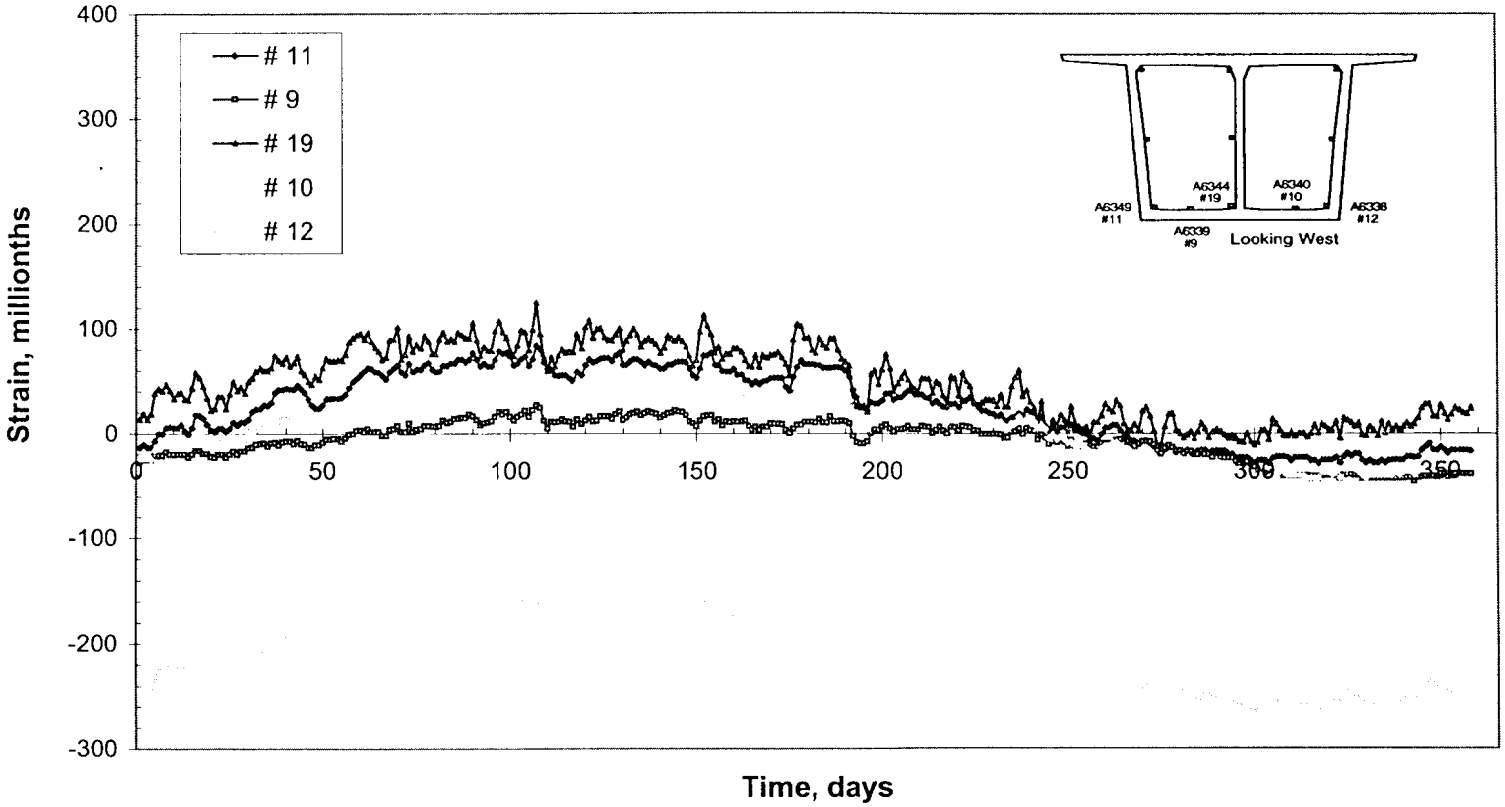


Figure 2.47 Concrete Compressive Strain in the Bottom Horizontal Section of Segment P14MS1 at 2:00 p.m. from 9/19/97 to 9/22/98

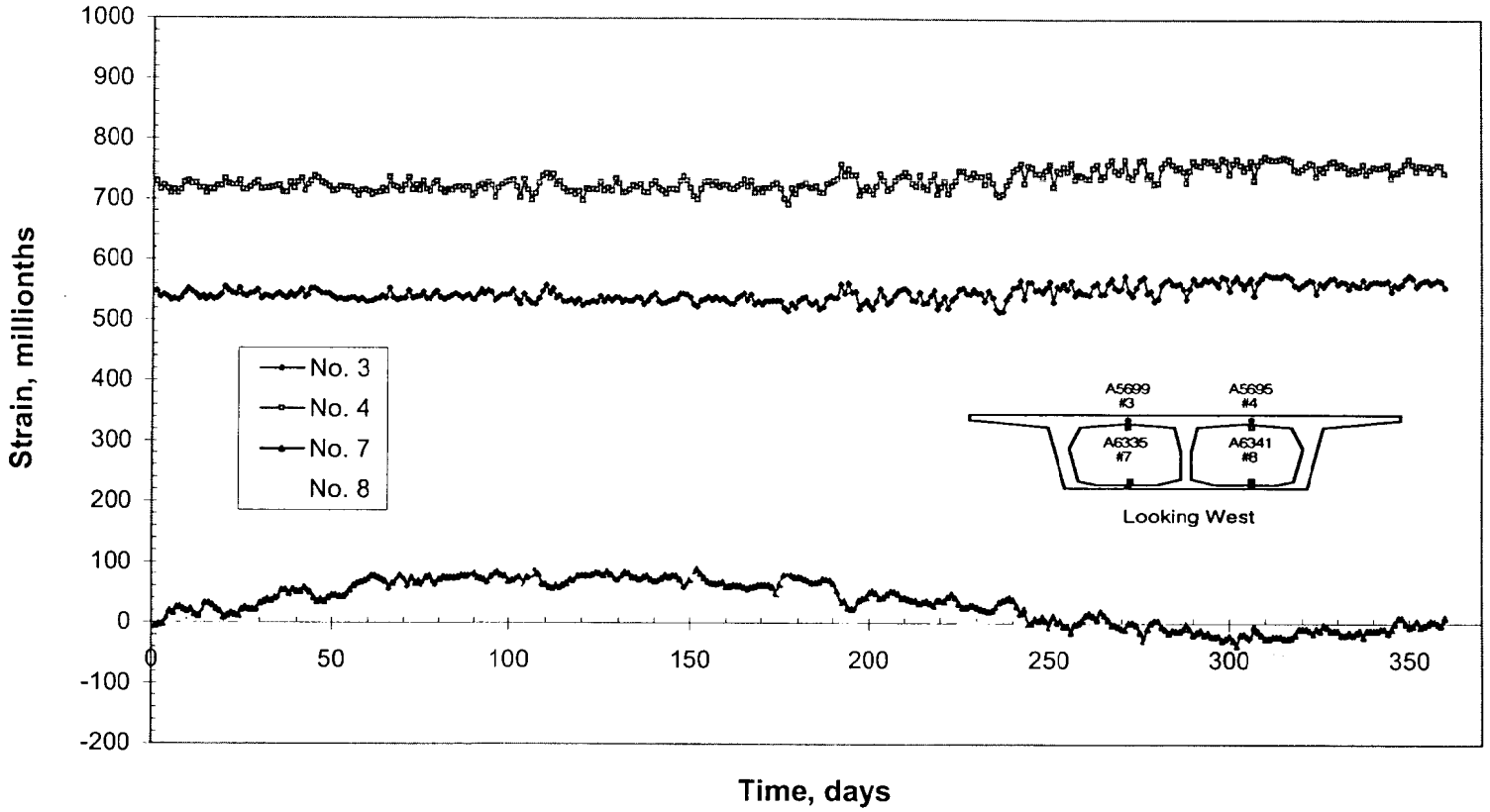


Figure 2.48 Concrete Compressive Strain in the Top Slab of the Main Span Closure Segment at 6:00 a.m. from 9/19/97 to 9/23/98

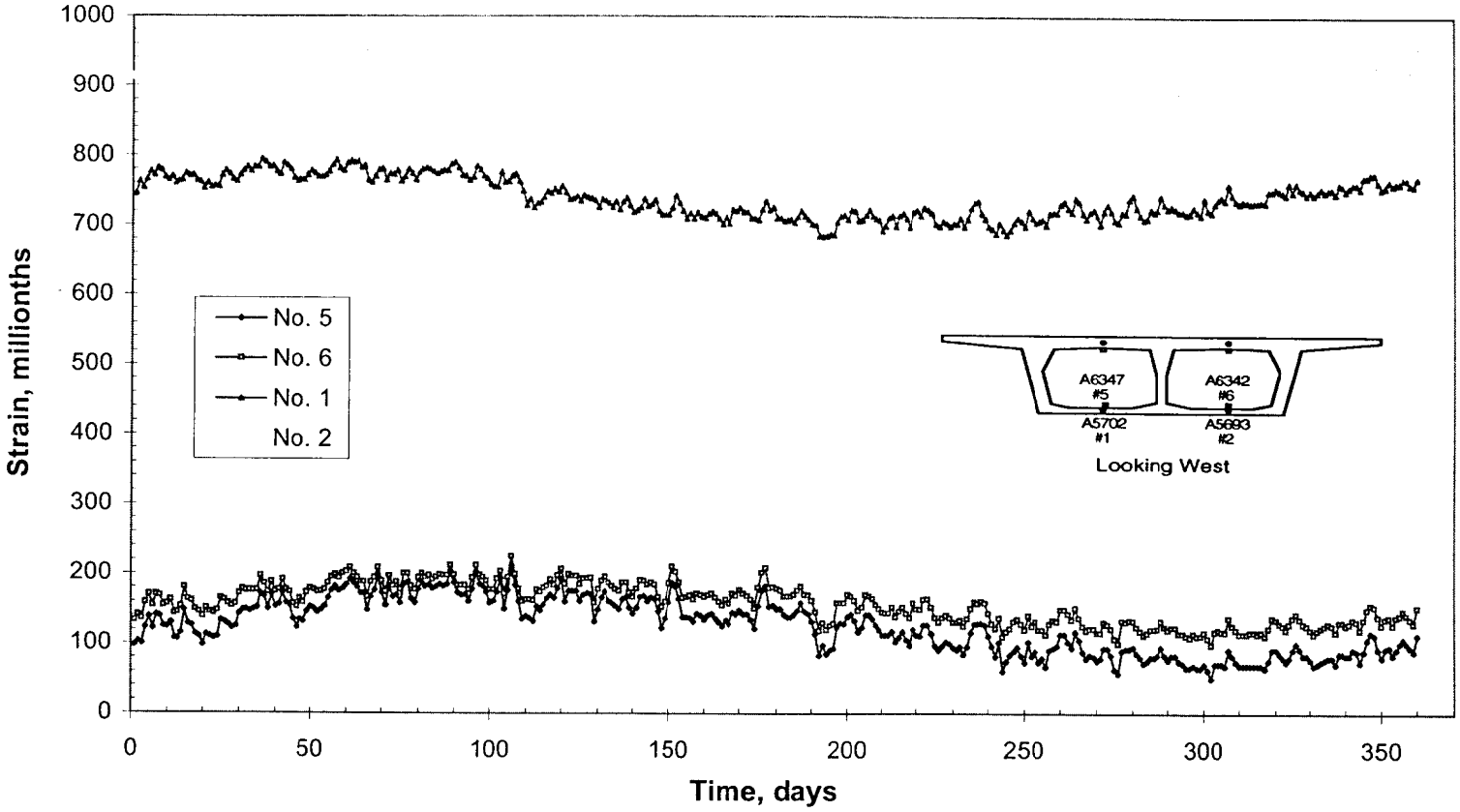


Figure 2.49 Concrete Compressive Strain in the Bottom Slab of the Main Span Closure Segment at 6:00 a.m. from 9/19/97 to 9/23/98

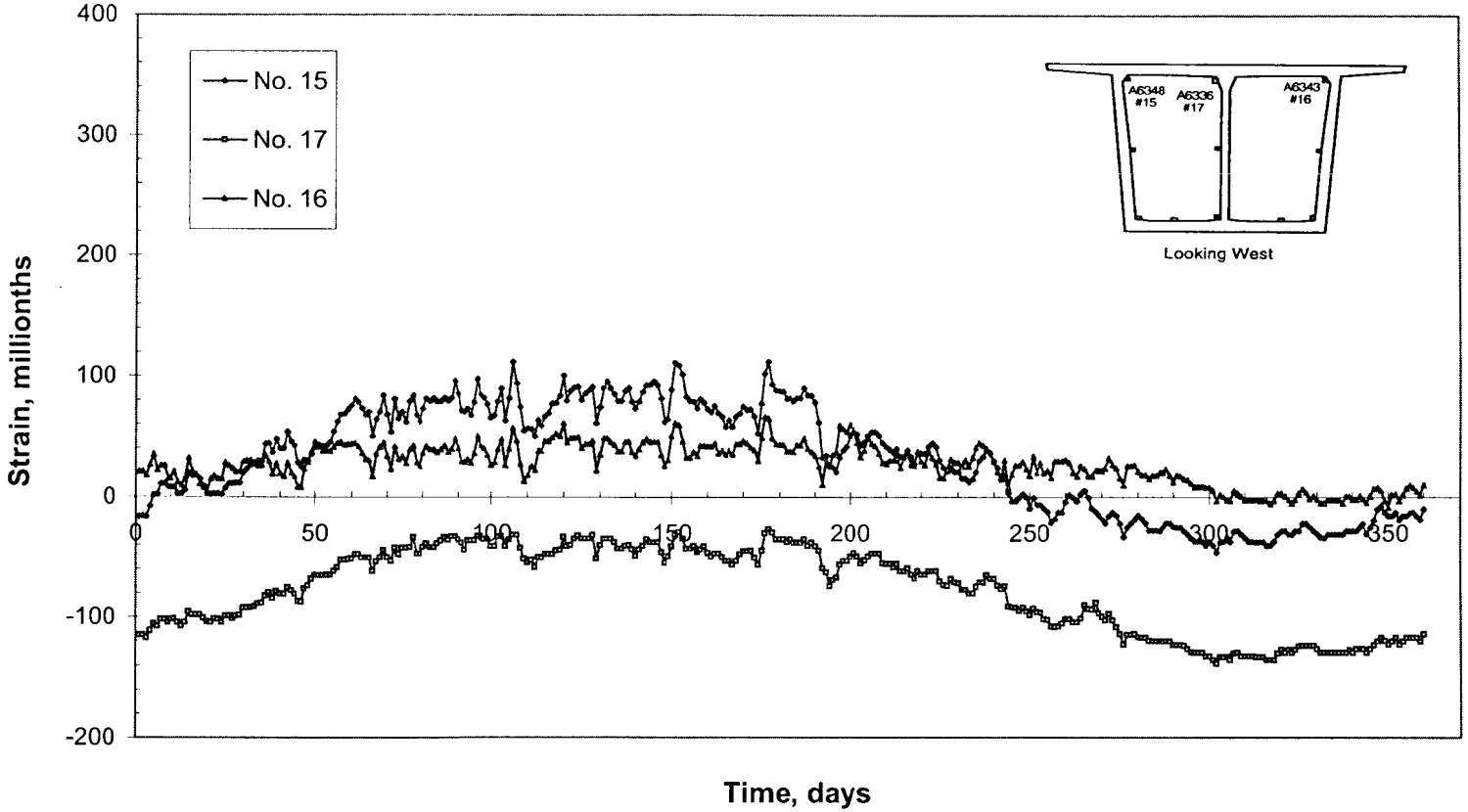


Figure 2.50 Concrete Compressive Strain in the Top Horizontal Section of Segment P14MS1 at 6:00 a.m. from 9/19/97 to 9/23/98

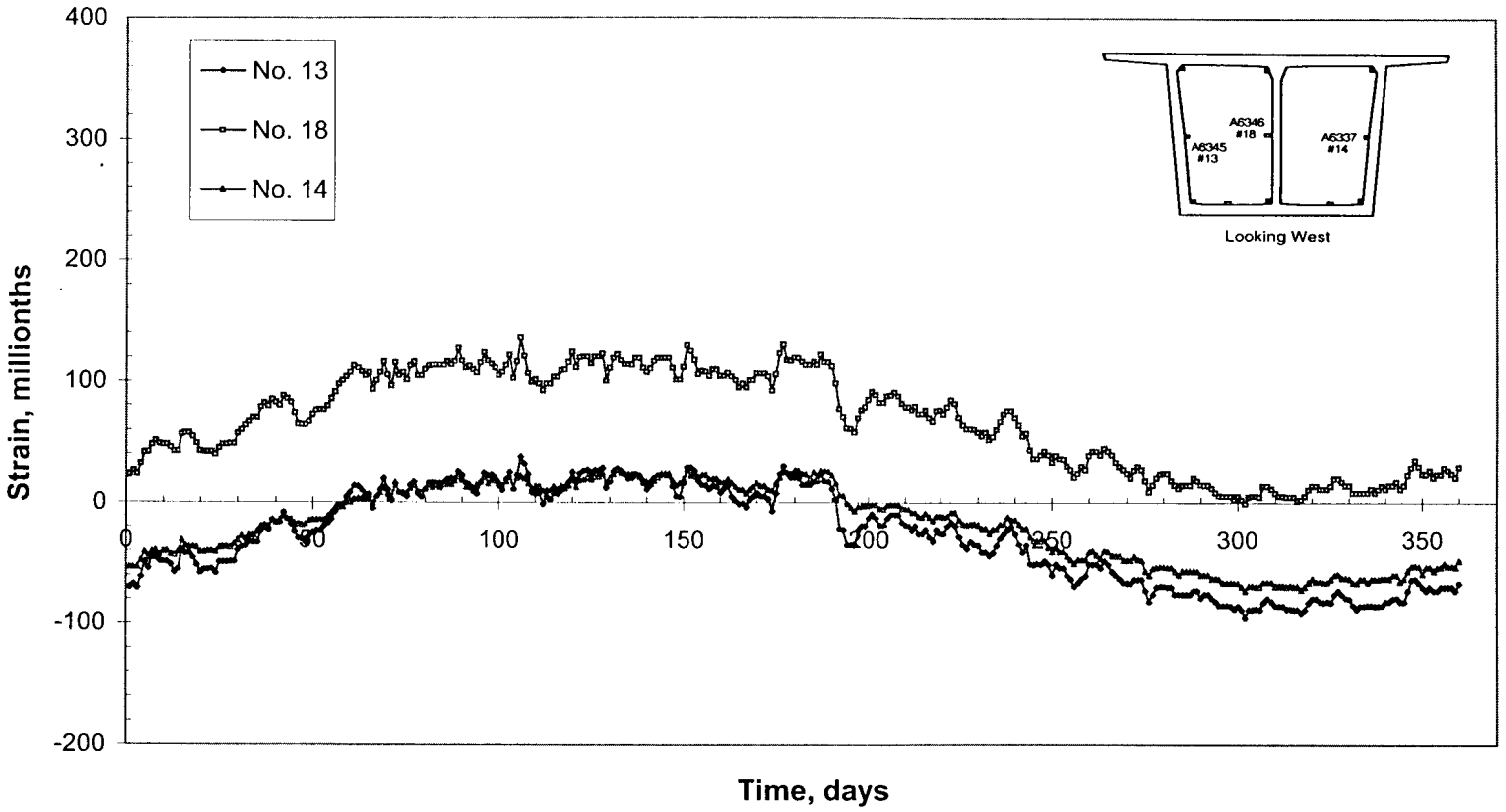


Figure 2.51 Concrete Compressive Strain in the Center Horizontal Section of Segment P14MS1 at 6:00 a.m. from 9/19/97 to 9/23/98

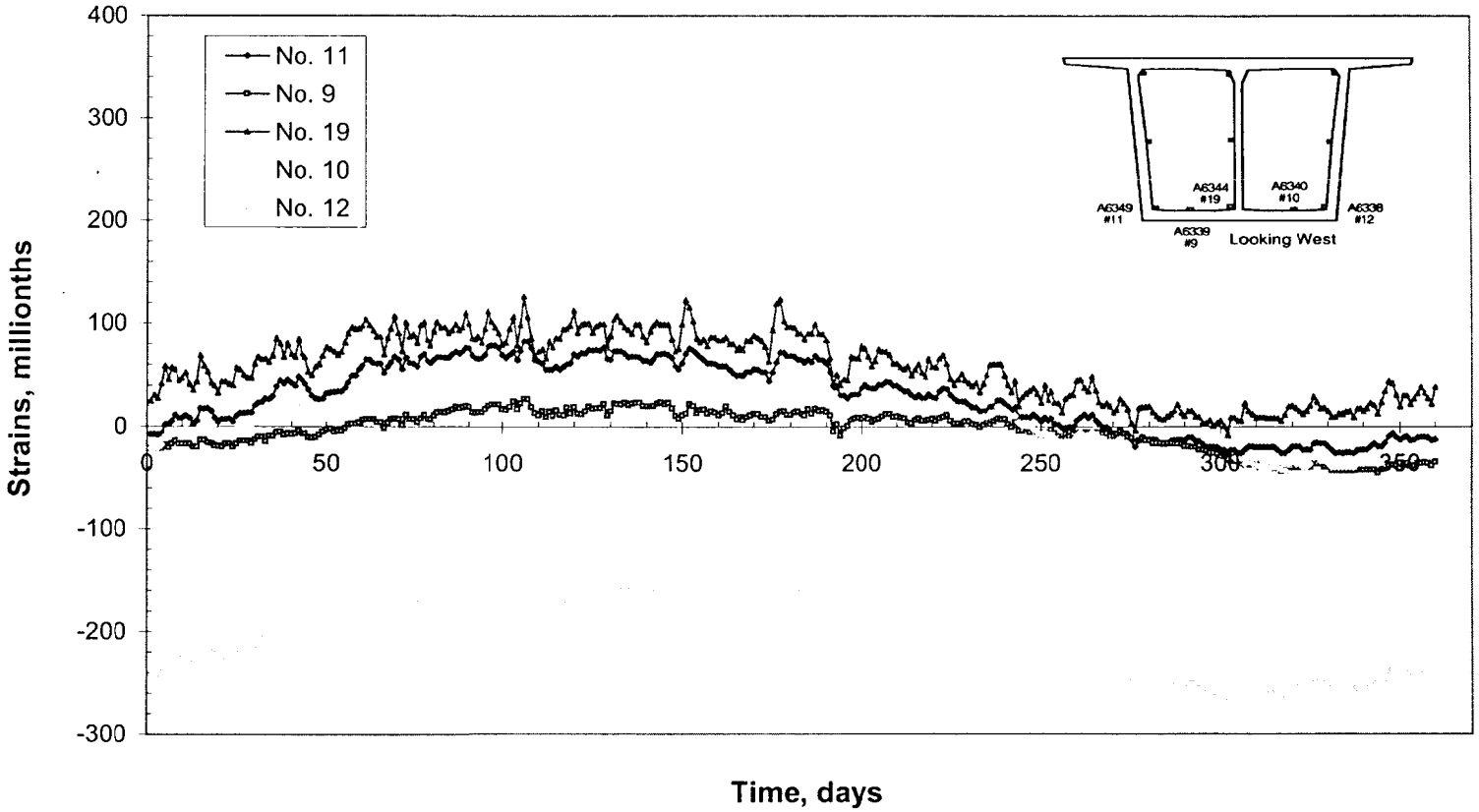


Figure 2.52 Concrete Compressive Strain in the Bottom Horizontal Section of Segment P14MS1 at 6:00 a.m. from 9/19/97 to 9/23/98

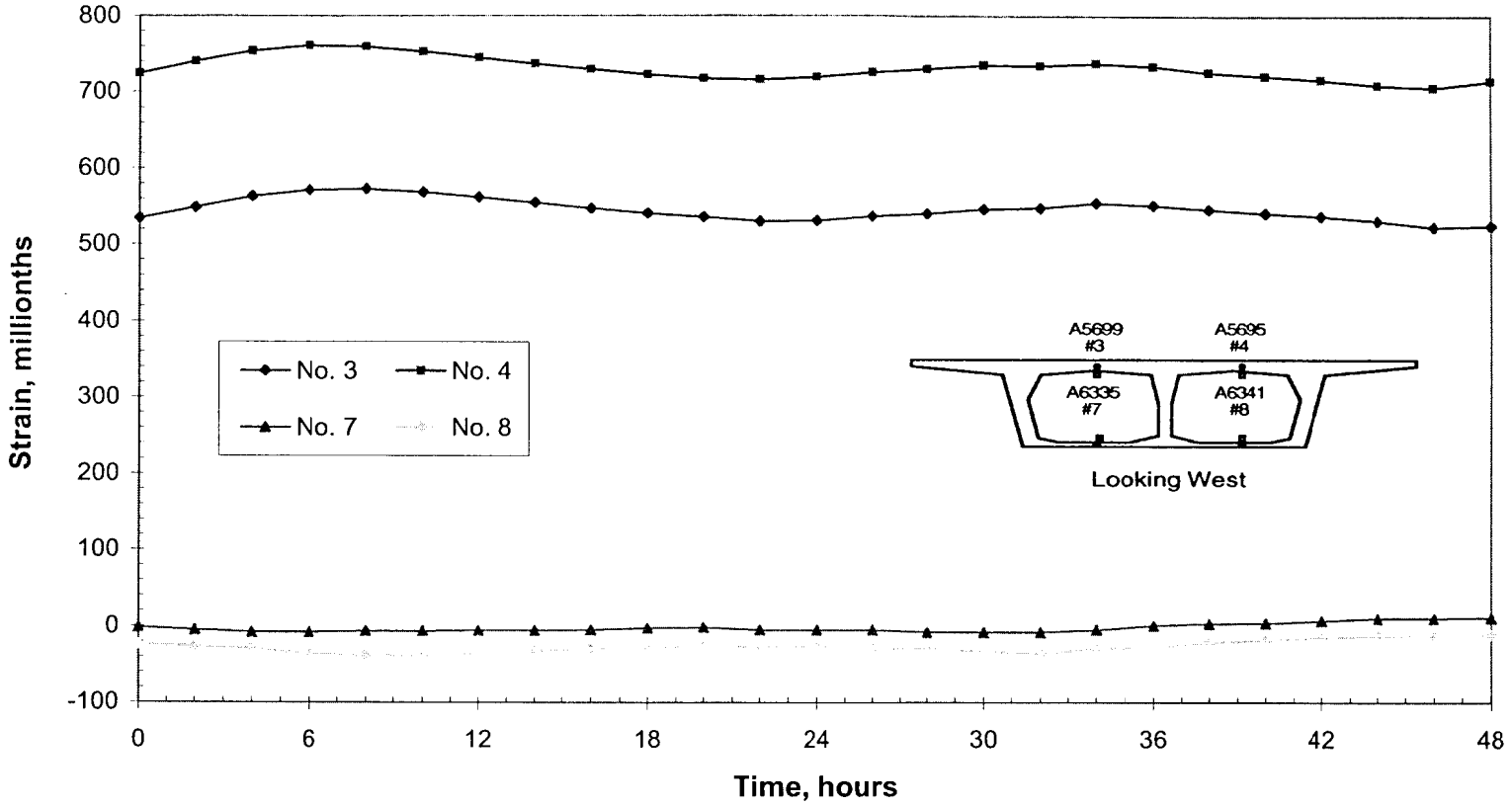


Figure 2.53 Concrete Compressive Strain in the Top Slab of the Main Span Closure Segment, 9/21/97, 12:00 p.m. to 9/23/97, 12:00 p.m.

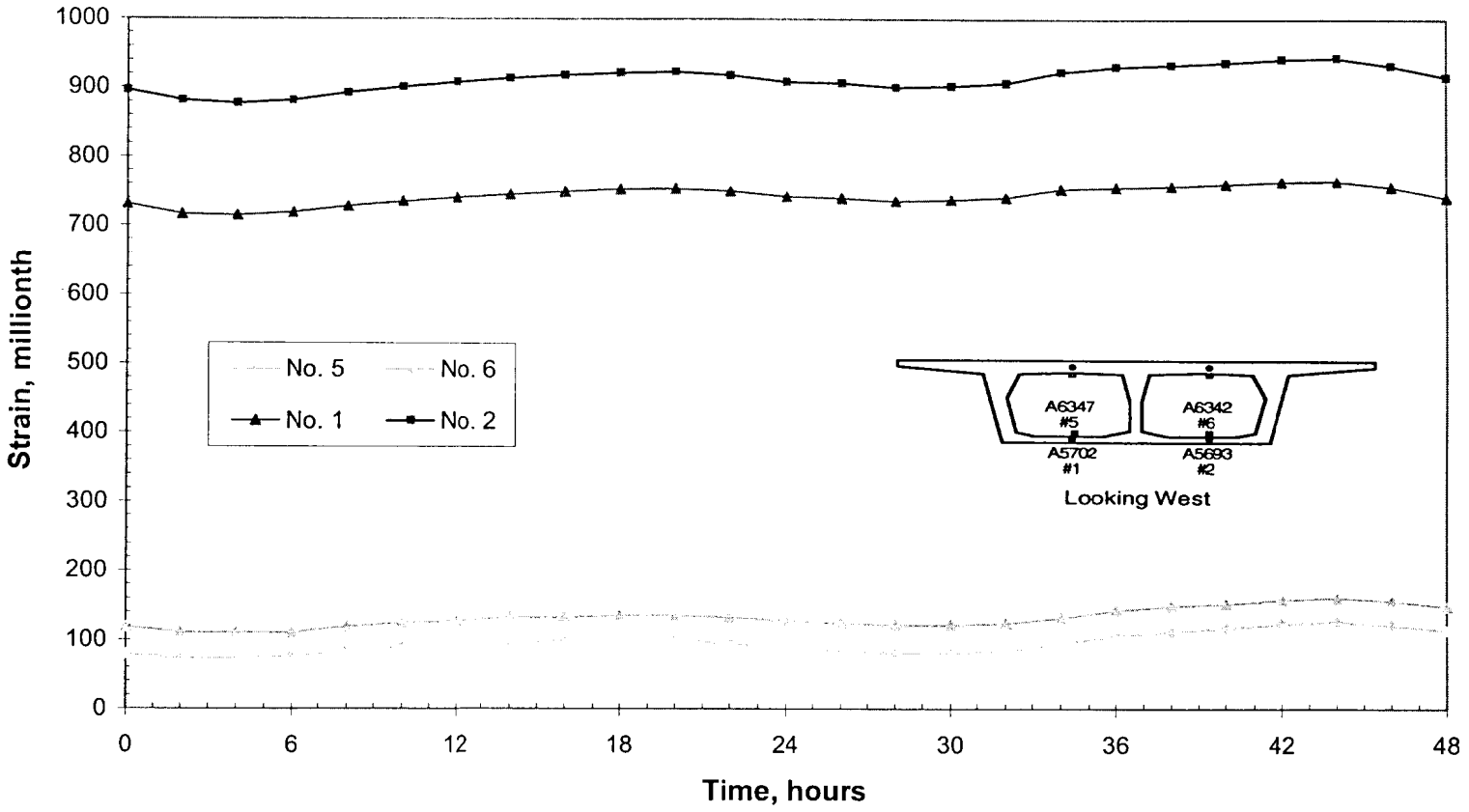


Figure 2.54 Concrete Compressive Strain in the Bottom Slab of the Main Span Closure Segment, 9/21/97, 12:00 p.m. to 9/23/97, 12:00 p.m.

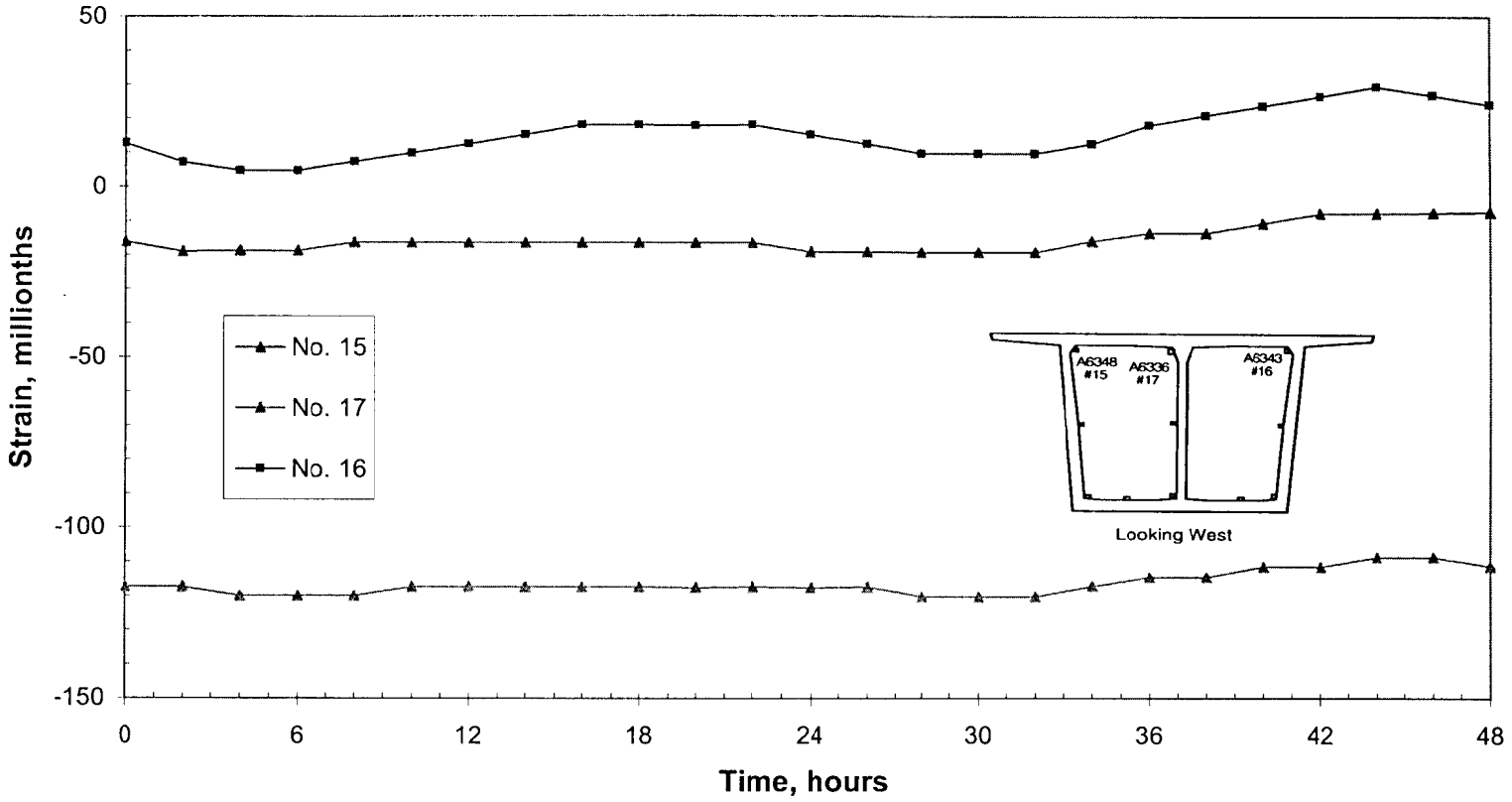


Figure 2.55 Concrete Compressive Strain in the Top Horizontal Section of Segment P14MS1, 9/21/97, 12:00 p.m. to 9/23/97, 12:00 p.m.

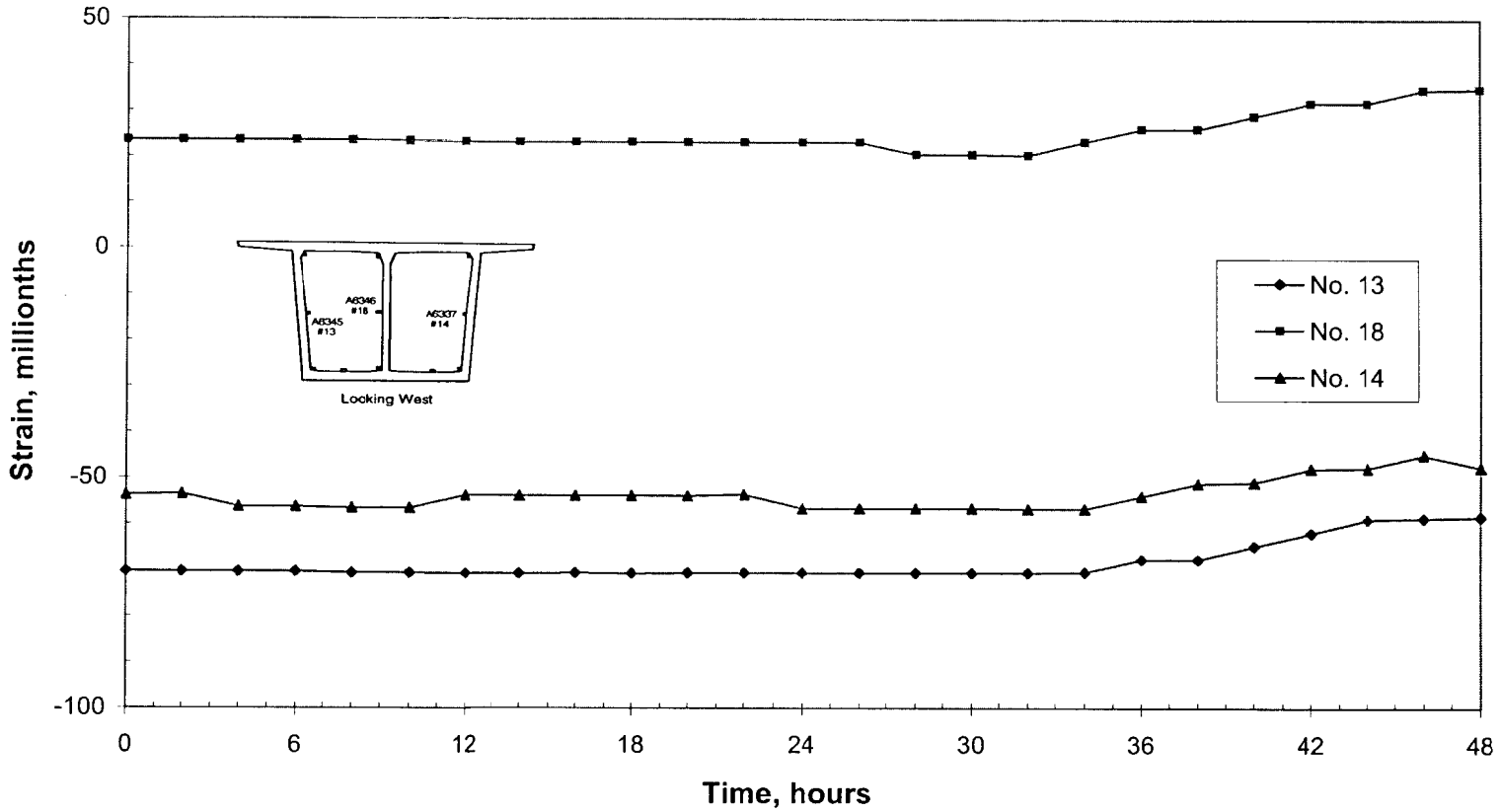


Figure 2.56 Concrete Compressive Strain in the Center Horizontal Section of Segment P14MS1, 9/21/97 12:00 p.m. to 9/23/97, 12:00 p.m.

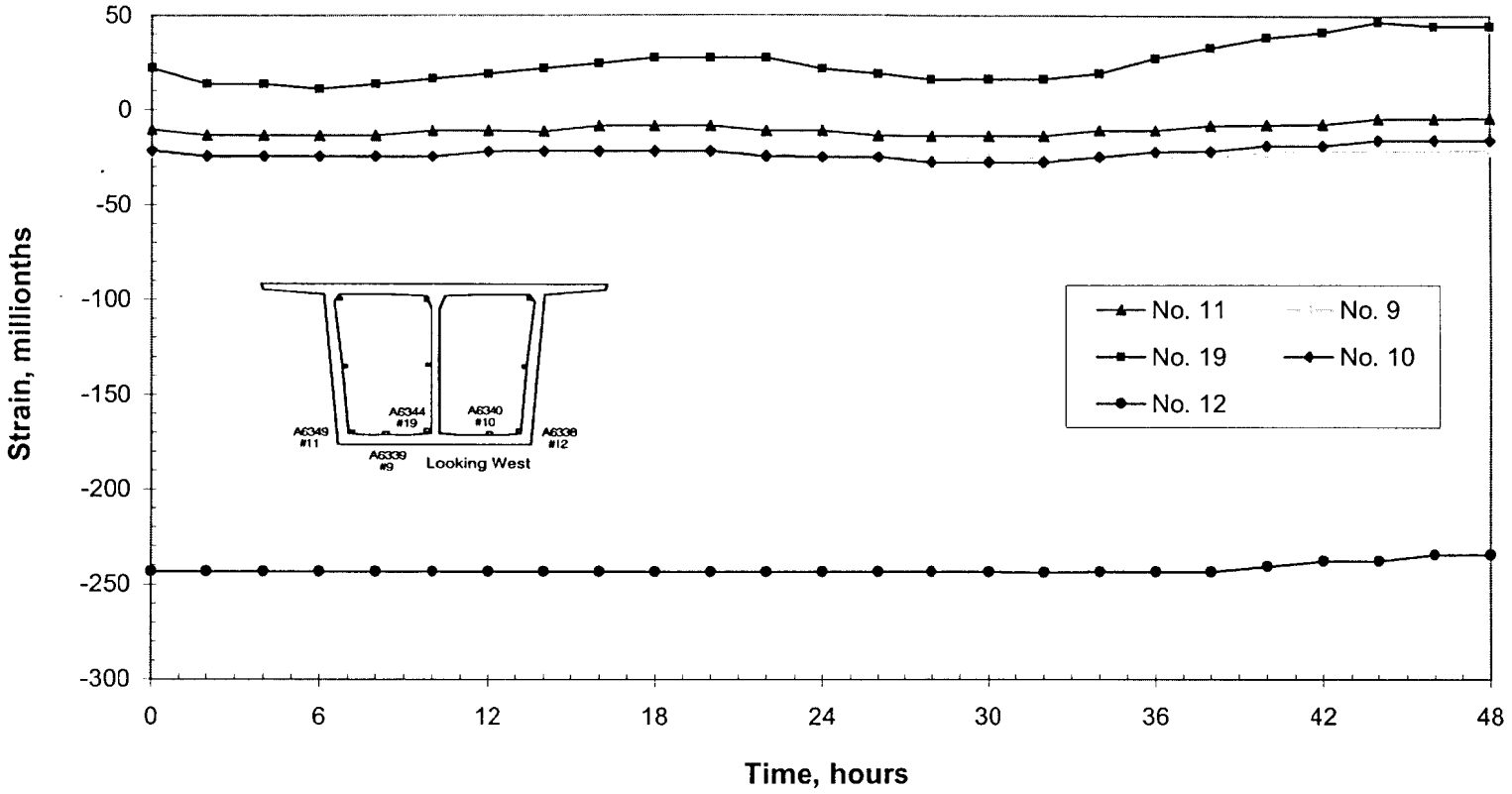


Figure 2.57 Concrete Compressive Strain in the Bottom of the Horizontal Section of Segment P14MS1, 9/21/97, 12:00 p.m. to 9/23/97, 12:00 p.m.

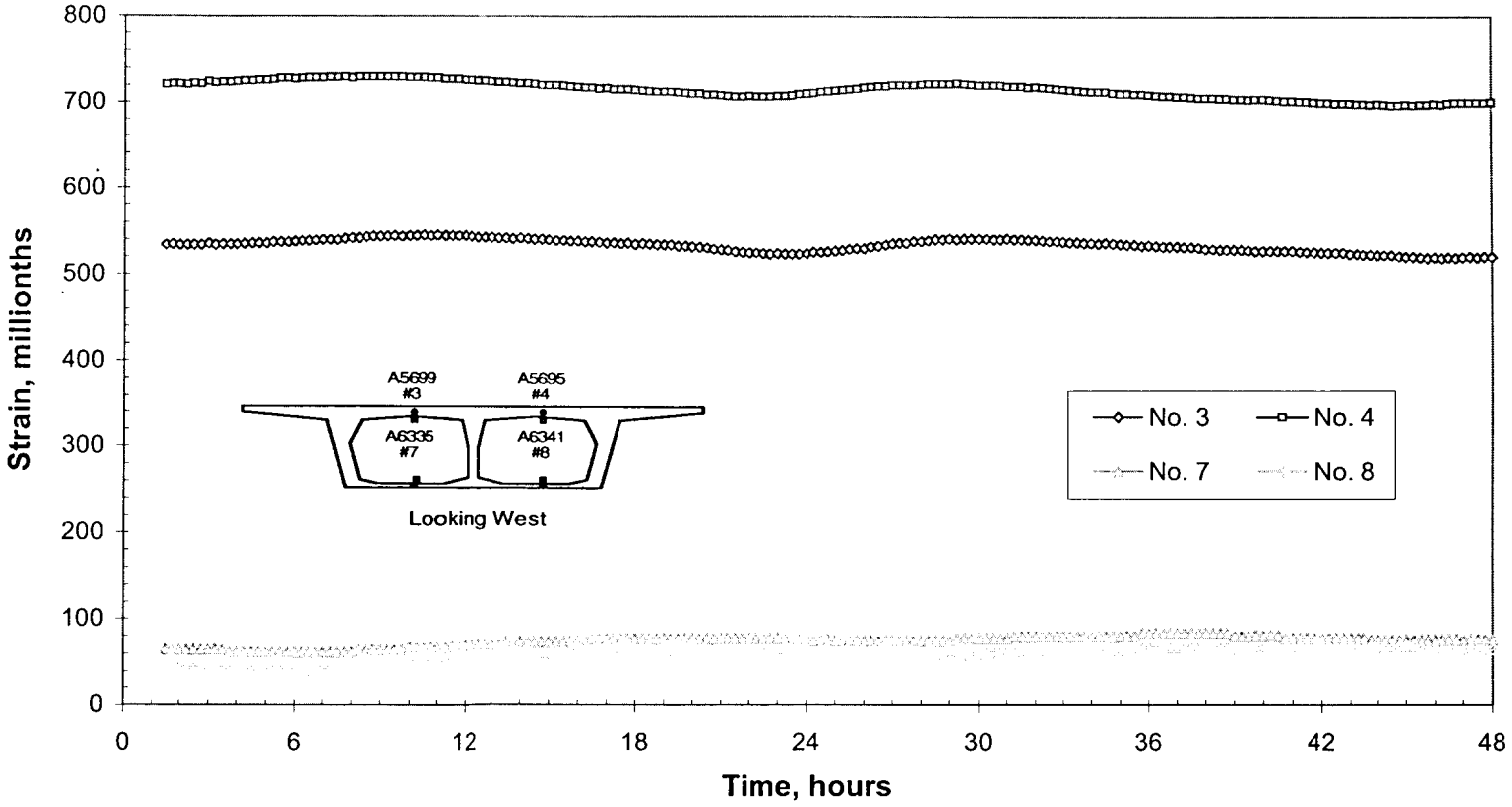


Figure 2.58 Concrete Compressive Strain in the Top Slab of the Main Span Closure Segment, 1/13/98 12:00 p.m. to 1/15/98 12:00 p.m.

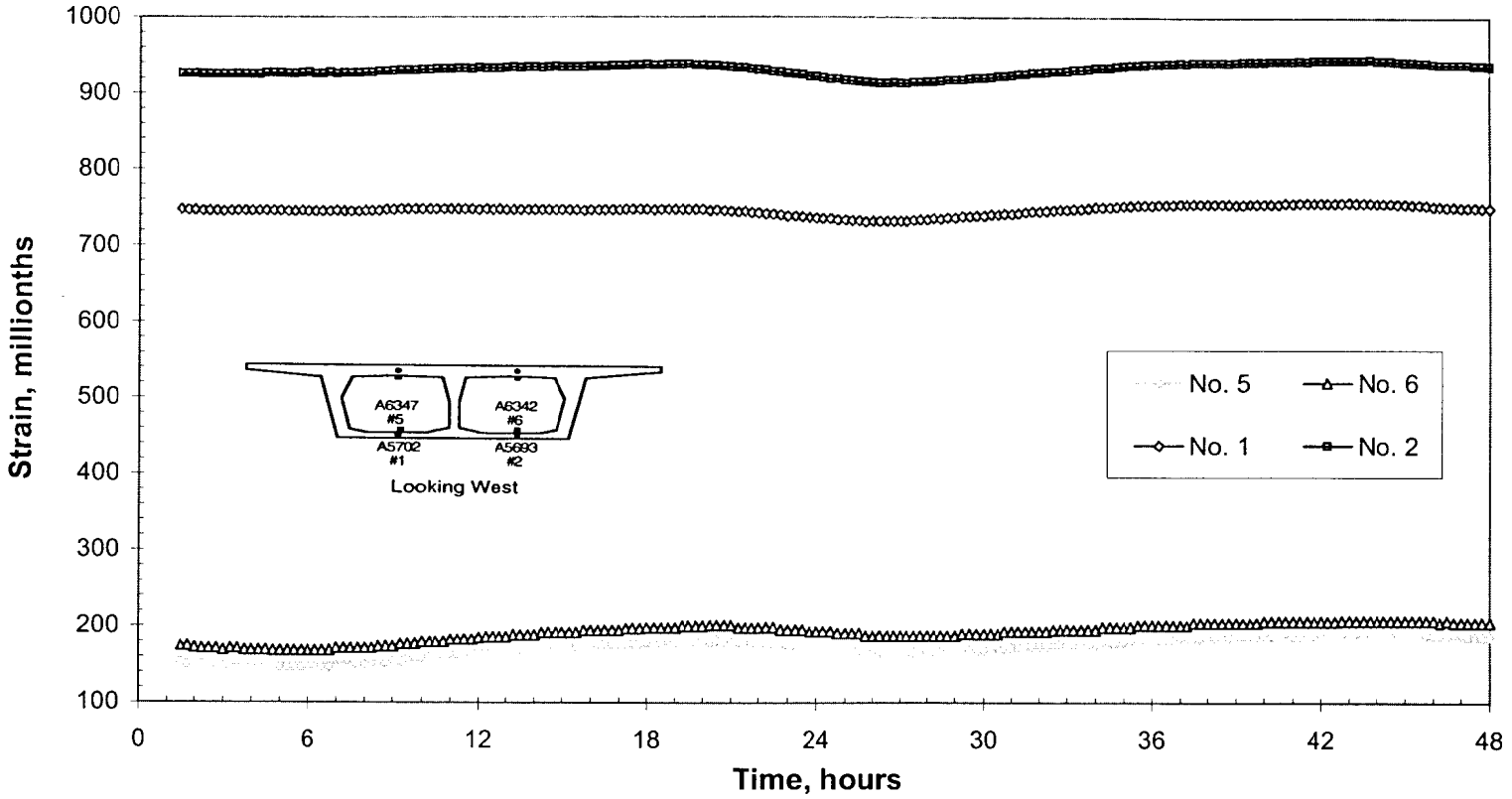


Figure 2.59 Concrete Compressive Strain in the Bottom Slab of the Main Span Closure Segment, 1/13/98, 12:00 p.m. to 1/15/98, 12:00 p.m.

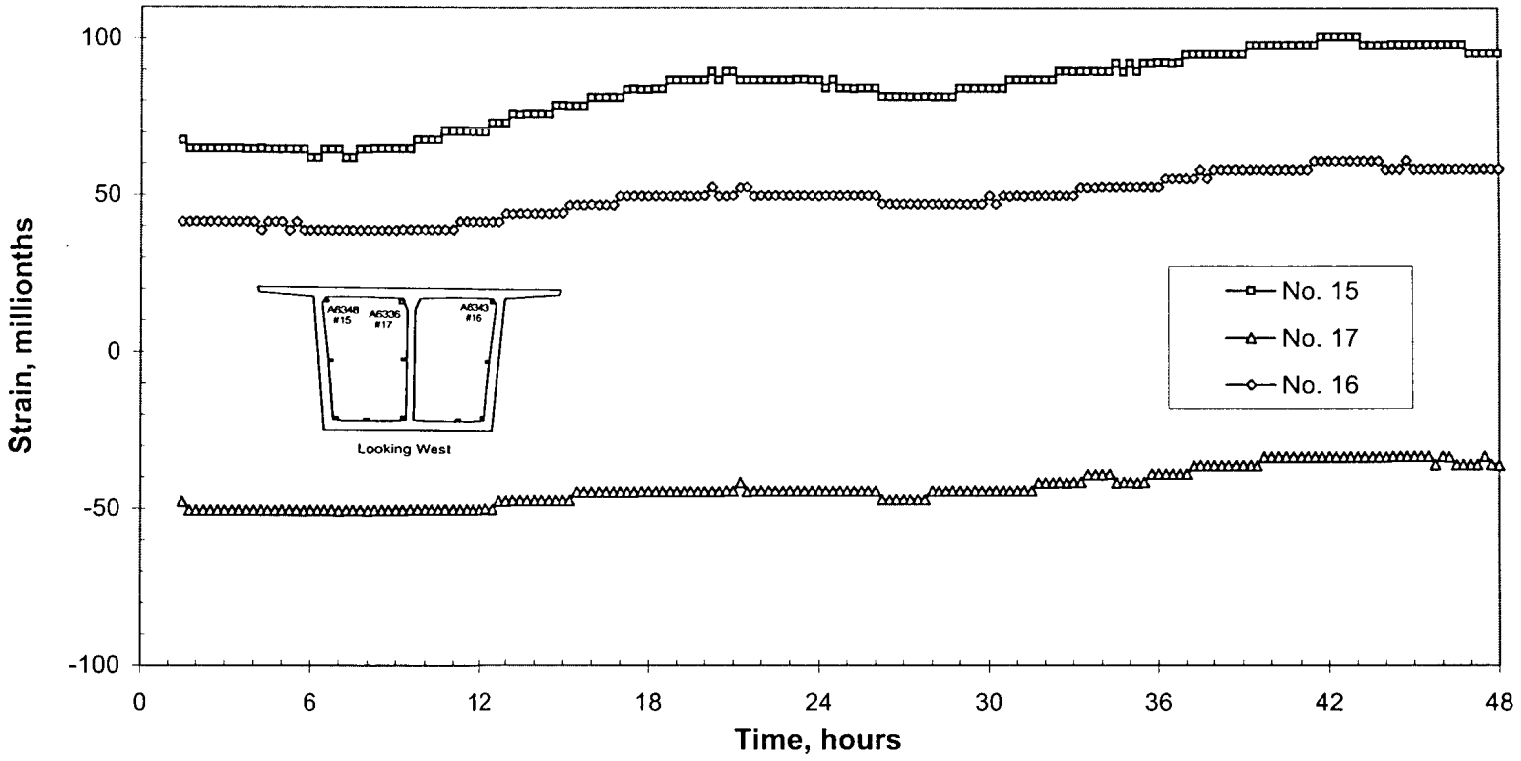


Figure 2.60 Concrete Compressive Strain in the Top Horizontal Section of Segment P14MS1, 1/13/98, 12:00 p.m. to 1/15/98, 12:00 p.m.

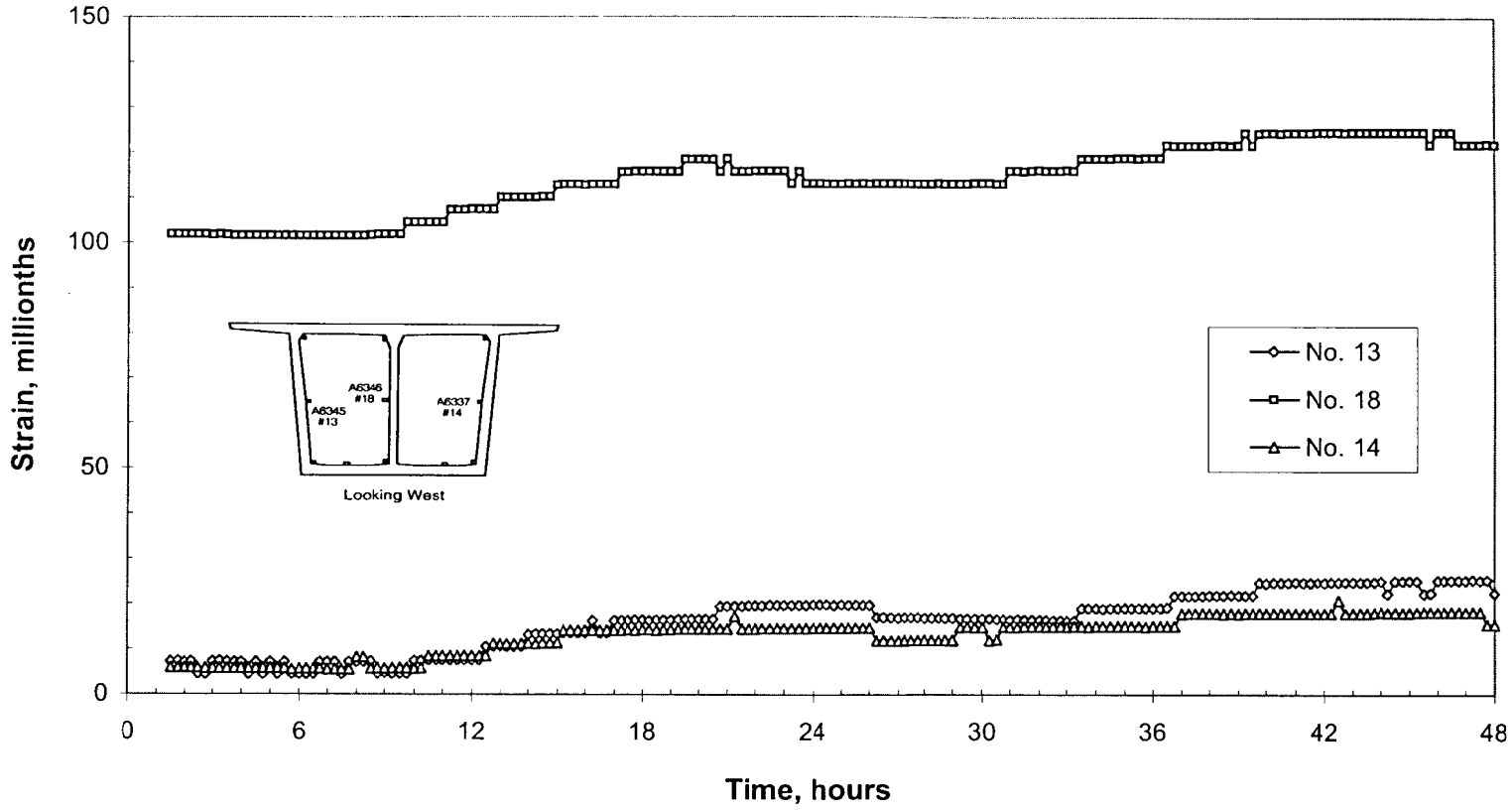


Figure 2.61 Concrete Compressive Strain in the Center Horizontal Section of Segment P14MS1, 1/13/98, 12:00 p.m. to 1/15/98, 12:00 p.m.

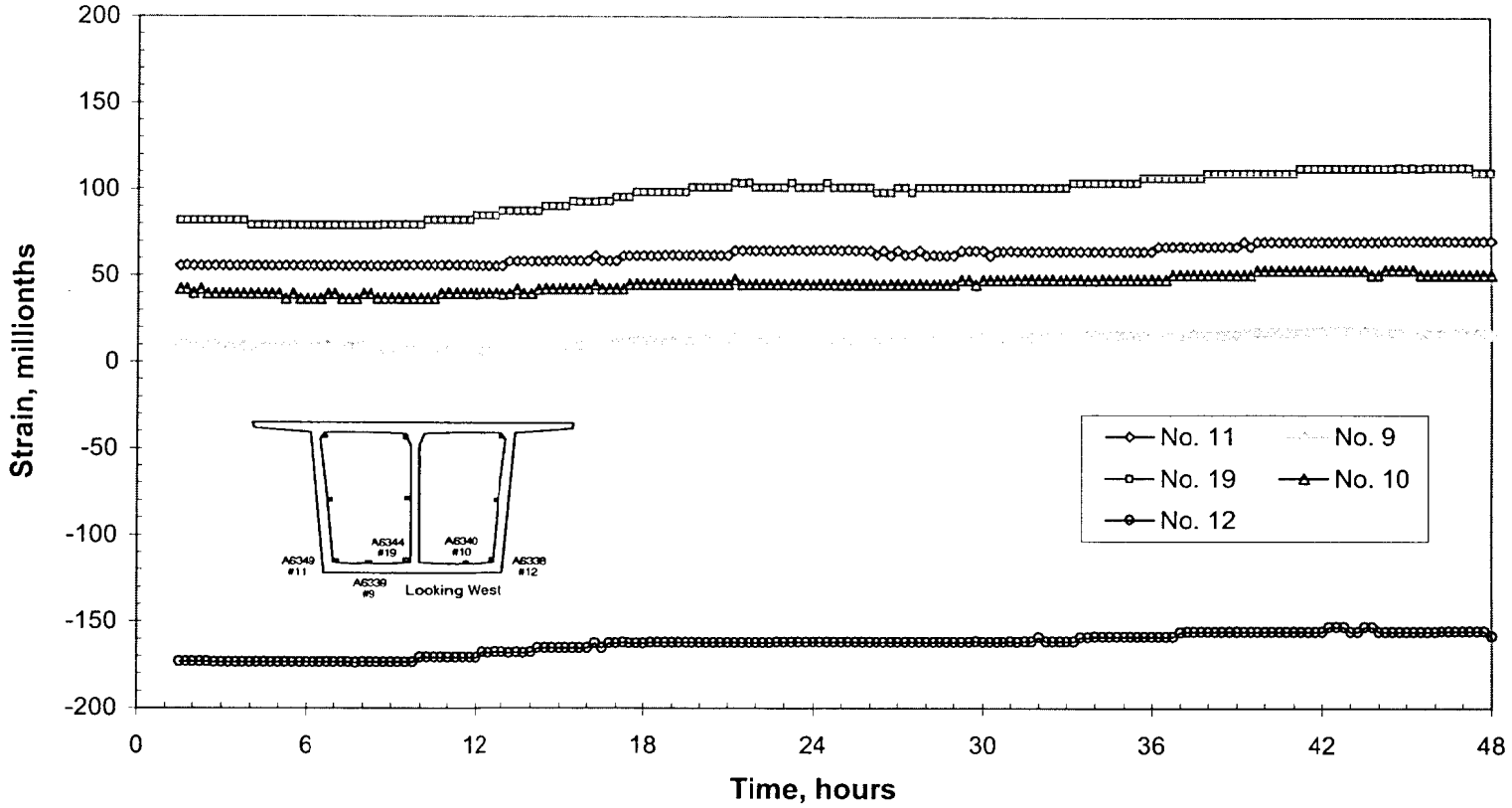


Figure 2.62 Concrete Compressive Strain in the Bottom Horizontal Section of Segment P14MS1, 1/13/98, 12:00 p.m. to 1/15/98, 12:00 p.m.

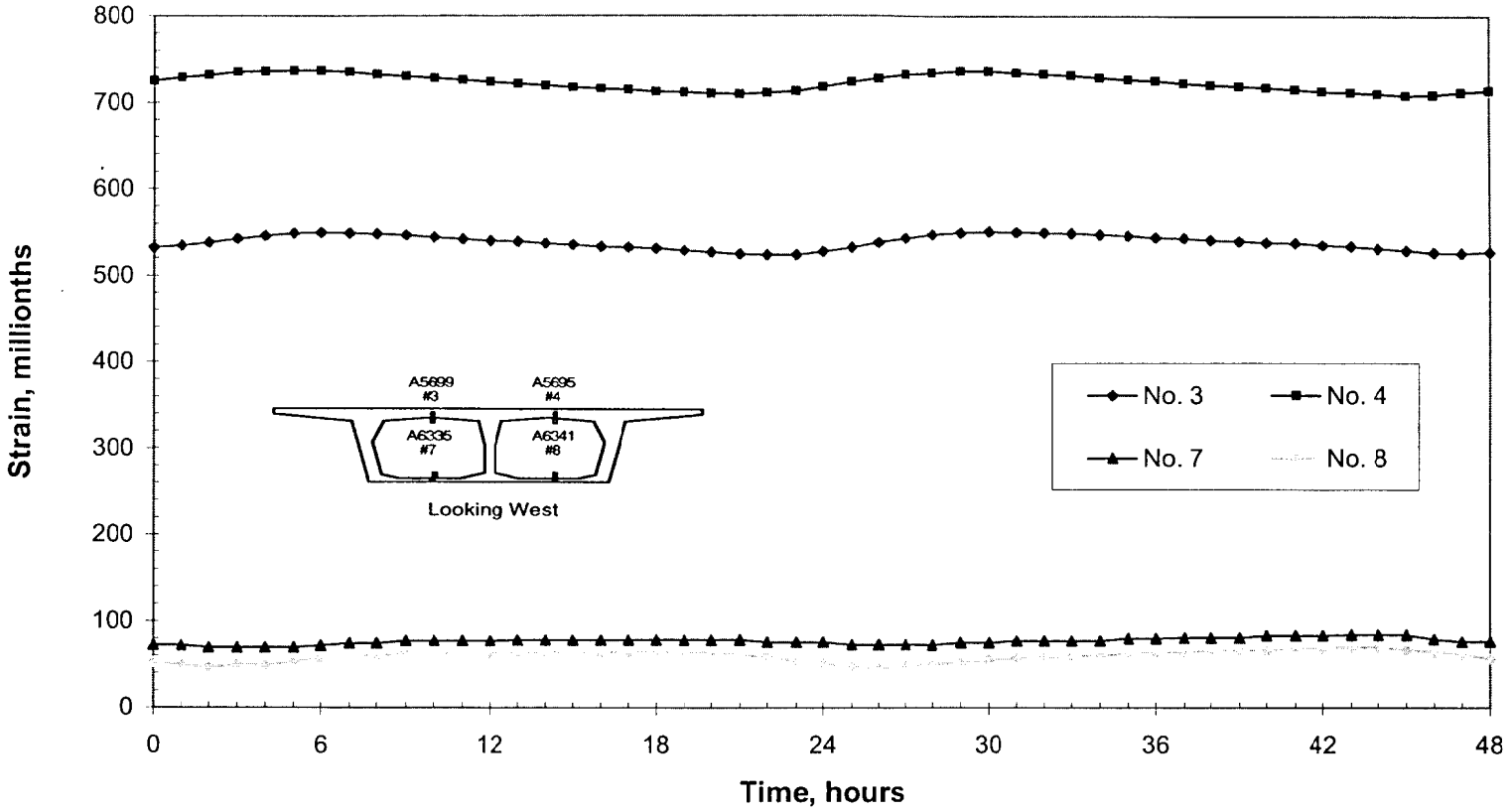


Figure 2.63 Concrete Compressive Strain in the Top Slab of the Main Span Closure Segment, 1/25/98, 12:00 p.m. to 1/27/98, 12:00 p.m.

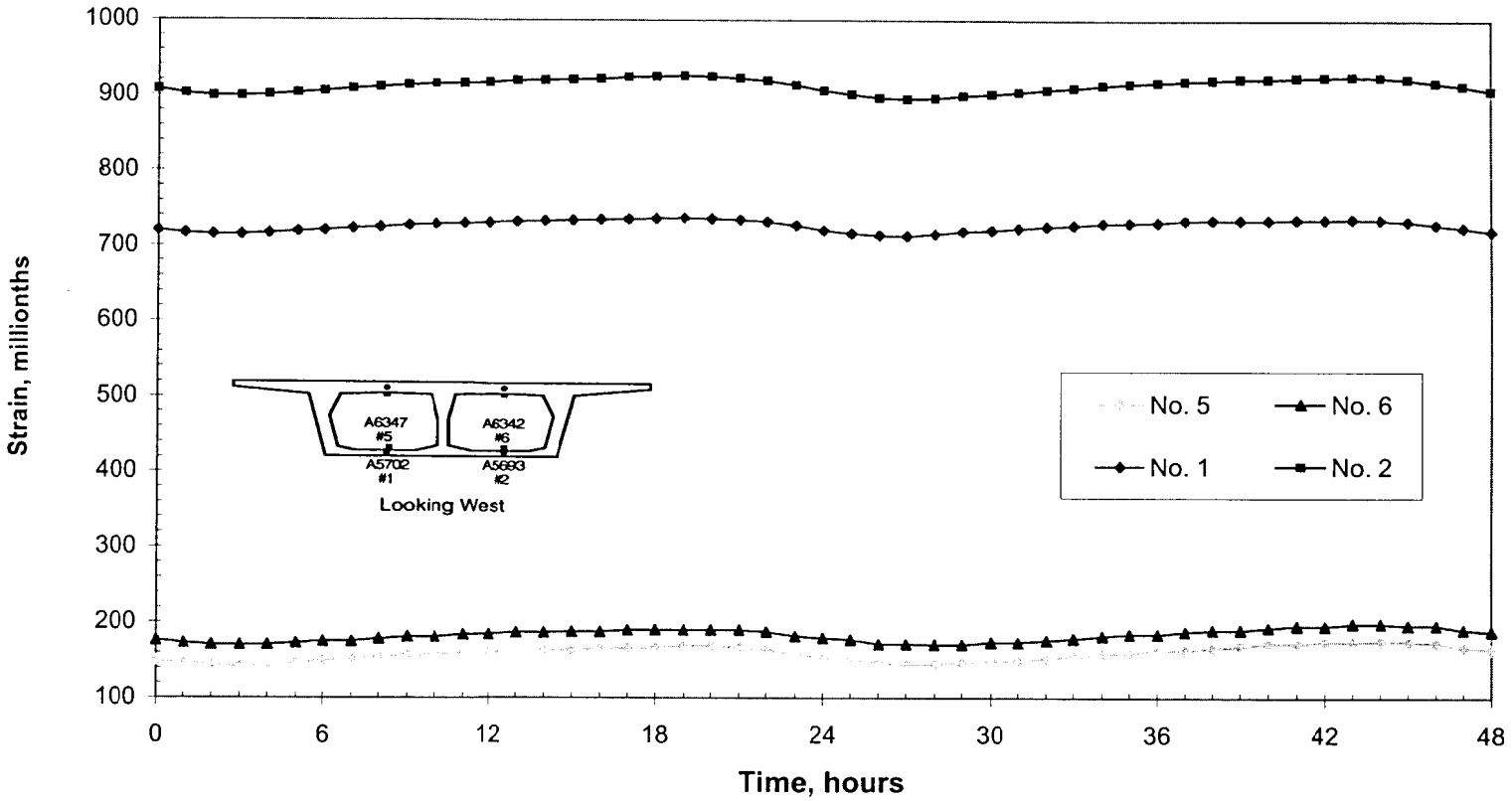


Figure 2.64 Concrete Compressive Strain in the Bottom Slab of the Main Span Closure Segment, 1/25/98, 12:00 p.m. to 1/27/98, 12:00 p.m.

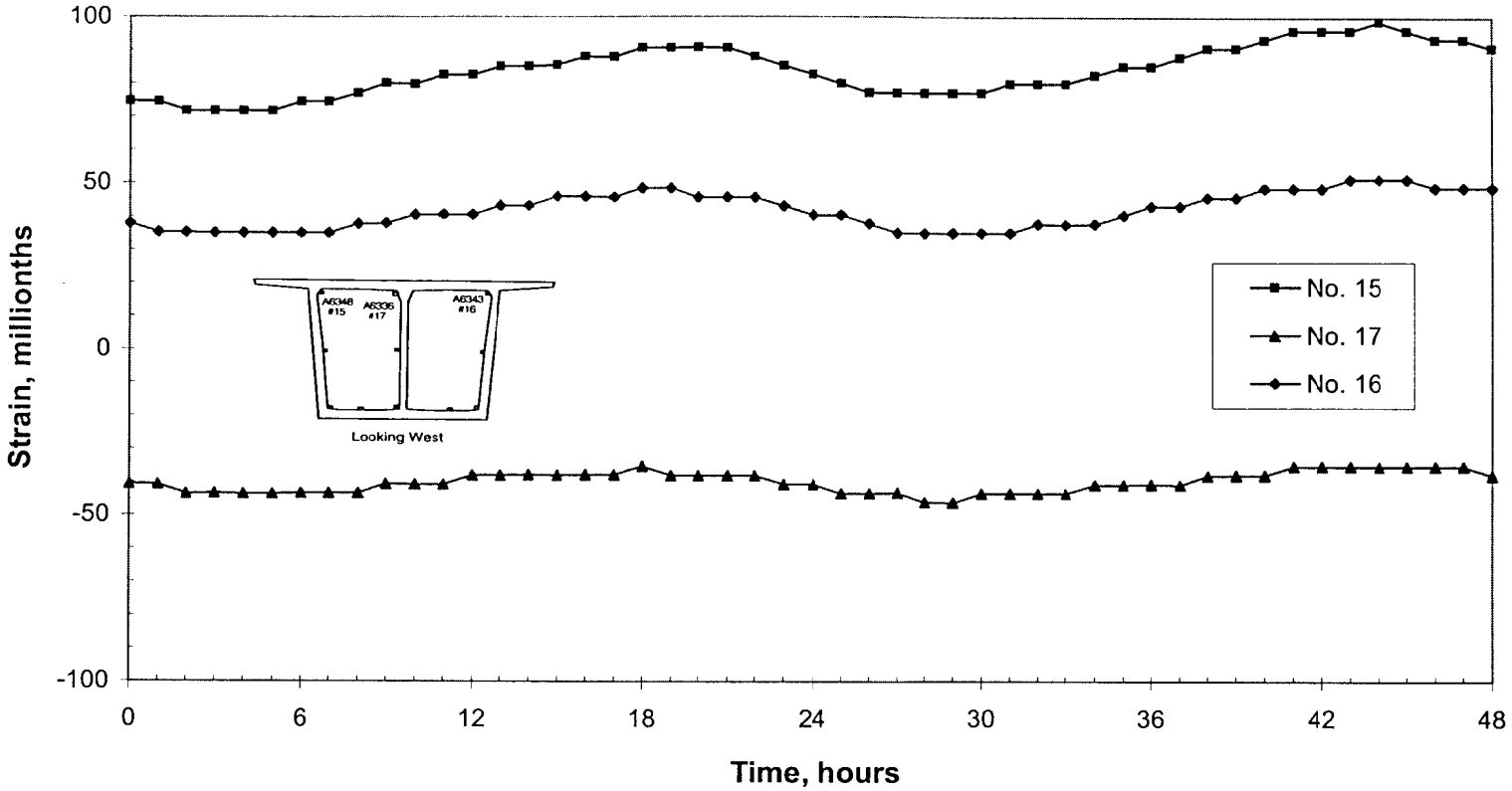


Figure 2.65 Concrete Compressive Strain in the Top Horizontal Section of Segment P14MS1, 1/25/98, 12:00 p.m. to 1/27/98, 12:00 p.m.

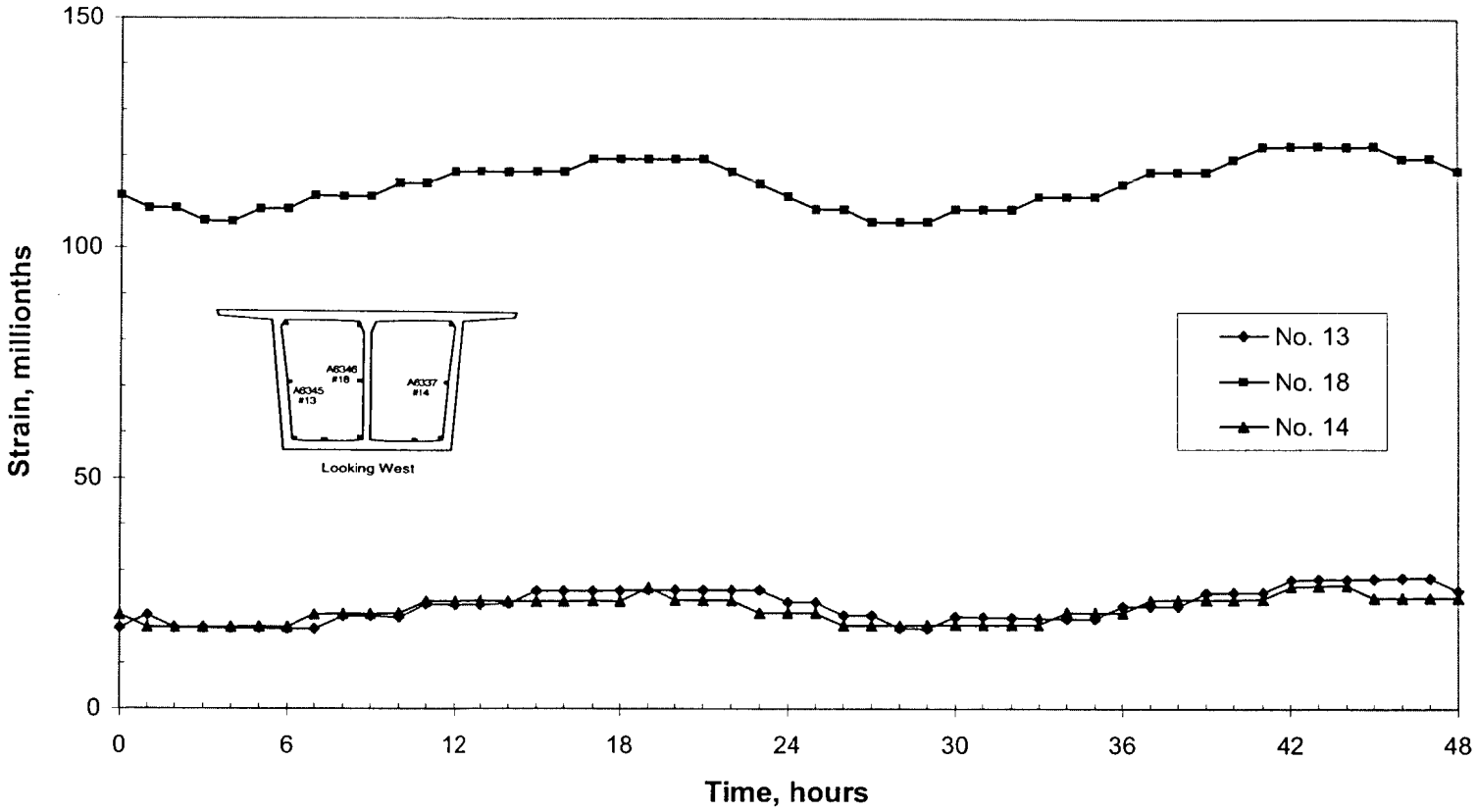


Figure 2.66 Concrete Compressive Strain in the Center Horizontal Section of Segment P14MS1, 1/25/98, 12:00 p.m. to 1/27/98, 12:00 p.m.

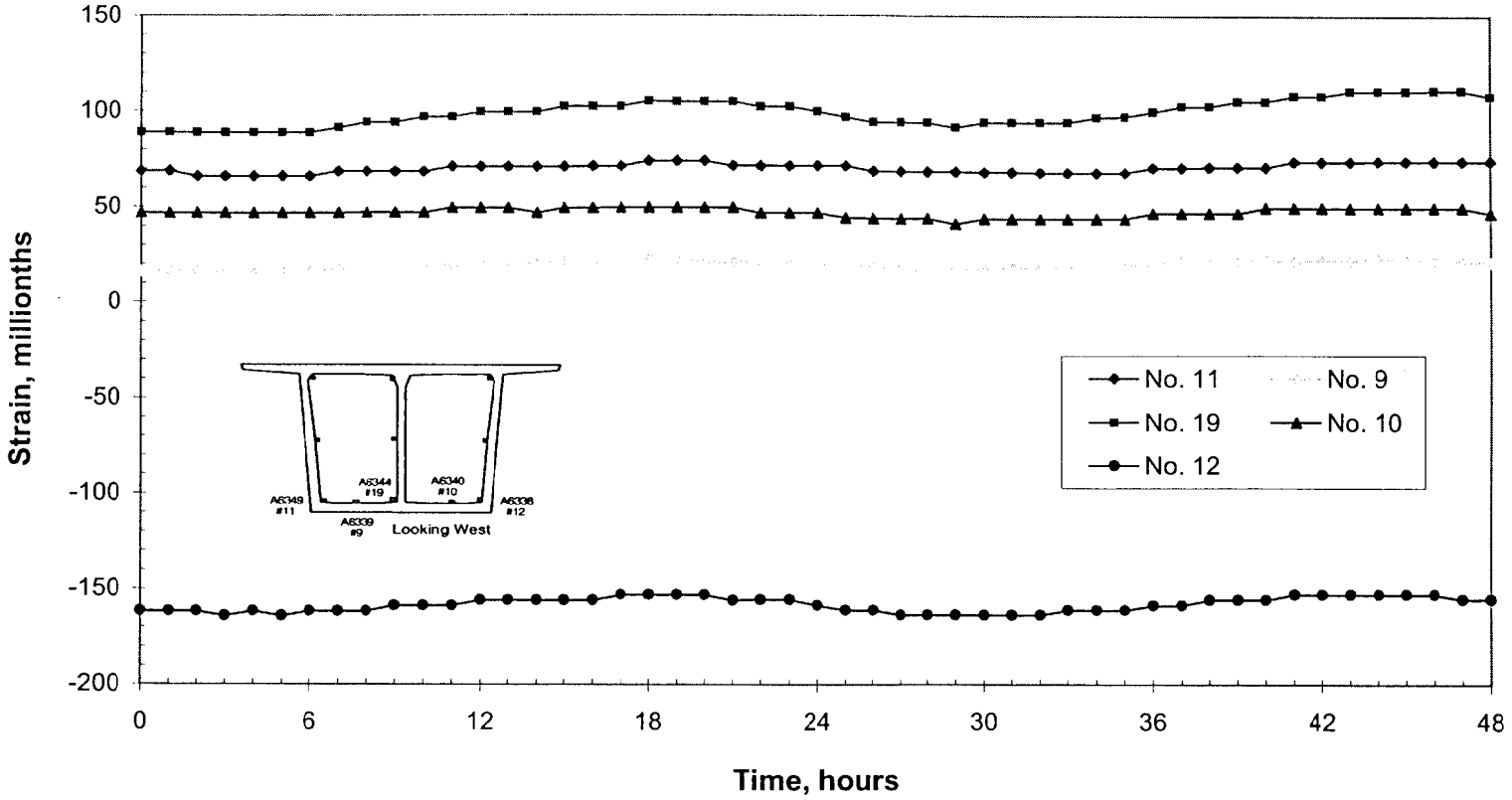


Figure 2.67 Concrete Compressive Strain in the Bottom Horizontal Section of Segment P14MS1, 1/25/98, 12:00 p.m. to 1/27/98, 12:00 p.m.

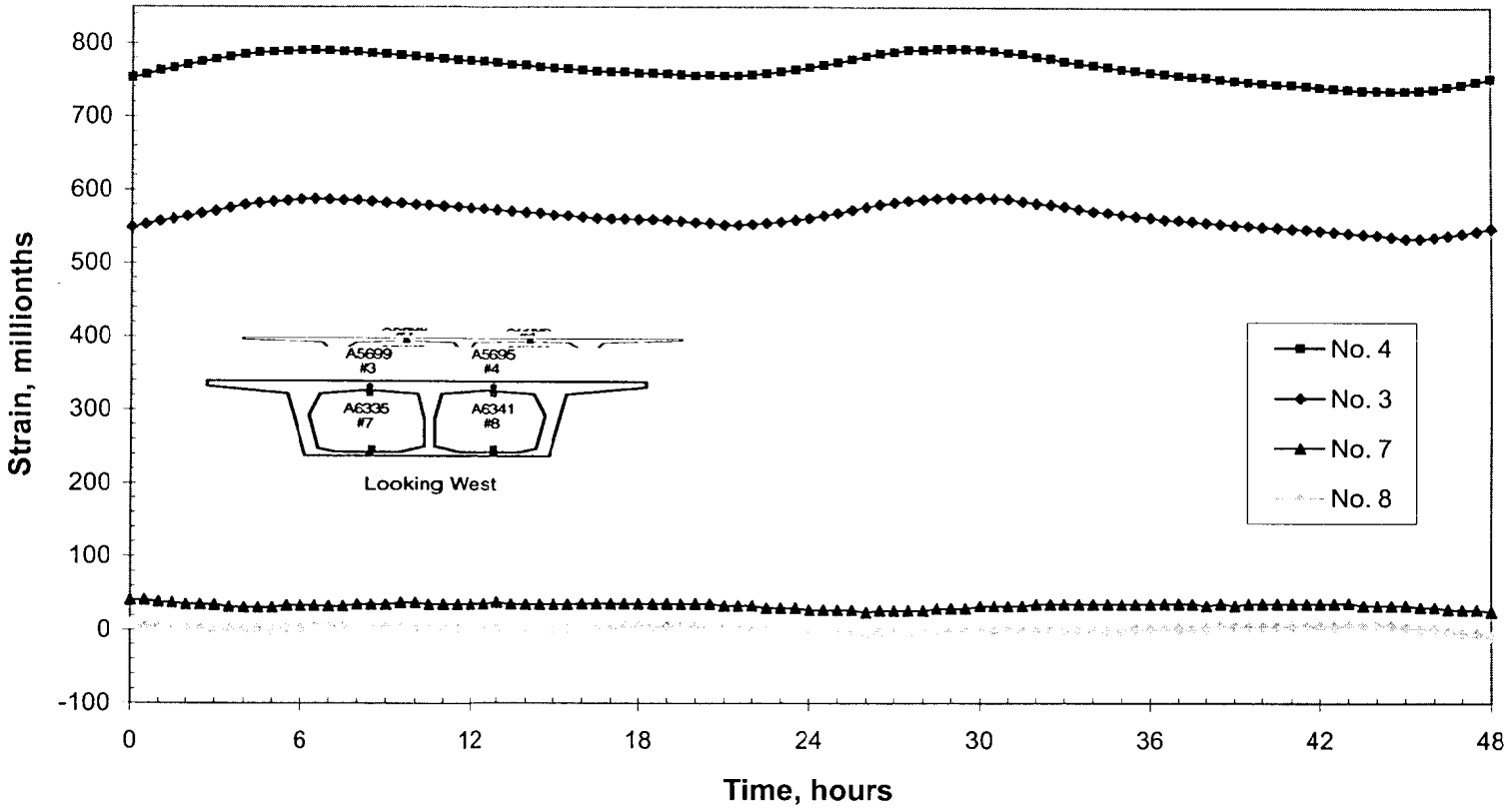


Figure 2.68 Concrete Compressive Strain in the Top Slab of the Main Span Closure Segment, 4/27/98, 12:00 p.m. to 4/29/98, 12:00 p.m.

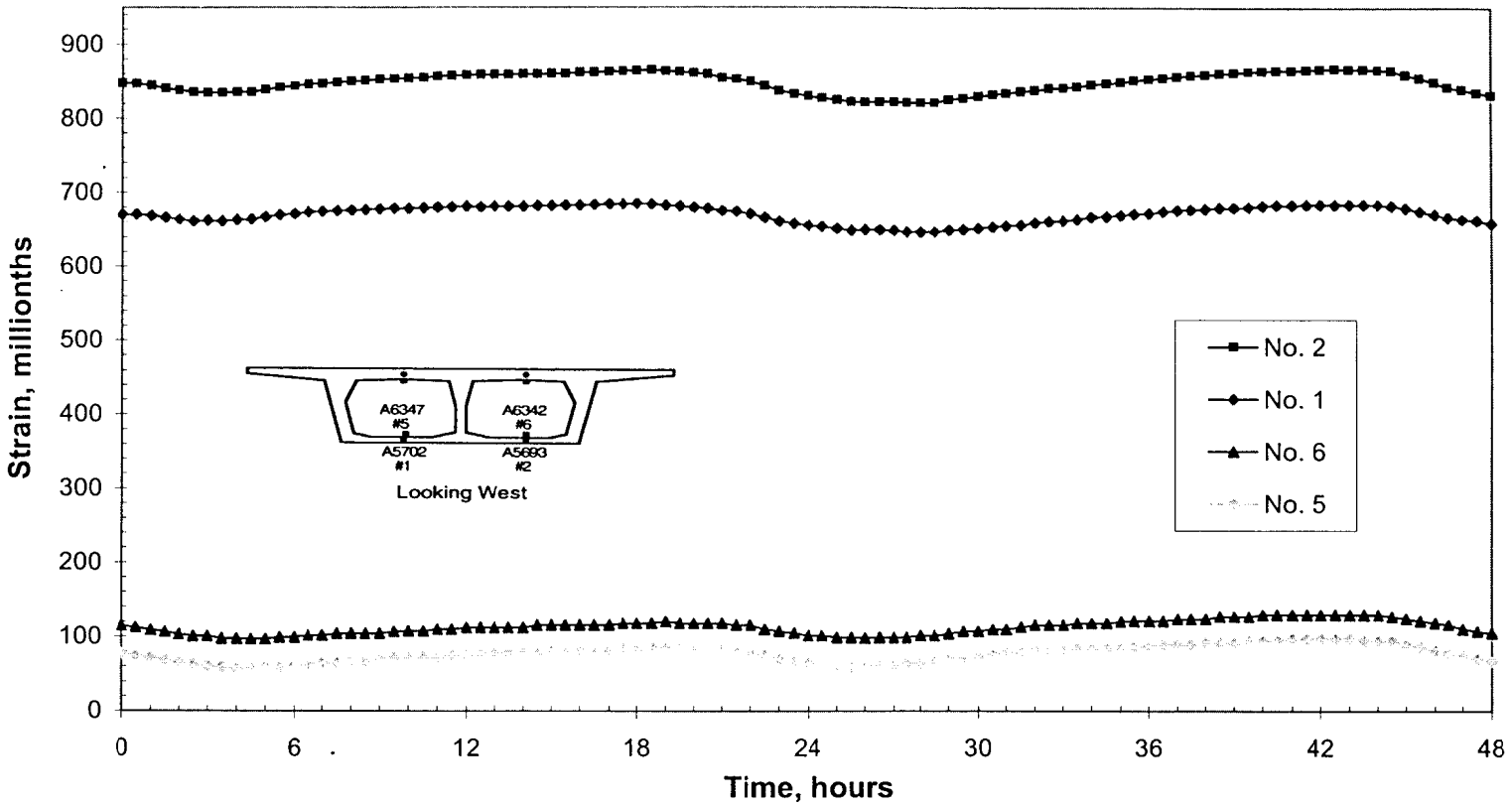


Figure 2.69 Concrete Compressive Strain in the Bottom Slab of the Main Closure Segment, 4/27/98, 12:00 p.m. to 4/29/98, 12:00 p.m.

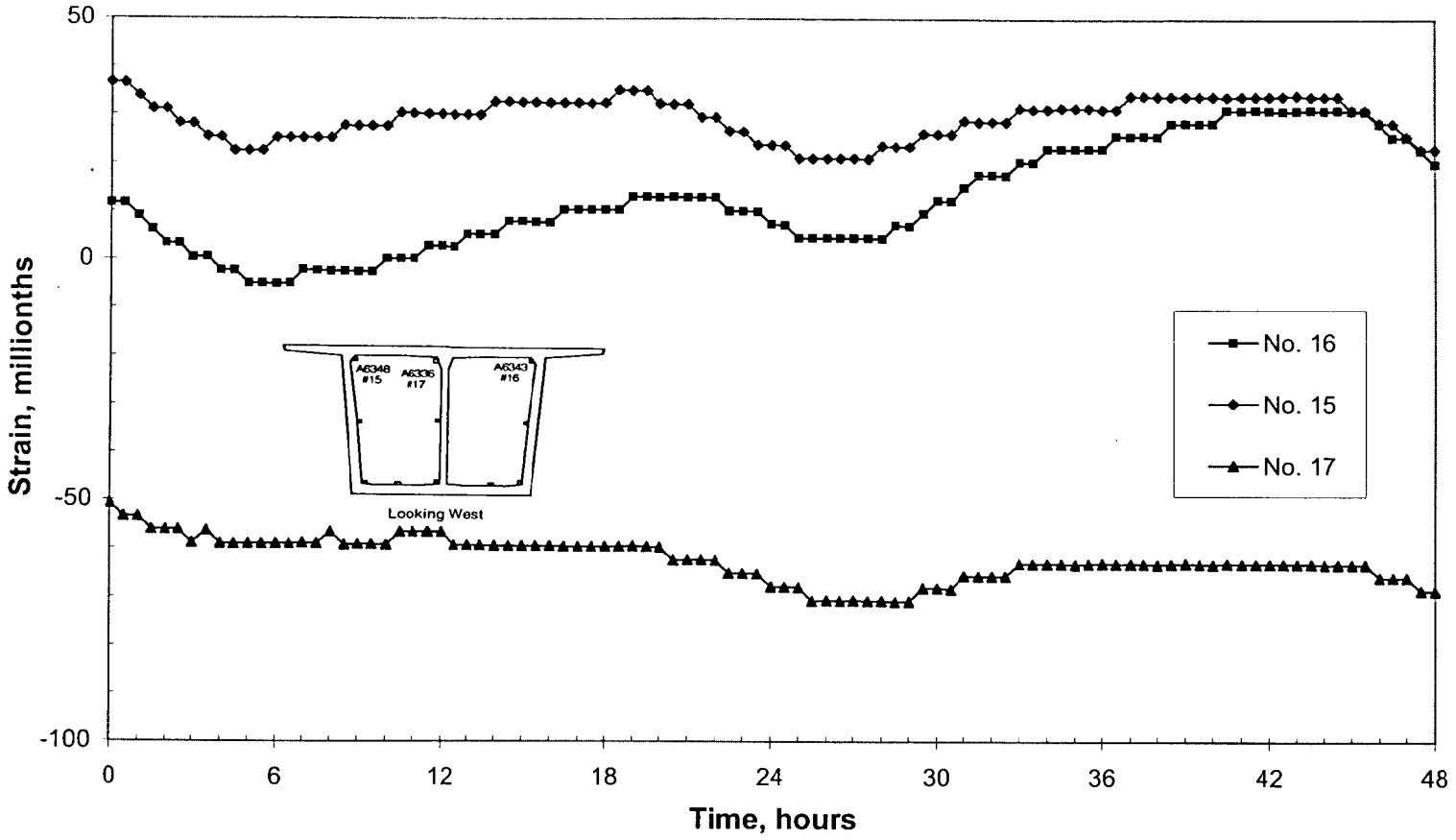


Figure 2.70 Concrete Compressive Strain in the Top Horizontal Section of Segment P14MS1, 4/27/98, 12:00 p.m. to 4/29/98, 12:00 p.m.

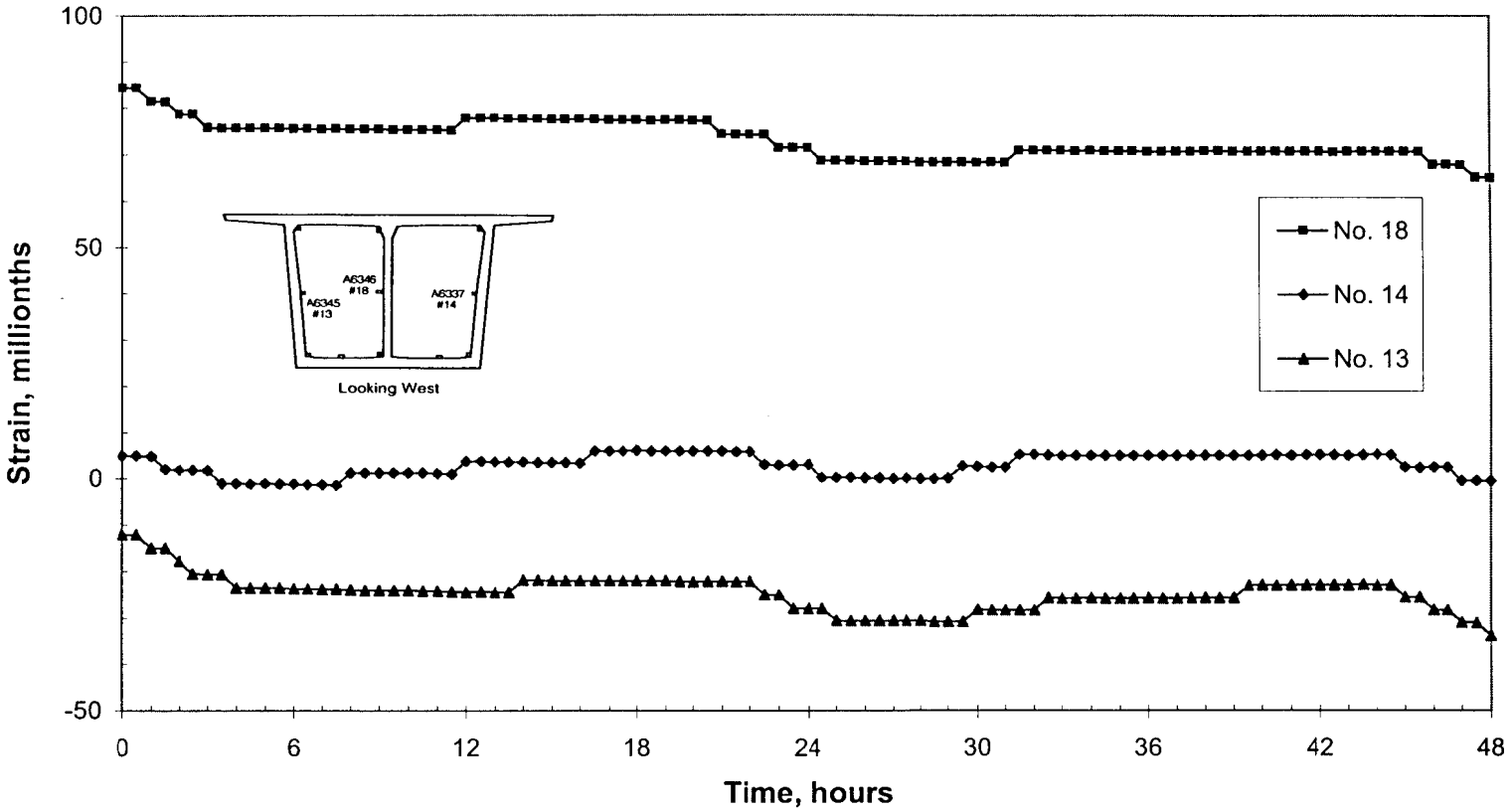


Figure 2.71 Concrete Compressive Strain in the Center Horizontal Section of Segment P14MS1, 4/27/98, 12:00 p.m. to 4/29/98, 12:00 p.m.

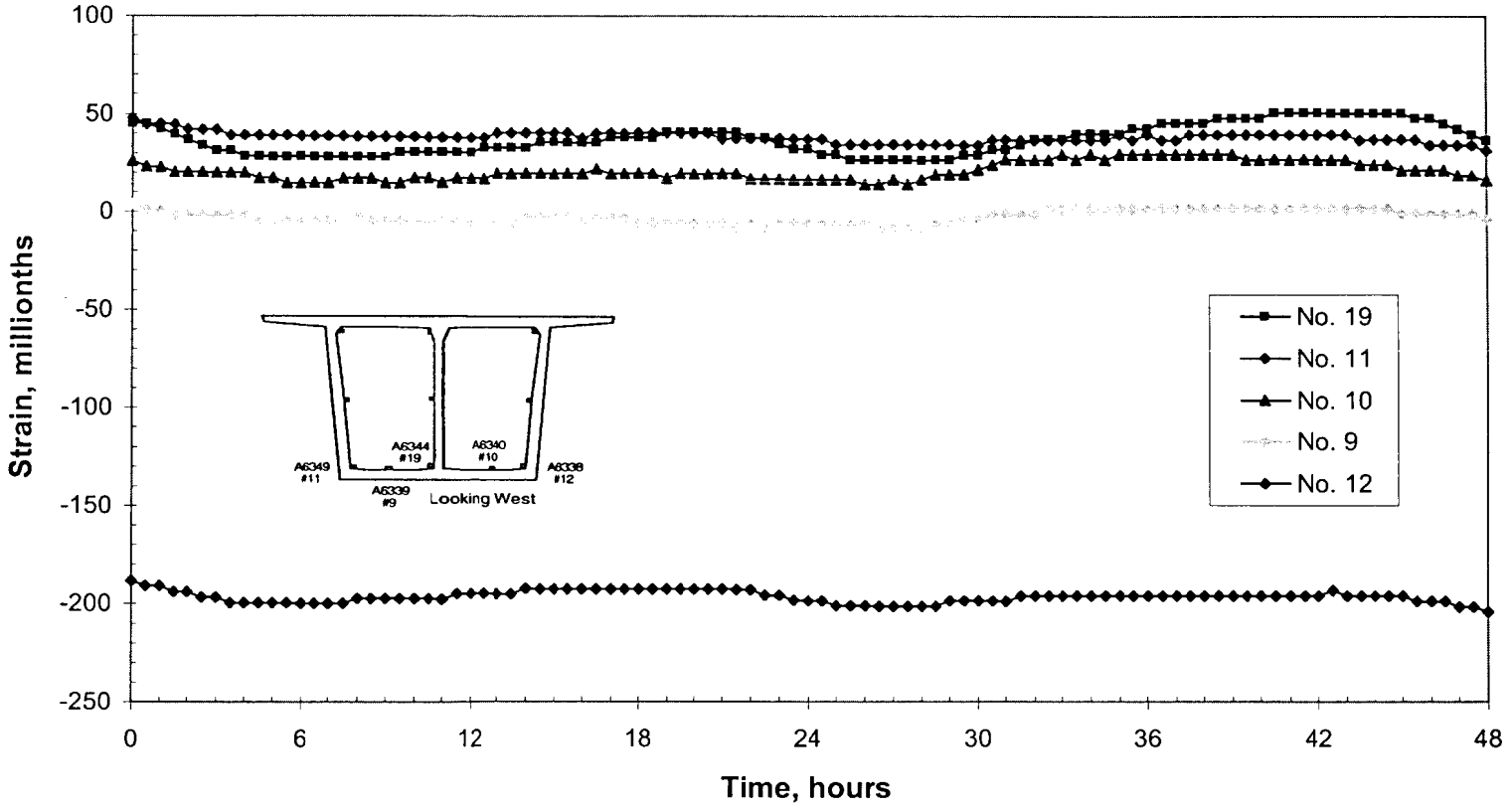


Figure 2.72 Concrete Compressive Strain in the Bottom Horizontal Section of Segment P14MS1, 4/27/98, 12:00 p.m. to 4/29/98, 12:00 p.m.

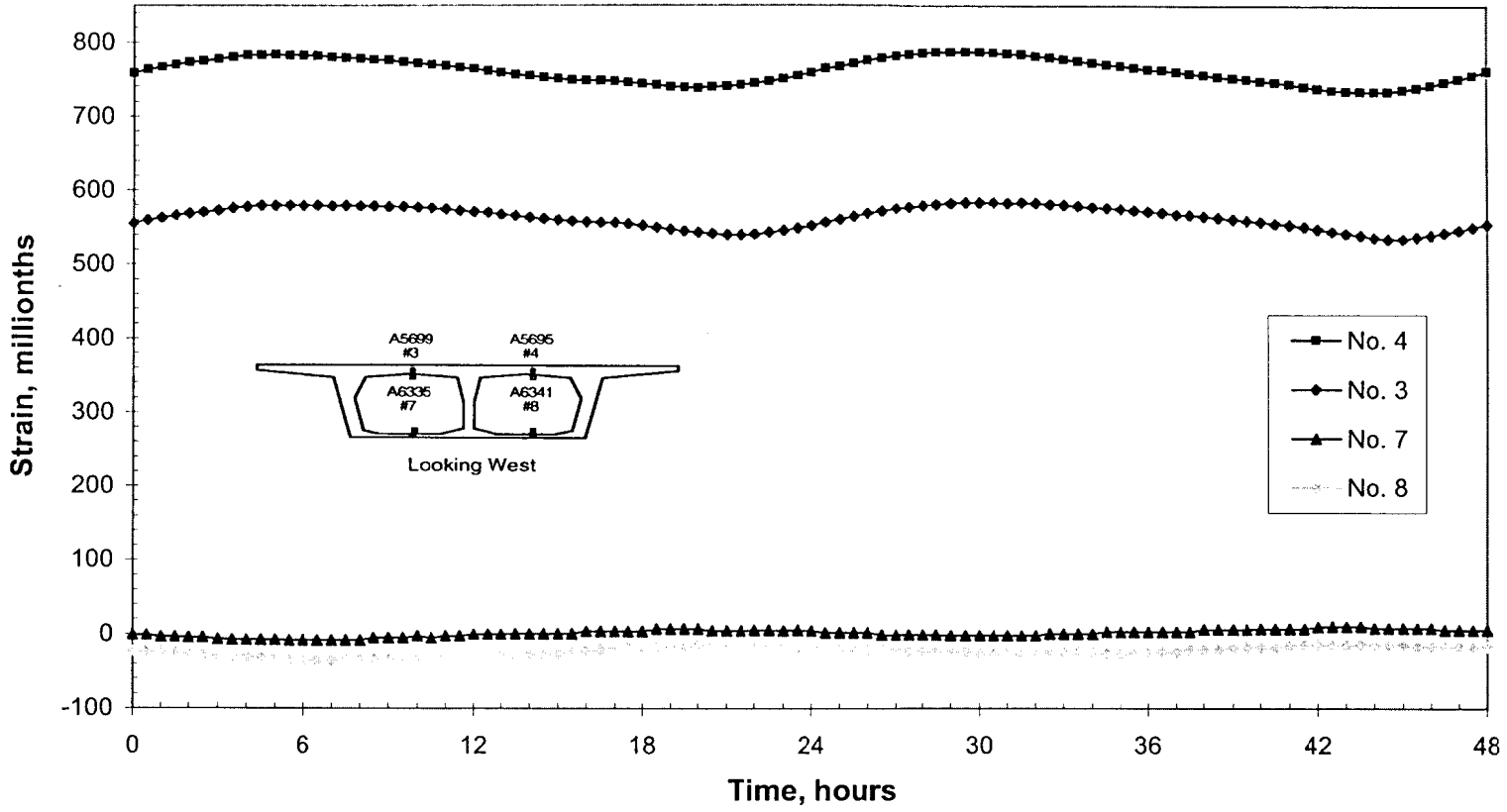


Figure 2.73 Concrete Compressive Strain in the Top Slab of the Main Closure Segment, 5/21/98, 12:00 p.m. to 5/23/98, 12:00 p.m.

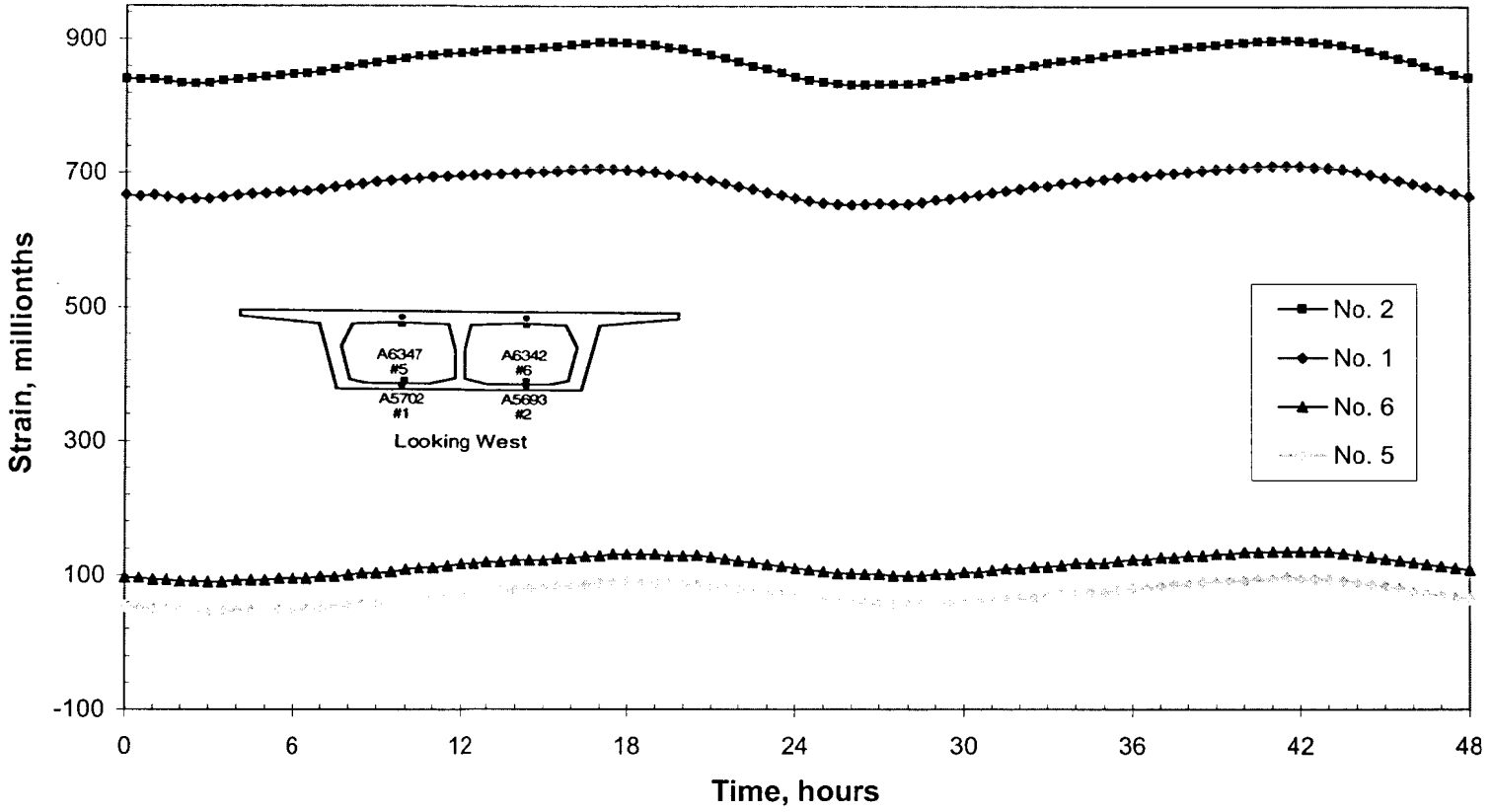


Figure 2.74 Concrete Compressive Strain in the Bottom Slab of the Main Closure Segment, 5/21/98, 12:00 p.m. to 5/39/98, 12:00 p.m.

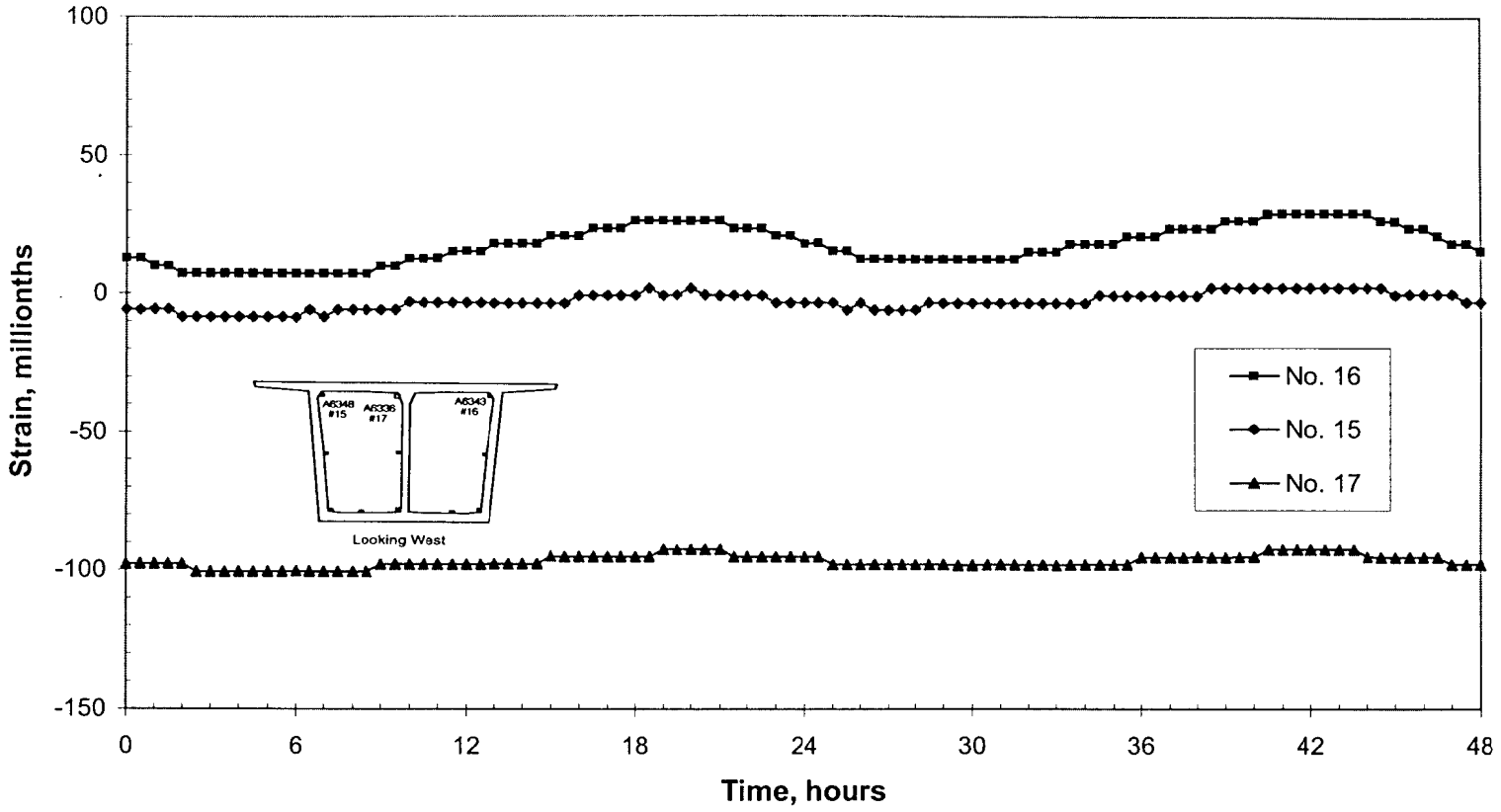


Figure 2.75 Concrete Compressive Strain in the Top Horizontal Section of Segment P14MS1, 5/21/98, 12:00 p.m. to 5/23/98, 12:00 p.m.

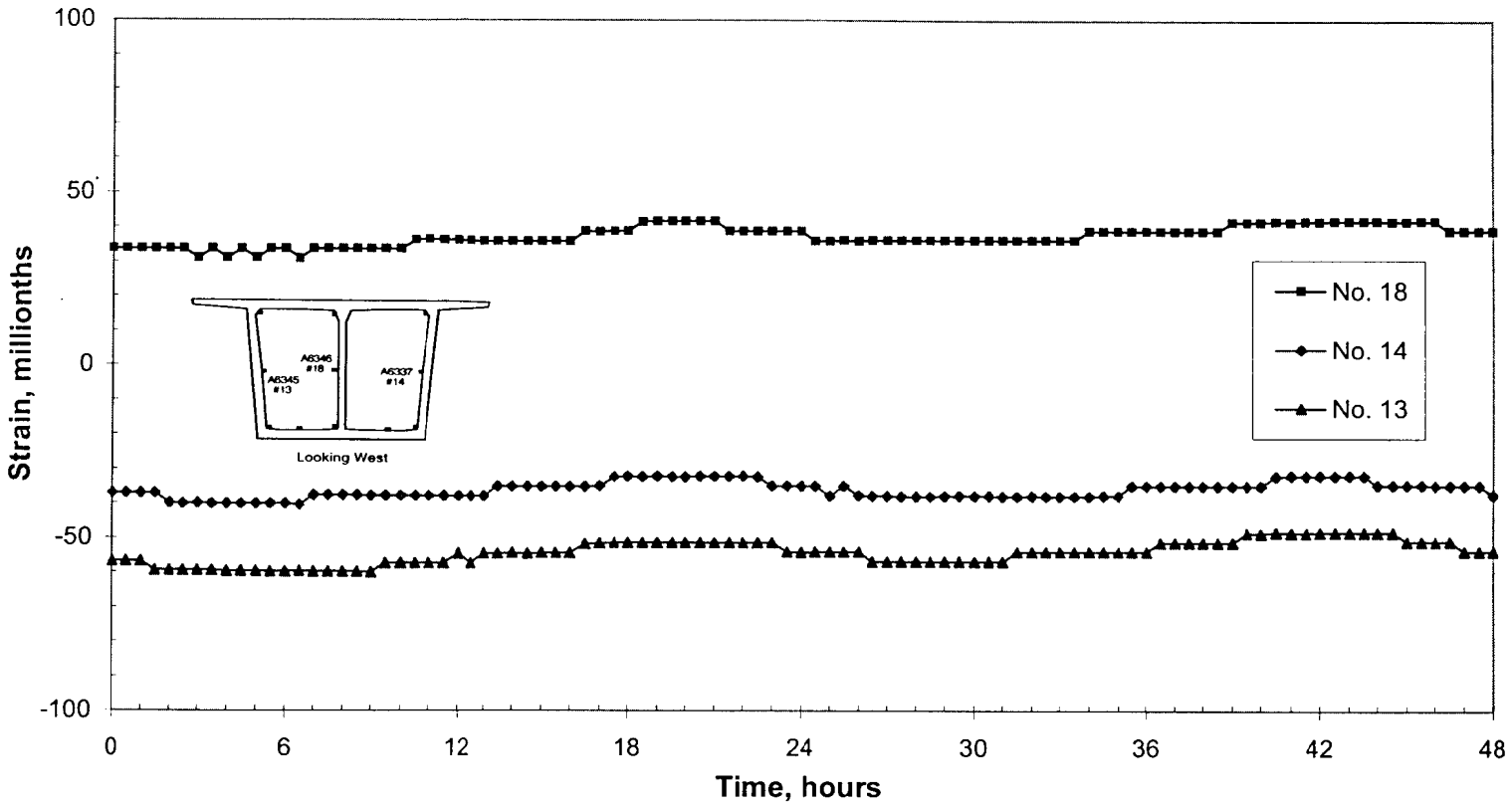


Figure 2.76 Concrete Compressive Strain in the Center Horizontal Section of Segment P14MS1, 5/21/98, 12:00 p.m. to 5/23/98, 12:00 p.m.

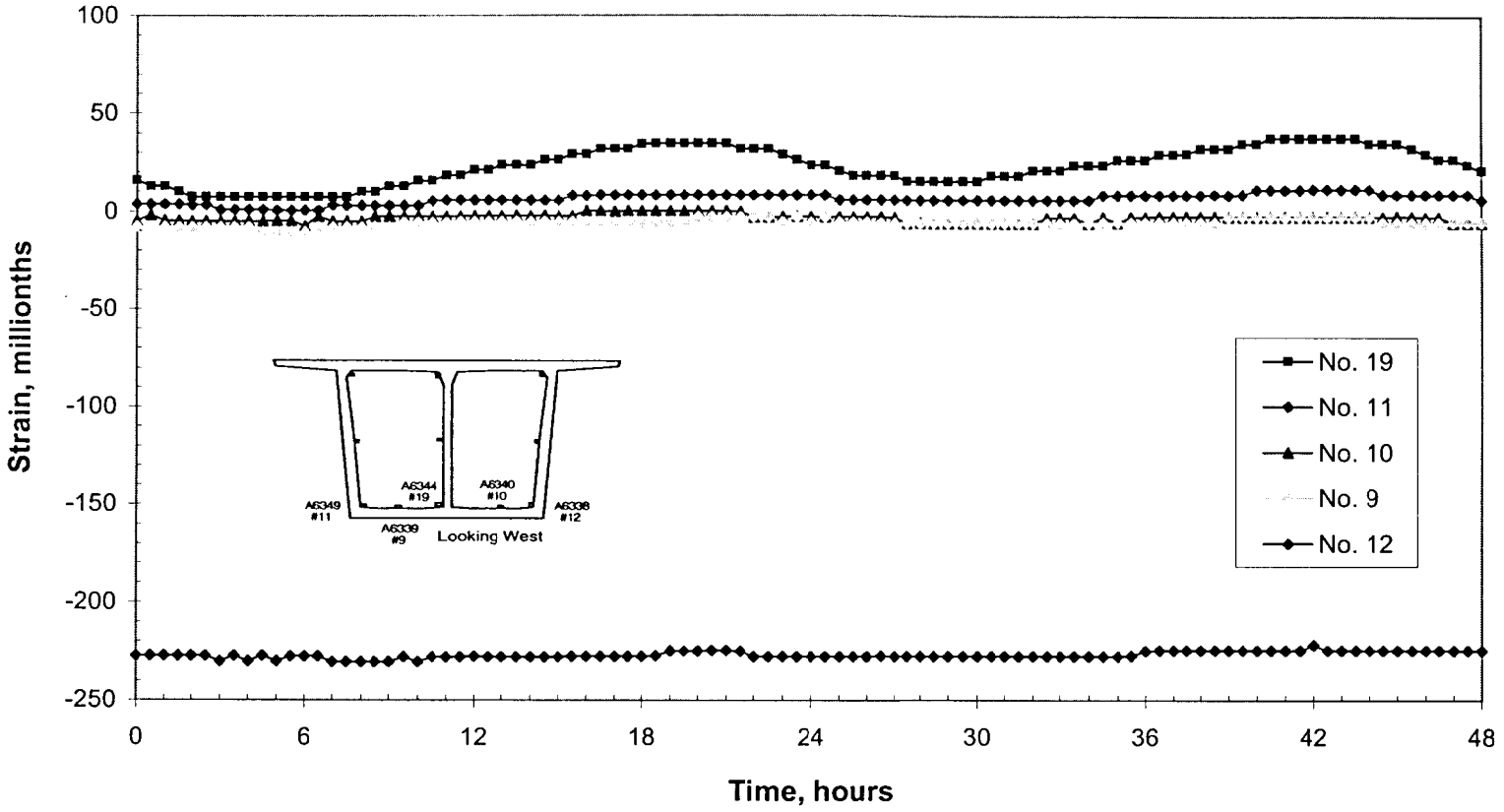


Figure 2.77 Concrete Compressive Strain in the Bottom Horizontal Section of Segment P14MS1, 5/21/98, 12:00 p.m. to 5/23/98, 12:00 p.m.

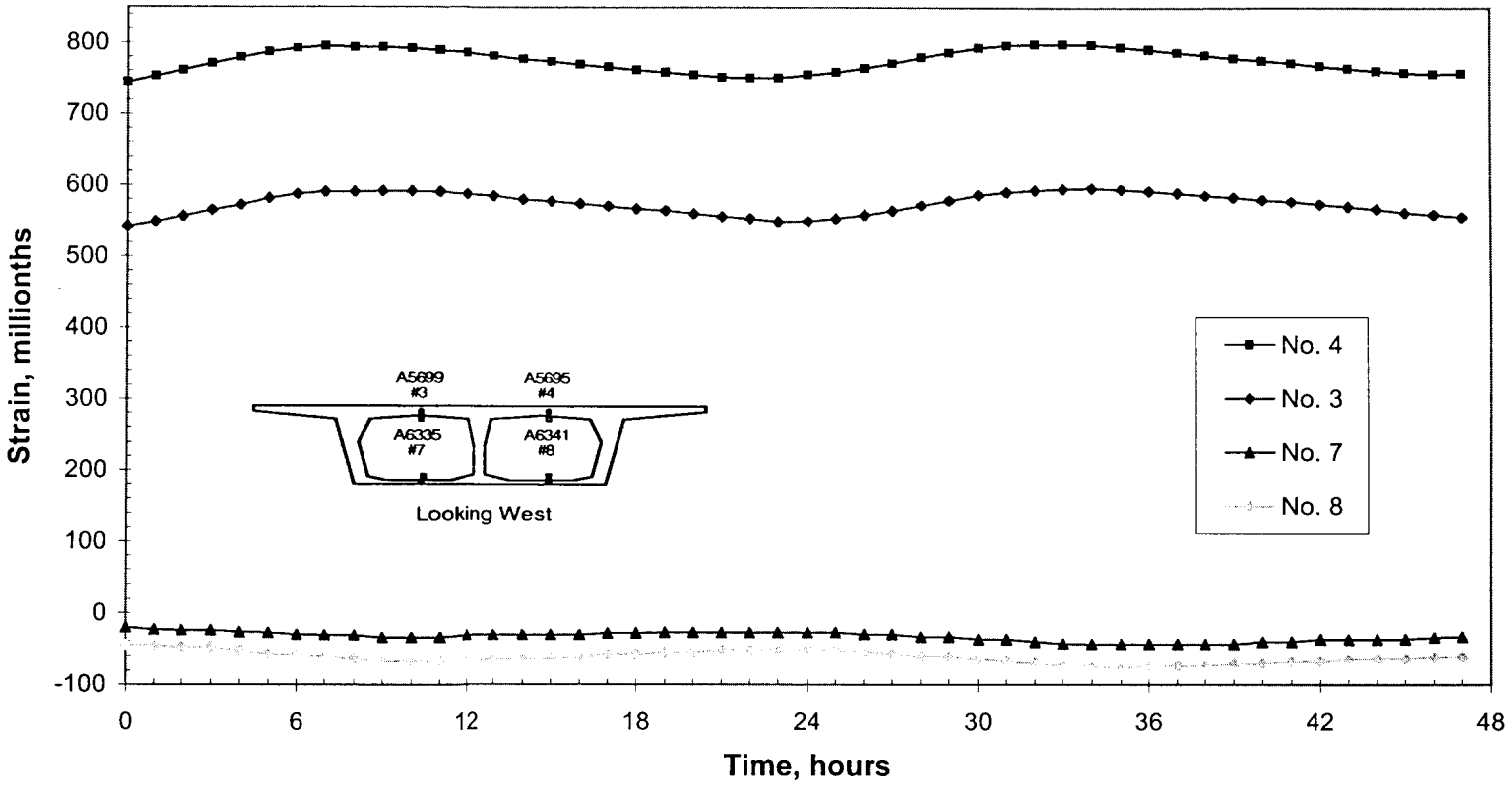


Figure 2.78 Concrete Compressive Strain in the Top Slab of the Main Closure Segment, 7/21/98, 12:00 p.m. to 7/23/98, 12:00 p.m.

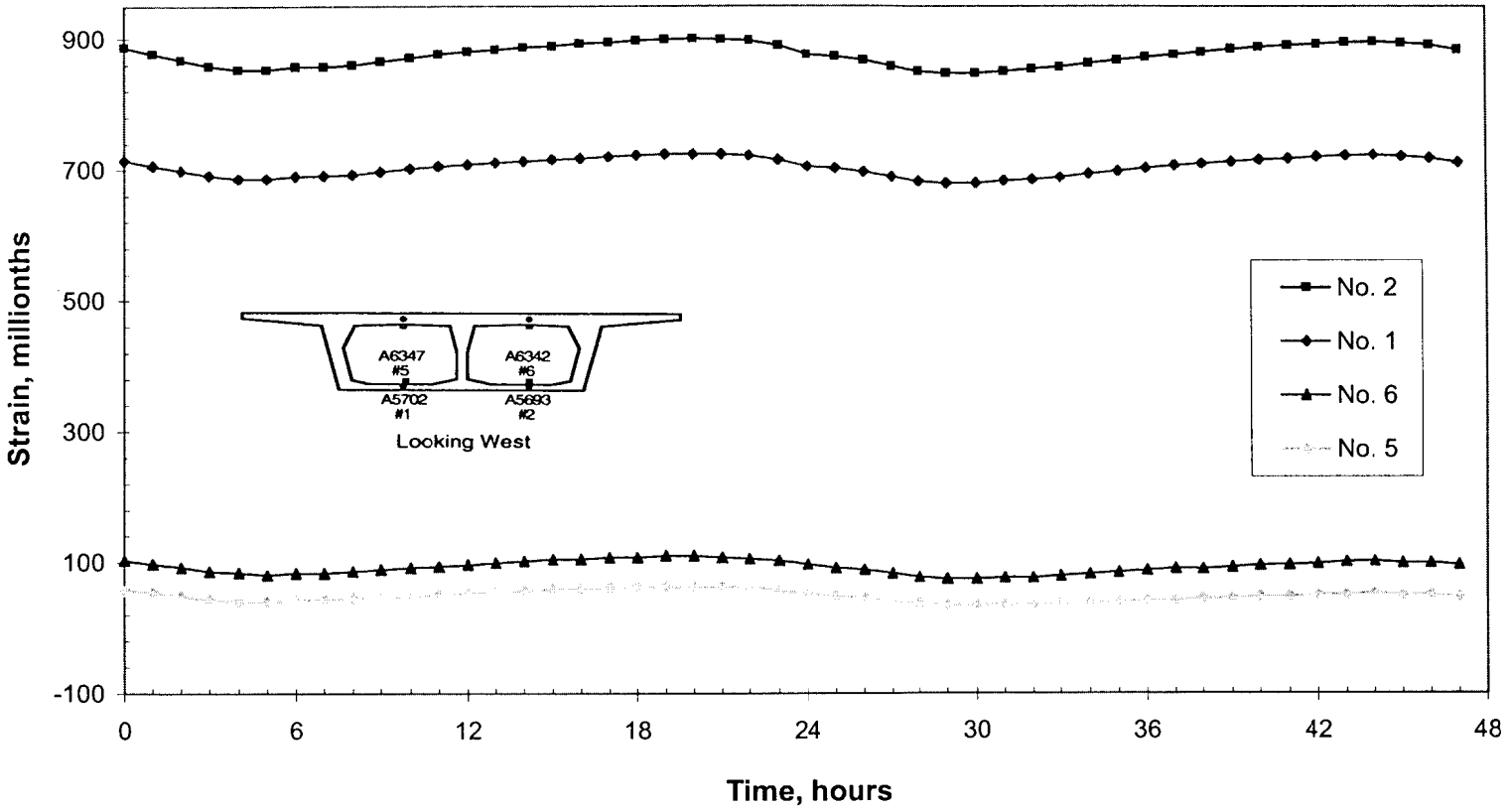


Figure 2.79 Concrete Compressive Strain in the Bottom Slab of the Main Closure Segment, 7/21/98, 12:00 p.m. to 7/23/98, 12:00 p.m.

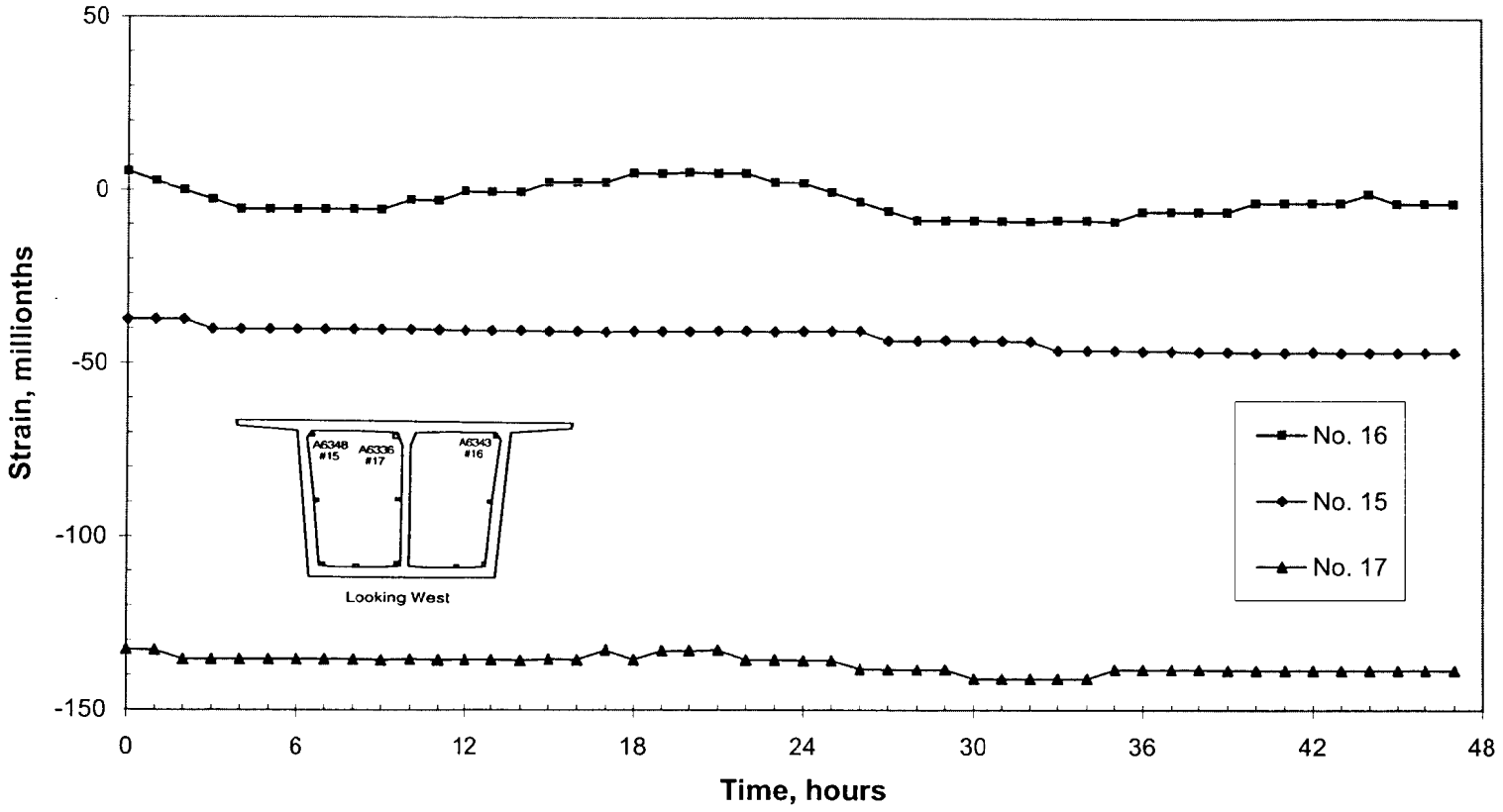


Figure 2.80 Concrete Compressive Strain in the Top Horizontal Section of Segment P14MS1, 7/21/98, 12:00 p.m. to 7/23/98, 12:00 p.m.

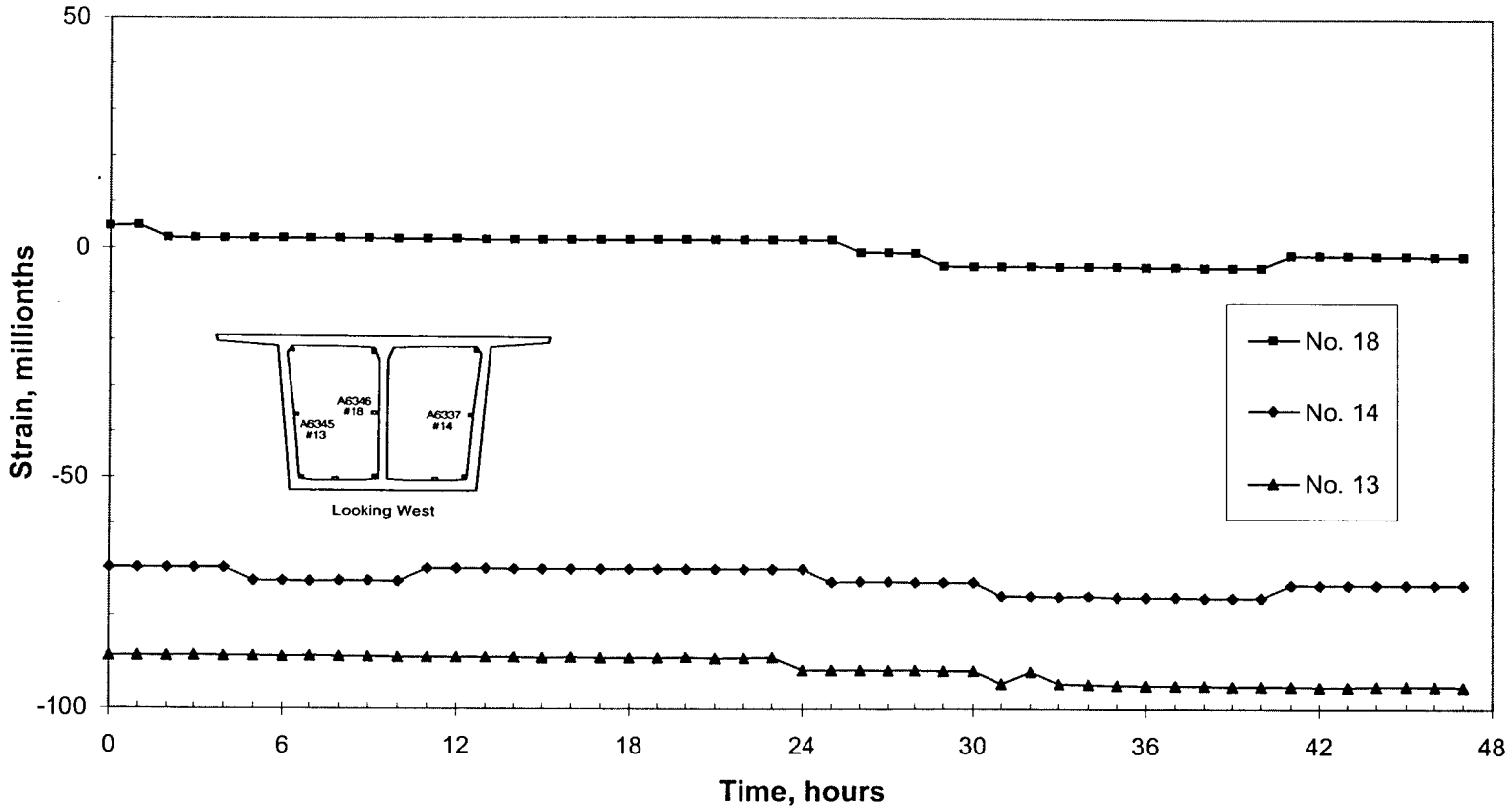


Figure 2.81 Concrete Compressive Strain in the Center Horizontal Section of Segment P14MS1, 7/21/98, 12:00 p.m. to 7/23/98, 12:00 p.m.

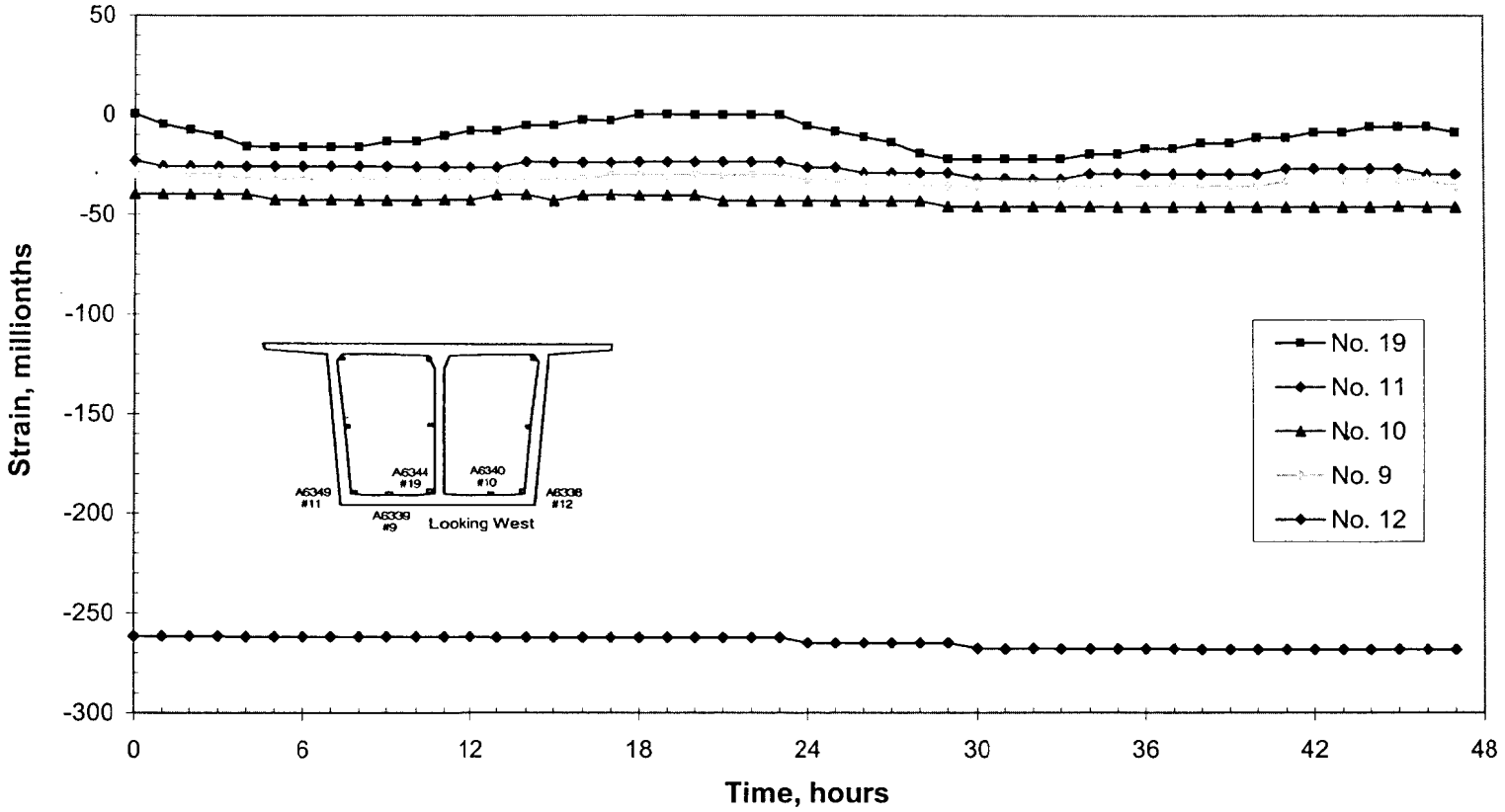


Figure 2.82 Concrete Compressive Strain in the Bottom Horizontal Section of Segment P14MS1, 7/21/98, 12:00 p.m. to 7/23/98, 12:00 p.m.

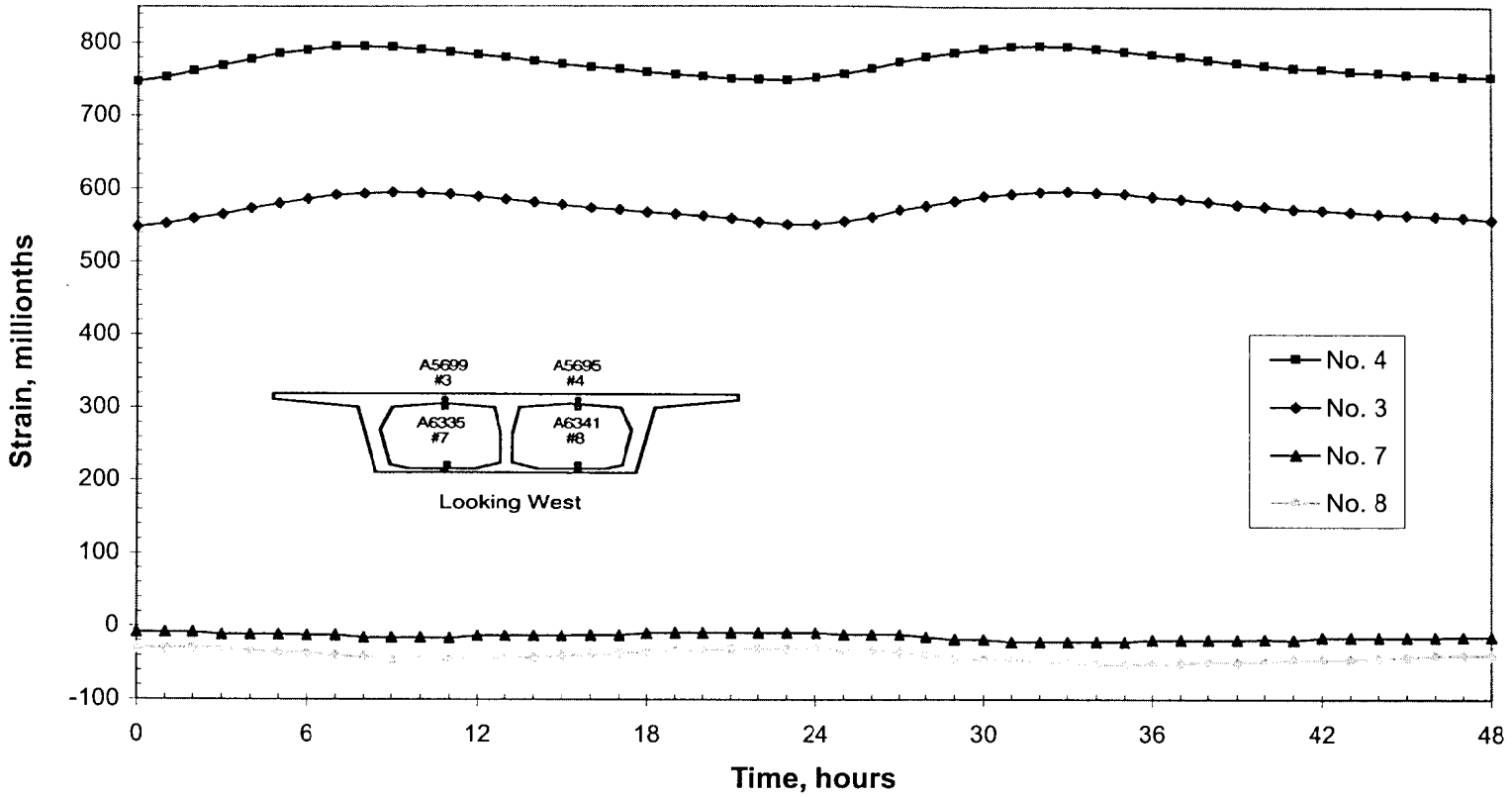


Figure 2.83 Concrete Compressive Strain in the Top Slab of the Main Closure Segment, 9/5/98, 12:00 p.m. to 9/7/98, 12:00 p.m.

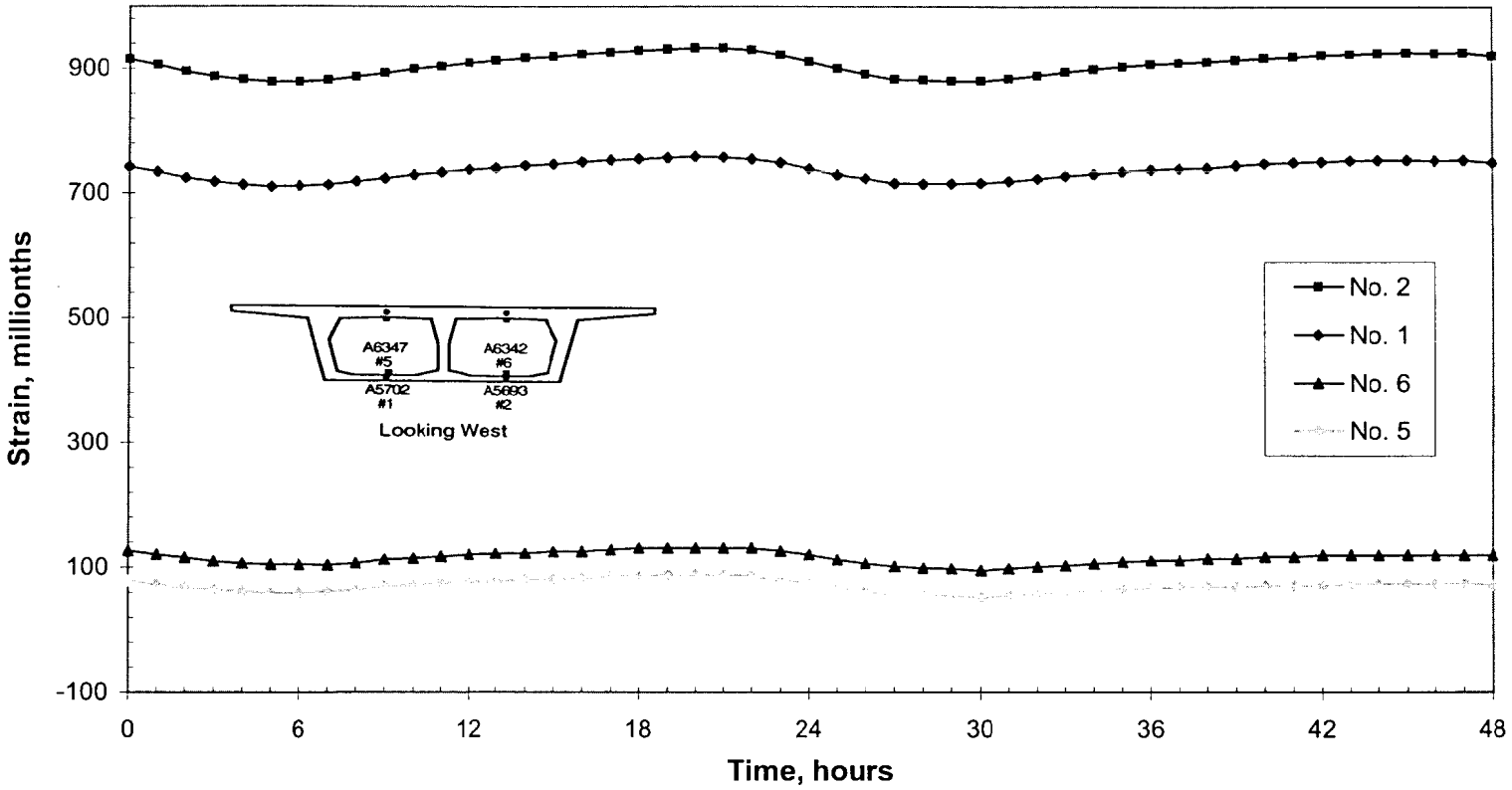


Figure 2.84 Concrete Compressive Strain in the Bottom Slab of the Main Closure Segment, 9/5/98, 12:00 p.m. to 9/7/98, 12:00 p.m.

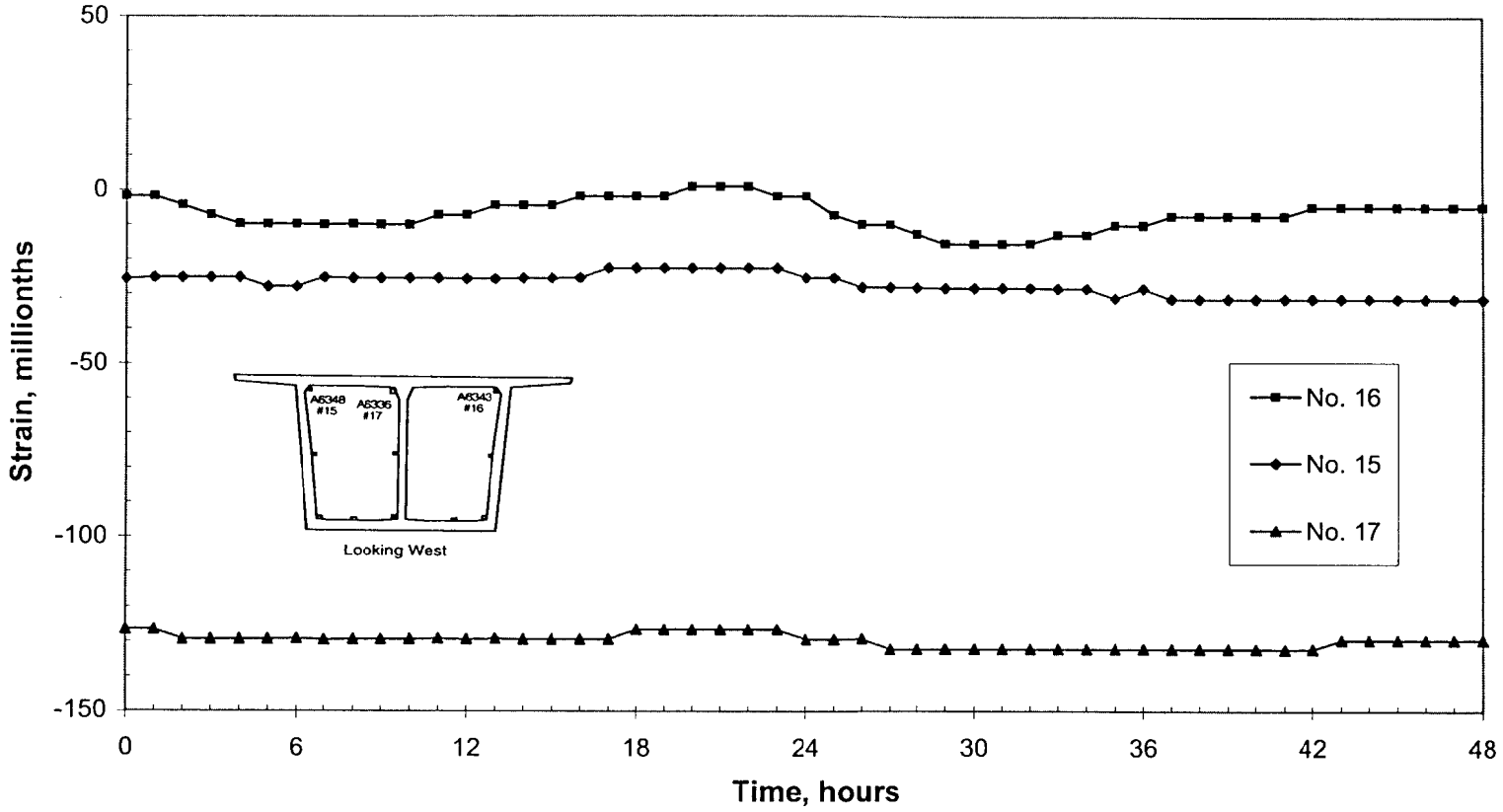


Figure 2.85 Concrete Compressive Strain in the Top Horizontal Section of Segment P14MS1, 9/5/98, 12:00 p.m. to 9/7/98, 12:00 p.m.

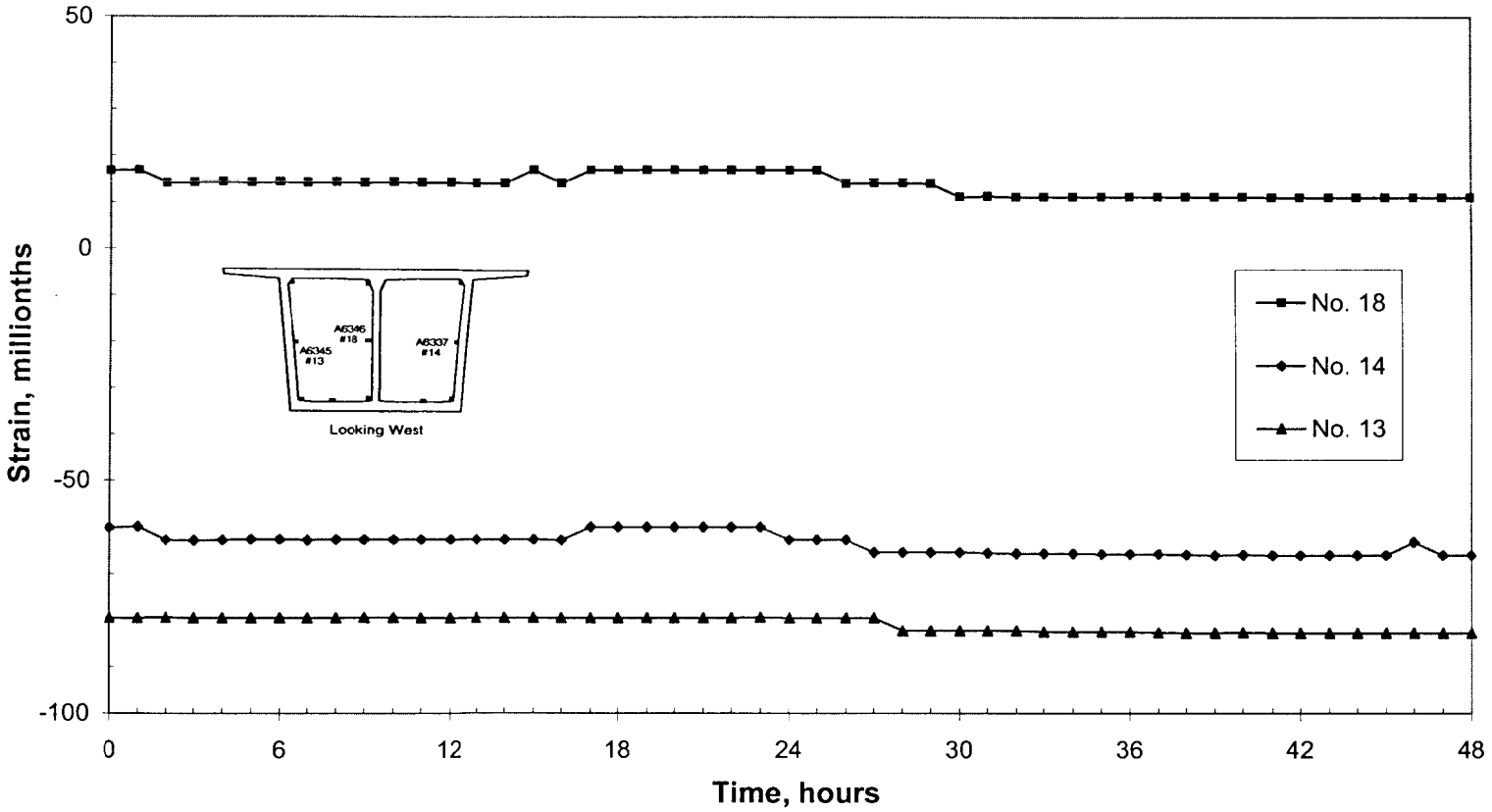


Figure 2.86 Concrete Compressive Strain in the Center Horizontal Section of Segment P14MS1, 9/5/98, 12:00 p.m. to 9/7/98, 12:00 p.m.

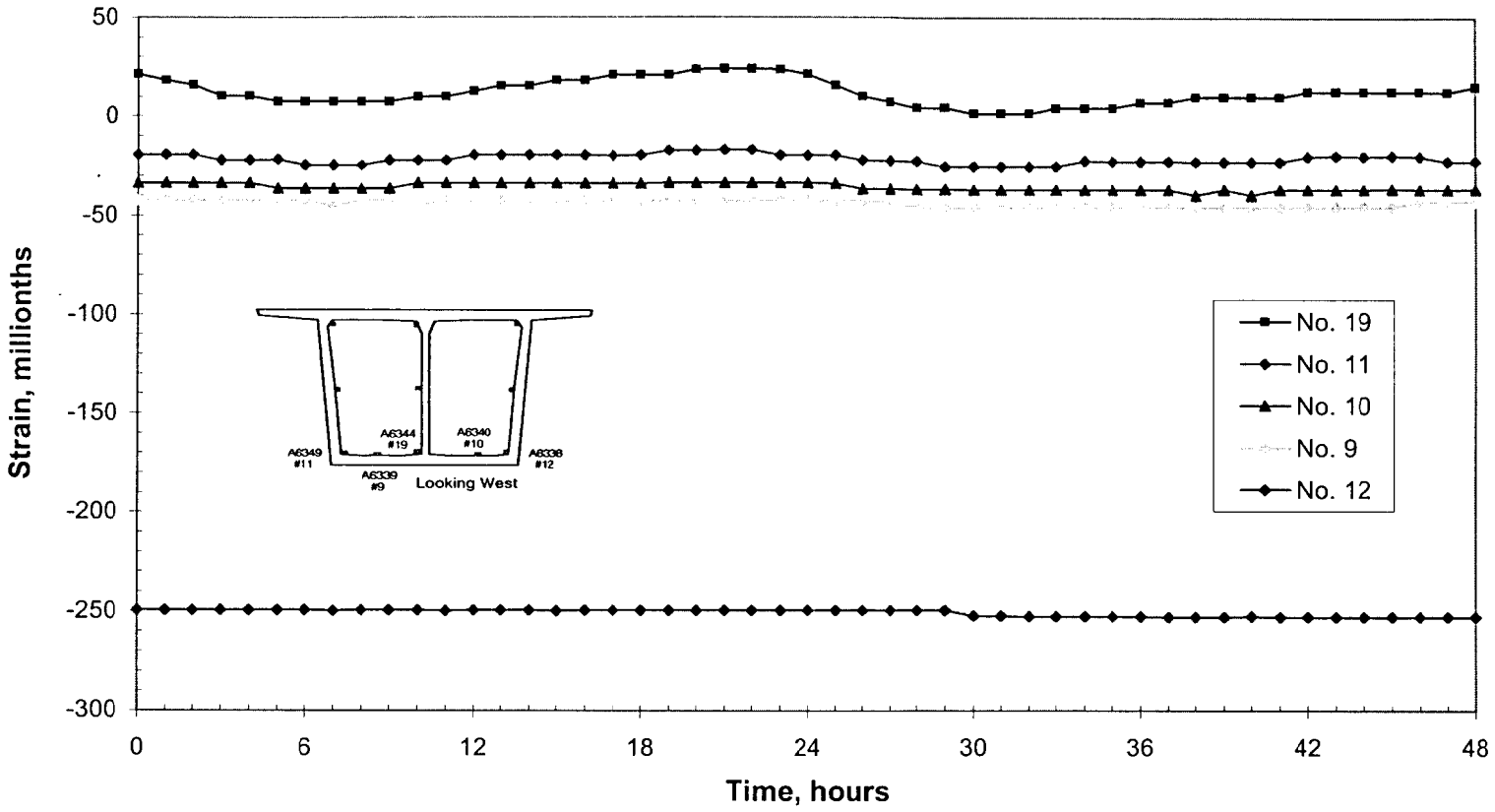


Figure 2.87 Concrete Compressive Strain in the Bottom Horizontal Section of Segment P14MS1, 9/5/98, 12:00 pm to 9/7/98, 12:00 pm

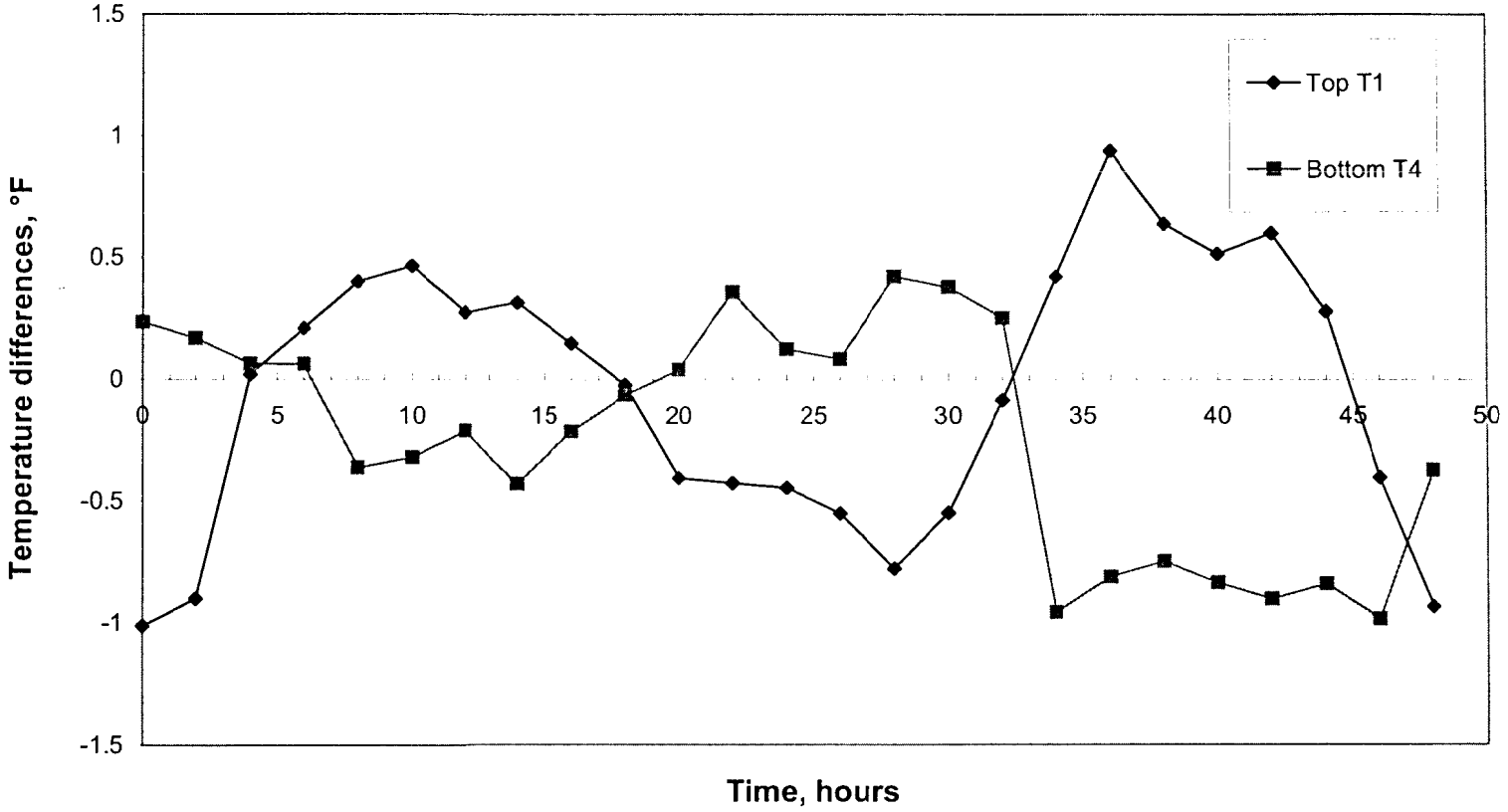


**Figure 2.88 Critical South and Noth Temperature Differences, 9/21/97 12:00 pm to 9/23/97 12:00 pm**

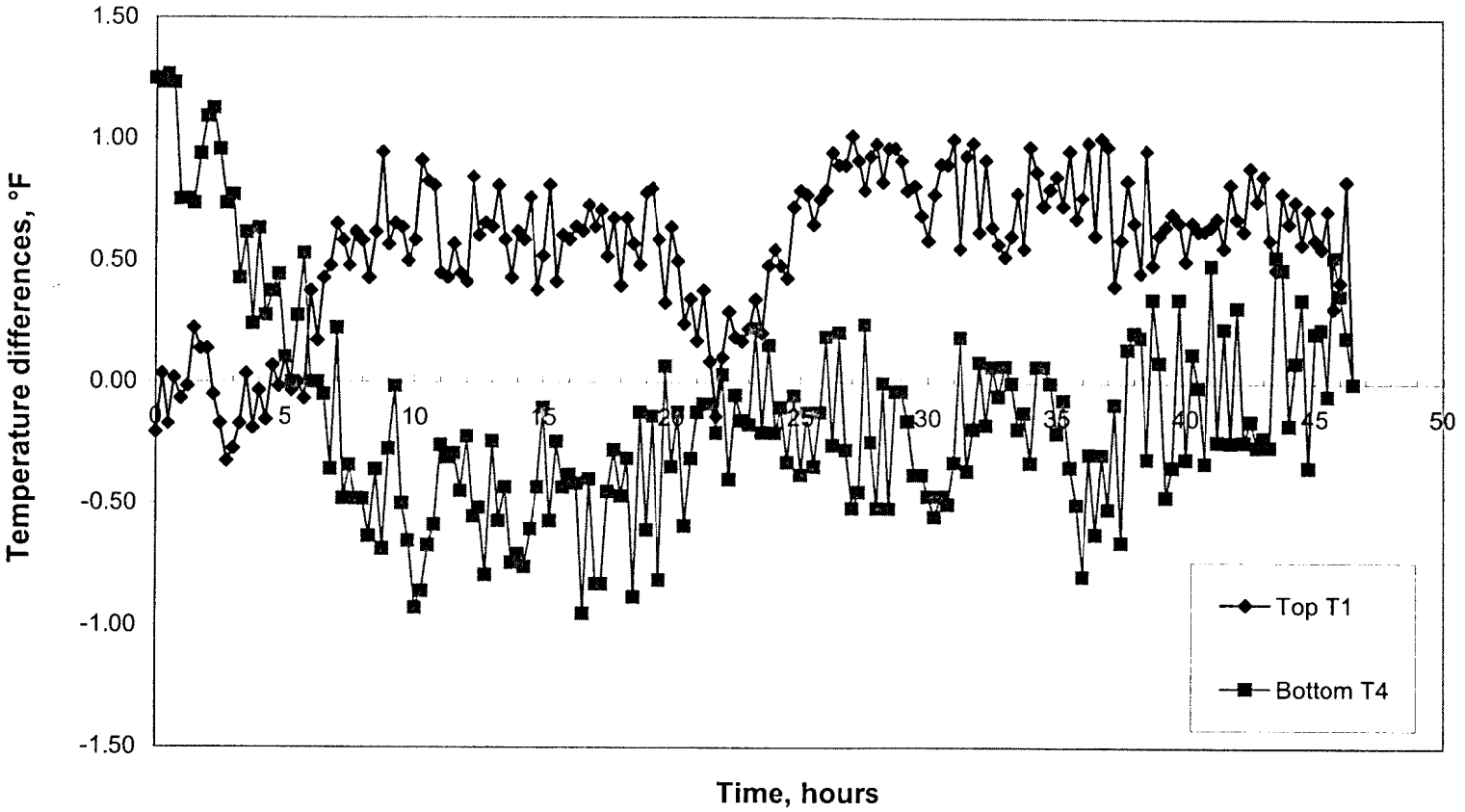


**Figure 2.89 Critical South and Noth Temperature Differences, 1/13/98 12:00 pm to 1/15/98 12:00 pm**

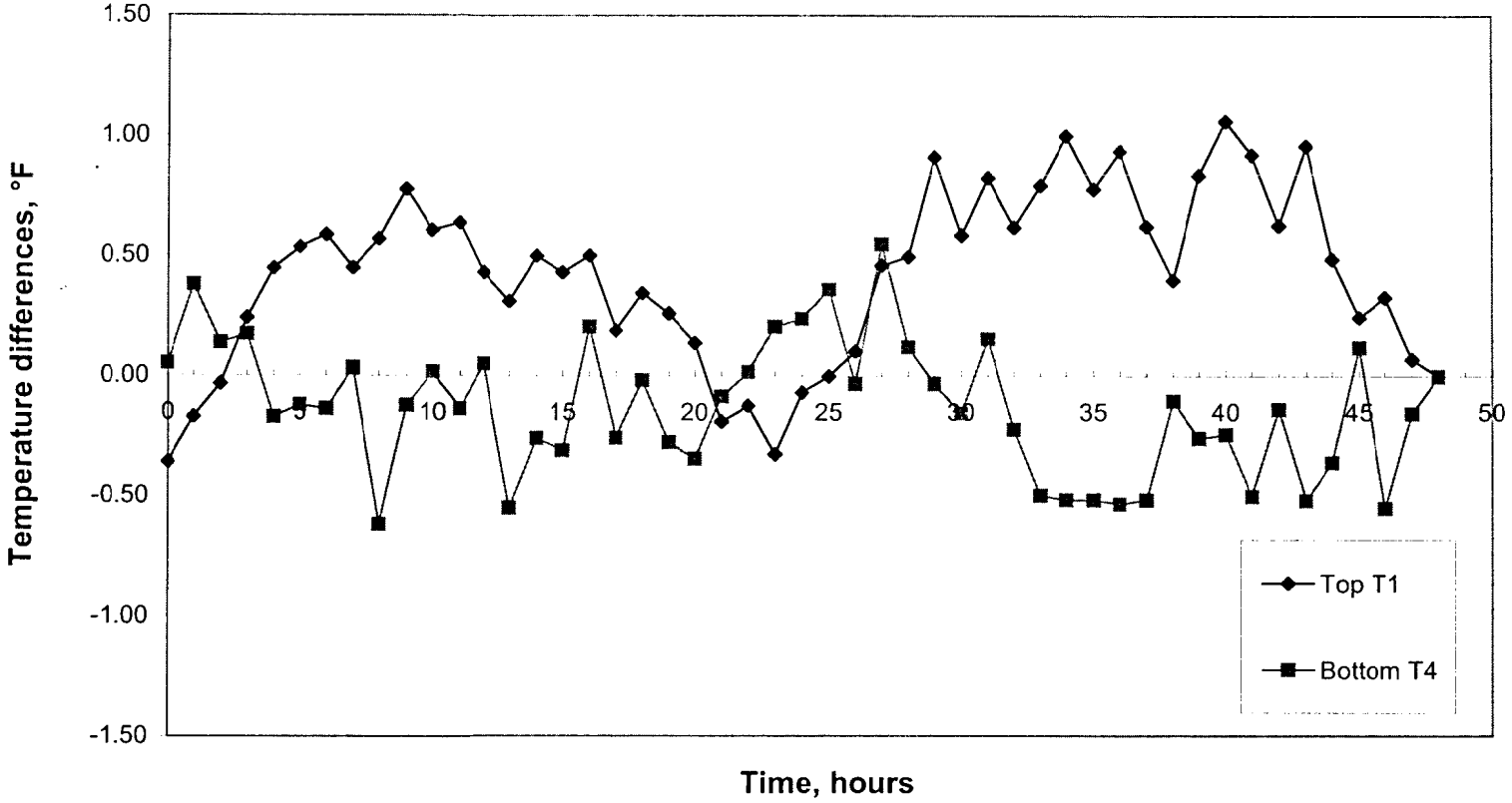


**Figure 2.90 Critical South and Noth Temperature Differences, 1/25/98 12:00 pm to 1/27/98 12:00 pm**

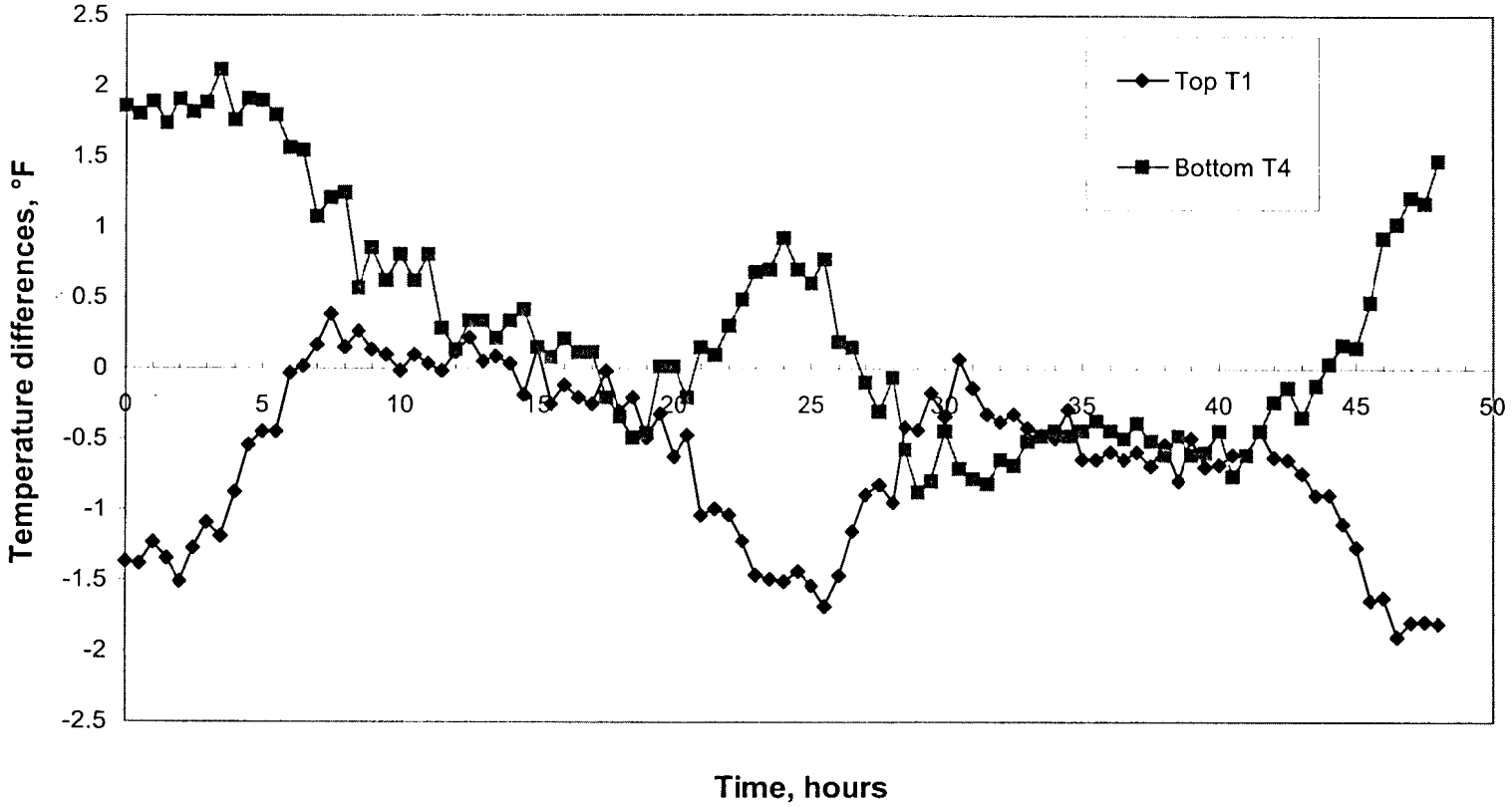


**Figure 2.91 Critical South and Noth Temperature Differences, 4/27/98 12:00 pm to 4/29/98 12:00 pm**

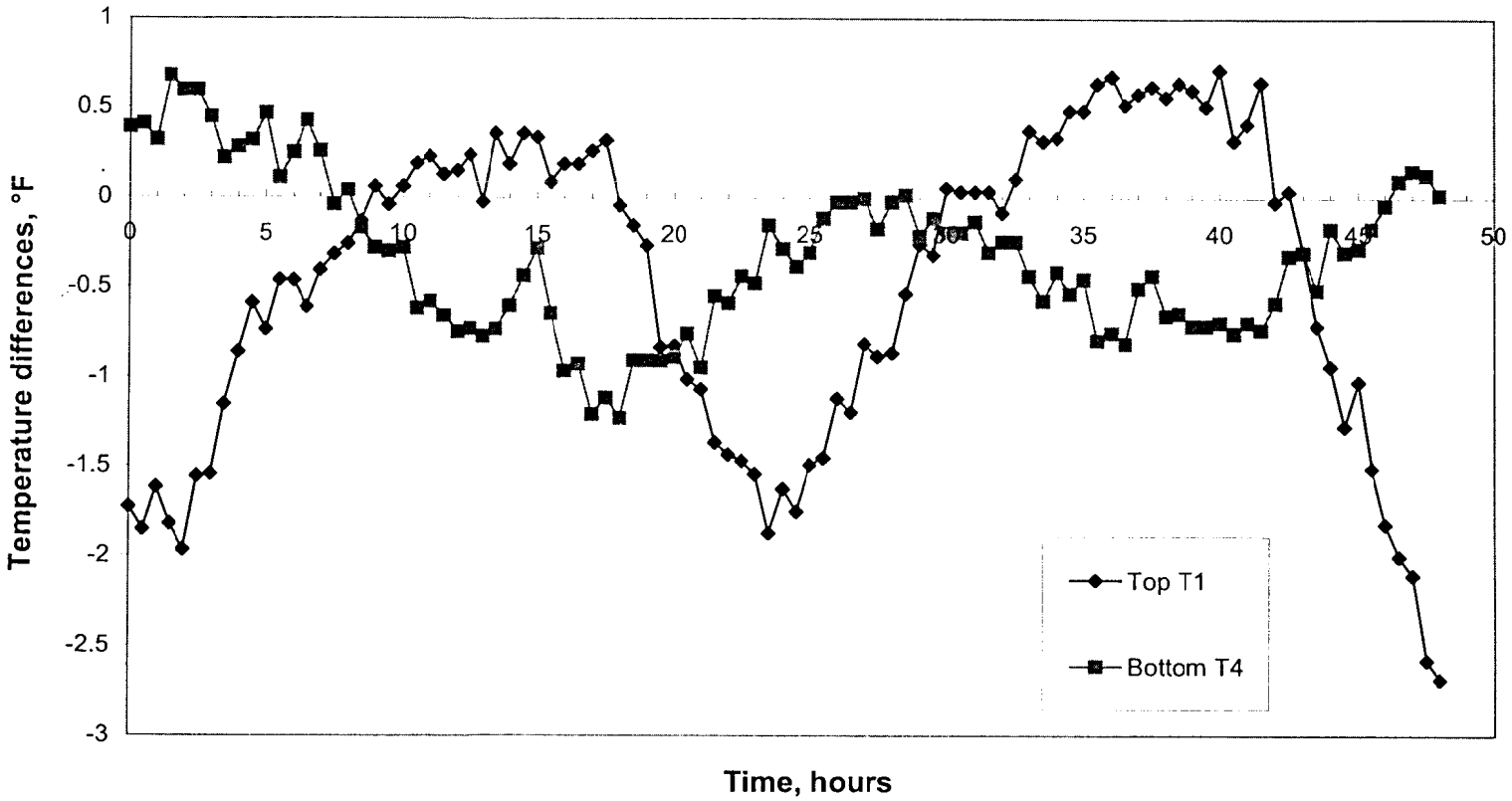


**Figure 2.92 Critical South and Noth Temperature Differences, 5/21/98 12:00 pm to 5/23/98 12:00 pm**

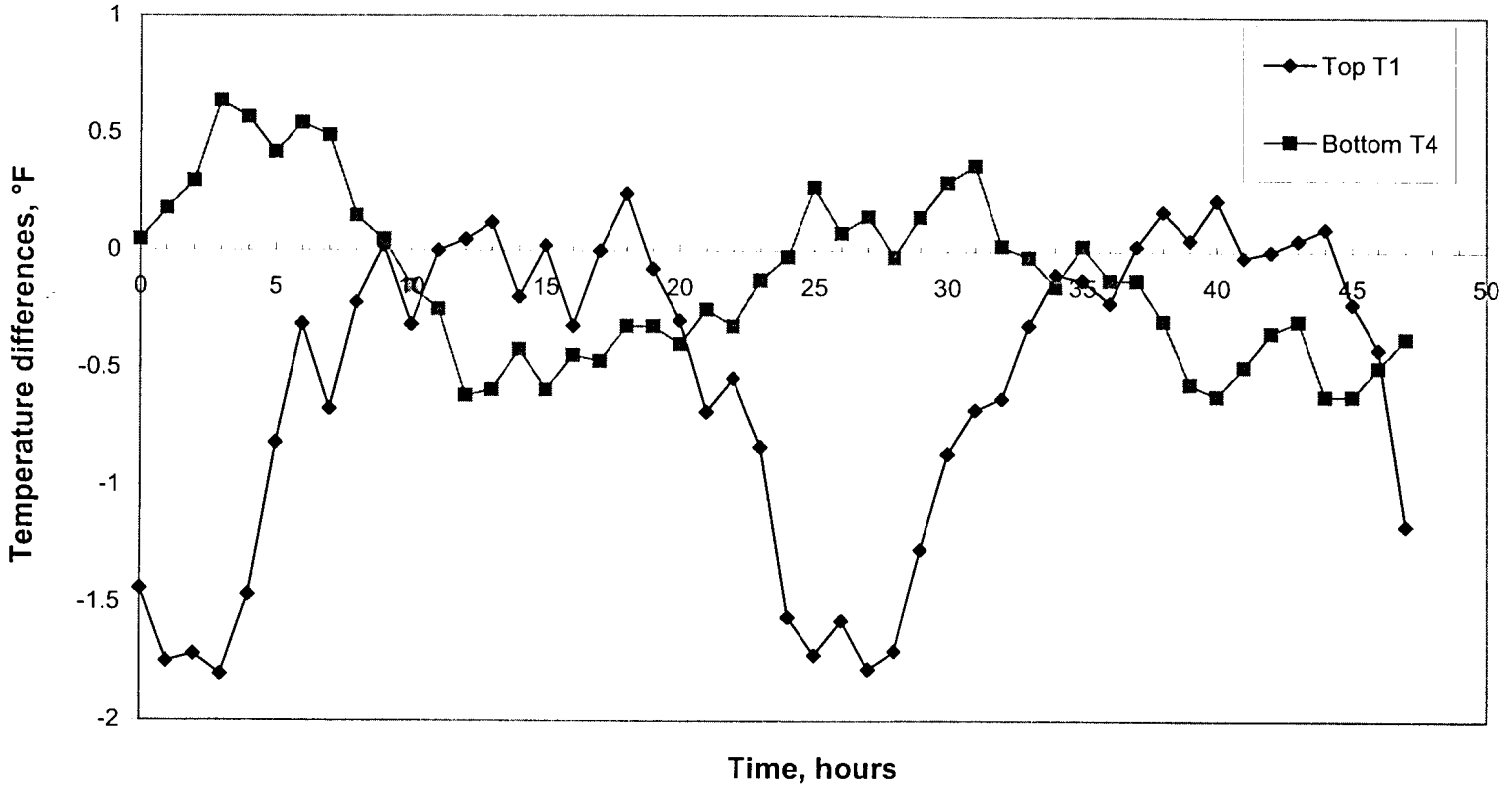


**Figure 2.93 Critical South and Noth Temperature Differences, 7/21/98 12:00 pm to 7/23/98 12:00 pm**

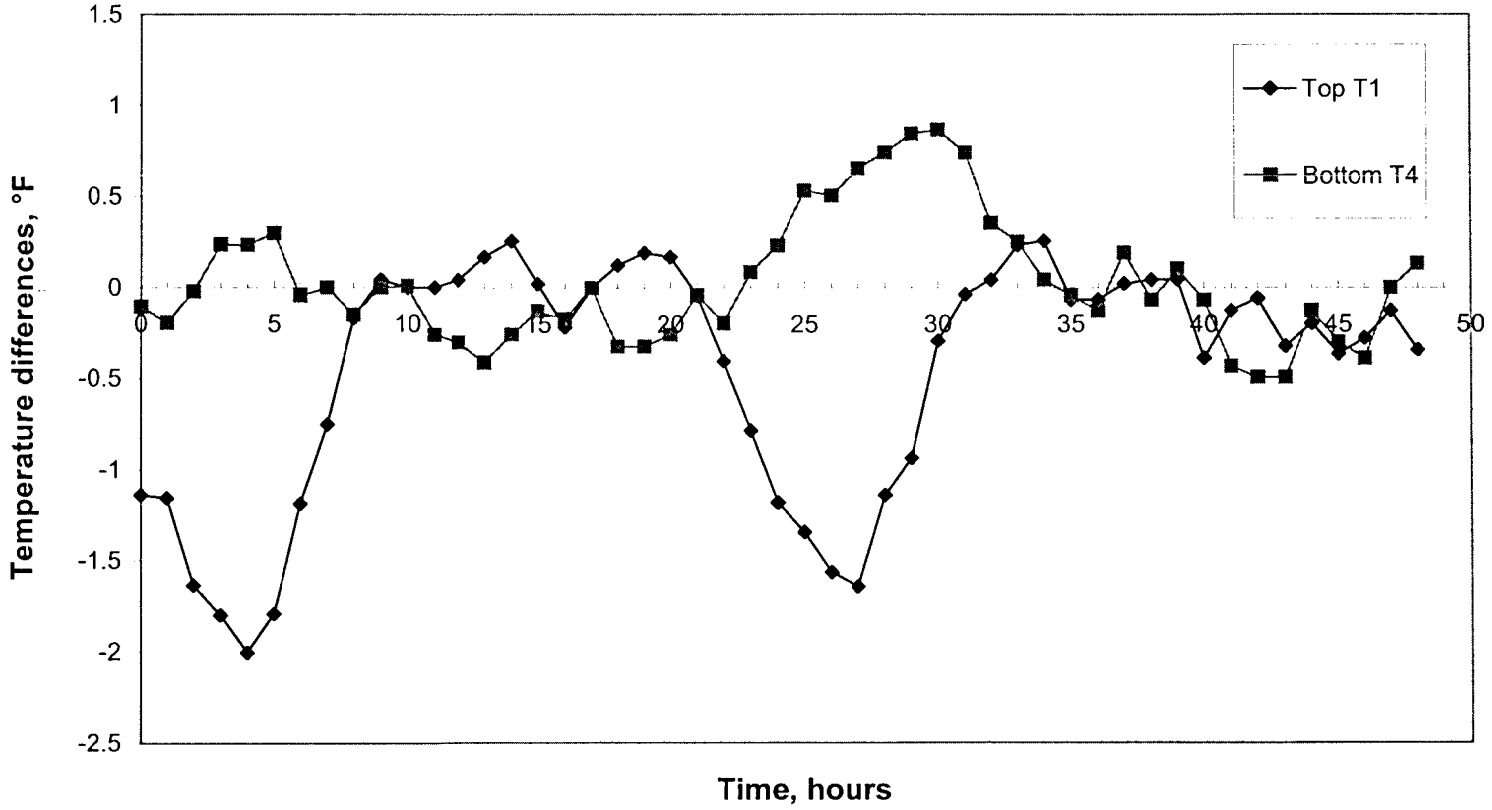


**Figure 2.94 Critical South and Noth Temperature Differences, 9/5/98 12:00 pm to 9/7/98 12:00 pm**

# 3.0 THERMAL DIFFERENTIALS AND GRADIENTS

## 3.1 Introduction

As temperature rises and falls, an unrestrained bridge structure responds through thermal movements. These can be classified into three types: longitudinal movements, transverse movements, and thermally induced curvature. In this study, we concentrate in longitudinal movements. It has been observed (Emerson 1977, 1982; Priestley and Buckle 1979) that the temperature fluctuations can be separated into two components: a uniform change and a gradient. The uniform temperature change causes a uniform longitudinal thermal movement. Temperature gradients also cause longitudinal thermal movements. However, the gradients in general are not linear within the thickness of the bridge. Since the strains are proportional to the temperature change, non-uniform temperature strains are induced. Thermal stresses follow due to restraint to expansion and rotation.

In this chapter bridge temperature fluctuations are further investigated. Specifically, the variation of the temperature differentials as well as the temperature gradients are studied. Based on the bridge data a probability density function is developed to model the distribution of the extreme temperature differentials, (Section 3.2). Bridge temperature gradients are also determined and compared to current AASHTO specifications, (Section 3.3).

The chapter also includes a discussion on the relation between temperature and strain variations, (Section 3.4).

### 3.2 Temperature Differentials

Until very recently bridge design specifications assumed a linear temperature distribution within the bridge superstructure in the form of a temperature differential between the top and bottom sides of the bridge. It is noticed from the original design of the Jamestown bridge that a temperature differential of 10 °F was used. In this section the data collected over the one year monitoring period are analyzed to develop a model for the distribution of such temperature differentials.

Temperature differentials between top and bottom slab at the main span closure section are investigated. These are calculated by subtracting the temperature in the bottom slab (BS-4) from the concrete temperature at the top of the bridge girder (TS-5). It is noted that these are simultaneous differentials, i.e. the subtraction takes place at the same time instants. Since we are interested to study the distribution of the extreme differentials, the highest or lowest temperature differentials are used from each day monitored. In order to study seasonal temperature differentials the data are divided in the corresponding seasons and each season is studied separately.

Figs. 3.1, 3.2, 3.3, and 3.4 show the variation of the extreme temperature differentials for fall, winter, spring and summer respectively. Histograms of the data are presented in Figs. 3.5, 3.6, 3.7, and 3.8. The figures indicate that temperature differentials of about 6 °F for fall and winter and 25 °F during spring and summer, were most frequently encountered between the top and bottom slabs of the box girder. The measured maximum positive temperature differential is 35 °F and occurred in the spring. Typically, maximum positive differentials occurred about 5 pm and maximum negative differentials about 4 am. The minimum temperature differential is –9°F and took place during winter. Note that positive temperature differentials represent a higher temperature in the top slab than the bottom slab.

Figure 3.9 presents the variation of the extreme temperature differentials for the whole year

of monitoring. About 42% of the temperature differentials are about 6 °F which is less than the 10 °F assumed during the original bridge design

It is noted that until the late 80's AASHTO specifications did not provide for temperature gradients for bridge design. Only changes of the mean temperature affecting longitudinal movement were considered. The Post Tensioning Institute (PTI) did recommend a linear temperature differential. Following this guideline a linear differential of 10 F for Group IV loads and 20 F for Group V loads (i.e. no live load and impact included in Group V) was used for the original design of Jamestown bridge. During the mid eighties it was realized that with longer spans having optimized sections bridge differentials could be important. NCHRP Report 276 (Imbsen et. al., 1985) suggested a nonlinear temperature gradient to be used for the design of bridges. Later AASHTO specifications adopted these guidelines with some modifications.

In order to be able to make future predictions on the probability of occurrence of certain temperature differentials, a probability density function is developed using the data of Fig. 3.9. A shifted lognormal probability model is used to model the extreme temperature differentials. The model is summarized in Kottegoda and Russo (1997) who provide the functions needed to develop the model based on the data at hand.

As a first step in the model development, the mean value, the standard deviation and the coefficient of skewness for the data are calculated. These are $\mu = 13.84$, $\sigma = 9.988$, and $\gamma_1 = 0.129$ respectively. According to Kottegoda and Russo , the shift parameter $\varepsilon$ is determined by the solution of a third order equation:

$$\gamma_1(\mu - \varepsilon)^3 - 3\cdot(\mu - \varepsilon)^2 \cdot \sigma - \sigma^3 = 0 \qquad (3.1)$$

The final value for the shift parameter, which is also known as the location parameter,

based on our data is $\varepsilon = -128.58$. Two additional parameters are needed for the definition of the shifted lognormal distribution. These are given by the following expressions:

$$\sigma_{\ln(X_{max}-\varepsilon)} = \sqrt{\ln\left[1+\left(\frac{\sigma}{\mu-\varepsilon}\right)^2\right]} \tag{3.2}$$

$$\mu_{\ln(X_{max}-\varepsilon)} = \ln(\mu-\varepsilon) - \frac{1}{2}\ln\left[1+\left(\frac{\sigma}{\mu-\varepsilon}\right)^2\right] \tag{3.3}$$

In Eqs. 3.2 and 3.3 $X_{max}$ corresponding to the extreme quantity under consideration, which in this case is the maximum temperature differential, $\mu$ and $\sigma$ are the mean and standard deviation of this quantity, and $\epsilon$ is a location parameter (shift). The probability density function (pdf) of the shifted lognormal distribution is given by:

$$f_{X_{max}}(x) = \frac{1}{\sigma_{\ln(X_{max}-\varepsilon)}\sqrt{2\pi}\cdot(x-\varepsilon)}\exp\left[-\frac{1}{2}\left(\frac{\ln(x-\varepsilon)-\mu_{\ln(X_{max}-\varepsilon)}}{\sigma_{\ln(X_{max}-\varepsilon)}}\right)^2\right] \tag{3.4}$$

For the data set of the one-year extreme temperature differentials of the Jamestown Bridge, the pdf of the shifted lognormal distribution, Eq. 3.4, becomes:

$$f_{X_{max}}(x) = \frac{1}{0.04647\cdot(x+218.58)}\exp\left[-1454.6\cdot\left(\ln(x+218.58)-5.448\right)^2\right] \tag{3.5}$$

where x = temperature differential.

The shifted lognormal distribution for the extreme temperature differentials at the main span closure segment is shown in Fig. 3.10. A good correlation is obtained between the calculated shifted lognormal function and the measured data.

### 3.3 Temperature Gradients

The seasonal peak temperature gradients within the bridge are presented in Figs. 3.11 through 3.17. A positive gradient is shown for the fall but both positive and negative gradients are indicated for the winter, spring and summer seasons. It is noted that the positive temperature gradients usually occurred in early afternoon, around 2:00 pm.to 3:00 pm. Negative temperature gradients were observed in early morning, around 6:00 am to 7:00 am.

The critical positive temperature gradient took place on April 27, 1998 at 2:30 p.m. A critical negative temperature gradient occurred twice during the one-year monitoring, on September 23, 1997 at 6:00 am and on January 15, 1998 at 7:00 am.

It is interesting to compare the observed extreme gradients with the AASHTO recommendations. Fig. 3.18 compares the observed maximum positive gradient to the 1994 AASHTO specifications as applied for the location of the Jamestown-Verrazzano bridge. Fig. 3.19 presents the comparison for the case of the extreme negative gradients.

Figs. 3.18 and 3.19 indicate that the top slab temperature gradients (including positive and negative gradients) are quite close to the AASHTO specification requirements. However, the bottom slab temperature gradients are higher for positive gradients and lower for negative ones compared with the1994 AASHTO recommendations. Similar observations are found elsewhere

(Shushkewich, 1998; Shiu, et al. 1991). It is noted that the AASHTO recommendations on temperature are based on the NCHRP Report 276 (Imbsen, et. al., 1985). According to that report a value of 5 °F was suggested for the bottom slab of the positive gradient and 8 °F was recommended for the case of the negative gradient. However, AASHTO specifies that in both positive and negative gradient cases the value should be taken as zero unless a site-specific study is made. Even then, the value cannot exceed 5 °F for positive gradients or 1.5 °F for negative gradients (Guide Specifications for Design and Construction of Segmental Concrete Bridges, 1999)..

### 3.4 Concrete Temperature-Strain Variations

In this section the strain changes induced by temperature variations are studied based on the data readings. Strain and temperature measurements at the mid span closure section over three 24-hour periods are used to evaluate the temperature induced strain variations. The three 24-hour periods correspond to the times that critical temperature gradients occurred.

Figures 3.20, 3.21, and 3.22 present the strain and temperature changes in the north girder of the main span section. It is noted that the embedded Carlson strain meters (#2 and #4; #1 and #3) exhibit higher strain variations than the retrofitted Carlson meters (#6 and #8; #5 and #7).

Fig. 3.20 shows a fall temperature variation of 25 °F while the extreme strain change is $50\times10^{-6}$in/in. During the winter, Fig. 3.21, temperature changes of 18.5 °F cause strain changes of $40\times10^{-6}$in/in. The strain and temperature changes are $50\times10^{-6}$in/in and 28 °F respectively during spring as shown in Fig. 3.22.

Fig. 3.23 presents the extreme temperature gradients at three time instants and the concrete strain variations between 6:00 a.m. and 2:00 pm within the corresponding 24-hour period. The

following observations can be made:

i) The negative temperature gradients induce strain variations in the opposite direction than the positive gradients.

ii) Te bigger the temperature changes the more the strain variations.

iii) Positive temperature gradients invoke compressive thermal stresses and negative temperature gradients induce tensile thermal forces in the bottom of the bridge.

Although such observations are intuitive they verify that the system responds as expected. It is noted that there are few strain meters for a more accurate evaluation but the results shown in Fig. 3.23 are in line with observations made during other bridge monitoring studies.

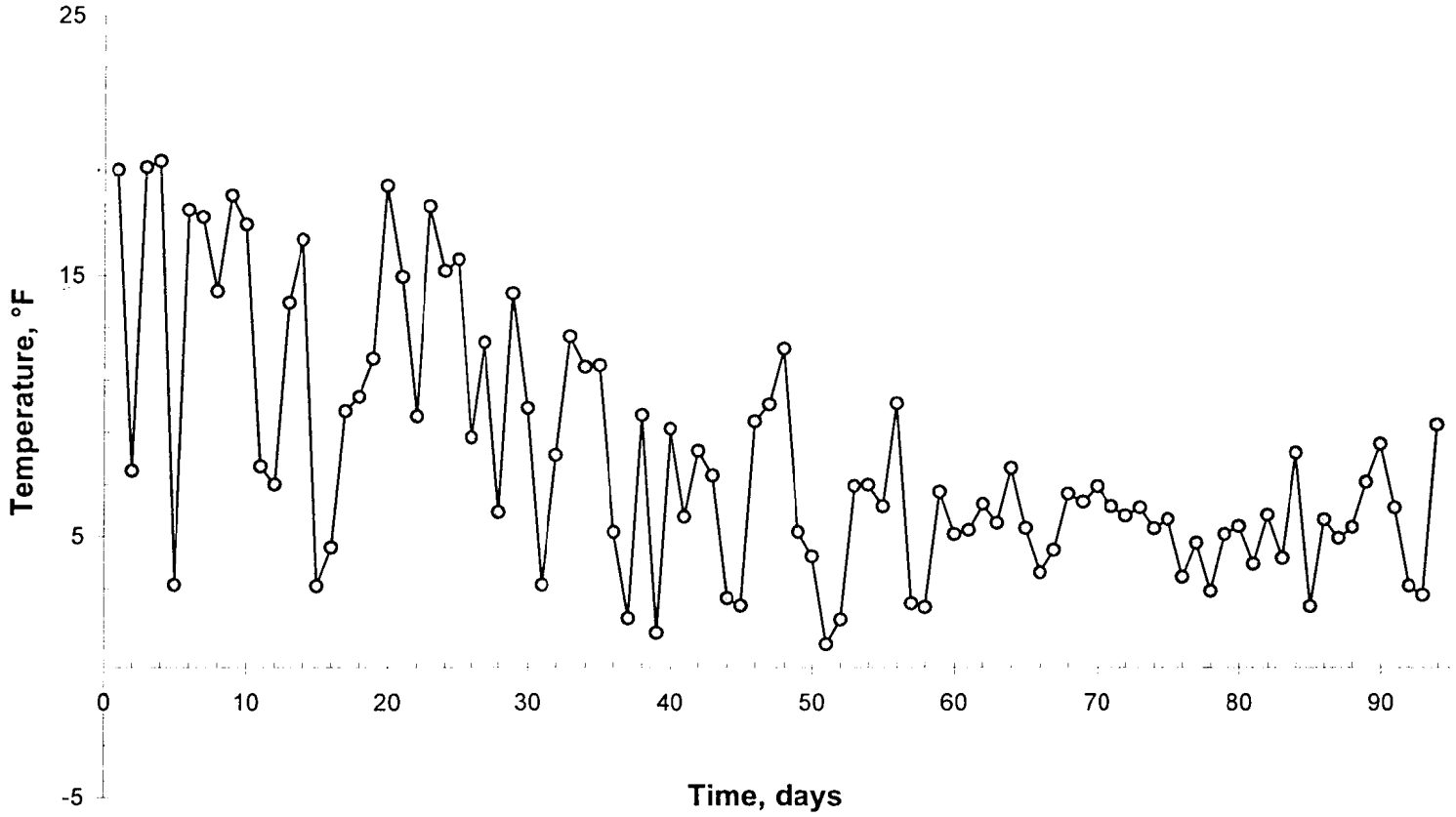


**Fig. 3.1 Fall Extreme Temperature Differentials**

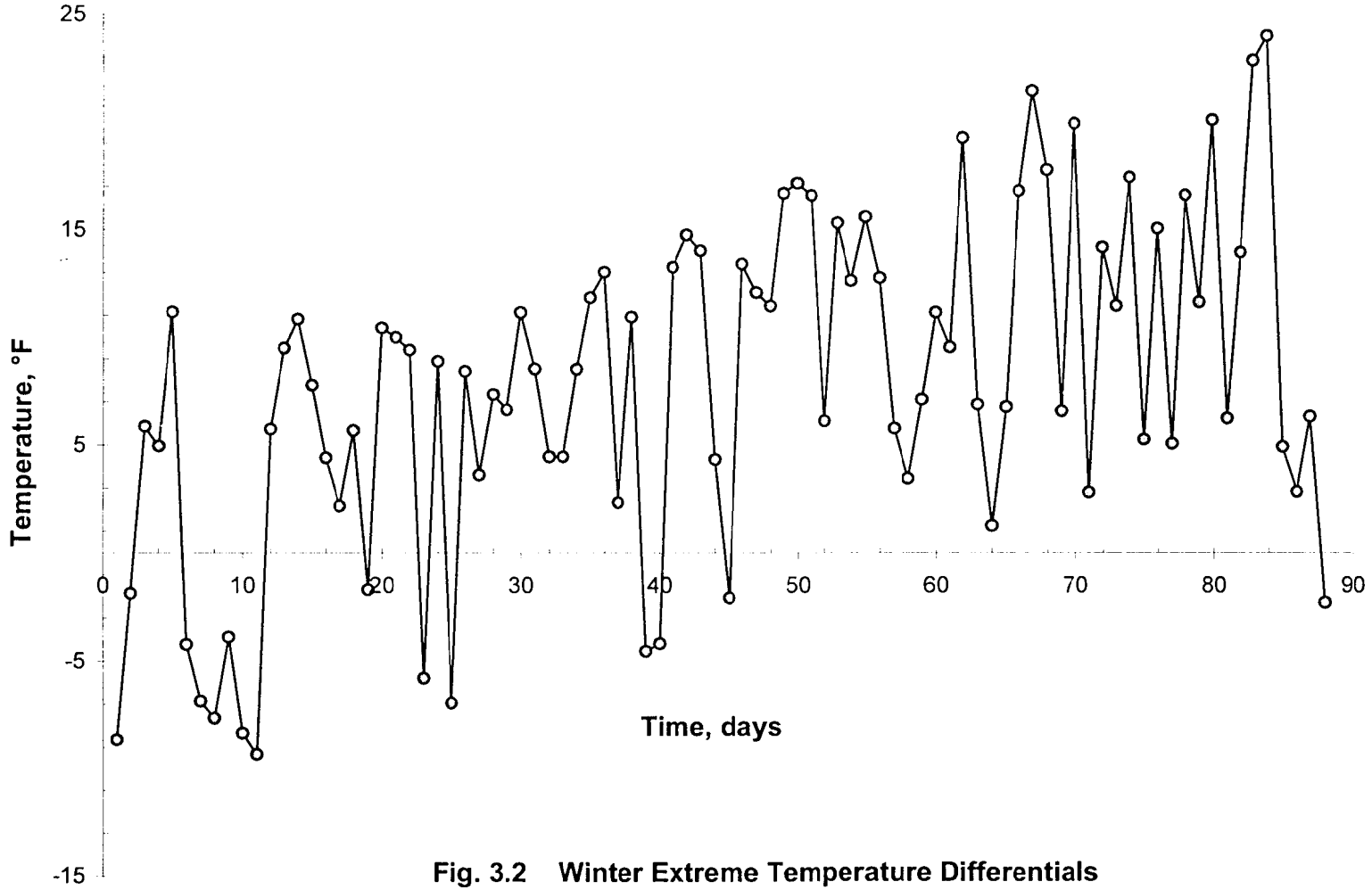


**Fig. 3.2 Winter Extreme Temperature Differentials**

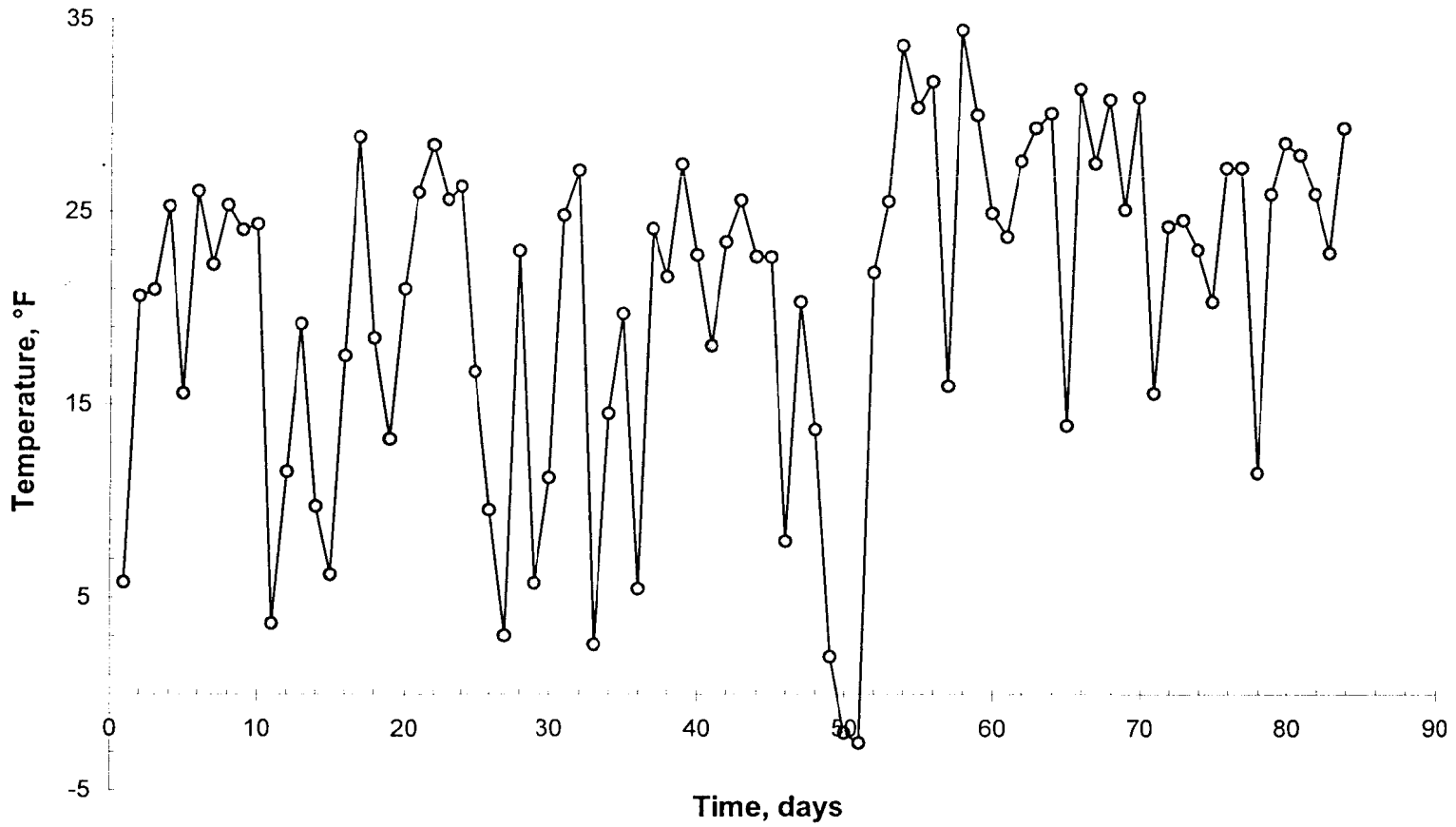


**Fig. 3.3 Spring Extreme Temperature Differentials**

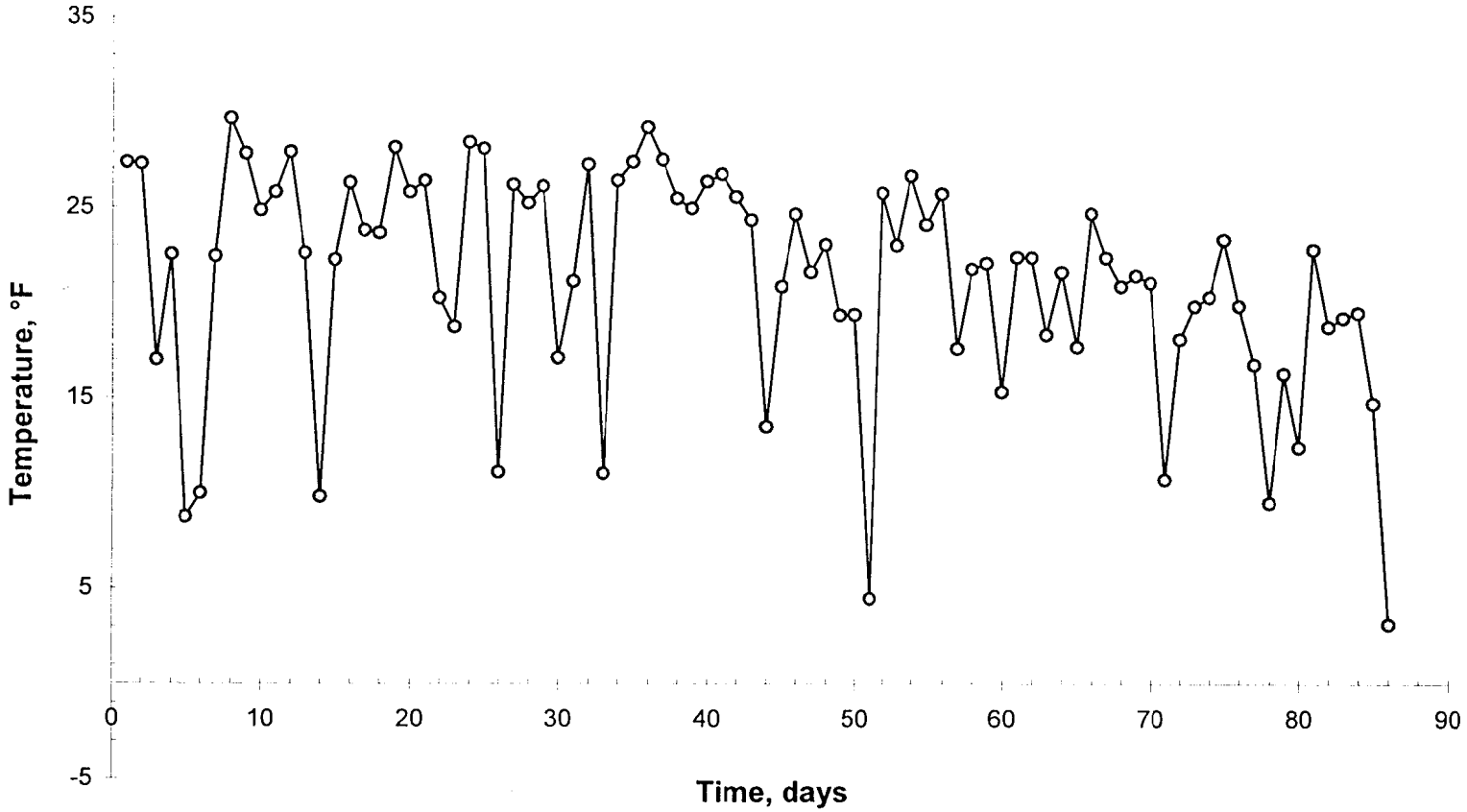


**Fig. 3.4 Summer Extreme Temperature Differentials**

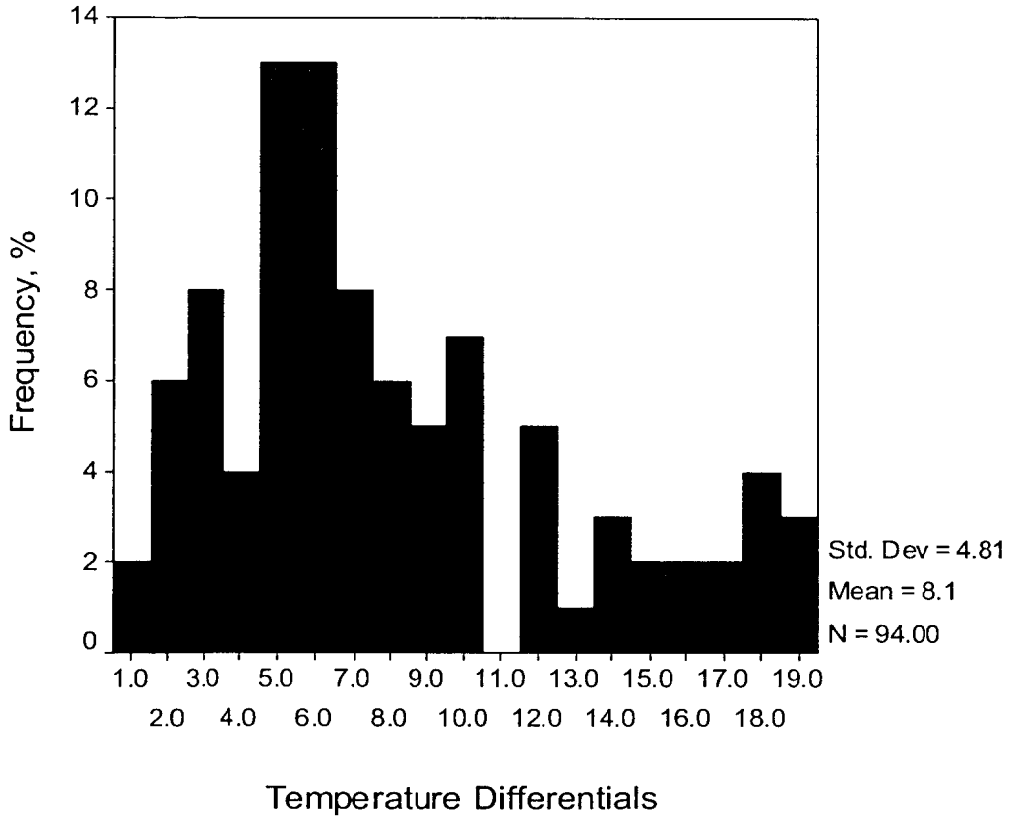


**Fig. 3.5 Fall Temperature Differential Frequency Occurrence**

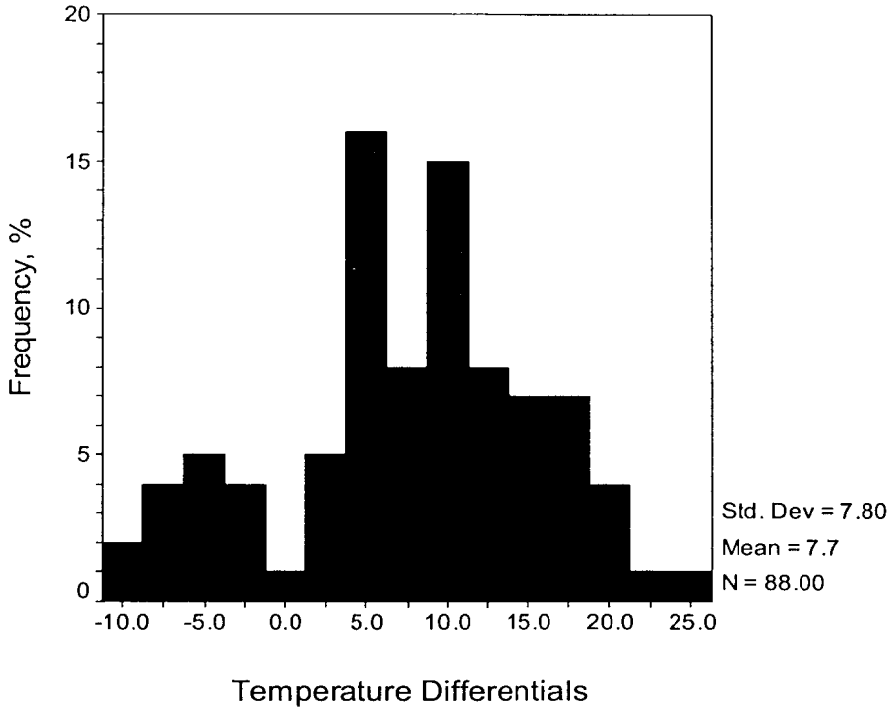


**Fig. 3.6 Winter Temperature Differential Frequency Occurrence**

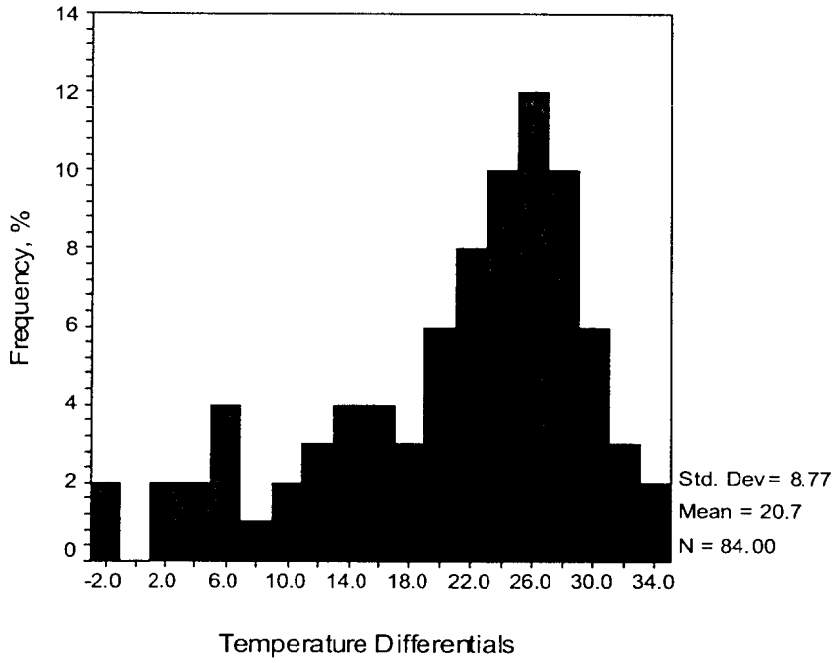


**Fig. 3.7 Spring Temperature Differential Frequency Occurrence**

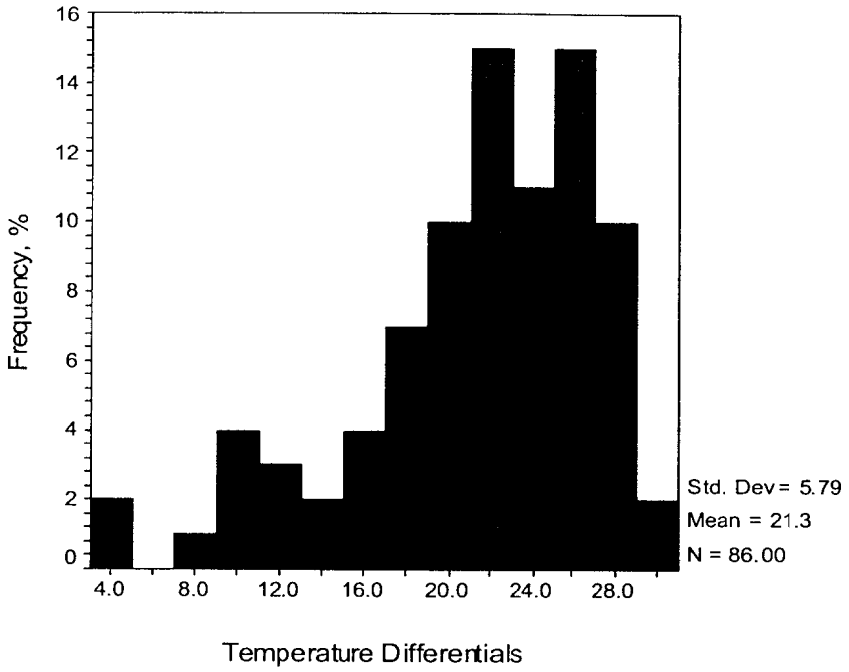


**Fig. 3.8 Summer Temperature Differential Frequency Occurrence**

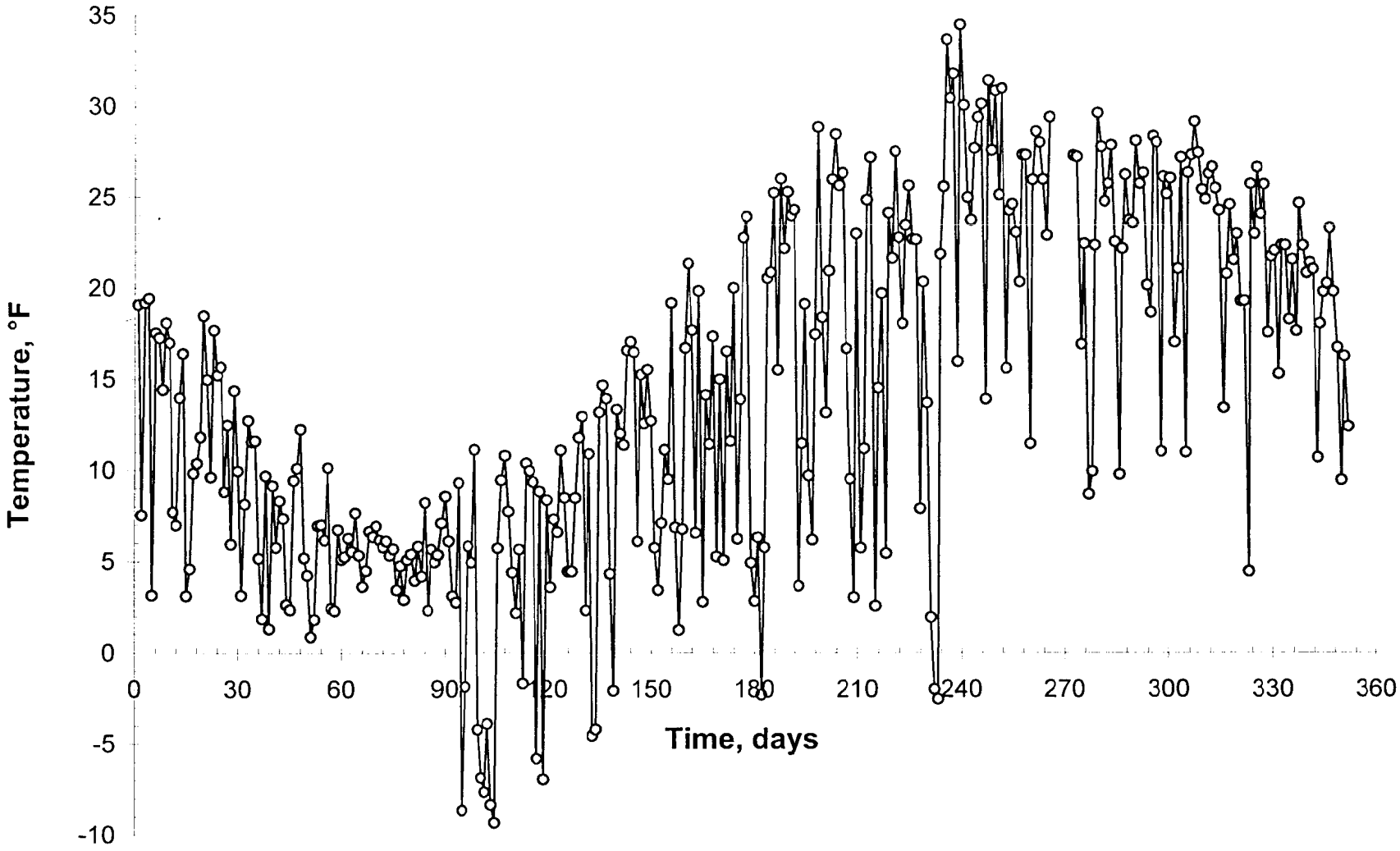


**Fig. 3.9 One-Year Extreme Temperature Differentials**

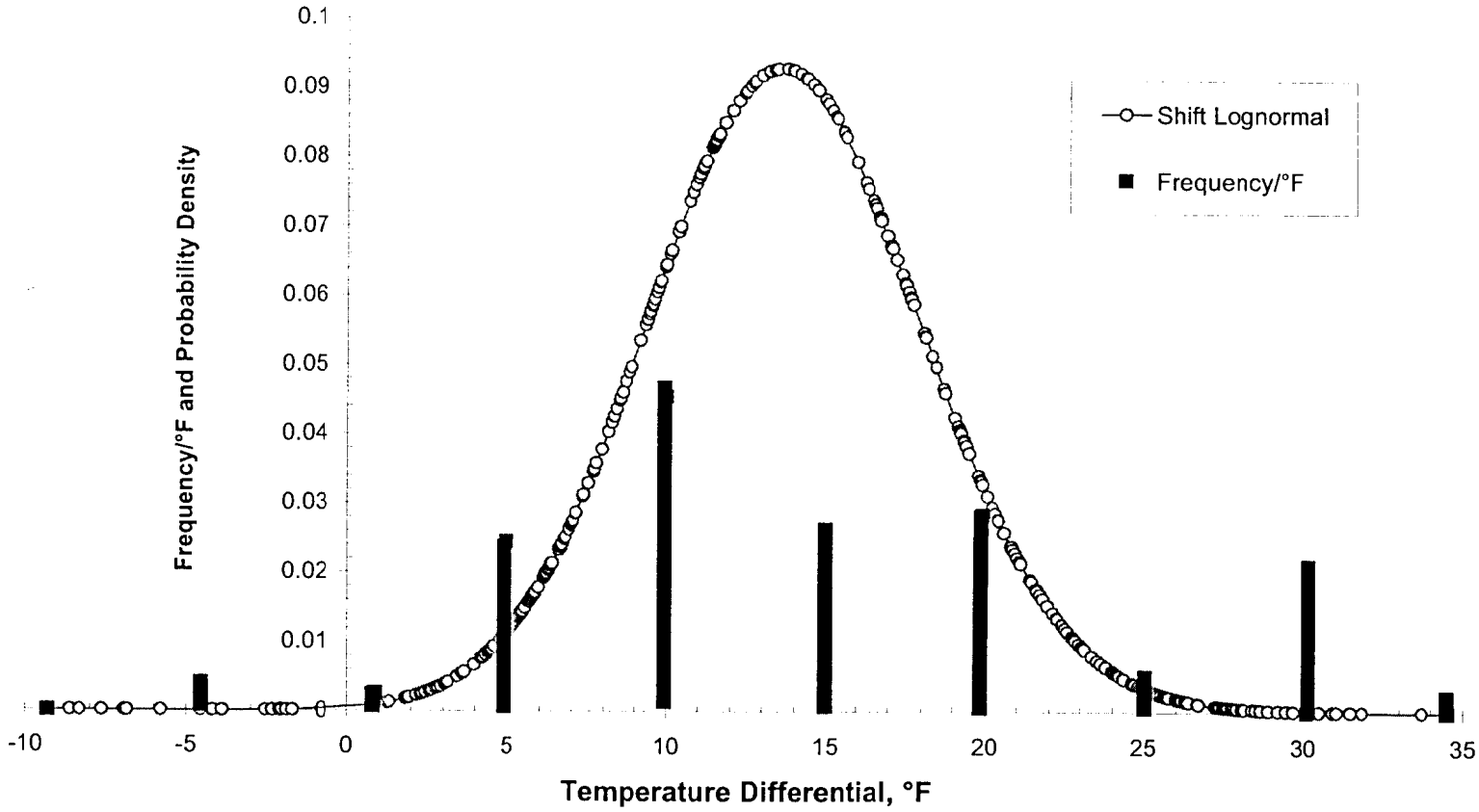


**Fig. 3.10 Shifted Lognormal Distribution Function and Measured Data Distribution at Main Span Closure Segment from 9/21/97 to 9/23/98**

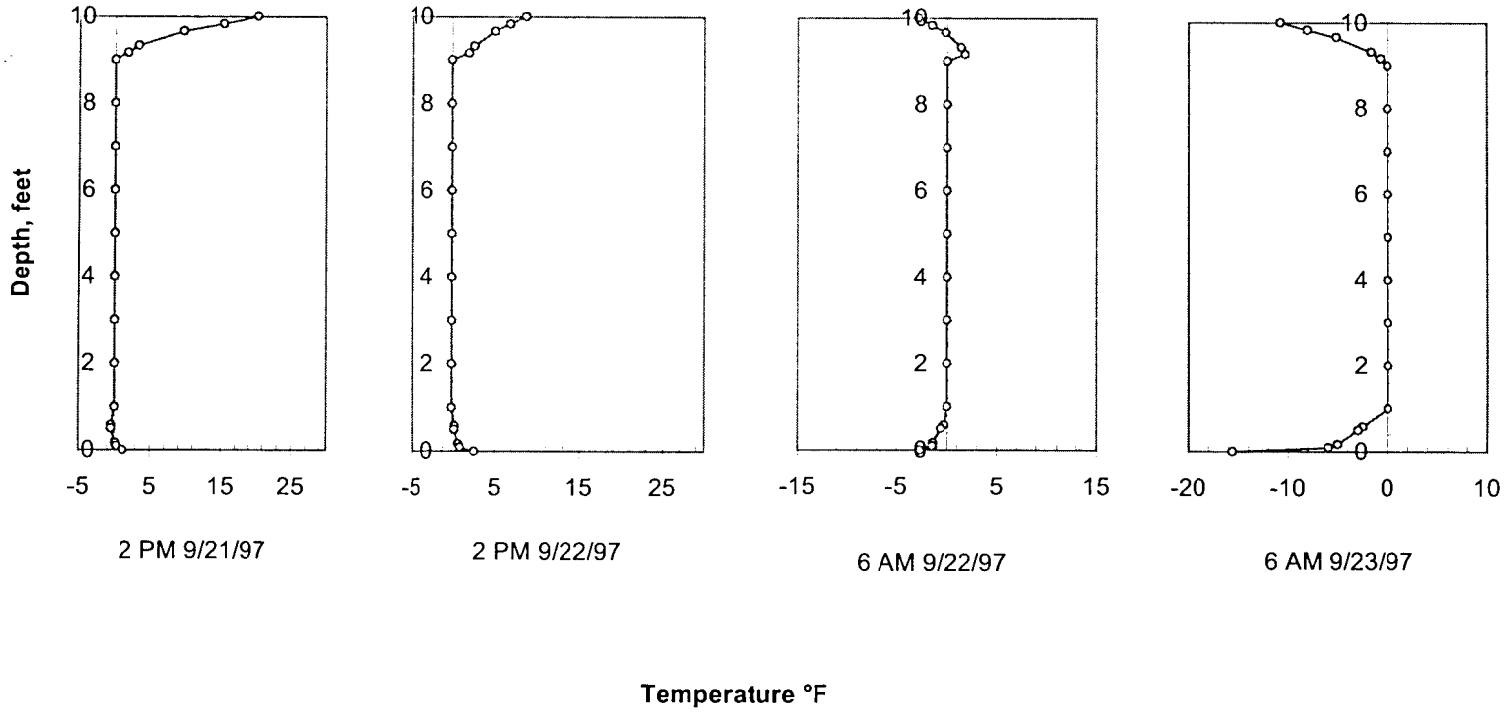


Fig. 3.11 Temperature Gradients for Fall at Main Span Closure Segment

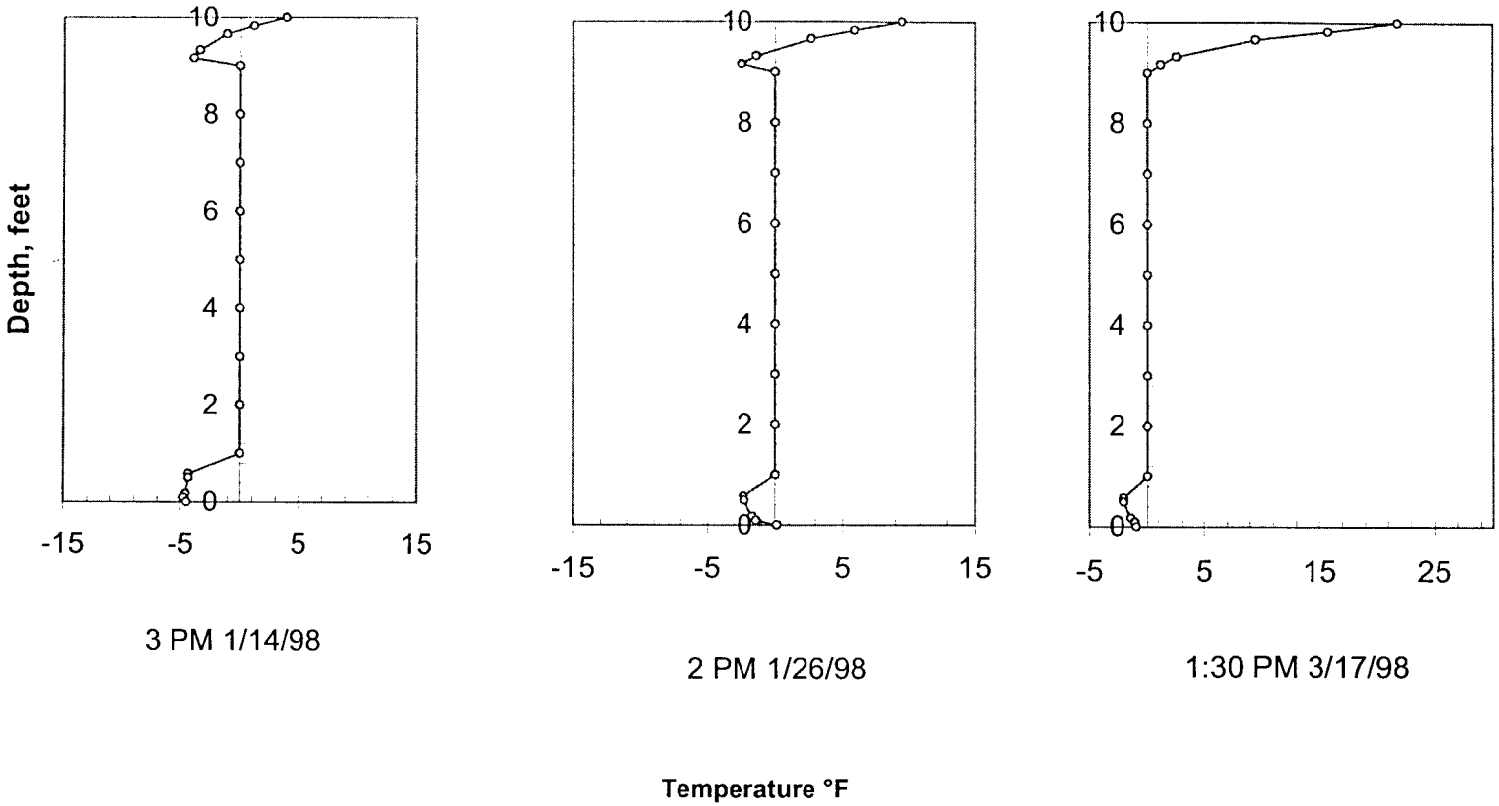


Fig. 3.12 Positive Temperature Gradients for Winter at Main Span Closure Segment

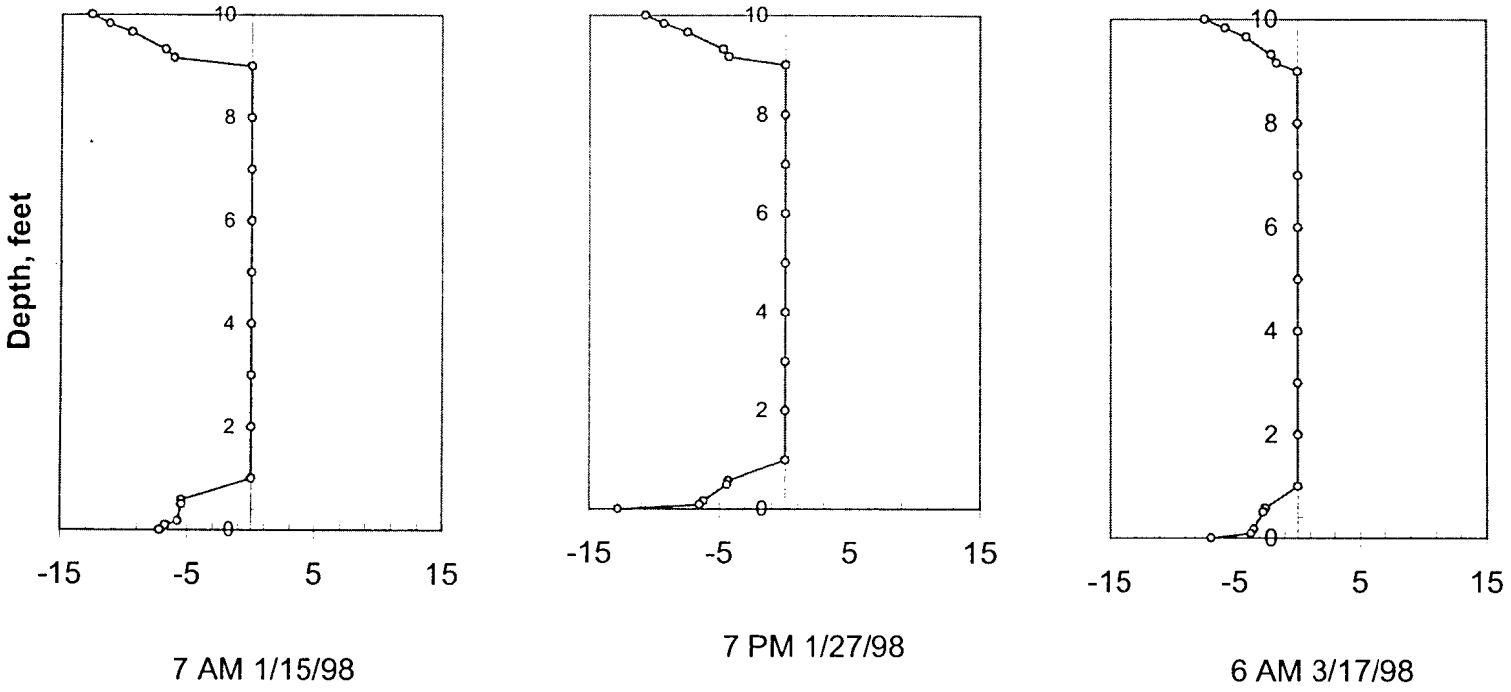


Fig. 3.13 Negative Temperature Gradients for Winter at Main Span Closure Segment

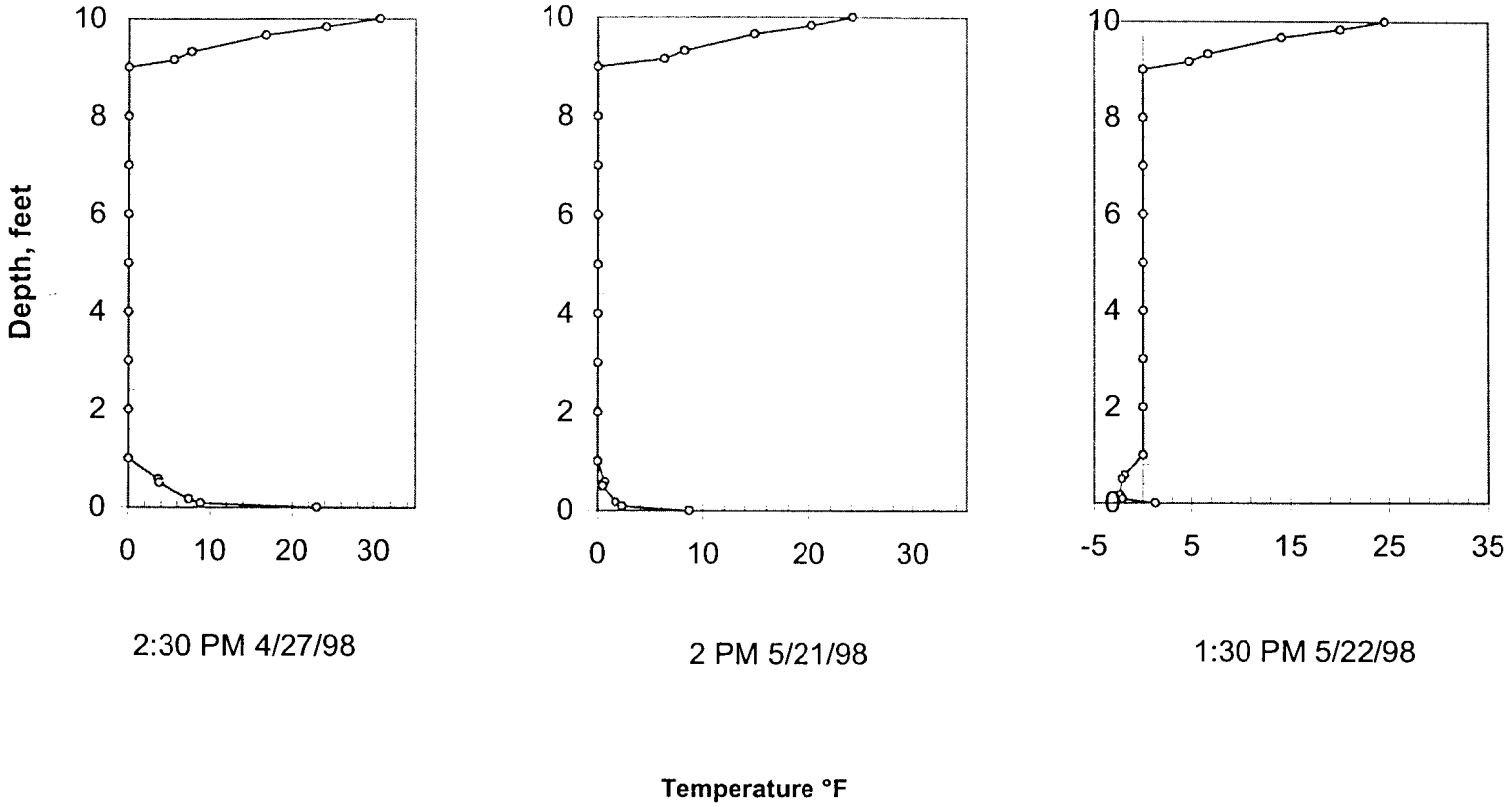


Fig. 3.14 Positive Temperature Gradients for Spring at Main Span Closure Segment

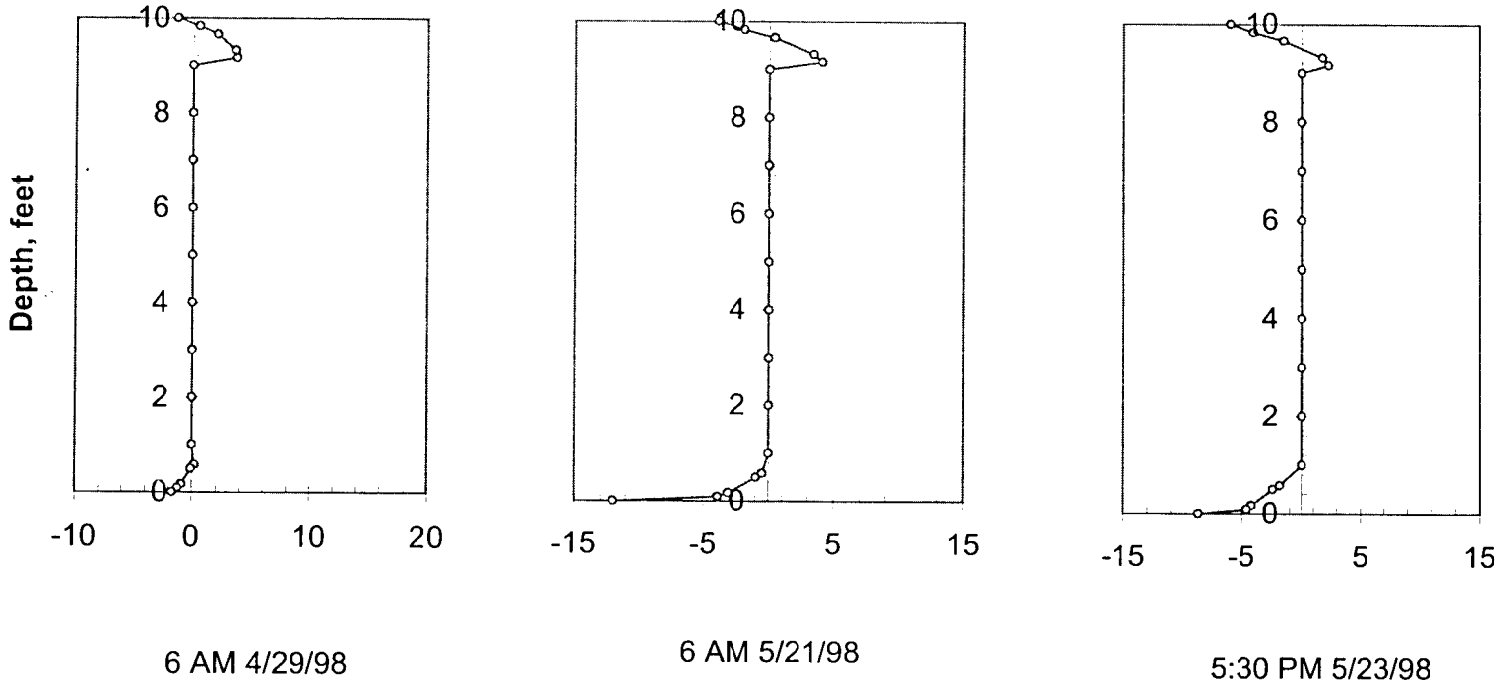


Fig. 3.15 Negative Temperature Gradients for Spring at Main Span Closure Segment

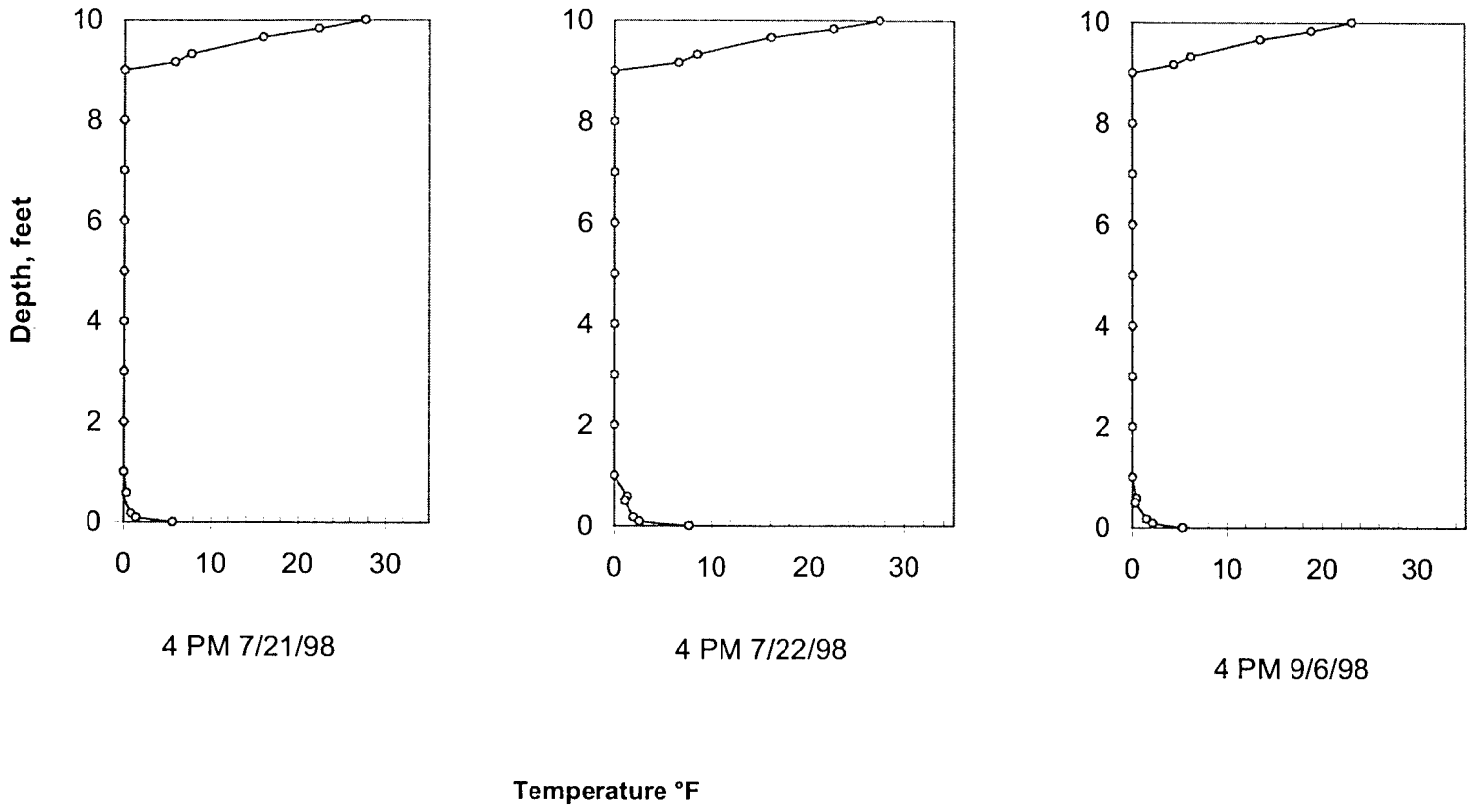


Fig. 3.16 Positive Temperature Gradients for Summer at Main Span Closure Segment

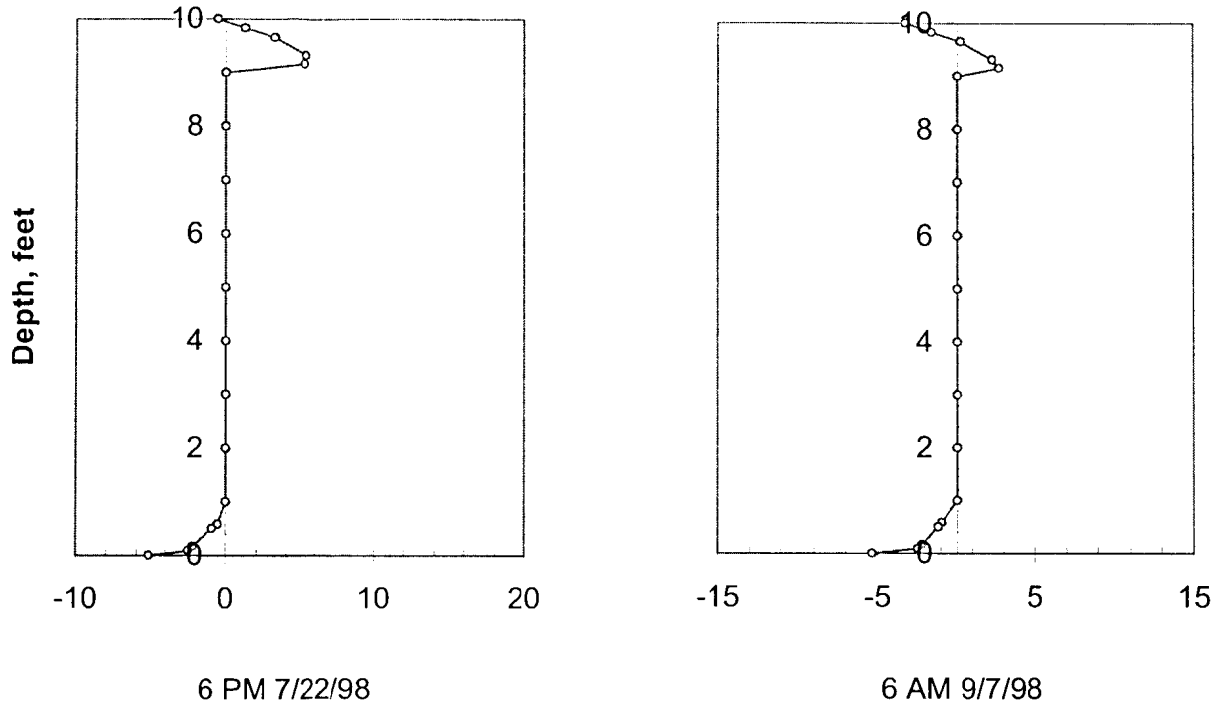


Fig. 3.17 Negative Temperature Gradients for Summer at Main Span Closure Segment

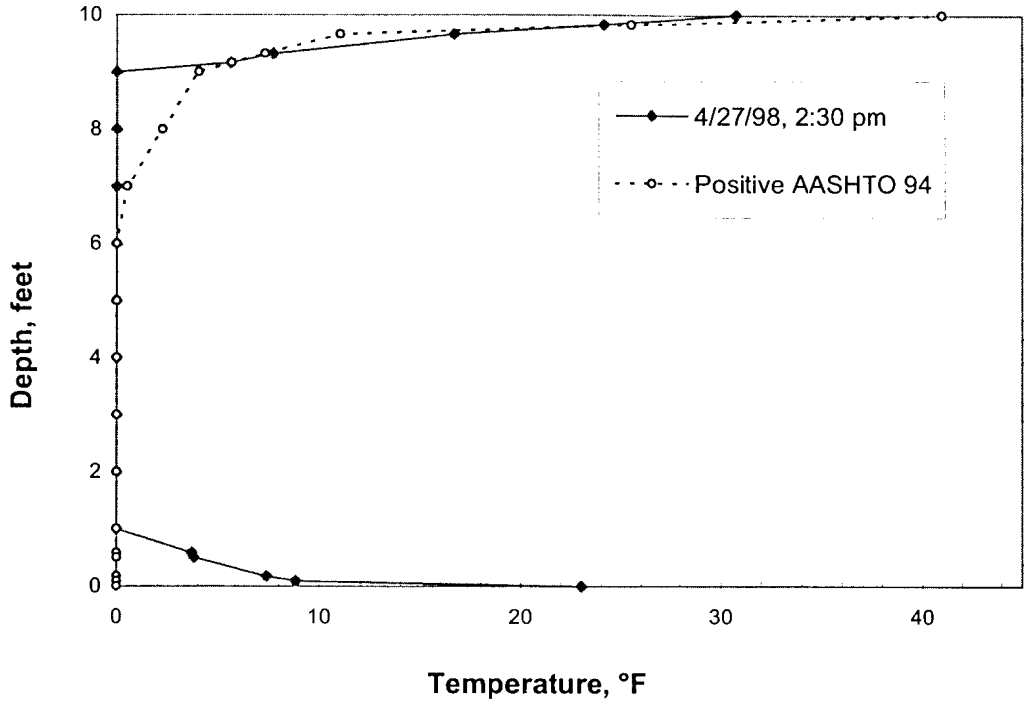


Fig. 3.18 Critical Positive Temperature Gradients for One Year Monitoring at Main Span Segment

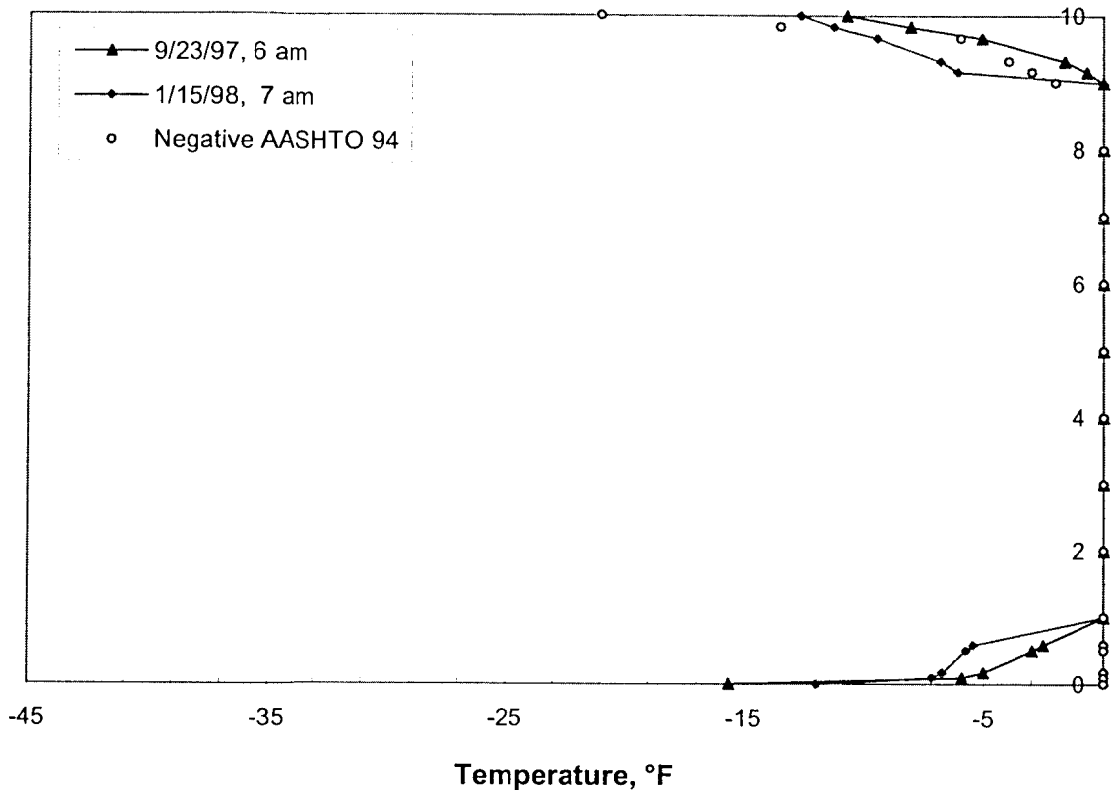


Fig. 3.19 Critical Negative Temperature Gradients of One Year Monitoring at Main Span Segment

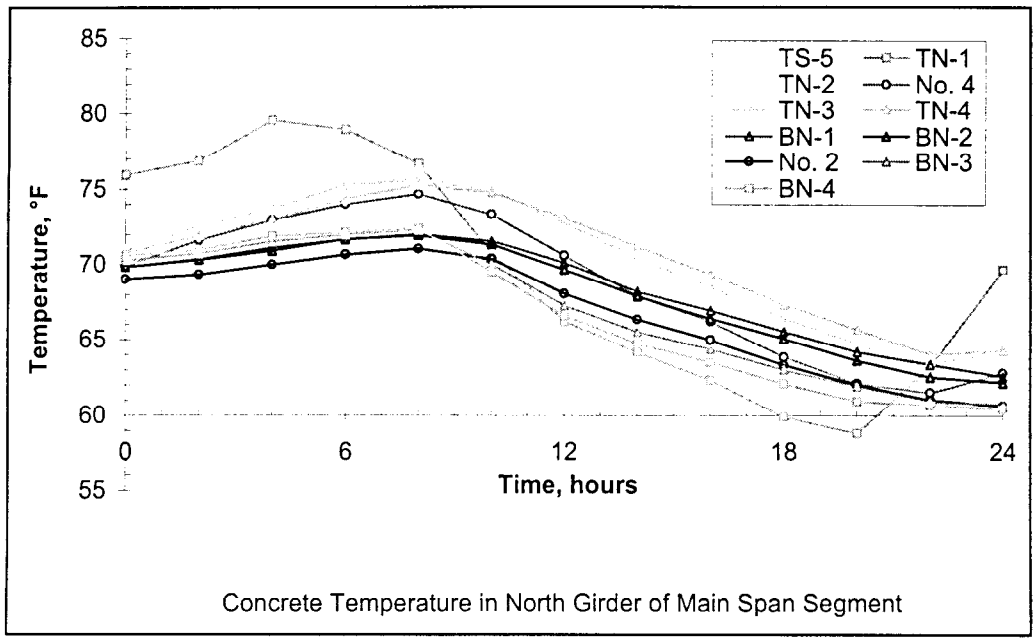


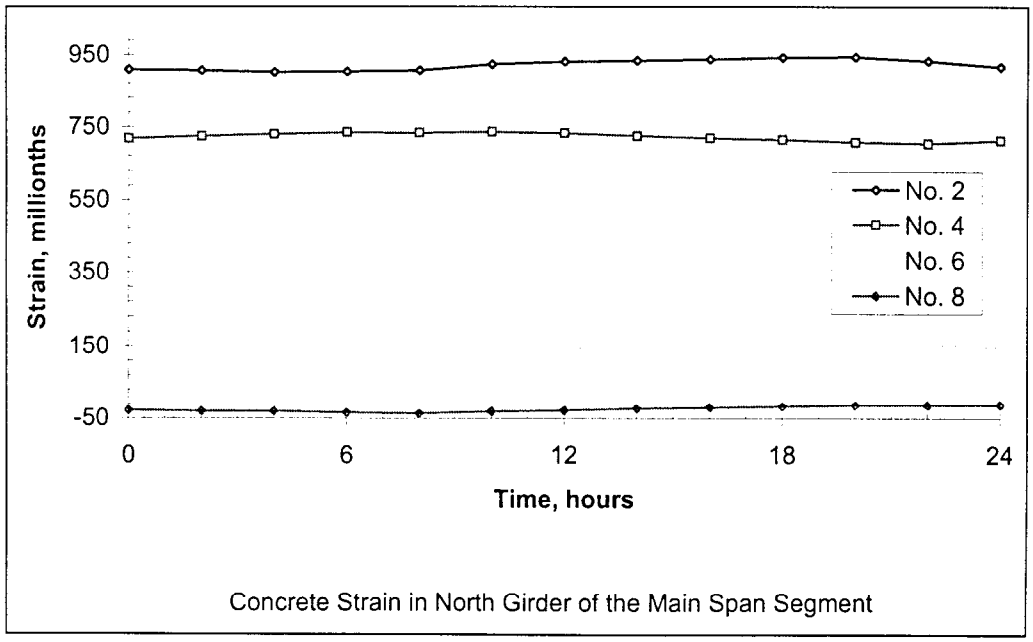


**Fig. 3.20 9/22-23/97 Temperature and Strain Variations from 12 pm - 12 pm**

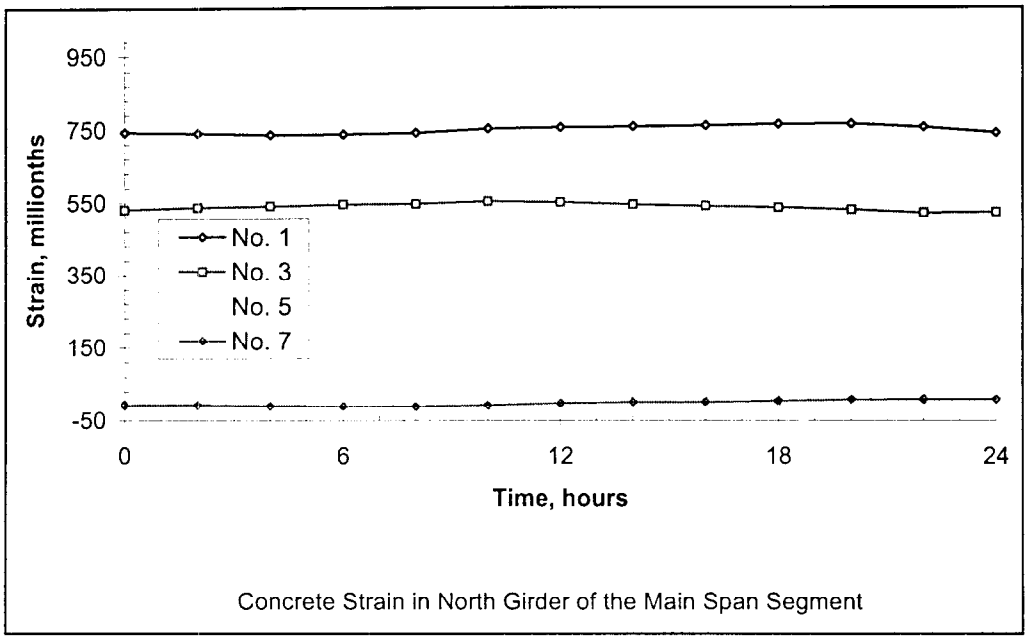


**Fig. 3.20 cont'd 9/22-23/97 Temperature and Strain Variations from 12 pm - 12 pm**

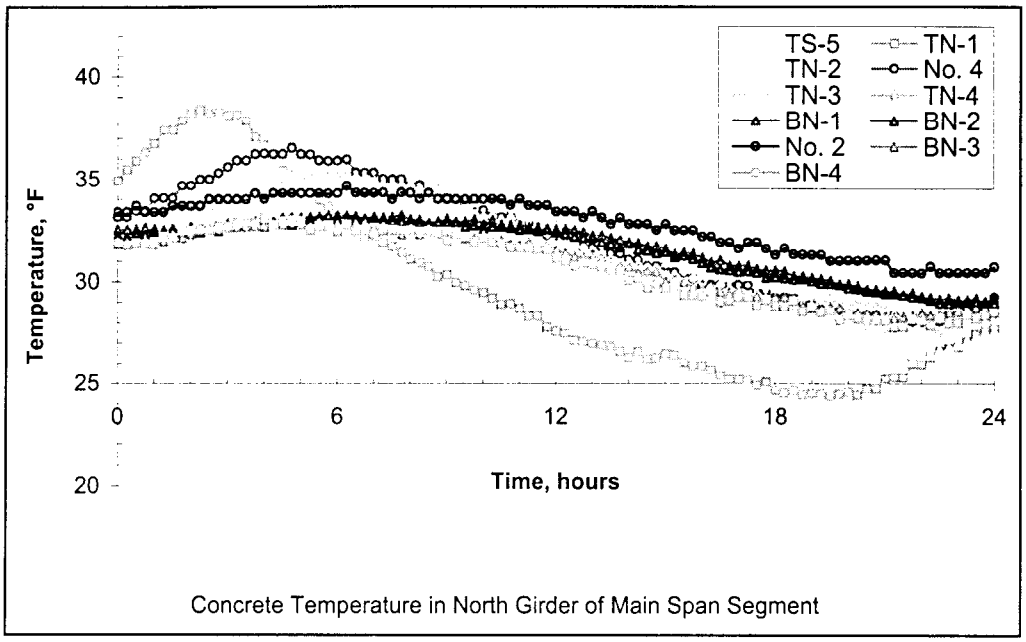


Concrete Temperature in North Girder of Main Span Segment

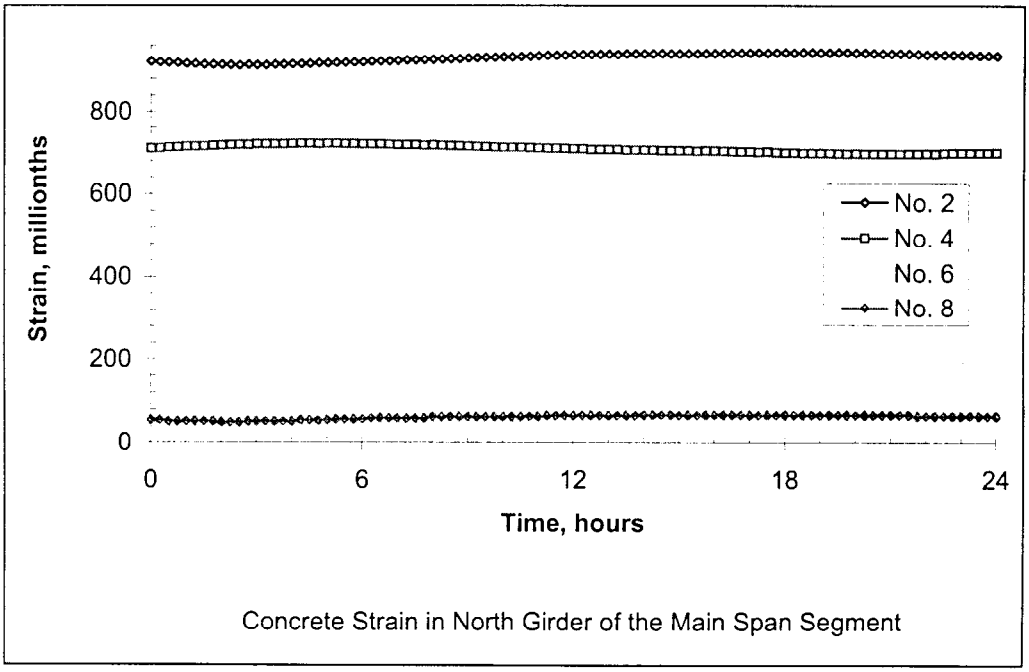


Concrete Strain in North Girder of the Main Span Segment

**Fig. 3.21 1/14-15/98 Temperature and Strain Variations from 12 pm - 12 pm**

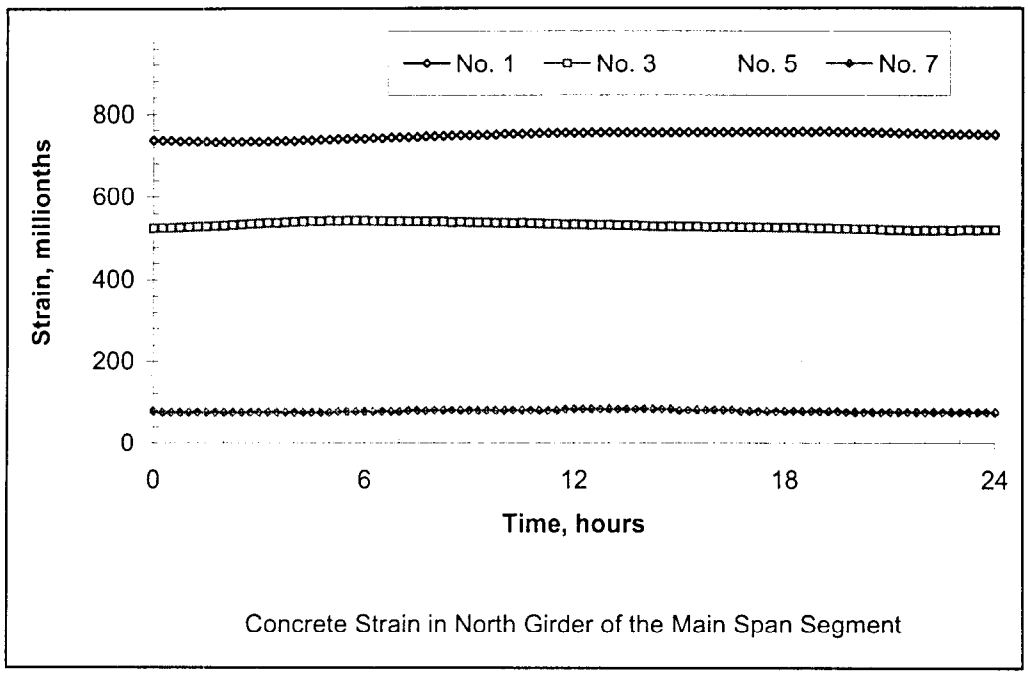


**Fig. 3.21 cont'd 1/14-15/98 Temperature and Strain Variations from 12 pm - 12 pm**

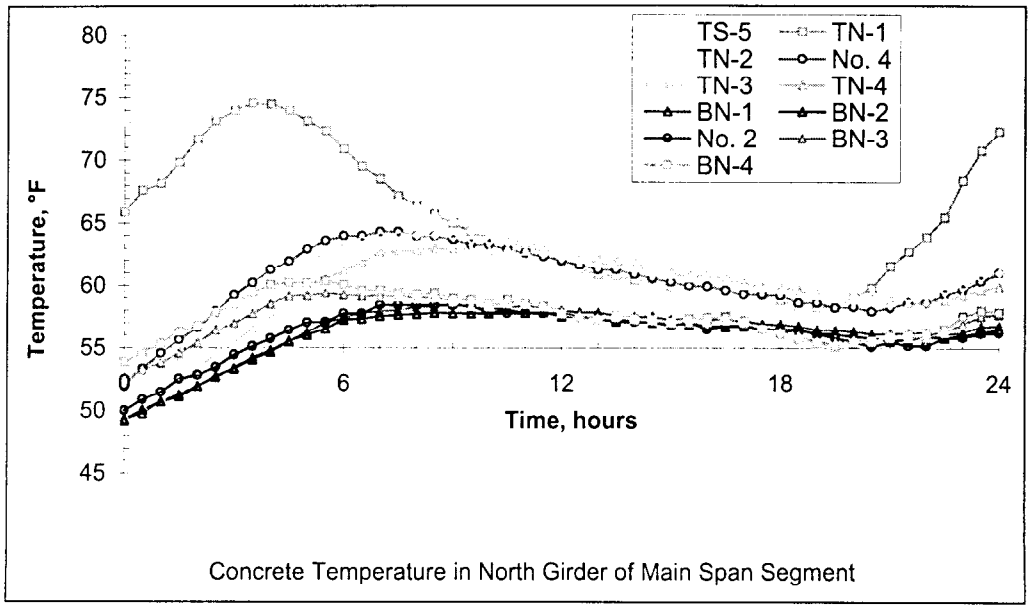


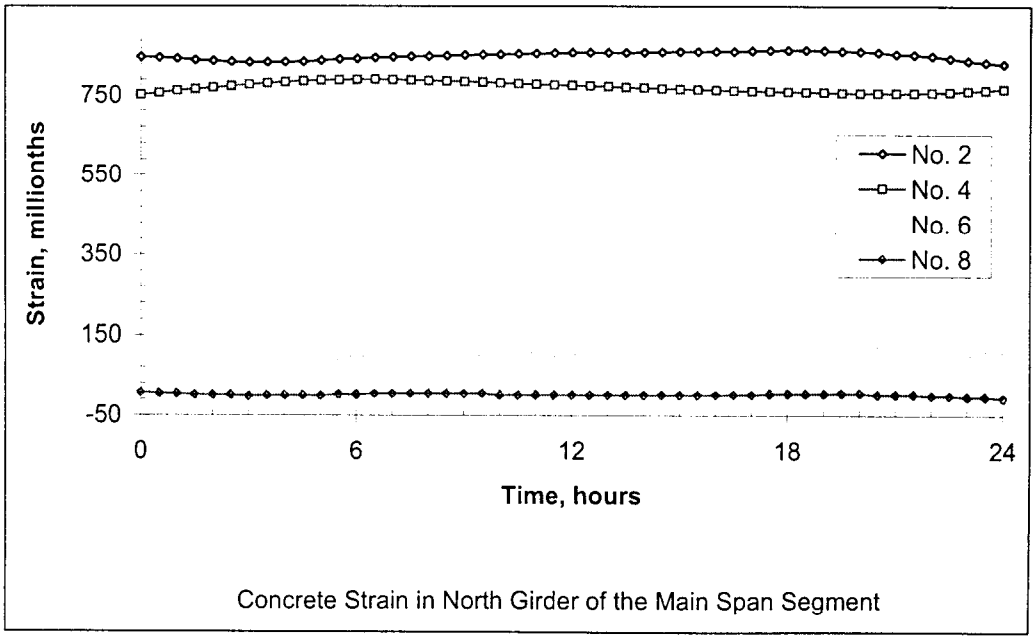


**Fig. 3.22 4/27-28/98 Strain Temperature Variations from 12 pm - 12 pm**

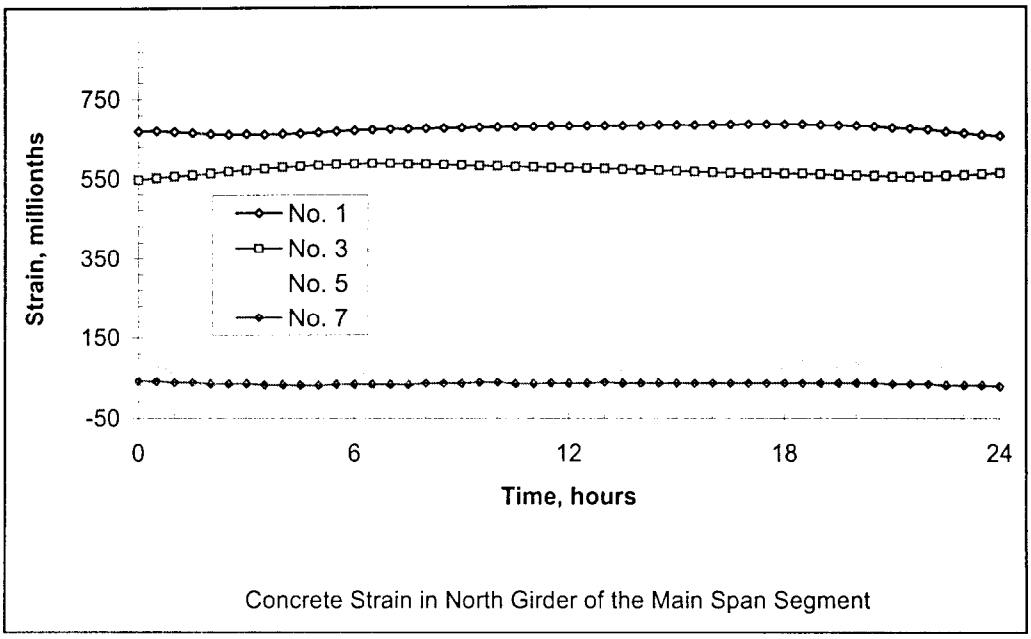


**Fig. 3.22 cont'd 4/27-28/98 Strain Temperature Variations from 12 pm - 12 pm**

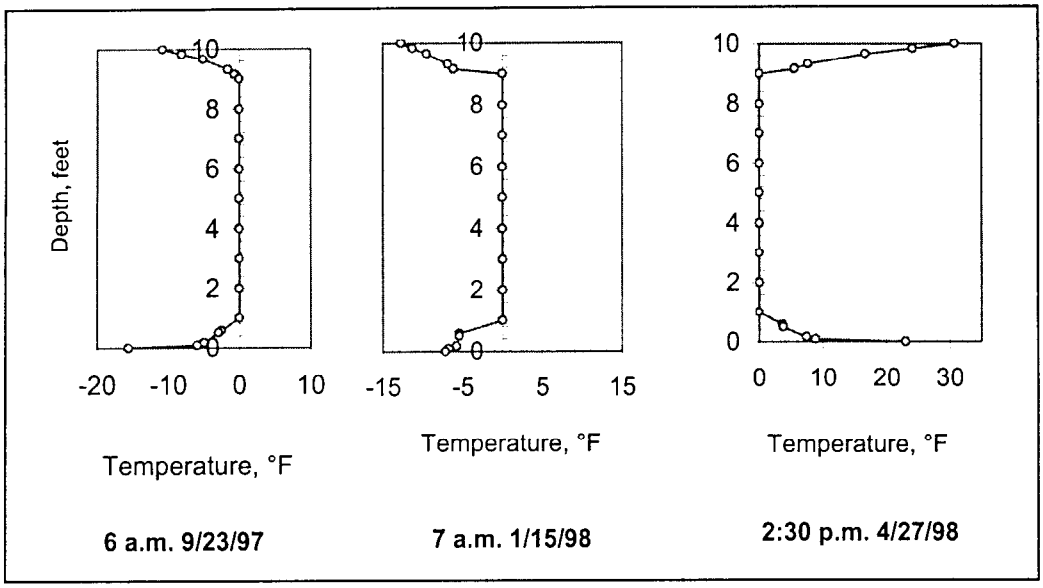


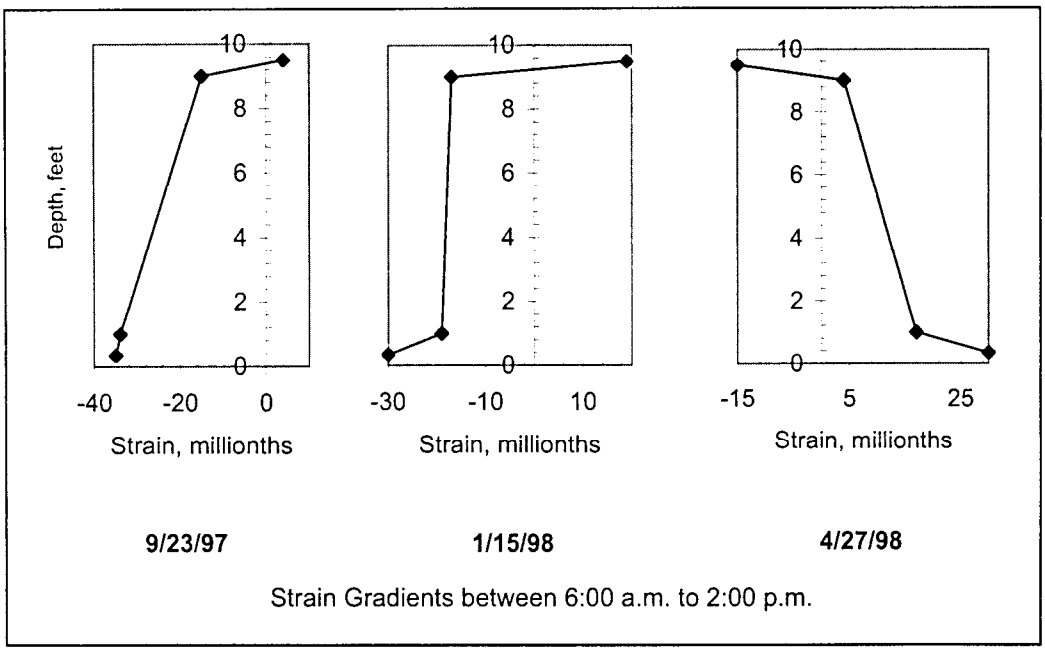


Fig. 3.23 Comparison of Vertical Temperature gradients and Strain Variations

# 4.0 STUDY OF CONCRETE SHRINKAGE AND CREEP STRAINS

## 4.1 Concrete Short Term Properties

Physical properties of the concrete used for the closure section of the bridge were determined by CTL (Weinman,1994). Concrete cylinders were cured in the same environment as the closure segment until one day prior to the testing which took place at CTL in Illinois. Results of the short-term tests, as presented in the CTL report, are summarized in Table 4.1.

**Table 4.1 - Short-Term Concrete Properties**

| Age, (days) | Compressive Strength, (psi) | Modulus of Elasticity, (ksi) | Coefficient of Thermal Expansion, ($10^{-6}$/°F |
|---|---|---|---|
| 3 | 4175 | 3200 | 6.45 |
| 7 | 5060 | 3250 | 5.67 |
| 28 | 6310 | 3445 | 6.93 |
| 90 | 5965 | 3500 | - |

## 4.2 Laboratory Shrinkage Tests

Long-term shrinkage tests were conducted in the CTL laboratory at a constant temperature of 73° F and a Relative Humidity of 50 %. The shrinkage tests began at concrete ages of 3, 7, and 28 days. It is noted that the concrete cylinders were covered, stored, and cured at the bridge site under the same environment as the closure segment. Hence, it can be assumed that drying started a day after they were removed from the forms. Results of the shrinkage tests as taken from the CTL report are shown in Table 4.2.

**Table 4.2 - Measured Shrinkage Strain of Concrete ($10^{-6}$)**

| Age in Days After Beginning of Test | Test Starting at 3 Days after Casting | Test Starting at 7 Days after Casting | Test Starting at 28 Days after Casting |
|---|---|---|---|
| 1 | 109 | 30 | 16 |
| 2 | 153 | 48 | 58 |
| 3 | 179 | 88 | 66 |
| 4 | 198 | 133 | 69 |
| 5 | 213 | 140 | 73 |
| 6 | 222 | 175 | 76 |
| 7 | 232 | 198 | 123 |
| 14 | - | 258 | 135 |
| 15 | 395 | - | - |
| 21 | 454 | 351 | 167 |
| 28 | 525 | 418 | 199 |
| 59 | 633 | 563 | 319 |
| 90 | - | 619 | 369 |
| 91 | 678 | - | - |
| 121 | 736 | - | - |
| 122 | - | 623 | 403 |
| 151 | 797 | - | - |
| 152 | - | 683 | 411 |
| 182 | - | 688 | 424 |
| 183 | 798 | - | - |
| 214 | 771 | 706 | 438 |
| 245 | 826 | 703 | 493 |
| 276 | 856 | 721 | 503 |
| 307 | - | 737 | 506 |

| | | | |
|---|---|---|---|
| 308 | 863 | - | - |
| 338 | 865 | - | - |
| 339 | - | 743 | 512 |
| 364 | - | - | 512 |
| 365 | 865 | 760 | - |

### 4.3 Analysis of Shrinkage Data

The relationship of shrinkage and time under constant temperature and humidity can be expressed by the square root of a hyperbolic function (Bazant et al.,1976). This relationship can be written as

$$\varepsilon_{sh}(t) = \varepsilon_{\infty}\left(\frac{t}{\tau_{sh} + t}\right)^{0.5} \tag{4.1}$$

where $\varepsilon_{\infty}$ = ultimate shrinkage strain

$\tau_{sh}$ = shrinkage square half-time

$\varepsilon_{sh}(t)$ = concrete shrinkage at time t

This relationship was used to curve fit the laboratory shrinkage data. Eq. (4.1) can be transformed into

$$\frac{1}{\varepsilon_{sh}^2} = \frac{\tau_{sh}}{\varepsilon_{\infty}^2}\cdot\frac{1}{t} + \frac{1}{\varepsilon_{\infty}^2} \tag{4.2}$$

The parameters $\varepsilon_\infty$ and $\tau_{sh}$ were found from a linear regression on the experimental data with the dependent variable taken as $1/(\varepsilon_{sh})^2$ and the independent variable as $1/t$. In this analysis $\varepsilon_{sh}$ is the measured shrinkage strain and t the duration of drying. As indicated in the literature, this approach is very sensitive to the values of shrinkage data obtained early in the testing history. If these readings are erratic, large differences can occur in the values for the constants $\varepsilon_\infty$ and $\tau_{sh}$. Consequently, to apply this approach to the laboratory data from the Jamestown Bridge early readings had to be omitted from the regression analysis.

For the three sets of shrinkage data the following constants were determined:

| **Start of Test (Days after specimen preparation)** | $\varepsilon_\infty$ | $\tau_{sh}$ | **First Data Point Considered** |
|---|---|---|---|
| 3 days | $946 \times 10^{-6}$ | 88 | 3 days |
| 7 days | $996 \times 10^{-6}$ | 171 | 7 days |
| 28 days | $522 \times 10^{-6}$ | 138 | 7 days |

Comparisons between calculated and measured shrinkage for the three sets of data are shown in Figs 4.1,4.2 and 4.3. Considering the sensitivity of this approach to initial test data, the figures indicate that Bazant's hyperbolic function, Eq. 4.1, is a good representation of the measured data.

## 4.4 Comparison of Measured Data and Shrinkage Predictions

There are various procedures to predict shrinkage in concrete structures. The Jamestown Bridge was designed for shrinkage according to the European Recommendations CEB-FIP Model Code 1978. A comparison is made between the measured lab data and a) the ACI Committee 209

recommendation, b) a modified version of CEB-FIP MC 1978 referred to as Improved CEB-FIP MC 78, and c) the latest European Recommendations CEB-FIP Model Code 90.

All guidelines predict concrete strains from the time that shrinkage started, $t_s$, which depends on the type of curing followed. In our case, specimens were cured on site under the prevailing conditions and it is assumed that shrinkage started one day after their preparation. Some assumptions of wet concrete properties had also to be made in the prediction equations, since this information is not available.

For shrinkage after 7 days in moist cured concrete the **ACI Committee 209** recommendation is the following:

$$(\varepsilon_{sh})_t = (\varepsilon_{sh})_u \frac{t - t_s}{35 + (t - t_s)} \tag{4.3}$$

where

$$(\varepsilon_{sh})_u = 780 \cdot \gamma_{sh} x 10^{-6} \tag{4.4}$$

and

$$\gamma_{sh} = \gamma_{cp} \cdot \gamma_{\lambda} \cdot \gamma_h \cdot \gamma_s \cdot \gamma_{\psi} \cdot \gamma_c \cdot \gamma_{\alpha} \tag{4.5}$$

where t = age of concrete at start of test, days

$t_s$ = age of concrete when shrinkage starts, typically immediately after the initial wet curing, days (assumed as 1)

$(\varepsilon_{sh})_t$ = concrete shrinkage strain at time t,

$(\varepsilon_{sh})_u$ = ultimate shrinkage strain,

$\gamma_{sh}$ = correction factor

$\gamma_{cp}$ = curing duration factor (for one day curing $\gamma_{cp}$=1.2)

$\gamma_\lambda$ = relative humidity factor ($\gamma_\lambda$=.9 for RH=50%)

$\gamma_h$ = size factor ( 1.0 for a 6 x 12 cylinder)

$\gamma_s$ = slump factor (assumed as 1.07)

$\gamma_\psi$ = fine aggregate factor ( assumed as 1.0)

$\gamma_c$ = cement factor ( assumed as 1.0)

$\gamma_\alpha$ = air content factor ( assumed as 1.0)

For the Jamestown bridge data, Eq. 4.3 reduces to:

$$(\varepsilon_{sh})_{t-t_s} = 901x10^{-6}\frac{t-t_s}{35+(t-t_s)} \tag{4.6}$$

Note that for shrinkage considered from a time different than the end of wet curing a differential approach can be followed. For example, to compare the ACI 209 provisions with the test data the following equation can be used:

$$(\varepsilon_{sh})_{t-t_o} = (\varepsilon_{sh})_{t-t_s} - (\varepsilon_{sh})_{t_o-t_s} \tag{4.7}$$

where $(\varepsilon_{sh})_{t\text{-}to}$ is the shrinkage strain of the specimens at concrete age t when measurements were initiated at time $t_o$. For the three sets of the Jamestown bridge data $t_o$=3, 7, and 28, and $t_s$=1.

The **improved CEB-FIP MC 78** approach provides the following relation for shrinkage, (Muller and Hilsdorf, 1990):

$$\varepsilon_{cs}(t,t_s,t_o) = \varepsilon_{s1}\cdot\left[\beta_s(t-t_s)-\beta_s(t_o-t_s)\right] \tag{4.8}$$

where $\varepsilon_{cs}$ = concrete shrinkage;

$\varepsilon_{s1}$ = basic shrinkage coefficient;

$\beta_s$ = coefficient describing the development of the shrinkage with time;

t = age of concrete;

$t_s$ = age of concrete at beginning of shrinkage;

$t_o$ = age of concrete at the moment from which the influence of shrinkage is considered.

The basic shrinkage coefficient $\varepsilon_{s1}$ is given by:

$$\begin{aligned} \varepsilon_{s1} &= -0.00069 \cdot \beta_{s1} \cdot \beta_{s2} \cdot \beta_{sH} \qquad \text{for} \quad 40 \le RH < 99\% \\ \varepsilon_{s1} &= +0.00011 \cdot \beta_{s1} \cdot \beta_{s2} \qquad \text{for} \quad RH \ge 99\% \end{aligned} \tag{4.9}$$

where RH is the ambient relative humidity (50% for our data). It is noted that the case of RH≥99% corresponds to submersion and the strain changes sign (expansion instead of shrinkage). The coefficients $\beta_{s1}$, $\beta_{s2}$, $\beta_{SH}$ are given by:

$\beta_{s1}$ = 0.85 for stiff consistency of the fresh concrete

= 1.00 for plastic consistency

= 1.15 for semi-fluid consistency

$\beta_{s2}$ = 1.0 for slowly, normal, or rapid hardening cement

= 1.2 for rapid hardening high strength cement

$$\beta_{SH} = 1 - \left(\frac{RH}{100}\right)^3 \tag{4.10}$$

The development of shrinkage with time is modeled with the function $\beta_s$ given by:

$$\beta_s = \left[ \frac{\bar{t}}{0.018 \cdot h_o^2 + \bar{t}} \right]^{0.6} \tag{4.11}$$

where $\bar{t} = t - t_s$ or $\bar{t} = t_o - t_s$

$h_o = (2A_c)/u$ (mm)

$A_c$ = area of the concrete section

u = perimeter in contact with the atmosphere.

For the Jamestown bridge data Eq. 4.8 becomes:

$$\varepsilon_{cs}(t, t_s, t_o) = -603.75 \cdot 10^{-6} \left[ \left( \frac{t - t_s}{104.516 + t - t_s} \right)^{0.6} - \left( \frac{t_o - t_s}{104.516 + t_o - t_s} \right)^{0.6} \right] \tag{4.12}$$

where $t_s$=1, and $t_o$=3,7,28 for the three data sets.

The latest **CEB-FIP MC 90** recommendation provides the following equation to calculate shrinkage:

$$\varepsilon_{cs}(t, t_s) = \varepsilon_{cso} \cdot \beta_s(t - t_s) \tag{4.13}$$

where $\varepsilon_{cso}$ = basic shrinkage coefficient, $\beta_s$=coefficient that describes the development of shrinkage with time, t=age of concrete in days, $t_s$=age of concrete at the beginning of shrinkage. The basic shrinkage coefficient is given by:

$$\varepsilon_{cso} = \varepsilon_s(f_{cm}) \cdot \beta_{RH} \tag{4.14}$$

with

$$\varepsilon_s(f_{cm}) = \left[160 + \beta_{sc}(90 - f_{cm})\right] \cdot 10^{-6} \tag{4.15}$$

where $f_{cm}$ is the mean compressive strength of concrete at 28 days (in Mpa), and $\beta_{sc}$ is a coefficient that depends on the type of cement according to:

$\beta_{sc}$ = 4 for slowly hardening cement

= 5 for normal or rapid hardening cement

= 8 for rapid hardening high strength cement

The coefficient $\beta_{RH}$ accounts for the effect of relative humidity, RH. For $40\% \leq RH \leq 99\%$ it is given by:

$$\beta_{RH} = -1.55 \cdot \left[1 - \left(\frac{RH}{100}\right)^3\right] \tag{4.16}$$

The development of shrinkage with time is given by:

$$\beta_s(t - t_s) = \left(\frac{t - t_s}{0.035 \cdot h_o^2 + t - t_s}\right)^{0.5} \tag{4.17}$$

with $h_o=(2A_c/u)$, $A_c$=area of cross section, and u=the perimeter of the cross section exposed to the atmosphere. Note that the units of $u_o$ in Eq. 4.17 are mm. For shrinkage considered from a time different than the end of wet curing, a differential approach can be followed. For example, to compare the CEB-FIP MC 90 provisions with the test data the following equation can be used:

$$\varepsilon_{cs}(t,t_s t_o) = (\varepsilon_{cs})_{t-t_s} - (\varepsilon_{cs})_{t_o - t_s} \tag{4.18}$$

where $(\varepsilon_{sh})_{t\text{-}to}$ is the shrinkage strain of the specimens at concrete age t given that measurements initiated at time $t_0$. For the data of Jamestown bridge, Eq. 4.18 becomes:

$$\varepsilon_{cs}(t,t_s,t_o) = 532.28 \cdot \left[ \left( \frac{t - t_s}{203.23 + t - t_s} \right)^{0.5} - \left( \frac{t_o - t_s}{203.23 + t_o - t_s} \right)^{0.5} \right] \tag{4.19}$$

The measured shrinkage (hyperbolic function) for the three data sets is compared with the ACI Committee 209 results, the Improved CEB-FIP MC 78 predictions, and the CEB-FIP MC 90 results in Figs. 4.4, 4.5, and 4.6. In all cases there is a good agreement between the ACI Committee 209 results and the Jamestown Bridge shrinkage data. The two European model codes (Improved MC 78 and MC 90) predict shrinkage strains that are in general close to each other but lower than the measured and ACI results. This may be due to different materials and conditions in Europe which may have influenced the predictive formulas. The relative positions of all curves are the same in each of the figures. The agreement between all methods is better for the 28 day test data. This may be due to the fact that a good amount of shrinkage already took place before measurements were begun. In all three cases the Jamestown bridge test data is higher than the predicted shrinkage.

## 4.6 Laboratory Creep Tests

Long-term creep tests were conducted by CTL during phase one of this research at a constant temperature of 73°F and a relative humidity of 50%. Three sets of tests were conducted corresponding to the three sets of shrinkage tests. For the first test, which started 3 days after casting, specimens were loaded to 1560 psi. The second test started 7 days after casting with specimens loaded to 1790 psi. The third test was initiated 28 days after casting with specimens loaded to a stress level of 2480 psi. Tests were conducted at different stress levels since creep depends on the applied stress and an effort was made to use stress levels which would approximate the stresses expected in the real structure. It is noted that creep depends on the stress level. Creep strains were calculated as the difference between the strain readings of the creep specimens and the strain readings of the shrinkage specimens. Specific creep was determined as the amount of concrete creep strain per unit stress. Results of the creep tests, as taken from the CTL report (Weinman1994), are shown in Table 4.3.

## 4.7 Comparison of Measured Data and Creep Predictions

Creep estimation in concrete structures is still under development. Various empirical creep models exist which try to describe the behavior of concrete at a macro-scale level. The Jamestown Bridge was designed for creep according to the European Recommendations CEB-FIP Model Code 1978. A comparison is made between the measured laboratory data and a) the ACI Committee 209 recommendation, b) a modified version of CEB-FIP MC 1978 referred to as Improved CEB-FIP MC 78, and c) the latest European Recommendation CEB-FIP Model Code 90. The quantity to be determined with these procedures and compared with the laboratory data is the specific creep, $\delta_t$, (also known as unit creep), which is defined as the creep per unit stress. All three recommendations

provide procedures for calculating the creep coefficient which is defined as the ratio of the creep strain over the elastic strain.

**Table 4.3 - Measured Creep Strain of Concrete**

| Age After Loading (days) | Test Starting at 3 Days after Casting | | Test Starting at 7 Days after Casting | | Test Starting at 28 Days after Casting | |
|---|---|---|---|---|---|---|
| | Creep Strain ($10^{-6}$) | Specific Creep ($10^{-6}$/psi ) | Creep Strain ($10^{-6}$) | Specific Creep ($10^{-6}$/psi ) | Creep Strain ($10^{-6}$) | Specific Creep ($10^{-6}$/psi ) |
| 1 | 173 | 0.111 | 264 | 0.148 | 193 | 0.078 |
| 2 | 269 | 0.173 | 404 | 0.226 | 293 | 0.118 |
| 3 | 336 | 0.215 | 463 | 0.259 | 314 | 0.127 |
| 4 | 351 | 0.225 | 475 | 0.265 | 374 | 0.151 |
| 5 | 399 | 0.256 | 506 | 0.283 | 408 | 0.165 |
| 6 | 433 | 0.278 | 510 | 0.285 | 443 | 0.179 |
| 7 | 478 | 0.307 | 534 | 0.298 | 466 | 0.188 |
| 14 | - | - | 633 | 0.354 | 568 | 0.229 |
| 15 | 571 | 0.307 | - | - | - | - |
| 21 | 631 | 0.404 | 727 | 0.406 | 644 | 0.260 |
| 28 | 688 | 0.441 | 811 | 0.453 | 736 | 0.297 |
| 59 | 837 | 0.536 | 971 | 0.542 | 834 | 0.336 |
| 90 | - | - | 1067 | 0.596 | 941 | 0.379 |
| 91 | 941 | 0.603 | - | - | - | - |
| 121 | 982 | 0.629 | - | - | - | - |
| 122 | - | - | 1116 | 0.623 | 984 | 0.397 |
| 151 | 1001 | 0.642 | - | - | - | - |

| Age After Loading (days) | Test Starting at 3 Days after Casting | | Test Starting at 7 Days after Casting | | Test Starting at 28 Days after Casting | |
|---|---|---|---|---|---|---|
| | Creep Strain ($10^{-6}$) | Specific Creep ($10^{-6}$/psi ) | Creep Strain ($10^{-6}$) | Specific Creep ($10^{-6}$/psi ) | Creep Strain ($10^{-6}$) | Specific Creep ($10^{-6}$/psi ) |
| 152 | - | - | 1134 | 0.634 | 1071 | 0.432 |
| 182 | - | - | 1193 | 0.667 | 1101 | 0.444 |
| 183 | 1023 | 0.656 | - | - | - | - |
| 214 | 1079 | 0.692 | 1216 | 0.679 | 1130 | 0.456 |
| 245 | 1082 | 0.694 | 1230 | 0.387 | 1188 | 0.479 |
| 276 | 1102 | 0.706 | 1314 | 0.734 | 1197 | 0.483 |
| 307 | - | - | 1320 | 0.737 | 1200 | 0.484 |
| 308 | 1102 | 0.706 | - | - | - | - |
| 338 | 1148 | 0.736 | - | - | - | - |
| 339 | - | - | 1318 | 0.736 | 1268 | 0.511 |
| 364 | - | - | - | - | 1288 | 0.519 |
| 365 | 1159 | 0.743 | 1315 | 0.735 | - | - |

Note that the specific creep, $\delta_t$, and the creep coefficient, $\nu_t$, are related by:

$$\delta_t = \frac{\nu_t}{E_{ci}} \tag{4.20}$$

where $E_{ci}$ is the initial modulus of elasticity of concrete given in Table 4.1.

According to the **ACI Committee 209** recommendation, the creep coefficient for loading at 7 days for moist cured concrete is given by:

$$\nu_t = \frac{t^{0.6}}{10 + t^{0.6}} \nu_u \tag{4.21}$$

where t = time in days after loading,

$\nu_t$ = concrete creep coefficient at time t,

$\nu_u$ = ultimate creep coefficient

The ultimate creep coefficient is given by

$$\nu_u = 2.35\gamma_c \tag{4.22}$$

where $\gamma_c$ is a correction factor given by:

$$\gamma_c = (\gamma_{la})(\gamma_\lambda)(\gamma_h)(\gamma_s)(\gamma_\psi)(\gamma_\alpha) \tag{4.23}$$

The various factors entering Eq. 4.23 relate to variations from the standard conditions assumed in Eq. 4.21 and are described as follows:

$\gamma_{la}$ = loading age factor, to accommodate for loading at an age different than 7 days. For moist cured concrete it is given as $\gamma_{la} = 1.25\ (t_{la})^{-0.118}$ where $t_{la}$ is the loading age in days. For the Jamestown bridge data, loading took place at 3, 7 and 28 days and the

corresponding values of $\gamma_{la}$ are 1.098, 0.994, and 0.8436.

$\gamma_\lambda$ = ambient relative humidity factor given as $\gamma_\lambda = 1.27 - 0.0067\lambda$, for $\lambda > 40$ with $\lambda$ the relative humidity in percent. For the Jamestown bridge data, $\lambda$=50% and $\gamma_\lambda$=0.935,

$\gamma_h$ = average thickness factor (1.0 for an average thickness of 6 in),

$\gamma_s$ = slump factor ( assumed as 1.0),

$\gamma_\psi$ = fine aggregate factor ( assumed as 1.0),

$\gamma_a$ = air content factor (assumed as 1.0).

Using all above values, Eq. 4.21 reduces into Eqs. 4.25, 4.26, and 4.27 for loading at 3, 7, and 28 days respectively.

$$v_t = 2.413\frac{t^{0.6}}{10 + t^{0.6}} \tag{4.24}$$

$$v_t = 2.183\frac{t^{0.6}}{10 + t^{0.6}} \tag{4.25}$$

$$v_t = 1.854\frac{t^{0.6}}{10 + t^{0.6}} \tag{4.26}$$

**The improved CEB-FIP MC78** approach provides the following relation for the creep coefficient, (Müller and Hilsdorf, 1990):

$$\phi(t,t_0) = \beta_a(t_0) + 0.4 \cdot \beta_d(t - t_0) + \phi_f \cdot \left[\beta_f(t) - \beta_f(t_o)\right] \tag{4.27}$$

where

$\beta_a(t_o)$ = rapid initial flow which develops during the first day after load application,

$\beta_d(t-t_o)$ = time development of delayed elasticity,

$\phi_f$ = basic flow coefficient

$\beta_f$ = time development of flow,

t = adjusted age of concrete (Eq. 4.28),

$t_o$ = adjusted age of concrete at time of load application (Eq. 4.28).

$$t, t_o = t_c + \sum^{i} \frac{T_i + 10}{30} \cdot \Delta t_i \geq 1 \tag{4.28}$$

$\Delta t_i$ = number of days where a mean daily temperature $T_i$ [°C] prevails.

The rapid initial flow is given by:

$$\beta_a(t_o) = 0.4 \cdot (1 - 0.2 \log t_o) \cdot \beta_{co} \geq 0 \tag{4.29}$$

The coefficients $\beta_{co}$ and $t_c$ take into account the consistency and type of cement. We will assume a normal, rapid hardening cement of plastic consistency for which $\beta_{co}$=1 and $t_c$=0.

The development of delayed elasticity with time is provided by:

$$\beta_d(t - t_o) = 1 - e^{\left[-0.5(t-t_o)^{0.3}\right]} \tag{4.30}$$

The basic flow coefficient, $\phi_f$, is given by:

$$\phi_f = \beta_{co}(6.5 - 0.05 \cdot RH) \tag{4.31}$$

where RH is the relative humidity in % (50 for our data).

Finally, the time development of flow is:

$$\beta_f(t) = 1 - e^{(1-t^{\beta_{th}})} \tag{4.32}$$

where

$$\beta_{th} = \frac{1}{15} \cdot \log(\frac{25700}{h_o}) \tag{4.33}$$

with $h_o = (2A_c)/u$ (mm)

$A_c$ = area of the concrete section

u = perimeter in contact with the atmosphere.

For the Jamestown Bridge data, Eq 4.27 reduces to Eqs. 4.34, 4.35, and 4.36 for loading at 3, 7, 28 days respectively.

$$\phi(t,t_o) = 3.964 - 0.4 \cdot e^{-0.5(\bar{t}-3.278)^{0.3}} - 4 \cdot e^{1-\bar{t}^{0.168}} \tag{4.34}$$

$$\phi(t,t_o) = 3.3865 - 0.4 \cdot e^{-0.5(\bar{t}-7.649)^{0.3}} - 4 \cdot e^{1-\bar{t}^{0.168}} \tag{4.35}$$

$$\phi(t,t_o) = 2.5151 - 0.4 \cdot e^{-0.5(\bar{t}-30.59)^{0.3}} - 4 \cdot e^{1-\bar{t}^{0.168}} \tag{4.36}$$

In Eqs. 4.34, 4.35, and 4.36 the adjusted time is given by:

$$\bar{t} = \frac{22.78 + 10}{30} t = 1.093t \tag{4.37}$$

where t is age of concrete in days.

The latest **CEB-FIP MC 90** recommendation provides the following equation to predict the creep coefficient:

$$\phi(t,t_o) = \phi_o \cdot \beta_c(t - t_o) \tag{4.38}$$

where $\varphi_o$ = notional creep coefficient, $\beta_c$= function that describes the development of creep with time after loading, t = age of concrete, and $t_o$ = age of concrete at start of loading. The notional creep coefficient is given by:

$$\phi_o = \phi_{RH} \cdot \beta(f_{cm}) \cdot \beta(t_o) \tag{4.39}$$

with

$$\phi_{RH} = 1 + \frac{1 - \frac{RH}{100}}{0.1 \cdot \sqrt[3]{h_o}} \tag{4.40}$$

$$\beta(f_{cm}) = \frac{16.8}{\sqrt{f_{cm}}} \tag{4.41}$$

$$\beta(t_o) = \frac{1}{0.1 + t_o^{0.2}} \tag{4.42}$$

where,

$f_{cm}$ = mean compressive strength of concrete in N / $mm^2$ at the concrete age of 28 days,

RH = relative humidity of ambient environment in %,

$h_o = 2A_c$ /u = notional size of member in mm, where $A_c$ is the cross-section and u is the perimeter of the structural member in contact with the atmosphere. For our data $h_o$=76.2

mm.

The development of creep with time is given by:

$$\beta_c(t - t_o) = \left[\frac{t - t_o}{\beta_H + t - t_o}\right]^{0.3} \tag{4.43}$$

with

$$\beta_H = 1.5 \cdot \left[1 + (0.012 \cdot RH)^{18}\right] \cdot h_o + 250 \leq 1500 \tag{4.44}$$

For the data of the Jamestown Bridge, the creep coefficient, Eq. 4.38, becomes:

$$\phi(t, t_o) = 5.5513 \cdot \frac{1}{0.1 + t_o^{0.2}} \left[\frac{t - t_0}{364.3 + (t - t_o)}\right]^{0.3} \tag{4.45}$$

where $t_o$=3,7, 28, and t=age of concrete in days. The specific creep can be obtained by dividing the creep coefficient by the modulus of elasticity of the concrete.

The measured specific creep for the three sets of data is compared with the ACI committee 209 prediction results, the improved CEB-FIP MC 78 prediction, and the CEB-FIP MC 90 results in Figs. 4.7, 4.8, and 4.9. In all cases the ACI 209 results are lower than the measured creep data whereas the CEB-FIP MC 90 and the Improved CEB-FIP MC 78 are higher. For specimens loaded at 7 days there is very good agreement between the experimental results and the two European guidelines. The agreement for all methods is reasonably good for the 28 days' test data.

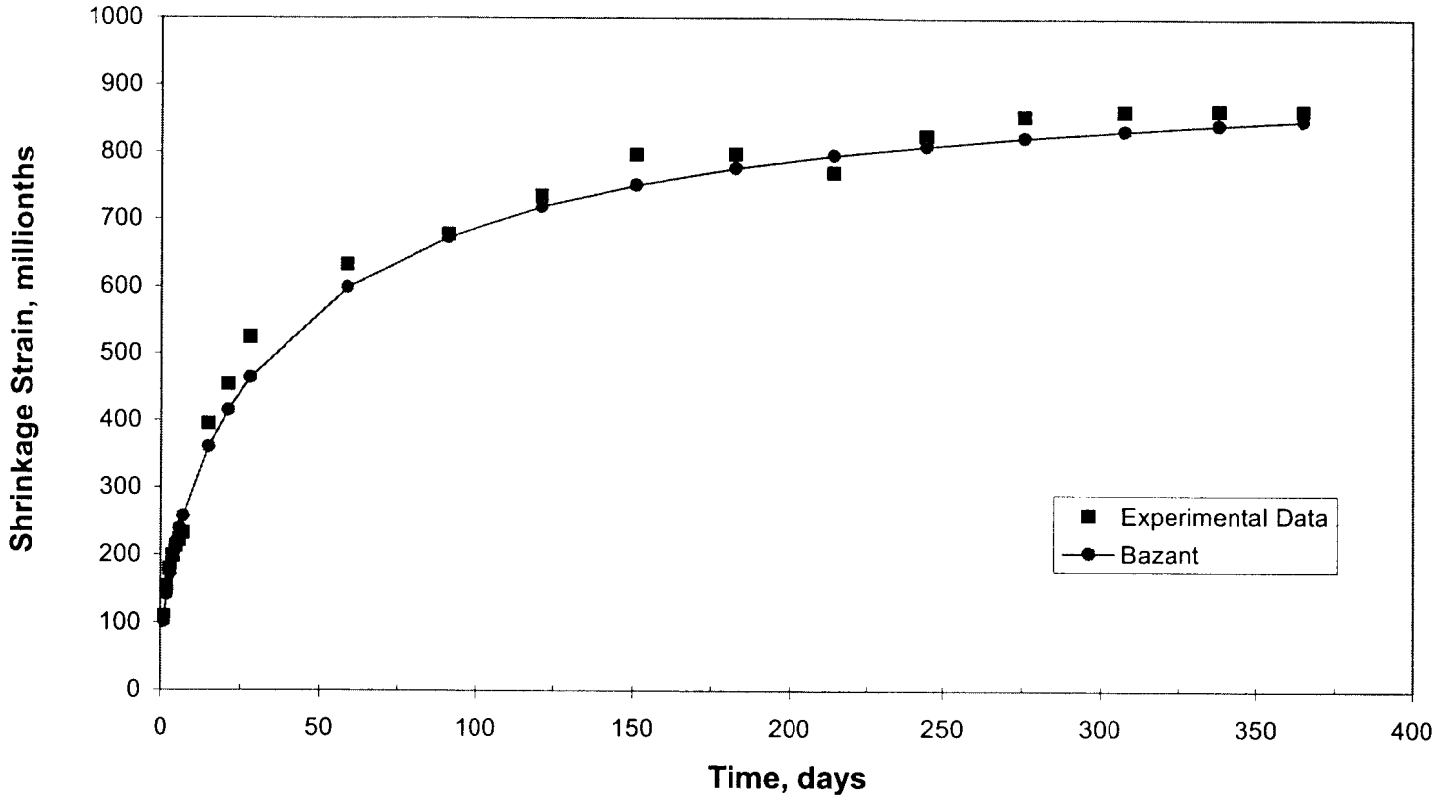


Figure 4.1 Comparison of Experimental Data with Bazant Hyperbolic Function for Specimens Tested 3 Days after Casting

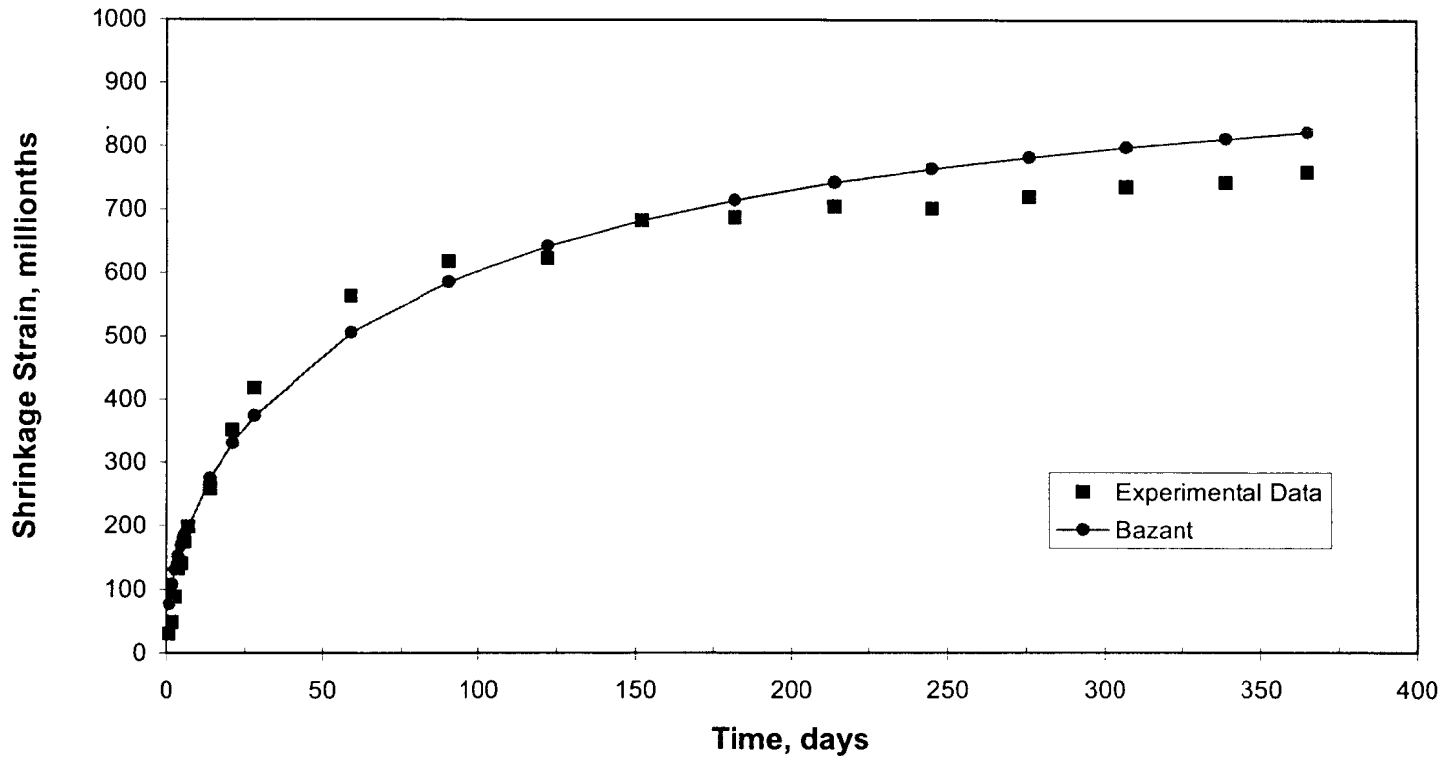


Figure 4.2 Comparison of Experimental Data with Bazant Hyperbolic Function for Specimens Tested 7 Days after Casting

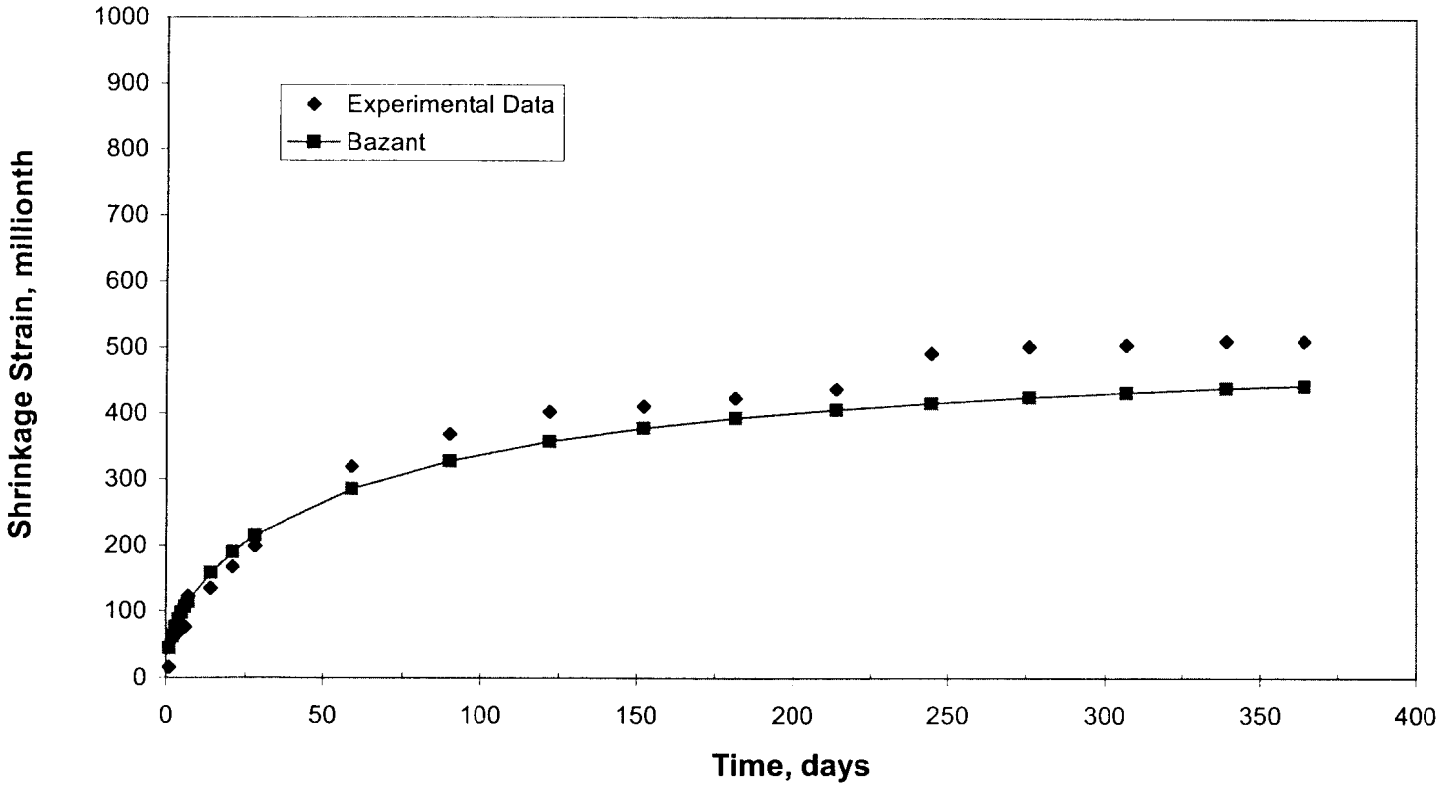


Figure 4.3 Comparison of Experimental Data with Bazant Hyperbolic Function for Specimens Tested 28 Days after Casting

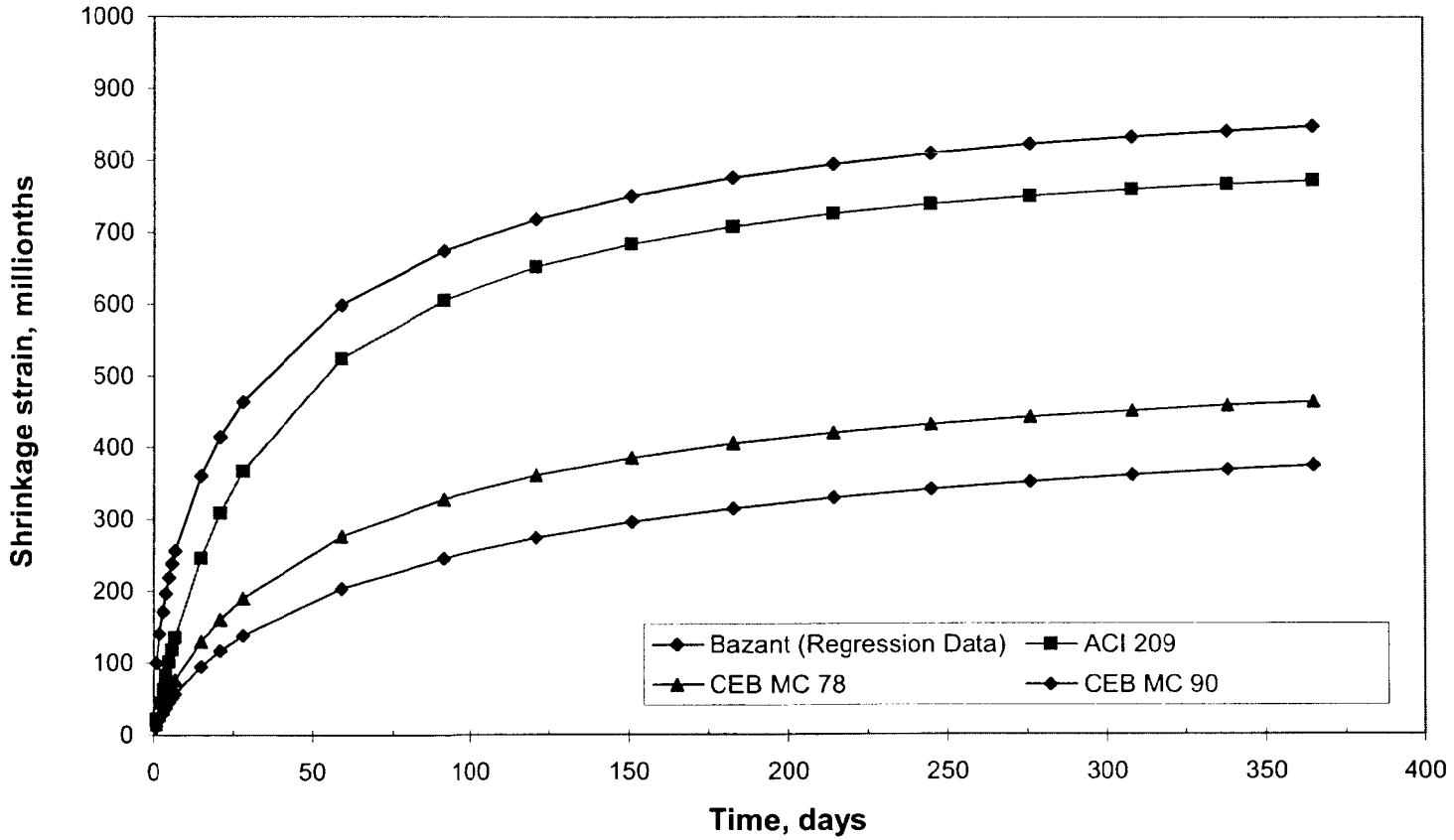


Figure 4.4 Concrete Shrinkage Prediction for Specimens Tested 3 Days after Casting

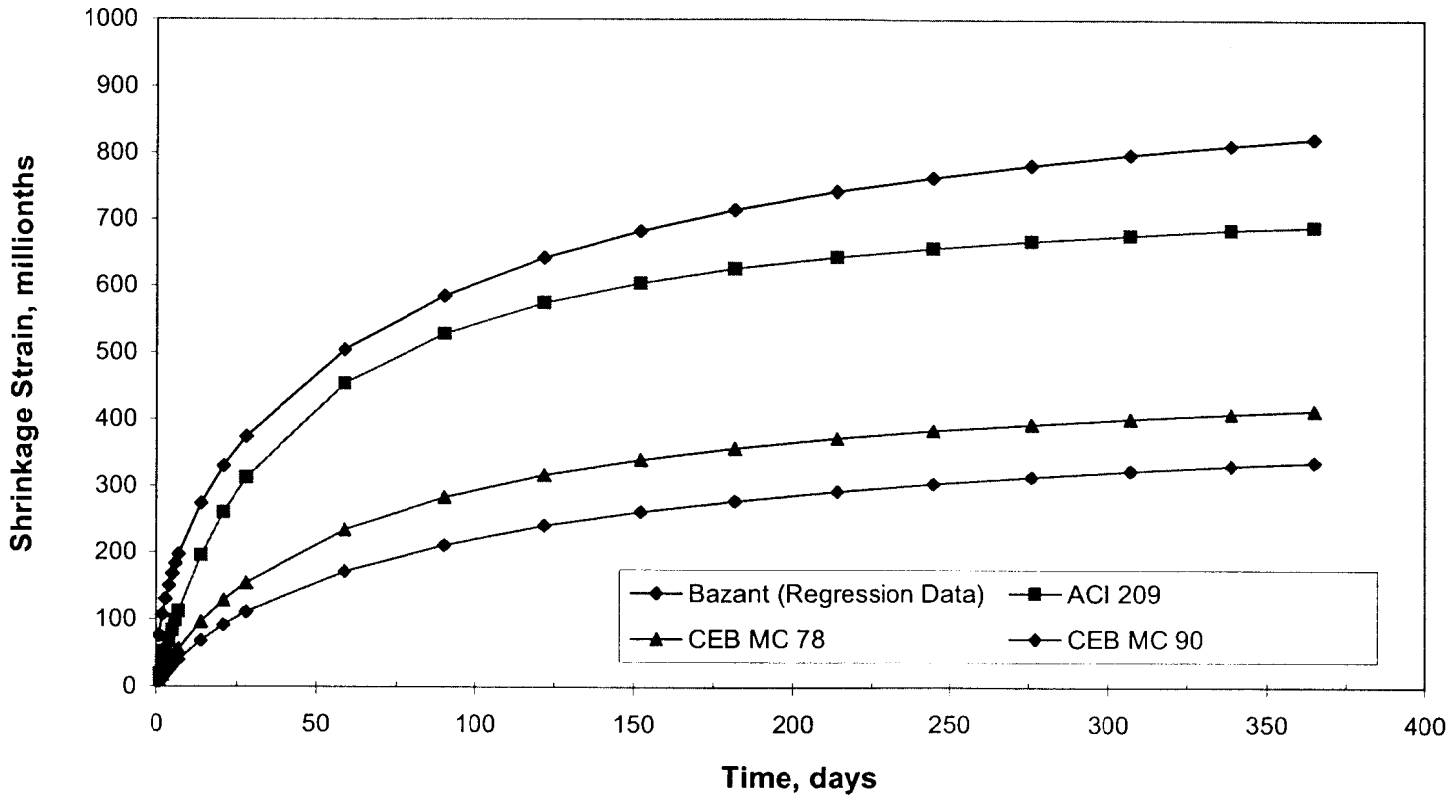


Figure 4.5 Concrete Shrinkage Prediction for Specimens Tested 7 Days after Casting

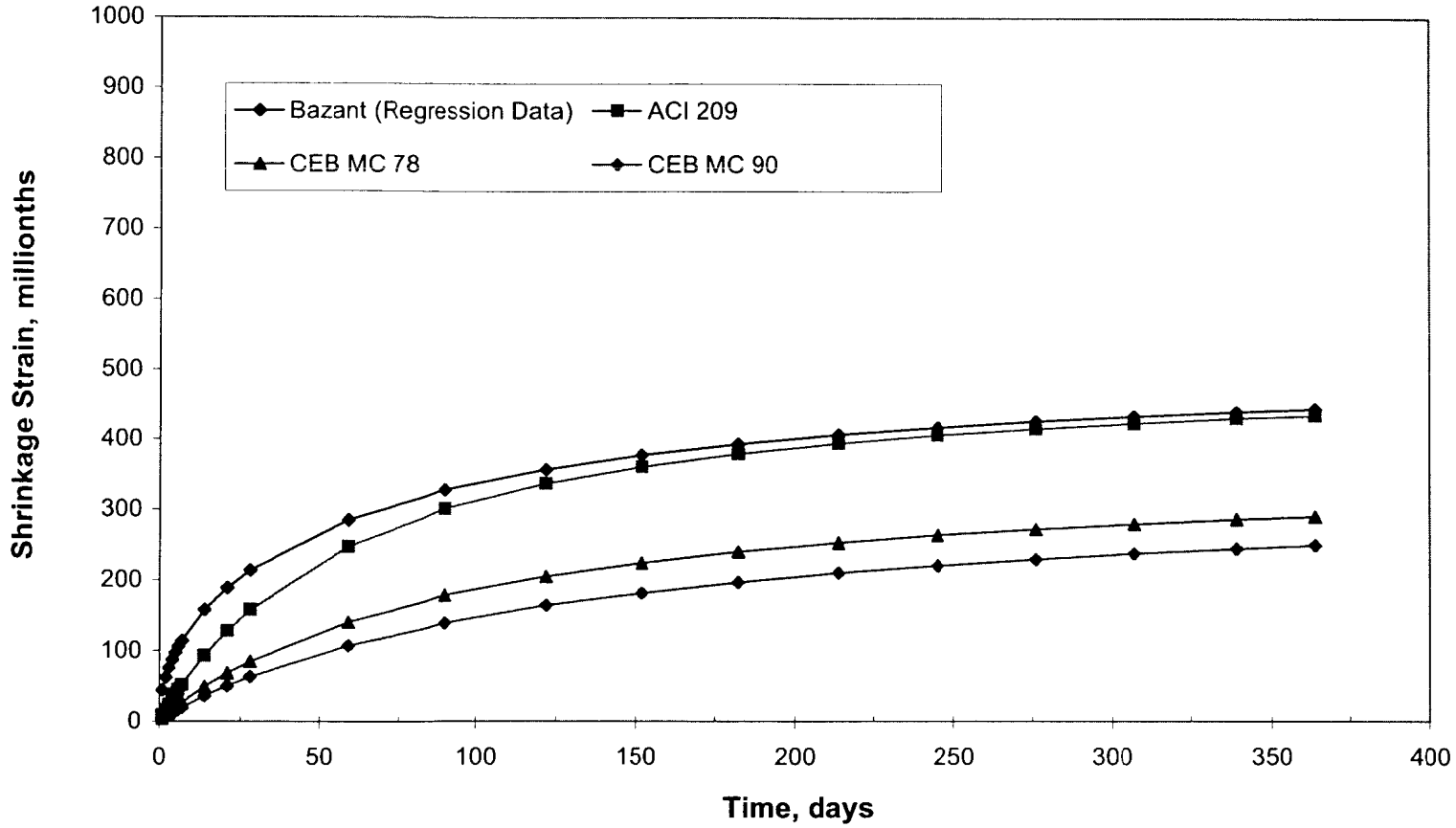


Figure 4.6 Concrete Shrinkage for Specimens Tested 28 Days after Casting

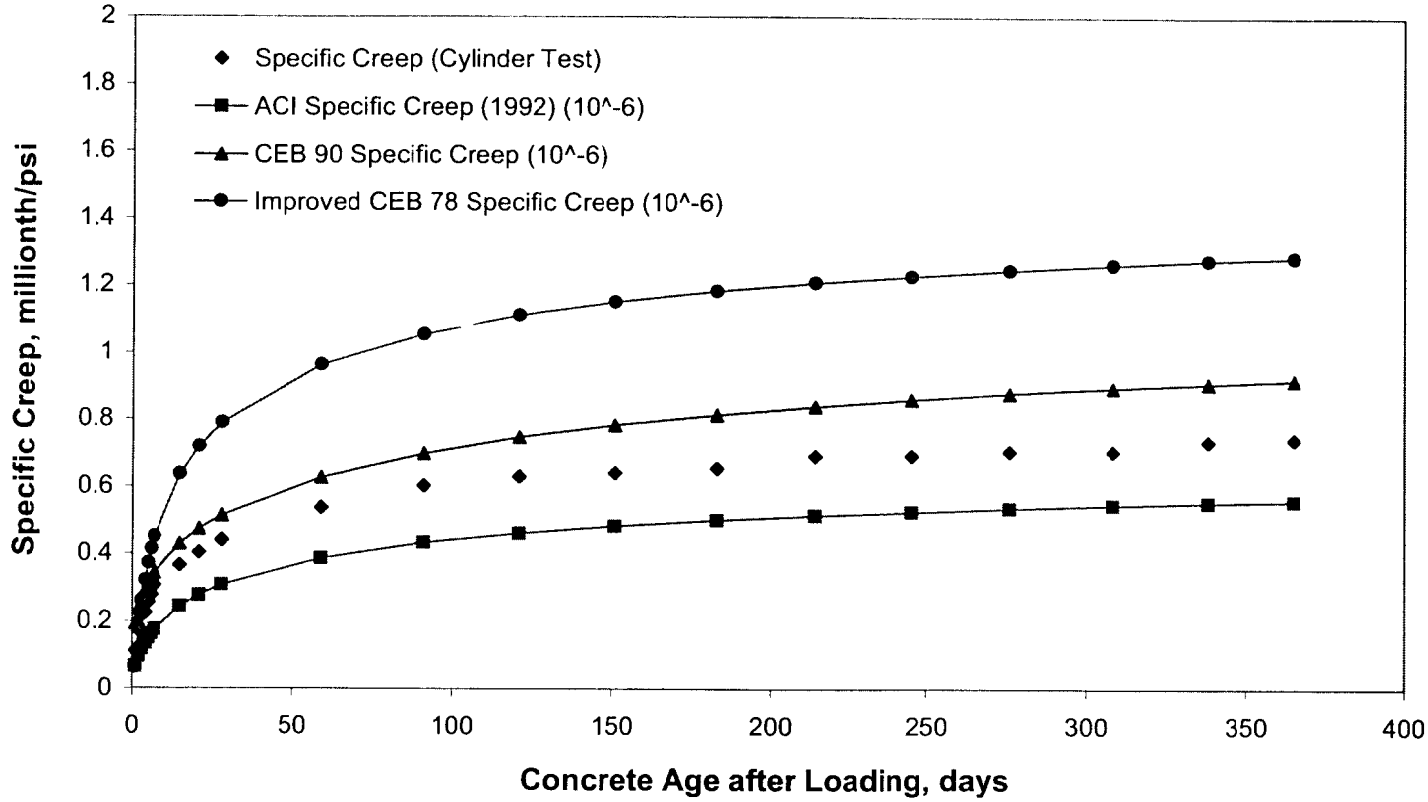


Figure 4.7 Concrete Specific Creep for Loading Start at 3 Days

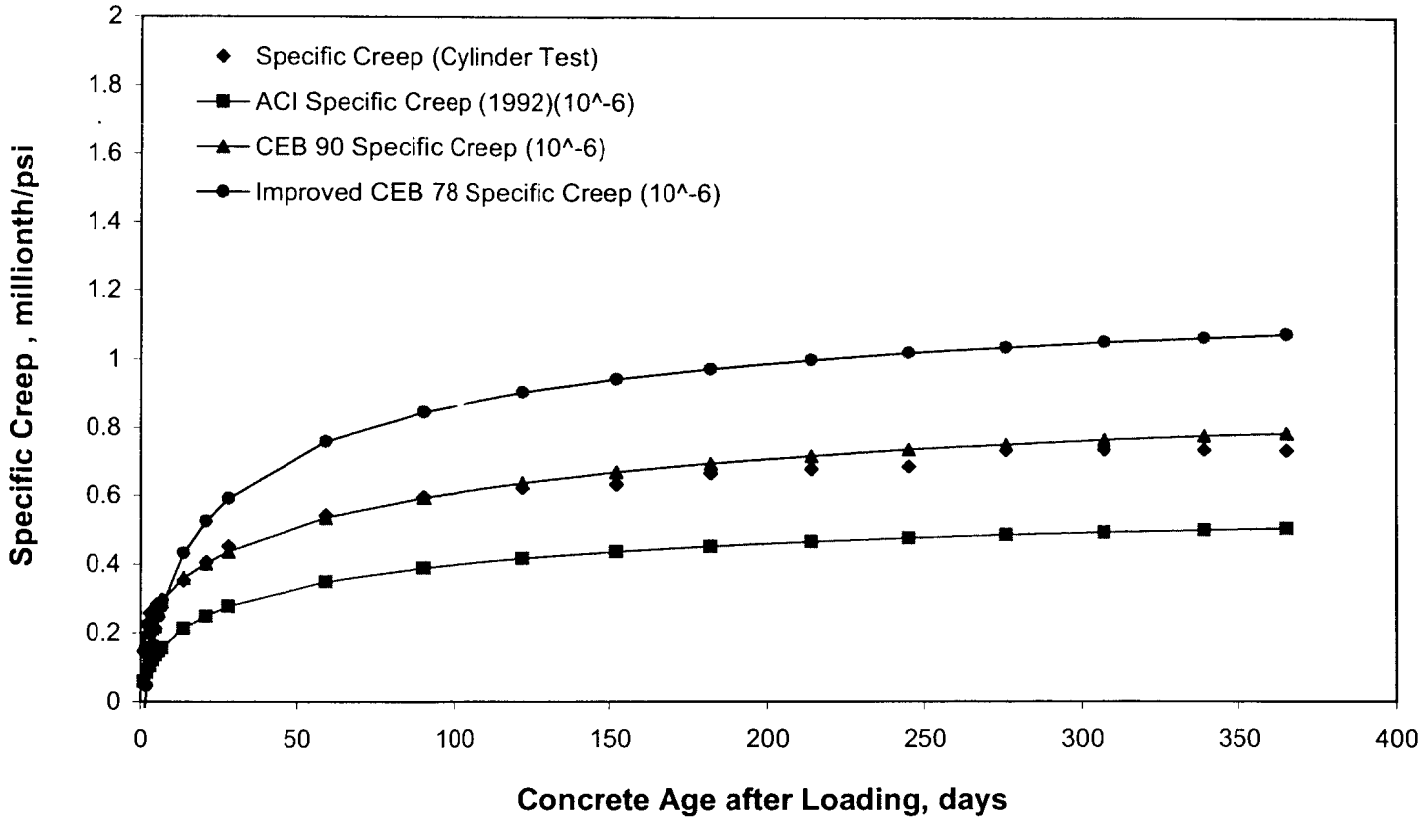


Figure 4.8 Concrete Specific Creep for Loading Starting at 7 Days

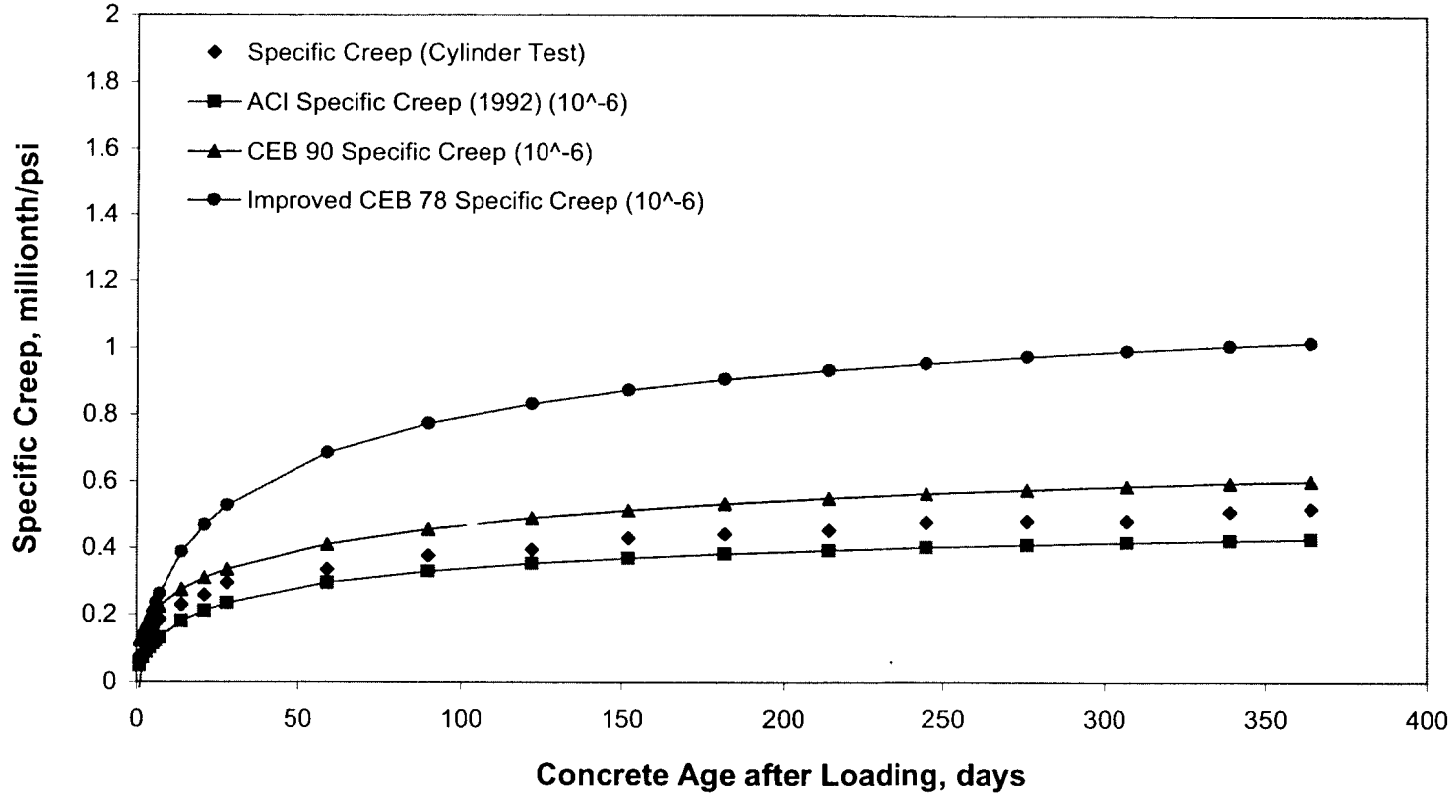


Figure 4.9 Concrete Specific Creep for Loading Starting at 28 Days

# 5. CONCLUSIONS AND RECOMMENDATIONS

This study provides an overview of the monitoring program implemented for Jamestown-Verrazano bridge to study long term thermal, creep and shrinkage affects. In particular, data from a one year period from Fall 1997 to Fall 1998 collected using an Automated Data Acquisition System are presented and analyzed.

The seasonal and diurnal temperature variations at the mid-span closure segment and an adjoining pier are collected and analyzed. The following observations can be made:

- Temperature variations follow clear seasonal patterns. Variations within the concrete superstructure are larger in early fall and late spring seasons.
- Temperature variations in the top slab are much larger than variations in the bottom slab.
- There is a clear nonlinear distribution of the temperatures within the bridge.
- There is a small temperature difference between the north and south cells. It is in the order of 3 °F at the pier but only 1.5 °F at the main span closure section. It is noted however that the sensors are not in the extreme locations of the cross sections. It is expected that temperature differences would be larger between the north and south tip of the cross section.
- Temperatures registered by the Carlson strain meters are lower that the values obtained by the thermocouples.

The distribution of the temperature differentials between the top and bottom of the bridge at the main span closure section is studied. A probability density function is developed to be used in making future predictions. The average difference is about 6 °F but differences as large as 35 °F are observed.

Temperature gradients at the main span closure section are developed. These compare well to the AASHTO bridge design guidelines. It is noted that a longer observation interval than the one

year followed here would give additional information. Concrete strains induced by temperature gradients are of the order of 50 x10 $^{-6}$ in/in.

Concrete shrinkage and creep strains have already taken place by the time of the observation. Shrinkage and creep test data provided by CTL are analyzed and compared to the ACI 209 specifications as well as two European Model codes, the Improved CEB-FIP 78 specification and the CEB-FIP 90 guidelines. In the case of the shrinkage strains the test data agree well with the ACI predictions whereas the European specifications give lower strains. The opposite is true for the case of the creep strains where test data agree with the CEB guidelines but are higher than the ACI specifications. However, the total strains are comparable for all cases. This agrees with other observations. For example, according to the Bridge Design Manual from the Prestressed Concrete Institute (PCI, 1997) several prediction formulas exist for creep and shrinkage. These are primarily based on either ACI Committee 209 or the CEB-FIP Model Code. It is the designer's option to use either the ACI committee 209 or CEB-FIP formulas. It is important however to recognize information from both sources should not be combined in the same design since the ACI procedure leads to higher shrinkage and lower creep values than the CEB-FIP method. It is noted that CEB-FIP Model Code 1978 was used during the original design of the bridge.

It is recommended that the monitoring is continued to analyze a longer pool of temperature data. In addition, a time analysis of the bridge can provide stresses which can be compared with measured values.

## REFERENCES


American Association of State Highway Officials, "AASHTO LRFD bridge Design Specifications." (1994). 1st ed., Washington, D. C.

American Association of State Highway Officials (AASHTO), Guide Specifications for Design and Construction of Segmental Concrete Bridges," 2nd Edition. Washington, D.C., 1999.

ACI Committee 209, (1992). "Prediction of Creep, Shrinkage, and Temperature Effects in Concrete Structures," *Report ACI 209R-92*, American Concrete Institute.

Bazant, Z.P., Osman, E., and Thonguthai, W. (1976). "Practical Formulation of Shrinkage and Creep of Concrete," *Materials and Structures*, 9(54), pp. 395-406.

CEB-FIP Model Code 1990, Comité Euro-International du Beton, *Bulletin No 195.*

Emerson M., "The Influence of the Environment on Concrete Bridge temperatures." *Bulletin d' Information CEB No. 154*, Paris, 1982, pp. 253-268.

Emerson, M., "The Calculation of distribution of Temperature in Bridges." *TRRL Laboratory Report 765*, Department of Transport, Transport and Road Research Laboratory, 1977, Crowthorne, Berkshire.

Kottegoda, N.T., and Russo, R., "Probability, Statistics, and Reliability for Civil and Environmental Engineers." *McGraw-Hill Companies*, Inc., 1997.

Müller, H.S., and Hilsdorf, H.K., (1990). "Evaluation of the Time Dependent Behavior of Concrete," *Bulletin No 199*, Comité Euro-International du Beton (CEB).

Priestley, M. J. N., and Buckle, I. G., "Ambient Thermal Response of Concrete Bridges." *Road Research Unit Bulletin No. 42*, Road Board, Wellington, New Zealand, 1979.

Shiu, K. N., Russell, H. G., and Tabatabai, H., (1991). "Instrumentation of the Red River Bridge at

Boyce, Louisiana." Louisiana Transportation Research Center, FHWA / LA - 91 / 233.

Shushkewich, K. W., "Design of Segmental Bridges for Thermal Gradient." *PCI Journal*, July-August 1998, Vol. 43, No. 4, pp. 120-137.

Tsiatas, G., McEwen, E., and Chen, H., "Monitoring of Long Term Creep and Temperature Behavior of the Jamestown-Verrazzano Bridge." *Interim Report II*, July 1998. University of Rhode Island, Structural Engineering.

Tsiatas, and Chen, H., "Monitoring of Long Term Creep and Temperature Behavior of the Jamestown-Verrazzano Bridge." *Interim Report I*, October 1997. University of Rhode Island.

Weinmann, T. L., and Russell, H.G., "Instrumentation of the Jamestown-Verrazzano Bridge at Jamestown, Rhode Island." *Report*, Construction Technology Laboratories, Inc. (CTL), Skokie, IL, March 1994.

Weinmann, T. L., Berley, A. D., and Reichenbach, R. K., "Operation Manual for the Datalogger System Installed in the Jamestown-Verrazzano Bridge at Jamestown, Rhode Island." *Report*, Construction Technology Laboratories, Inc. (CTL), Skokie, IL, October 1997.

## APPENDIX A

This Appendix summarizes the equations used for the reduction of the data from the Carlson strain meters (1). Each Carlson strain meter has the following properties:

$T_f$ = gage factor in Degrees/Ohm

C = calibration constant

$R_o$ = resistance @ 0 °F (gage factor)

Two readings are taken from each Carlson strain meter, the 3-Lead Resistance (3L), and the Resistance Ratio ($R_T$). The temperature $T_C$ is obtained using the following equation:

$$T_C=(3L-R_o)T_f$$

The corrected strain @ 73 °F is then obtained by:

$$\varepsilon_{73}=100(R_T-R_I)C+(T_C-T_R)\alpha_G-(T_C-T_R)\alpha_C$$

where $T_R$ = reference temperature (73 °F), $\alpha_G = 6.7 \times 10^{-6}$ ppm/°F (coefficient of thermal expansion for the gage), $\alpha_c = 6.35 \times 10^{-6}$ ppm/ °F (coefficient of thermal expansion for concrete).

The value of interest is the corrected strain minus the corrected strain at initial reading given by:

$$-(\varepsilon_{73}-\varepsilon_{73}zero)$$

where $\varepsilon_{73}$ zero is the corrected strain @ 73 °F (for chosen "zero" reading). The minus sign in the above equation is provided for plotting purposes to give a positive value to compressive strains. Zero readings used for gages 1 through 4 were the first readings obtained on 5/9/92. Zero readings used for gages 5 through 19 were the readings obtained on 5/14/92.